ANALYSIS OF POWER DEPOSITION PATTERNS AND ULTRASONIC PHASED ARRAYS FOR LOCALIZED HYPERTHERMIA

BY

KENNETH BLAIR OCHELTREE

B.S., Virginia Polytechnic Institute and State University, 1982
M.S., University of Illinois, 1984

THESIS

Submitted in partial fulfillment of the requirements
for the degree of Doctor of Philosophy in Electrical Engineering
in the Graduate College of the
University of Illinois at Urbana-Champaign, 1987

Urbana, Illinois

ABSTRACT

This thesis examines theoretically the determination of the desired power deposition pattern for localized hyperthermic treatment and the potential for providing precision local hyperthermia by using ultrasonic phased arrays. A method for calculating ultrasonic fields and examples of field patterns produced by square ultrasonic sources are presented. Temperature distributions are calculated from power deposition patterns by using a finite difference solution to the bioheat transfer equation. The combination of these two methods allows calculation of temperature distributions produced by a given applicator design.

The power deposition patterns that are required to uniformly raise (and maintain) the temperature throughout the tumor to hyperthermic levels are examined. A method is discussed which uses the steady state bioheat transfer equation and the desired temperature distribution in normal and tumor tissues to calculate the desired steady state power deposition pattern. This approach is demonstrated analytically for half-space, cylindrical, and spherical tumor models. Transient power deposition patterns are derived from the time dependent bioheat transfer equation, and analytical solutions are developed for half-space and spherical tumor models. A three dimensional numerical method is presented which allows calculation of time dependent power deposition patterns for arbitrarily shaped

tumors.

A method is discussed which uses the steady state bioheat transfer equation and the desired temperature distributions in normal and tumor tissues to aid in ferromagnetic seed placement and ultrasonic scan path determination. Methods for forming the required power deposition patterns using practical hyperthermia systems are examined. The design considerations for an ultrasonic hyperthermia phased array are discussed.

An examination is made of an ultrasonic stacked linear phased array applicator for hyperthermia designed for deep heating. The power deposition pattern for this applicator is compared to that for a fixed focus applicator for a circular scan path. The high intensity necessary for generating hyperthermia by scanning a focal region and the large number of focal locations required to cover a typical tumor volume limit the applicability of phased array focal scanning. A method is presented for producing enlarged foci with a phased array so that the required number of scan locations is significantly reduced.

ACKNOWLEDGEMENTS

My appreciation is extended to my thesis advisor Professor Leon Frizzell for his time, his support, and the freedom given in this project. Thanks are given to Professors Richard Magin and Charles Cain for beneficial discussions that assisted this work. Additionally, appreciation is extended to Professors Floyd Dunn and John Chato for serving on my committee and their helpful comments. Robert Cicone deserves special thanks for his exacting and aesthetic drafting work. Wanda Elliott receives my appreciation for her administrative assistance and her help in preparing this manuscript. My deepest appreciation goes to those mentioned above and the following who made the Bioacoustics Research Laboratory a home away from home and a place to remember: George Bark, Kay Carnes, Tom Cavicchi, Felice Chu, Joe Cobb, Nancy Dimond, Dr. Mike Haney, John McCarthy, Billy McNeill, Mike Niesman, Jim Novak, Professor Burks Oakley, Professor William O'Brien, Scott Smith, Harold Underwood, Professor Bruce Wheeler, Jian Zhang, and many others who are not named, but not forgotten.

The support of this project by Labthermics Technologies, Inc., a Caterpillar Fellowship, and the National Institutes of Health Training Grant CA 09067 is gratefully acknowledged.

TABLE OF CONTENTS

CHAPTER 1

INTRODUCTION

The application of hyperthermia to cancer therapy was inspired by observations of the spontaneous regression of tumors due to fever. This led to the injection of toxins for artificially inducing a fever, producing hyperthermia of unpredictable duration and unmeasurable dosage. The applications of hyperthermia that followed this primative approach were described by Neymann in 1938 and included: electric current diathermy at 1 MHz, radiothermy at 10 to 100 MHz, and electromagnetic induction at 12 MHz (Short and Turner, 1980).

The first therapeutic applications of ultrasound began around the time of Neymann's report and were published in 1944 (Horvath, 1944). After a period of enthusiastic growth in the 1940's for this new cancer therapy, pessimistic results led to a resolution in 1949 that ultrasound was unsuitable for cancer therapy and its usage should be stopped (Florrisson, 1949). However, basic laboratory studies on the bioeffects of ultrasound continued (Kremkau, 1979).

Laboratory results that suggested sensitivity of tumor tissue to heat have led to a resurgence of interest in hyperthermia in the last two decades (Kremkau, 1979). The heat sensitivity was not an intrinsic property of the tumor tissue, but was due to the prevailing conditions of nutritional deprivation, chronic hypoxia and low pH found in

the interior of a tumor (Hahn, 1984). Early hyperthermia systems provided regional heating so that, with the heat sensitivity of the tumor tissue, more tumor tissue than normal tissue would be affected. Results were promising, but the heat sensitivity alone was not enough to provide a sufficient difference in the rate of cell death between normal and tumor tissues; local hyperthermia was proposed to provide additional selectivity. Local hyperthermia involves elevation of the tumor temperature above that of the surrounding normal tissue, so that both the temperature differential and the heat sensitivity differential cause additional tumor cell killing.

This thesis examines theoretically the determination of the desired power deposition patterns and the potential for providing precision local hyperthermia by using ultrasonic phased arrays. In Chapter 2, the methods used for calculating ultrasonic fields and temperature distributions are described. The ultrasonic field calculation has been presented previously (Ocheltree, 1984), and is included for completeness. Additionally, field patterns produced by square ultrasonic sources are presented, allowing the characterization of the field for square hyperthermia applicators (Underwood, 1986). Temperature distributions are calculated from power deposition patterns by using a finite difference solution to the bioheat transfer equation. The combination of these two methods allows calculation of temperature distributions produced by a given applicator design.

Hyperthermia system design has concentrated on developing configurations that allow control of power deposition patterns. In Chapters 3 and 4, methods for the determination of the power deposition pattern required to produce a desired temperature distribution for hyperthermia treatment are presented, and these results are applied to general applicator design in Chapter 5. In Chapter 3, a method is discussed which uses the steady state bioheat transfer equation and the desired or target temperature distributions in normal and tumor tissues to calculate the desired steady state power deposition patterns. This prospective thermal dosimetry approach is demonstrated analytically for three tumor models: an infinite half-space model, an infinite cylinder model, and a spherical model. A three dimensional numerical method is demonstrated for two different tumor geometries.

In Chapter 4, the power deposition patterns that are required to uniformly raise (and maintain) the temperature throughout the tumor to hyperthermic levels are examined. The power deposition patterns are derived from the time dependent bioheat transfer equation. This is demonstrated analytically for an infinite half-space tumor model and a spherical tumor model. A three dimensional numerical method is presented which allows calculation of time dependent power deposition patterns for arbitrarily shaped tumors. This method is applied to an example of a spherical tumor.

A method is discussed in Chapter 5 which uses the steady state bioheat transfer equation and the target

temperature distributions in normal and tumor tissues to aid in ferromagnetic seed placement and ultrasonic scan path determination. The results of Chapters 3 and 4 are applied to general applicator design and utilization.

In Chapter 6, the design considerations for an ultrasonic hyperthermia phased array are discussed. Both frequency and applicator size are examined in their relation to such factors as optimum efficiency, gain, and underlying bone heating. A range of acceptable values for each design parameter is presented.

In Chapter 7, an examination of an ultrasonic stacked linear phased array applicator for hyperthermia designed to heat tumors at depths from 5 to 10 cm is made (Ocheltree et al., 1984). The power deposition pattern for this applicator is compared to that for a fixed focus applicator for a circular scan path. The power deposition pattern for the stacked linear phased array shows hot spots that are not observed for the mechanically scanned fixed focus applicator. The overall performance of the stacked linear phased array applicator compared to that of a fixed focus applicator is summarized.

The high intensity necessary for generating hyperthermia by scanning a focal region and the large number of focal locations required to cover a typical tumor volume limit the applicability of phased array focal scanning. In Chapter 8, a method is presented for producing enlarged foci with a phased array so that the required number of scan locations is significantly reduced. Advantages as well as

limitations of this method are discussed.

In Chapter 9, recommendations for future work on hyperthermia linear phased arrays are given, along with discussion of other promising designs. The overall potential of ultrasound phased array hyperthermia is discussed.

CHAPTER 2

METHODS FOR CALCULATION OF ULTRASONIC FIELDS AND TEMPERATURE DISTRIBUTIONS

2.1 Sound Field Calculation

The sound field due to a circular piston vibrating in an infinite, plane, rigid baffle has been the subject of many papers and has been well characterized (Zemanek, 1970). Since a circular piston has only one descriptive dimension, namely the radius in wavelengths, and axial symmetry is present, the field for a range of sizes of circular sources can be presented in a series of field cross-sections. Due to the availability of calculated fields for circular pistons, one can often characterize the field of a device by examining published results, and an efficient field calculation routine is not required.

The fields due to rectangular pistons cannot be characterized as easily since rectangular sources have two descriptive dimensions, lacking the axial symmetry characteristic of circular sources (Freedman, 1959). Complete characterization of the field for a source of one size requires a series of field cross-sections. Therefore, the task of calculating and presenting the field patterns for rectangular sources is two degrees more complex than that of presenting circular piston fields due to the additional descriptive dimension and the lack of radial symmetry. These additional degrees of complexity make an

efficient field calculation method, such as described below, very desirable.

2.1.1 Methods

The presence of the plane rigid baffle yields the following expression for the sound pressure amplitude, p_o, at a point

$$p_o = \frac{j\rho c}{\lambda} \int_S u \frac{e^{-(\alpha+jk)r}}{r} dS \qquad (2.1)$$

where the integration is over the complete radiating surface S, ρ is the density of the medium, c is the phase velocity of the sound waves, u is the velocity amplitude of the piston, λ is the wavelength, k is the wave number, α is the attenuation coefficient, and r is the distance between the field point and an elemental area of the piston. This integral is often evaluated by using Huygen's principle and summing the contribution from closely spaced point sources representing the radiating surface.

A more efficient approach has been developed that uses the summation of the contributions of small rectangular sources to represent the radiating surface (Ocheltree, 1984). This method is implemented by dividing the source into a number of elements that are too large to be represented as point sources. The total pressure p_o at a point in the field is then the sum of the pressure contributed from each element:

$$p_o = \frac{j\rho c}{\lambda} \sum_{n=1}^{N} u_n \iint_{\Delta A} \frac{e}{r}^{-(\alpha+jk)r} \, dA \tag{2.2}$$

where N is the number of elements of size $\Delta A = \Delta h \Delta w$ and u_n is the complex surface velocity for element n. The complex surface velocity u_n is the same for all elements when a simple rectangular source is considered. For a phased array, u_n is used to represent the different phase and magnitude of the velocity on each element of the array. The center of element n (subelement n in the case of a multielement transducer) is denoted by (x_n, y_n) to simplify the analysis that follows. To simplify the integration, a coordinate system in x_o and y_o with its origin centered on an element is defined as shown in Fig. 2.1. Using these relations in Eq. (2.2) yields

$$p_o = \frac{j\rho c}{\lambda} \sum_{n=1}^{N} u_n \int_{-\frac{\Delta h}{2}}^{\frac{\Delta h}{2}} \int_{-\frac{\Delta w}{2}}^{\frac{\Delta w}{2}} \frac{e}{r}^{-(\alpha+jk)r} \, dx_o \, dy_o \tag{2.3}$$

where

$$r = \sqrt{z^2+(x-x_n-x_o)^2+(y-y_n-y_o)^2} \ . \tag{2.4}$$

Up to this point all expressions for the pressure have been exact. To find an expression for the pressure that is easily evaluated numerically, suitable approximations and their regions of applicability are defined.

By choosing Δh and Δw to be small, the distance to the field point is made much greater than the dimensions of the source and the Fraunhofer approximation can be applied. To

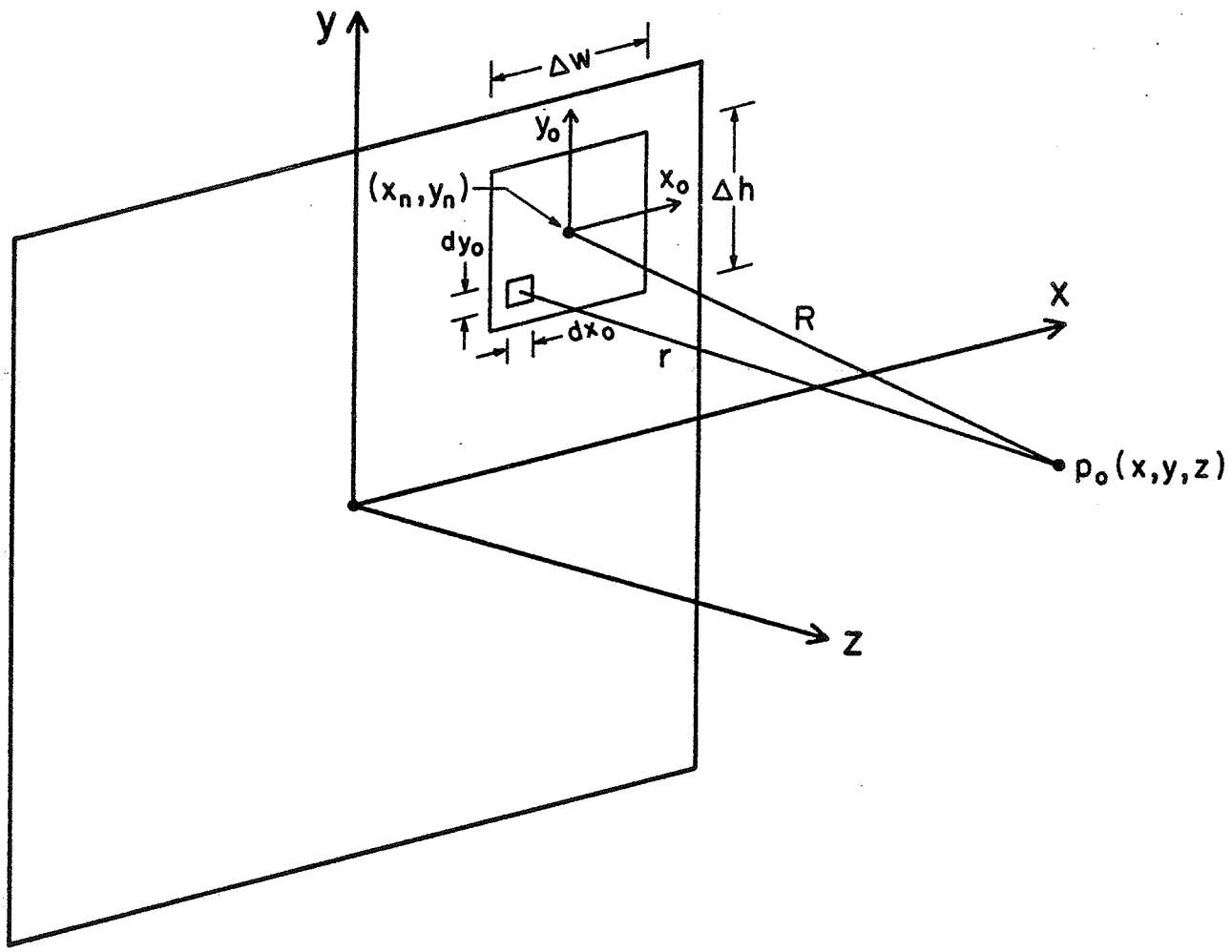

Figure 2.1. Coordinate system and geometry used for rectangular radiator method.

simplify application of the Fraunhofer approximation, we define the intermediate variables $x_n' = x - x_n$ and $y_n' = y - y_n$. The Fraunhofer approximation takes the distance from the origin of the element to the point of interest in the field

$$R = \sqrt{z^2+(x-x_n)^2+(y-y_n)^2}$$

$$R = \sqrt{z^2+x_n'^2+y_n'^2} \tag{2.5}$$

to be large compared to x_o and y_o, i.e., $R >> x_o$ and $R >> y_o$. Thus,

$$e^{-(\alpha+jk)\sqrt{z^2+(x_n'-x_o)^2+(y_n'-y_o)^2}} =$$

$$e^{-(\alpha+jk)\sqrt{R^2-2x_n'x_o-2y_n'y_o+x_o^2+y_o^2}} \tag{2.6}$$

Using the first two terms of a binomial expansion of the radical on the right side of Eq. (2.6) yields

$$e^{-(\alpha+jk)\sqrt{z^2+(x_n'-x_o)^2+(y_n'-y_o)^2}} \cong$$

$$e^{-(\alpha+jk)\,(R-x_n'x_o/R-y_n'y_o/R+x_o^2/2R+y_o^2/2R)} \tag{2.7}$$

For $kx_o^2/2R + ky_o^2/2R$ small compared to π, omission of these terms produces a negligible phase error and gives the expression

$$e^{-(\alpha+jk)\sqrt{z^2+(x_n'-x_o)^2+(y_n'-y_o)^2}} \cong e^{-(\alpha+jk)(R-x_n'x_o/R-y_n'y_o/R)}. \quad (2.8)$$

Substituting this equation into Eq. (2.3), and assuming $1/r \cong 1/R$ and substituting into Eq. (2.3) give

$$p_o = \frac{j\rho c}{\lambda} \sum_{n=1}^{N} \frac{u_n}{R} e^{-(\alpha+jk)R} \int_{-\frac{\Delta w}{2}}^{\frac{\Delta w}{2}} e^{(\alpha+jk)\frac{x_n'x_o}{R}} dx_o \int_{-\frac{\Delta h}{2}}^{\frac{\Delta h}{2}} e^{(\alpha+jk)\frac{y_n'y_o}{R}} dy_o. \quad (2.9)$$

The assumption that $e^{\alpha x_n'x_o/R} \cong 1$ for $\Delta w > x_o > -\Delta w$ and the equivalent condition for y_o are used to reduce the two integrals in Eq. (2.9) to Fourier transform expressions which upon evaluation yield

$$p_o = \frac{j\rho c \Delta A}{\lambda} \sum_{n=1}^{N} \frac{u_n}{R} e^{-(\alpha+jk)R} \operatorname{sinc}\left(\frac{kx_n'\Delta w}{2R}\right) \operatorname{sinc}\left(\frac{ky_n'\Delta h}{2R}\right). \quad (2.10)$$

Equation (2.10) is a straightforward expression for the pressure due to a rectangular source, but is only useful if the approximations used are applicable. The three assumptions used to derive Eq. (2.10) are that $kx_o^2/2R + ky_o^2/2R$ is small compared to π, $1/r \cong 1/R$, and $e^{\alpha x_n'x_o/R} \cong 1$. Since the maximum values of x_o and y_o are $\Delta w/2$ and $\Delta h/2$, respectively, these conditions can be expressed as: 1) $\cos(k\Delta w^2/8R + k\Delta h^2/8R) \cong 1$, 2) $r/R \cong 1$, and 3) $e^{\alpha(x_n'\Delta w + y_n'\Delta h)/2R} \cong 1$.

These conditions provide limitations on the sizes of Δw and Δh that can be used for computation. The first condition provides the limitation on Δw that $\pi >> k\Delta w^2/8R$. This condition can be rewritten as $R >> \Delta w^2/4\lambda$, which is equivalent to the provision that the field point be in the

farfield for a source of size Δw. Since z is less than R, an equivalent condition is $z >> \Delta w^2/4\lambda$. A constant F can be defined such that the first condition is given by the following relation:

$$\Delta w \leq \sqrt{\frac{4\lambda z}{F}} . \qquad (2.11)$$

The constant F represents the distance from the source to the field point relative to the distance to the nearfield-farfield transition for a source of size Δw. The inequality sign in Eq. (2.11) has been retained so that Δw may be chosen to be smaller than the value an equality would yield, such that the exact area of the source can be represented. Likewise, a similar relation applies to the selection of Δh.

The use of Eq. (2.11) for determining Δw and Δh ensures that the second and third conditions are satisfied. Also, significant cancellation of errors occurs from one side of an element to the other side, so that actual errors are less than would be predicted by a first order approximation and a second order analysis is required to establish an upper bound on the error.

Equation (2.10) was implemented on a VAX 11/730 with Δw and Δh as given by Eq. (2.11). The relationship between the size of the element and z, given by Eq. (2.11), was used to minimize computation time by reducing the number of elements as the distance from the array increased. This preserved the same degree of accuracy for the entire field, but reduced computation time. Examples of the results of

applying this method of computation to a square source and a phased array are given in Appendices A and B, respectively.

2.1.2 Results and Discussion

The rectangular radiator method was used to calculate the acoustic field for a range of sizes of square sources radiating in a lossless medium. The fields are illustrated in Figs. 2.2 to 2.8 using contour plots of the -3 and -6 dB levels for a longitudinal section in the x-z (y = 0) plane (coordinates are given in Fig. 2.1), with the field normalized at each axial (z) distance. Included with these results are plots of the normalized axial intensity. Axial distances were made relative to the nearfield-farfield transition distance (length of source squared divided by four times the wavelength) to remove frequency dependence and to aid in comparison with the results for a circular source as computed by Zemanek. This normalized field approaches a limiting pattern as the source size becomes much larger than a wavelength, a behavior observed for a circular source as well (Zemanek, 1971). As a single cross section is not completely sufficient to characterize the field for a square source, a section taken diagonally (x = y) through a 2 wavelength square source is shown in Fig. 2.9 to illustrate that the field does not vary significantly from the y = 0 section shown in Fig. 2.4.

Sound pressure contours for a circular source, as produced by Zemanek, are shown in Fig. 2.10. The differences between the field for a circular source and a

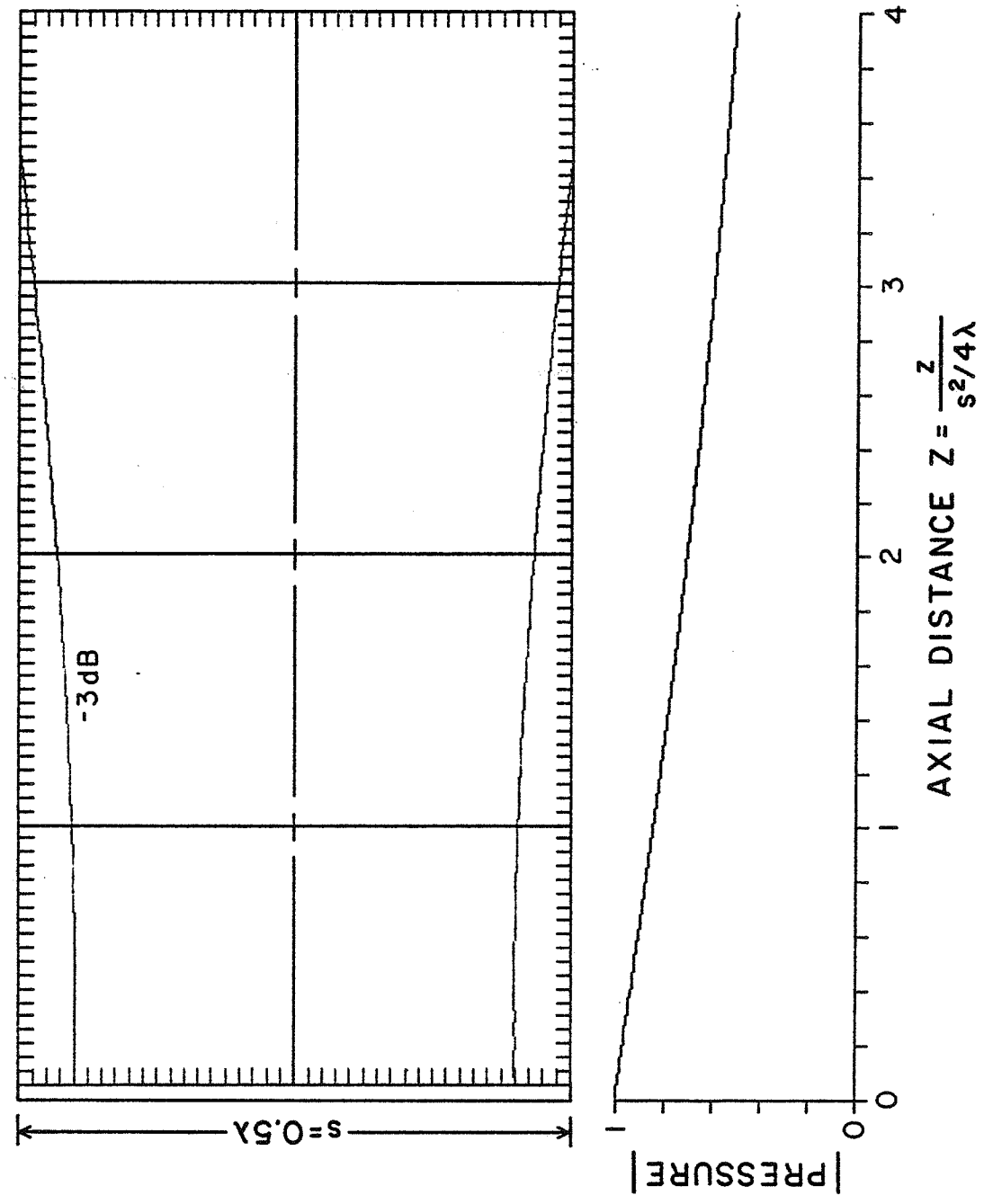

Figure 2.2. Square source with sides equal to 0.5λ; (a) sound pressure contour and (b) normalized magnitude of on-axis pressure.

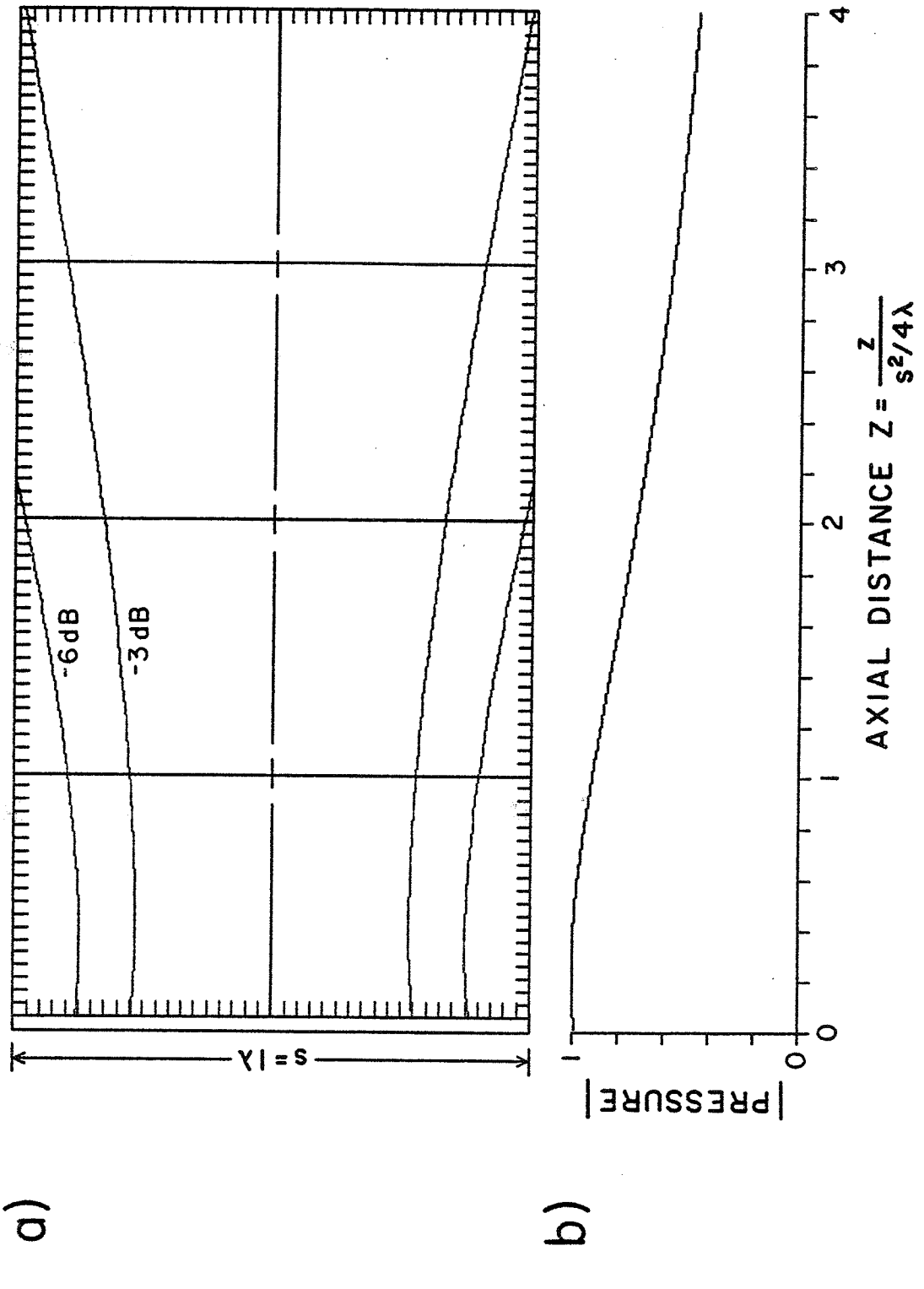

Figure 2.3. Square source with sides equal to 1λ; (a) sound pressure contour and (b) normalized magnitude of on-axis pressure.

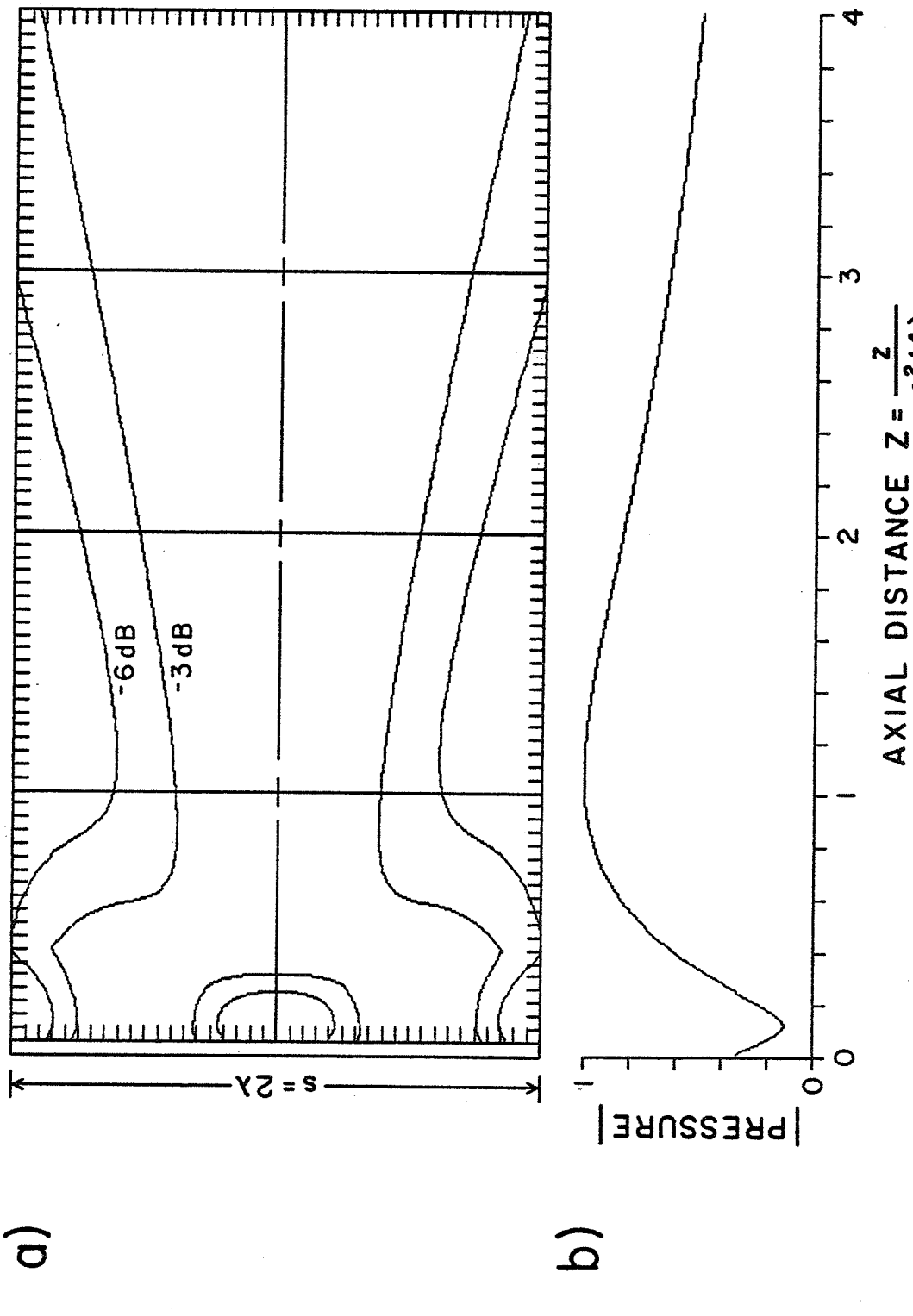

Figure 2.4. Square source with sides equal to 2λ; (a) sound pressure contour and (b) normalized magnitude of on-axis pressure.

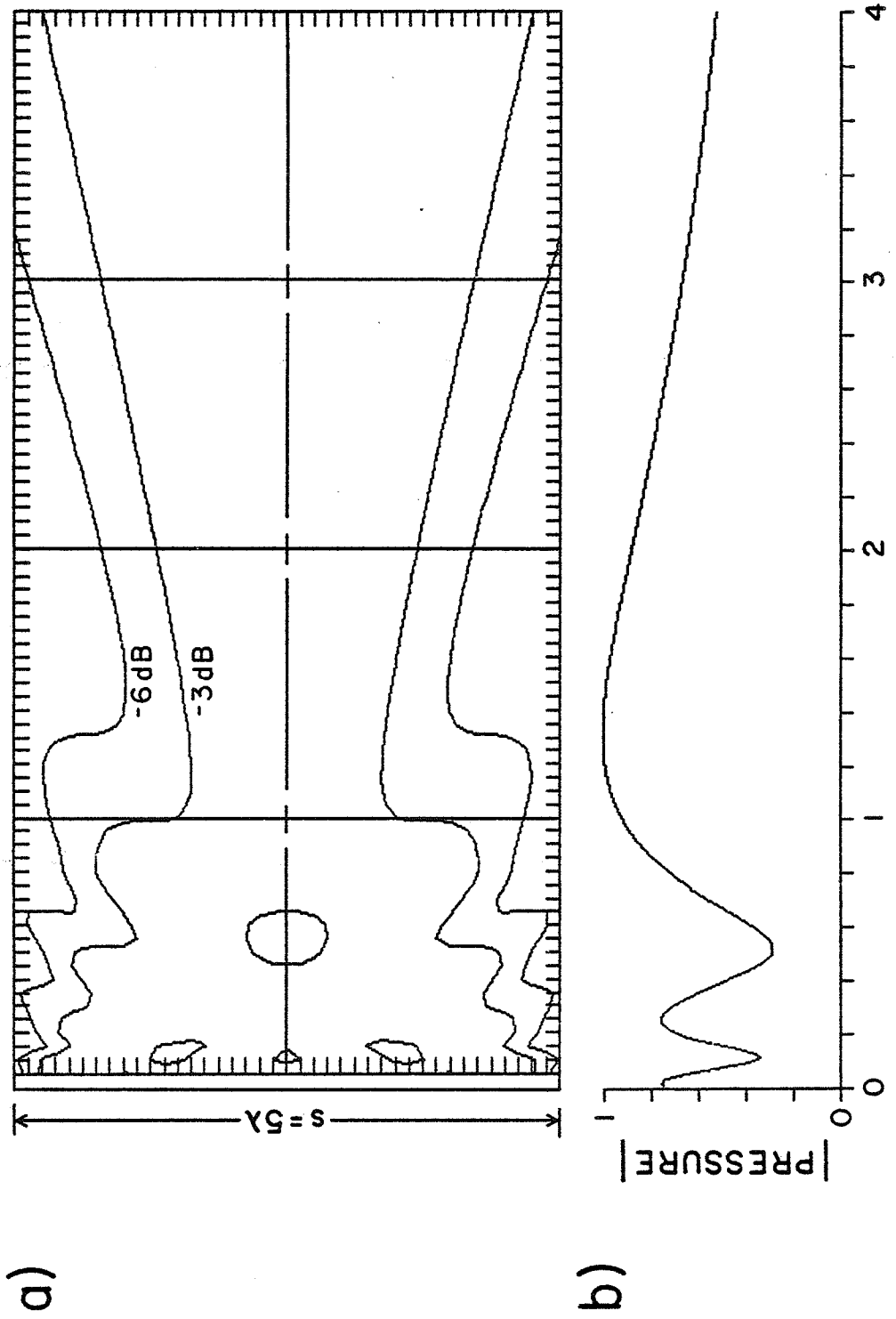

Figure 2.5. Square source with sides equal to 5λ; (a) sound pressure contour and (b) normalized magnitude of on-axis pressure.

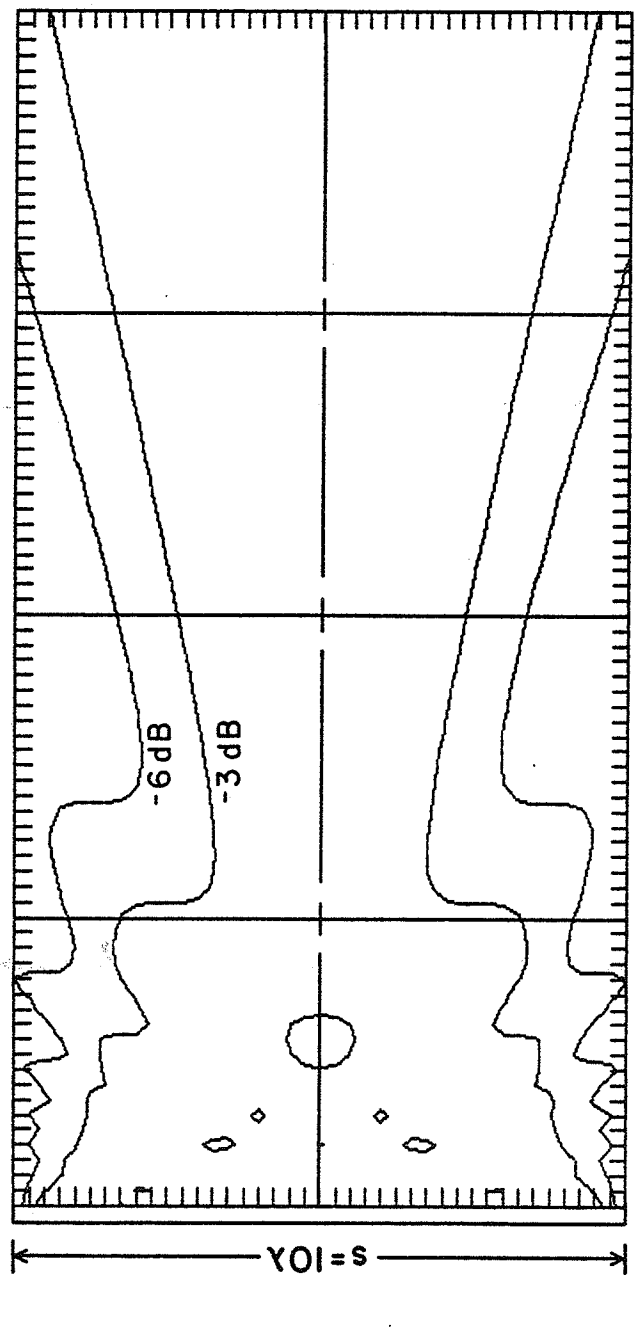

Figure 2.6. Square source with sides equal to 10λ; (a) sound pressure contour and (b) normalized magnitude of on-axis pressure.

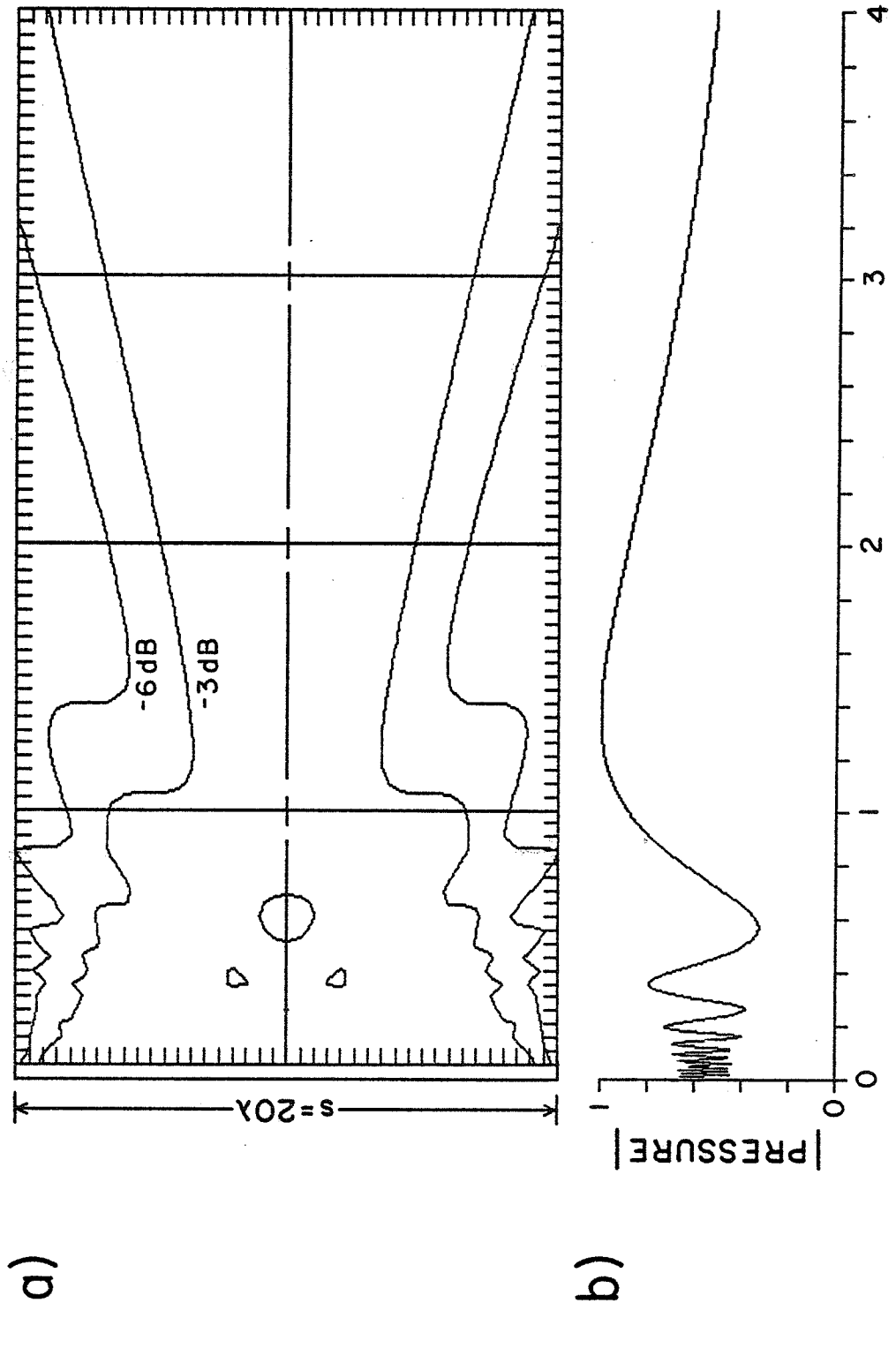

Figure 2.7. Square source with sides equal to 20λ; (a) sound pressure contour and (b) normalized magnitude of on-axis pressure.

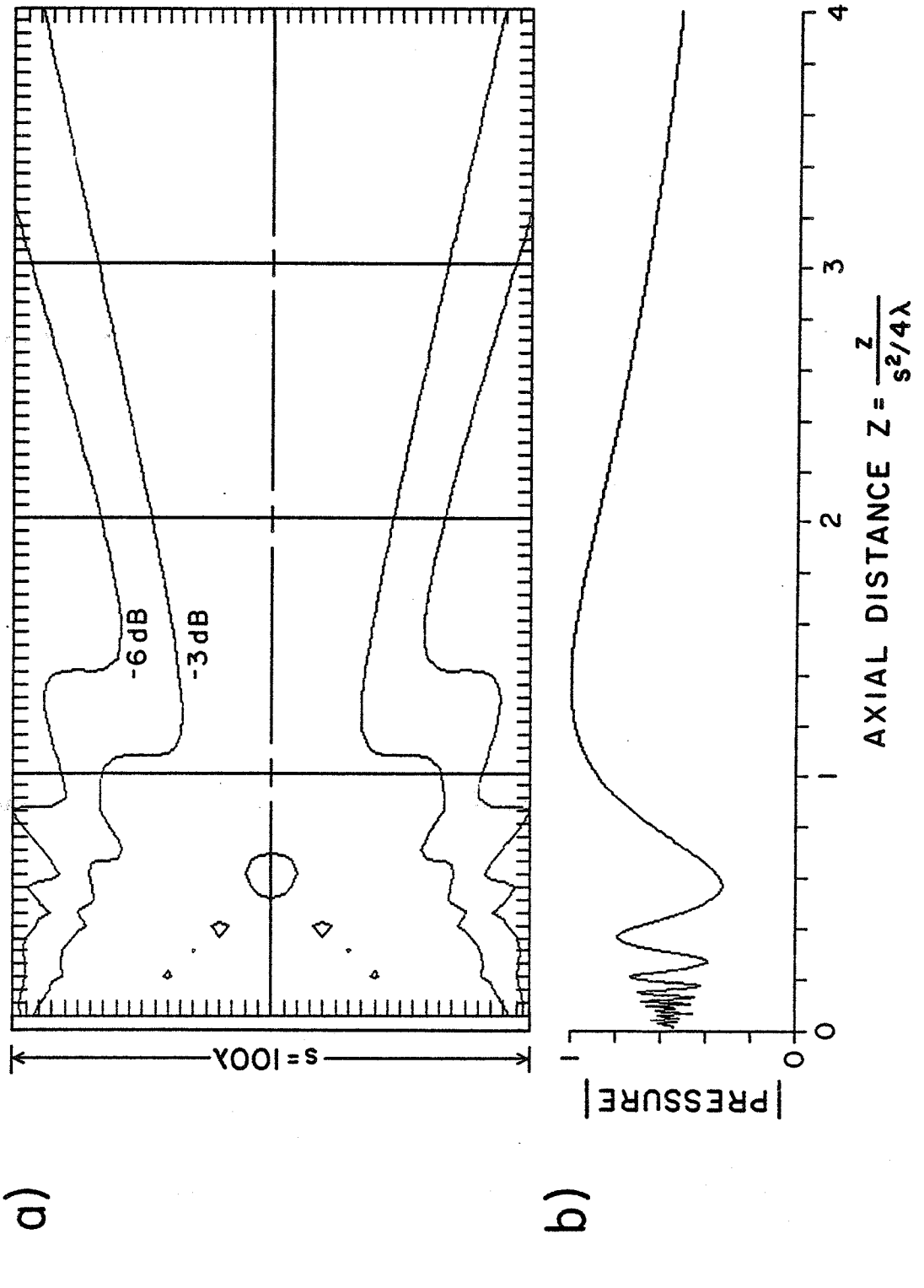

Figure 2.8. Square source with sides equal to 100λ; (a) sound pressure contour and (b) normalized magnitude of on-axis pressure.

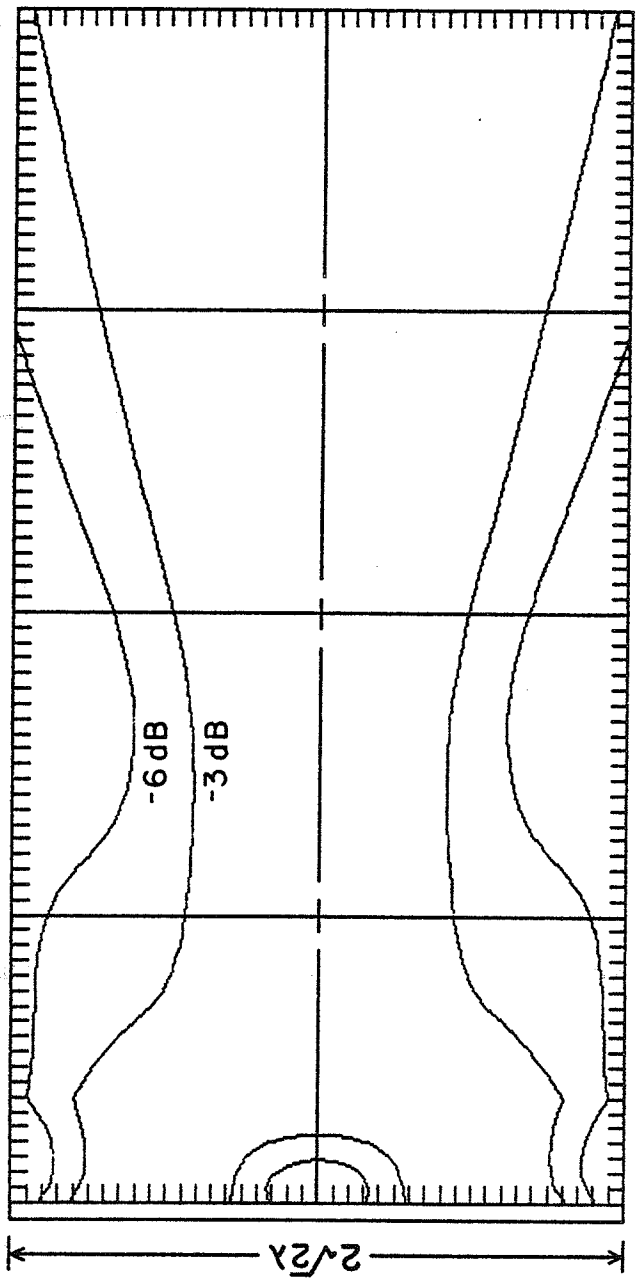

Figure 2.9. Square source with sides equal to 2λ; sound pressure contour for section with $x = y$ (see Fig. 2.1).

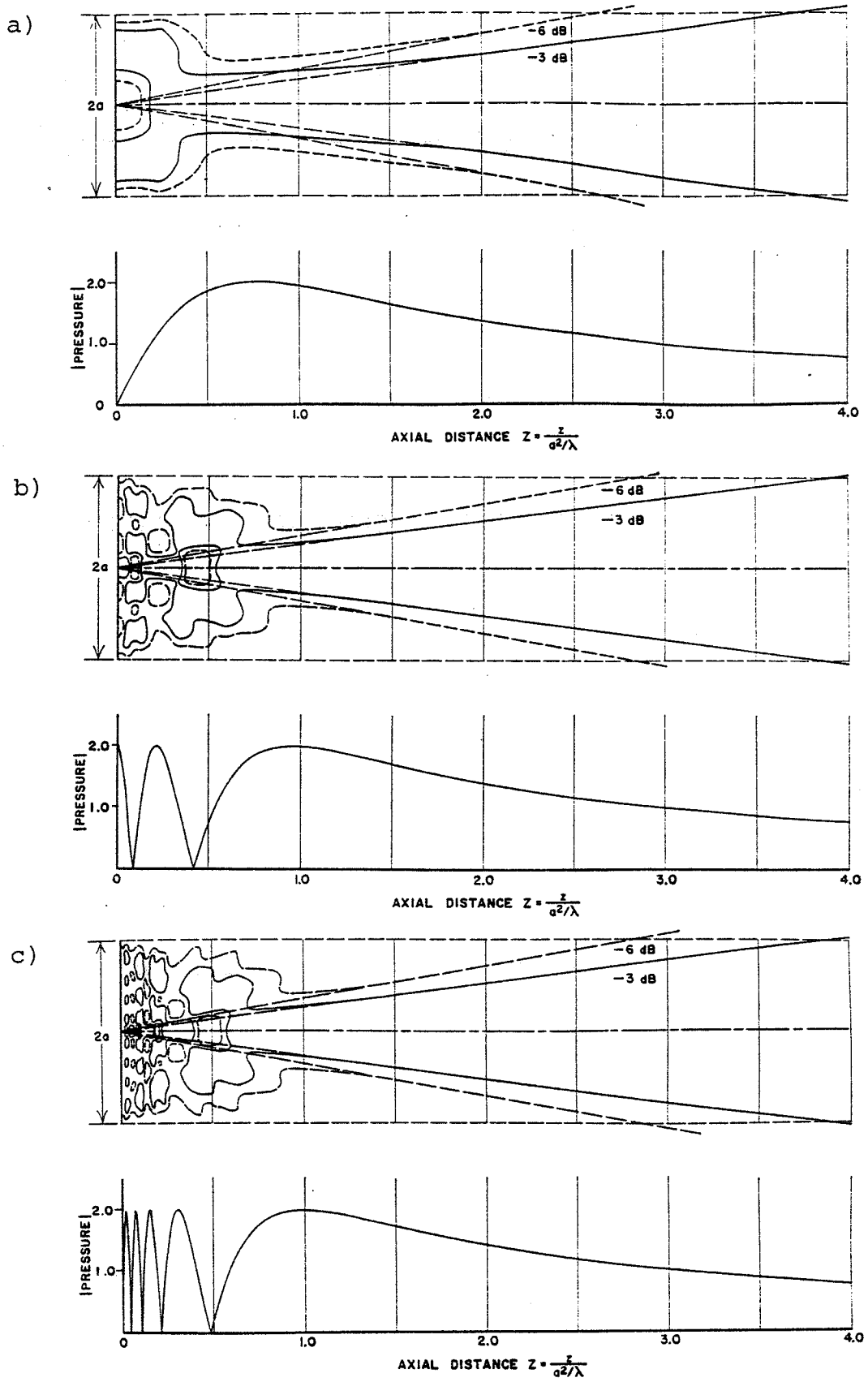

Figure 2.10. Sound pressure contours and normalized magnitudes of on-axis pressure for circular sources of diameters (a) 2.0 λ , (b) 5.0 λ , and (c) 10.0 λ (From Zemanek, 1971).

square source is evident. A square source lacks the on-axis nulls and lateral variation of the field which occurs in the field of a circular source. Similarities exist in the beam widths and locations of on-axis minima for similarly sized circular and square sources. The more uniform behavior of the square source in the nearfield makes it better suited for usage as a surface hyperthermia applicator (Underwood et al., 1987).

The field for a rectangular source of dimensions suitable for a linear phased array element, one half of a wavelength by ten wavelengths, is shown for two perpendicular sections in Figs. 2.11 and 2.12, with each contour plot having axial distances relative to the source dimension in the plane of the field section. Thus, the axial fields shown in Figs. 2.11(b) and 2.12(b) are actually the same: the axial distances in each figure are relative to different nearfield-farfield transition distances. The similarities of the field sections for this rectangular source with those for equivalently sized square sources, Figs. 2.2 and 2.6, respectively, demonstrate the near independence of the field pattern across each direction of a rectangular source. Accordingly, the length of a rectangular source in one direction, e.g., x, has little effect on the beamwidth produced in the other direction, y, of the source.

Knowledge of the sound pressure field allows calculation of the power deposition, which is the source of heat for raising the temperature of tissues in hyperthermia.

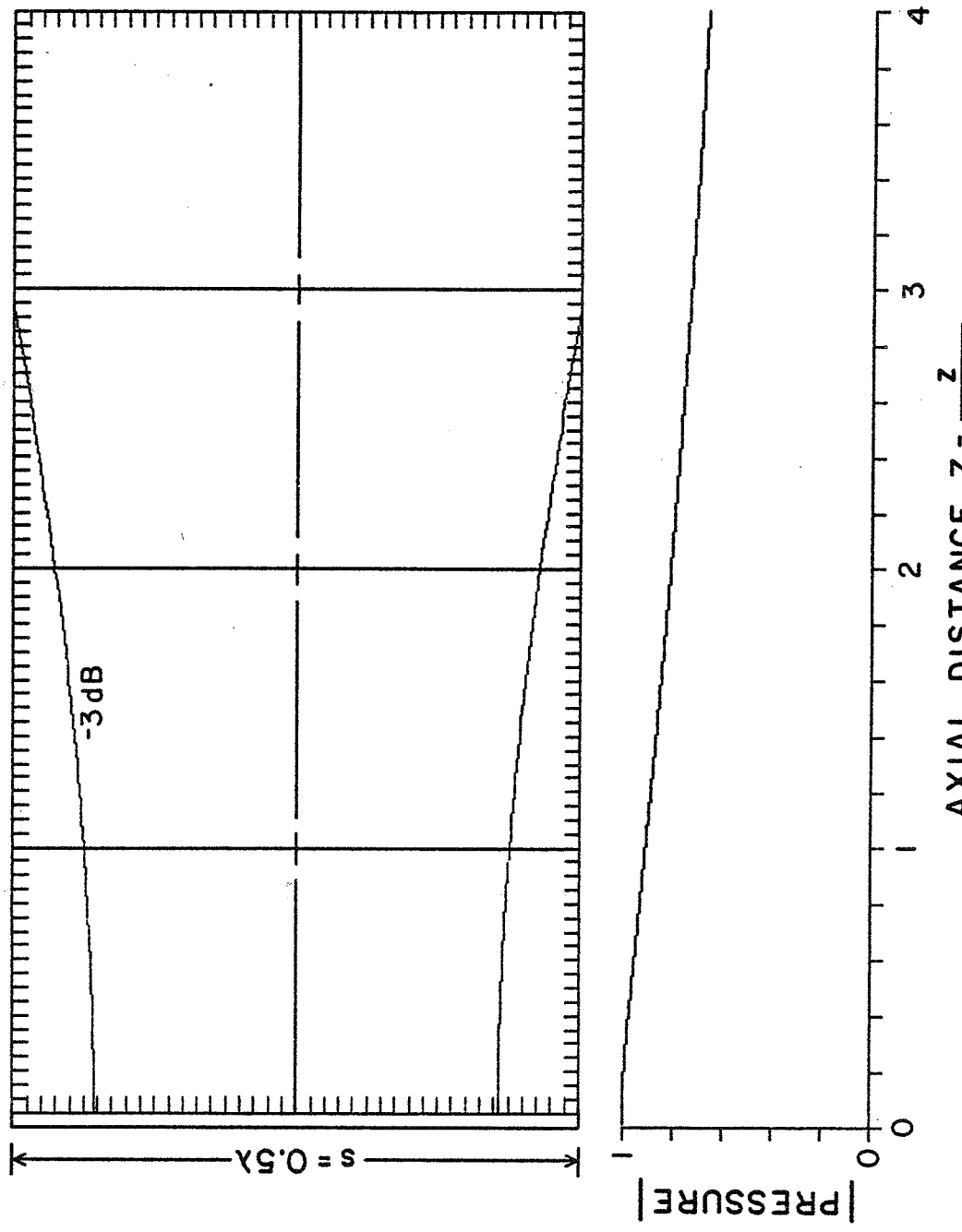

Figure 2.11. Rectangular source with sides equal to 0.5λ and 10.0λ; (a) sound pressure contour and (b) normalized magnitude of on-axis pressure. Field shown is in the plane of the 0.5λ length with z distances relative to the nearfield-farfield distance for a square source with sides of length 0.5λ.

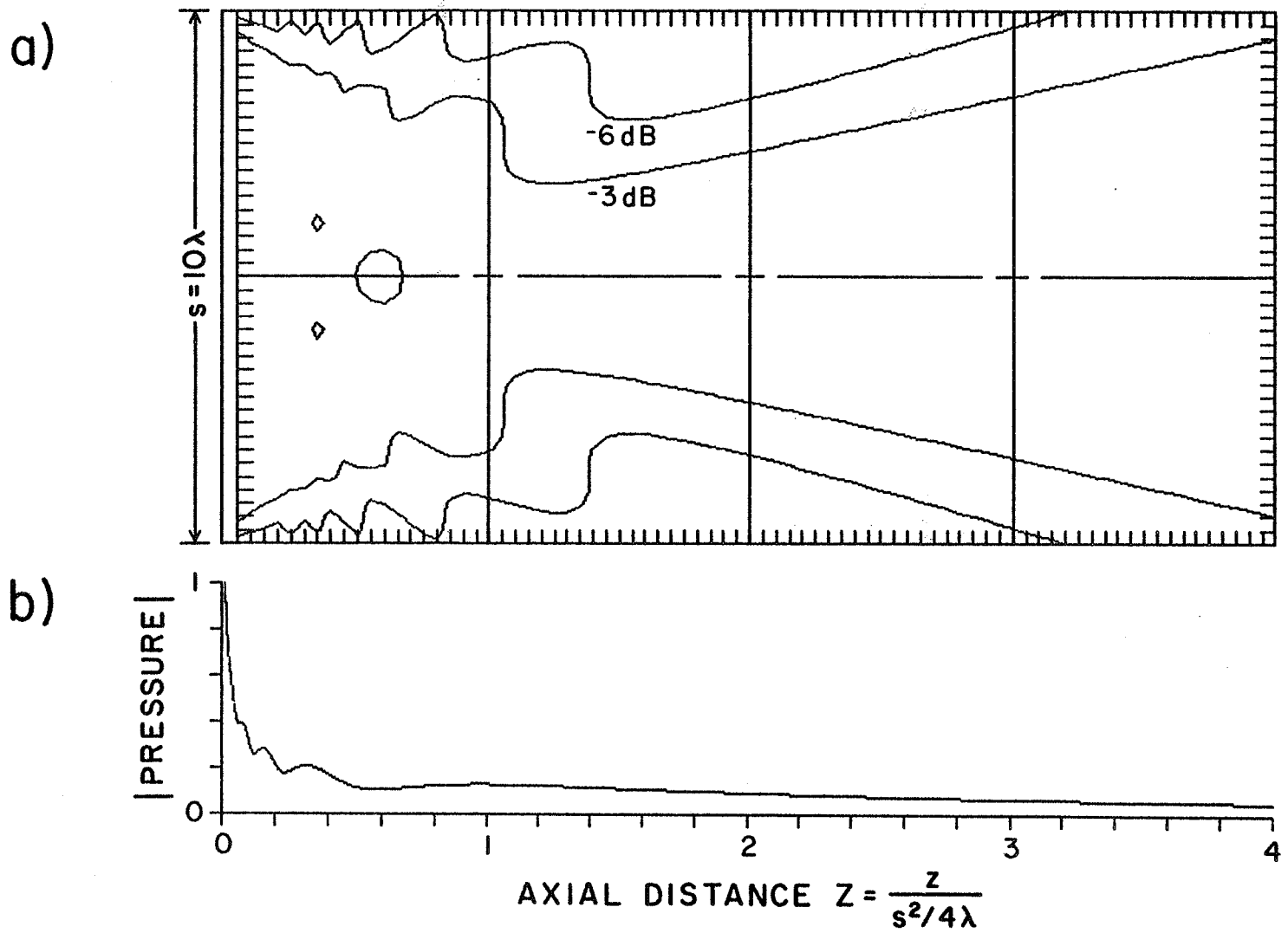

Figure 2.12. Rectangular source with sides equal to 0.5λ and 10.0λ; (a) sound pressure contour and (b) normalized magnitude of on-axis pressure. Field shown is in the plane of the 10.0λ length with z distances relative to the nearfield-farfield distance for a square source with sides of length 10λ.

The power deposition can be calculated from the sound pressure, assuming the effects of shear viscosity can be ignored, using

$$Q_p = \alpha p_o^2/\rho c \qquad (2.12)$$

(Nyborg, 1981; Cavicchi, 1984). The power deposition pattern calculated using Eq. (2.12) can be used with the bioheat transfer equation to determine temperature elevation.

2.2 Finite Difference Solution to Bioheat Transfer Equation

The bioheat transfer equation, a heat conduction equation with a heat sink term representing the effects of blood flow, can be used to model tissue for the calculation of temperature elevation. The time dependent bioheat transfer equation is given by

$$\rho C \frac{dT}{dt} = K\nabla^2 T - W_b C_b T + Q_p \qquad (2.13)$$

where ρ is the tissue density (kg/m^3), C is the specific heat of the tissue ($J/kg/^oC$), K is the thermal conductivity of the tissue ($W/m/^oC$), T is the difference of the tissue temperature and the arterial blood temperature (^oC), W_b is the blood perfusion rate ($kg/m^3/s$), C_b is the specific heat of blood ($J/kg/^oC$), and Q_p is the local power deposition (W/m^3). The parameter values are given in Table 2.1 and are used in all following analyses except where blood perfusion is varied as indicated in the relevant figures.

Table 2.1. Parameters used for tumor models.

Parameter	Variable	Value
Thermal conductivity	K (K_n, K_t)	0.55 W/m/^{o}C
Arterial blood temperature		37.0 ^{o}C
Blood perfusion rate	W_b (W_{bn}, W_{bt})	1.67 kg/m^3/s
Specific heat of blood	C_b	4000 J/kg/^{o}C
Tissue density		1070 kg/m^3
Specific heat of tissue	C	3500 J/kg/^{o}C
Desired tumor temperature	T_o	6.0 ^{o}C
Duration of initial heating phase	t_o	360 s
Sound amplitude absorbtion coefficient	ρ	0.1 nep/cm/MHz

The bioheat transfer equation can be solved numerically using finite difference and finite element techniques (Myers, 1971). Although the finite element method is particularly well suited to irregular geometries, the example geometries constructed for this investigation do not require this flexibility. and the more direct finite difference method will be applied.

2.2.1 Differential Equation Representation

The basis of the finite difference approach is the representation of derivatives by using differences. The first derivative of T at point m can be approximated as

$$\left.\frac{dT}{dx}\right|_m = \frac{1}{2\Delta x}\,(T_{m+1} - T_{m-1}) \tag{2.14}$$

where T_m designates the temperature at the m^{th} point and Δx is the spacing between adjacent points. Likewise, the second derivative can be approximated as

$$\left.\frac{d^2T}{dx^2}\right|_m = \frac{1}{2\Delta x^2}\,(T_{m-1} - 2T_m + T_{m+1})\,. \tag{2.15}$$

Similar approximations for the time derivative can be used; however, the majority of work to follow will concentrate on maintaining constant hyperthermic temperature levels where the time dependent term is equal to zero.

The steady state bioheat transfer equation is

$$0 = K\nabla^2 T - W_b C_b T + Q_p. \tag{2.16}$$

In one dimension, the del operator represents a second

derivative, and the bioheat transfer equation can be approximated as

$$0 = \frac{K}{\Delta x^2}\,(T_{m-1} - 2T_m + T_{m+1}) - W_b C_b T + Q_p, \tag{2.17}$$

which can be solved for the temperature at node m

$$T_m = \frac{K}{2K + \Delta x^2 W_b C_b}\left(\frac{\Delta x^2 Q_p}{K} + T_{m-1} + T_{m+1}\right). \tag{2.18}$$

A solution in cylindrical coordinates, with no angular variation, was also used for this study. The temperature at node (m,n), $T_{m,n}$, where m denotes the radial coordinate and n the linear coordinate, is given by

$$T_{m,n} = \frac{K}{4K + \Delta x^2 W_b C_b}\left[\frac{\Delta x^2 Q_p}{K} + \left(1 + \frac{\Delta x}{2r_m}\right)T_{m+1,n} + \left(1 - \frac{\Delta x}{2r_m}\right)T_{m-1,n} + T_{m,n-1} + T_{m,n+1}\right]. \tag{2.19}$$

A solution in three dimensions has the same form as the one dimensional solution

$$T_{k,m,n} = \frac{K}{6K + \Delta x^2 W_b C_b}\left[\frac{\Delta x^2 Q_p}{K} + T_{k-1,m,n} + T_{k+1,m,n} + T_{k,m-1,n} + T_{k,m+1,n} + T_{k,m,n-1} + T_{k,m,n+1}\right]. \tag{2.20}$$

Each of these equations characterizes the temperature at a given point in terms of the temperature at surrounding points.

These approximations to the differential equation are evaluated at each point iteratively, known as the Gauss-Seidel method, until each new value is within a set tolerance of the previous value (Myers, 1971). Such direct iteration is slow in converging. A faster convergence is obtained by using successive overrelaxation, where each new

value T^{new} is obtained by adding weighted values of the result of the appropriate finite difference equation T^{eq} to the old solution T^{old}

$$T^{new} = wT^{eq} + (1 - w)T^{old} \qquad (2.21)$$

where w is the relaxation factor. For successive overrelaxation, w takes on a value between 1 and 2, with the optimum value dependent on the geometry and tissue parameters. A value of 1.86, determined by Charles A. Cain to be optimum for his cylindrical geometry model (Cain, 1985), was typically used and provided sufficiently rapid convergence.

2.2.2 Boundary Condition Representation

A complete solution to the bioheat transfer equation using finite differences requires a choice of boundary conditions for the modeled region as well. Boundary conditions need to be chosen at both the skin surface and the model borders in the body interior. The effect of the choice of boundary conditions is minimized by modeling a volume sufficiently larger than the tumor so that the entire region of significant temperature elevation is within the model volume. The boundary condition at the skin surface is most simply modeled by assuming that the skin is bathed with a fluid maintained at a constant temperature, thus fixing the skin surface temperature.

Two simple ways of modeling the heat transfer at the borders of the modeled region within the body are (1) fixing

the temperature at the normal body core value and (2) fixing the derivative of the temperature as zero. Fixing the temperature at the boundary is equivalent to providing sufficient cooling at the boundary to maintain the boundary temperature at the fixed value. Setting the derivative of the temperature to zero at the boundary represents fixing the heat flow across the boundary to zero, so that all heat is either conducted through the skin surface or removed through blood perfusion. The analyses that follow will use the condition that the derivative of the temperature equals zero on the boundary. This boundary condition was chosen since it provides an indication of when a larger model volume is required by the presence of hyperthermic temperature levels extending to the model boundary.

Details of the specific models used in this investigation are provided with the relevant discussions in succeeding chapters. The programs used for these calculations are included in Appendices C through F.

CHAPTER 3
STEADY STATE POWER DEPOSITION PATTERNS FOR LOCALIZED HYPERTHERMIA

3.1 Introduction

Localized hyperthermic treatment of tumors has been accomplished with both invasive and noninvasive systems. Invasive techniques include the use of ferromagnetic seeds (Stauffer et al., 1980; Stauffer et al., 1984) and interstitial microwave antennas (Taylor, 1980; Strohbehn, 1980; Lyons et al., 1984). Numerous noninvasive applicator systems have been employed which use several different modalities including magnetic induction (Oleson, 1984; Storm et al., 1980), microwaves (Kantor, 1981), and ultrasound (Marmor et al., 1980; Lele and Parker, 1982; Corry et al., 1984; Fessenden et al., 1984; Nussbaum et al., 1986; Hynynen, 1986a). More recent implementations of these techniques allow more precise control of the power deposition pattern. To employ fully the increased flexibility of these systems, it is desirable to determine the power deposition pattern required to treat a specific tumor most effectively.

The bioheat transfer equation has been successfully applied to the prediction of the temperature elevation produced by hyperthermia applicators in the presence of blood perfusion (Cravalho et al., 1980; Halac et al., 1983; Dickinson, 1984; Roemer et al., 1984; Strohbehn and

Roemer, 1984) and its limitations have been discussed (Chen and Holmes, 1980; Bowman, 1981; Jain, 1983). In general, the time dependent bioheat transfer equation must be used to determine the change in temperature with time and is considered in Chapter 4 where the initial heating of tumors is discussed. Because much of a hyperthermia treatment period involves the maintenance of a steady temperature, the steady state heating conditions are evaluated in this chapter. For this, the bioheat equation can be applied in its steady state form:

$$0 = K\nabla^2 T - W_b C_b T + Q_p^{ss} \qquad (3.1)$$

where the superscript ss indicates the steady state value, with variables as defined for Eq. (2.13). Parameter values for the models that follow are given in Table 2.1, except where blood flow is varied as indicated in the relevant figure.

In the application of Eq. (3.1) to comparative thermal dosimetry, a power deposition pattern is used to calculate the resultant temperature distribution. This approach works well for determining the temperature field produced by a given applicator or scan path, in the case of a scanned focal region produced by ultrasound or microwaves. However, such an approach yields no direct information regarding the placement of interstitial sources, best applicator design, or most appropriate scan path to achieve a desired temperature distribution in a given tumor.

From a clinical perspective, it is preferable to choose

the desired temperature distribution and use a hyperthermia applicator to produce that distribution, as nearly as possible. The first step in the process is the calculation of the power deposition pattern required to maintain the target temperature distribution. Then the computed power deposition pattern can be approximated with a real applicator and scan path. The calculation of the desired power deposition pattern should also provide insight into the designs of more useful applicators and scan paths. A technique for calculating power deposition patterns from temperature distributions follows.

3.2 Theory

The one-to-one nature of the relationship between a power deposition pattern and its associated temperature distribution makes possible the calculation of temperature distributions from power deposition patterns and vice versa. One direction of this one-to-one relationship is well known and easily observed, i.e., that under steady state conditions, for a given region and given boundary conditions, a given power distribution produces a single temperature distribution, in accordance with the steady state bioheat transfer equation (Eq. (3.1)). The one-to-one nature of this transformation in the other direction is evident when the steady state bioheat transfer equation (Eq. (3.1)) is rewritten to solve for the applied power:

$$Q_p^{ss} = -K\nabla^2 T + W_b C_b T. \qquad (3.2)$$

Substitution of a given temperature distribution for the same region into this equation yields a single power distribution. Since a power distribution produces a single temperature distribution and a temperature distribution is associated with just one power distribution, the one-to-one relationship is established.

However, choosing a temperature profile with a large change in temperature over a very short distance, as is desirable at the boundary of a tumor, will result in a power deposition pattern which contains regions of negative power deposition. This is illustrated in the one dimensional model of Fig. 3.1(a) where the desired temperature distribution changes from a constant T_o within the tumor to zero in a linear fashion over a distance dx. The corresponding power deposition pattern (Fig. 3.1(b)), computed using the numerical method described in Section 3.3, contains negative power deposition. Since no noninvasive means to apply cooling (negative power deposition) exist, it is necessary to apply a constraint which will limit the computed power deposition pattern to only positive values.

Requiring that $Q_p^{ss} \geq 0$ in Eq. (3.2) yields

$$\frac{W_b C_b T}{K} \geq \nabla^2 T. \tag{3.3}$$

The largest spatial rate of temperature change which satisfies this constraint is obtained by setting the two terms of Eq. (3.3) equal, which is equivalent to setting

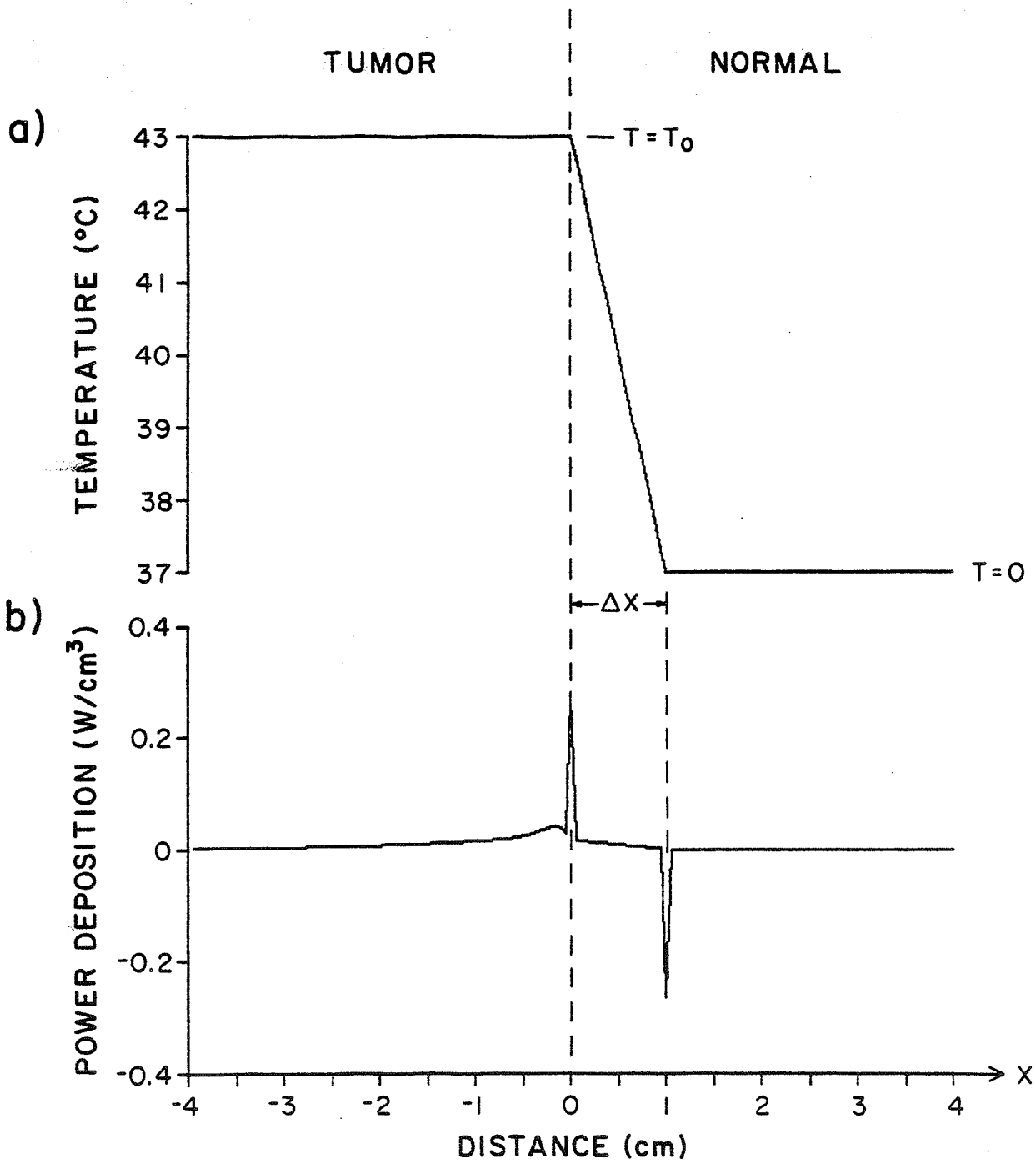

Figure 3.1. Temperature distribution (a) and associated numerically calculated power deposition pattern (b) for model consisting of half spaces of tumor and normal tissues. Nonhomogeneous perfusion was used for this example.

$Q_p^{ss} = 0$. Thus, by setting $Q_p^{ss} = 0$ outside the tumor the power deposition will be positive everywhere and the spatial rate of change of temperature will be as large as possible at the tumor boundary. This approach has been used in all analyses which follow including the half-space, cylindrical, and spherical tumor models illustrated in this section.

3.2.1 Half-Space Tumor Model

To illustrate the calculation of the power deposition distribution from the temperature distribution, an example is considered which consists of infinite half spaces of normal and tumor tissues. Since T will be a function of x only, the bioheat equation is reduced to its one dimensional form and Eq. (3.1) can be rewritten as

$$\frac{d^2T}{dx^2} - \frac{W_b C_b T}{K} + \frac{Q_p^{ss}}{K} = 0. \tag{3.4}$$

The objective of this analysis is to determine the power deposition pattern required to maintain the temperature T of all points within the tumor, $x < 0$, to T_o and to elevate the temperature of the normal tissue as little as possible.

For $x < 0$, the temperature is fixed at T_o and d^2T/dx^2 in this region is zero. Thus, in the tumor region, Eq. (3.4) reduces to

$$Q_p^{ss} = W_{bt} C_b T_o \tag{3.5}$$

where the additional subscript t indicates values for tumor tissue. The value for W_{bt} can vary within the tumor region; but as long as $T = T_o$, Eq. (3.5) holds and Q_p^{ss} can be

determined analytically.

In the region $x > 0$, Eq. (3.4) takes the form

$$\frac{d^2T}{dx^2} - \frac{W_{bn}C_bT}{K_n} = 0, \tag{3.6}$$

since the area of consideration is outside the tumor region and no heat deposition in normal tissue is desired. The additional subscript n indicates values for normal tissue. Taking K_n and W_{bn} to be constants, solving Eq. (3.6) for T, and applying the boundary condition $T = T_o$ at $x = 0$ give

$$T = T_o e^{-\sqrt{W_{bn}C_b/K_n}\, x} \tag{3.7}$$

for the temperature in the normal tissue. A cross-section of the temperature T in the half-space model is shown in Fig. 3.2(a).

Knowledge of the complete temperature distribution allows calculation of the power deposition pattern. The power deposition within the tumor region was determined in Eq. (3.5), and since power deposition in normal tissue was defined to be zero, the only remaining power deposition to be determined is that at the tumor-normal tissue boundary. For the power deposition at the infinitely thin boundary to contribute to heating, it must be in the form of a delta function. Letting P_{hs}^{ss} be the strength of the delta function at the boundary for the steady state solution of the half-space model, where the subscript hs indicates the half-space model, the power deposition is given by

$$Q_p^{ss} = P_{hs}^{ss}\delta(x) + W_{bt}C_bT_o u(-x) \tag{3.8}$$

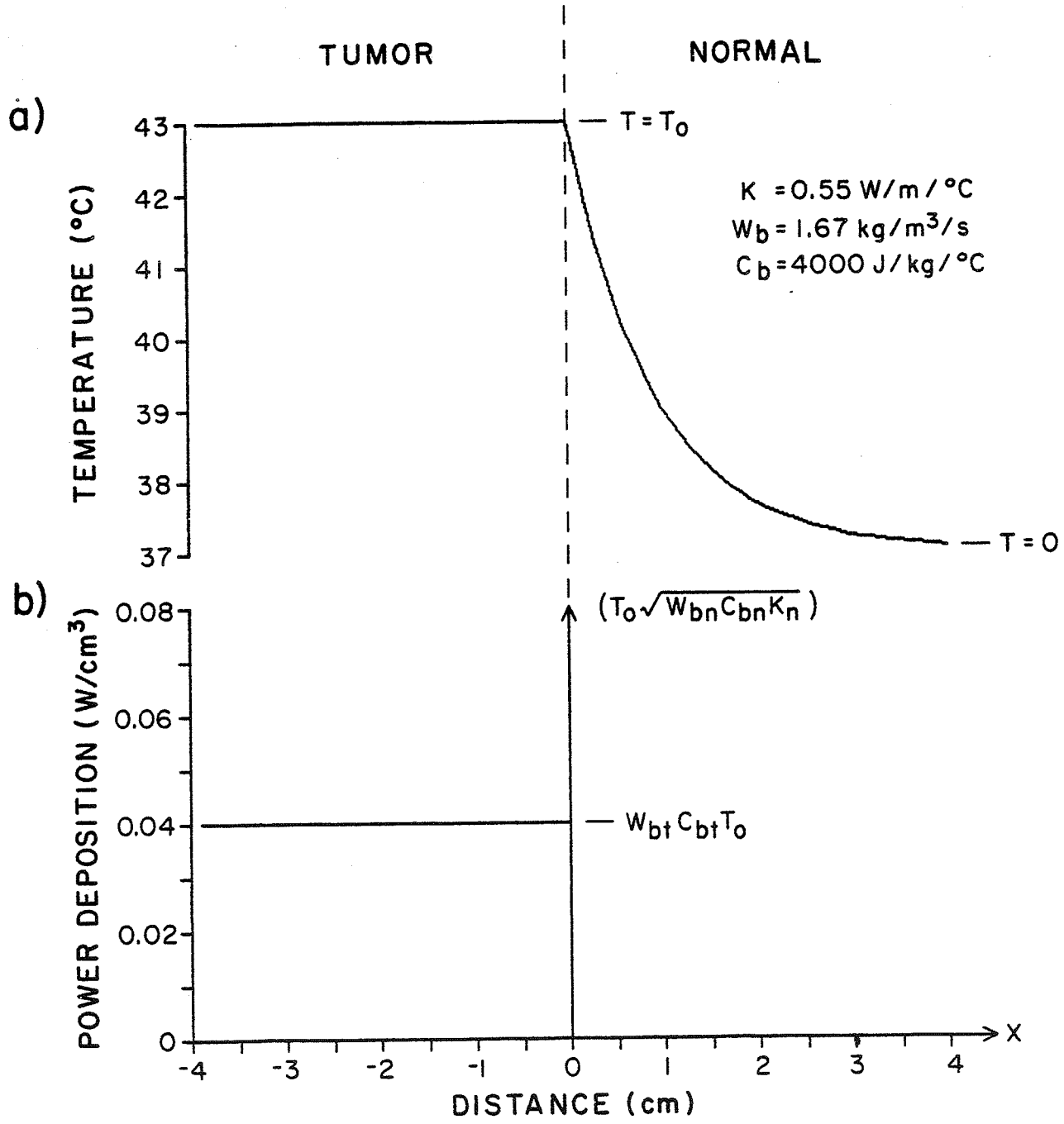

Figure 3.2. Temperature (a) and power deposition (b) distributions in the half-space tumor model.

where $o(x)$ is a unit delta function centered on the tumor-normal tissue boundary and $u(-x)$ is a unit step function (1 for $x < 0$, 0 for $x > 0$). Substituting Q_p^{ss} into Eq. (3.4) and integrating from $x = 0^-$ to 0^+ yield

$$P_{hs}^{ss} = -K \left.\frac{dT(x)}{dx}\right|_{0^-}^{0^+}. \tag{3.9}$$

Evaluating the derivative of T at $x = 0^-$ and 0^+ and substituting into Eq. (3.9) give

$$P_{hs}^{ss} = T_o \sqrt{W_{bn} C_b K_n}. \tag{3.10}$$

The complete power deposition pattern required to produce a uniform temperature within the tumor half space for this model is shown in Fig. 3.2(b).

3.2.2 Infinite Cylinder Tumor Model

A model also considered in this study is an infinitely long cylindrical tumor, which has application in many of the circularly symmetric bioheat transfer models. The infinite extent of the tumor limits the applicability of this model to approximations for the midsection of a cylindrical tumor, although a complete analytical solution for a finite length cylinder tumor could be solved using the same method. The bioheat transfer equation is transformed into cylindrical coordinates, with the angular and z dependent terms omitted due to angular symmetry and infinite z extent, to yield

$$\frac{r^2 d^2T}{dr^2} + \frac{r dT}{dr} - \frac{W_b C_b r^2 T}{K} + \frac{r^2 Q_p^{ss}}{K} = 0. \tag{3.11}$$

In the tumor region, where $r < r_o$, the temperature is fixed at T_o so that the derivatives of T are zero and Eq. (3.11) reduces to Eq. (3.5). In normal tissue, where $r > r_o$, the power deposition is taken as zero, and Eq. (3.11) becomes

$$\frac{r^2 d^2T}{dr^2} + \frac{r dT}{dr} - \frac{W_{bn} C_b r^2 T}{K_n} = 0. \tag{3.12}$$

Equation (3.12) is Bessel's equation of order zero which has a solution of the form

$$T = G\, J_0(j\sqrt{W_{bn}C_b/K_n}\, r) + H\, N_0(j\sqrt{W_{bn}C_b/K_n}\, r) \tag{3.13}$$

where J_0 and N_0 are zeroth order Bessel functions and G and H are unknown constants. Rewriting this in terms of real valued Bessel functions yields

$$T = G'\, I_0(\sqrt{W_{bn}C_b/K_n}\, r) + H'\, K_0(\sqrt{W_{bn}C_b/K_n}\, r) \tag{3.14}$$

where I_0 and K_0 are Bessel functions of imaginary arguments and G' and H' are constants. As r approaches infinity, T must approach zero, but I_0 increases without bound; therefore, the constant G' must be zero. The constant H' can be determined by evaluating Eq. (3.14) (with G' = 0) at the boundary $r = r_o$, where $T = T_o$. Substitution of these constants into Eq. (3.14) gives

$$T = \frac{T_o\, K_0(r\sqrt{W_{bn}C_b/K_n})}{K_0(r_o\sqrt{W_{bn}C_b/K_n})} \tag{3.15}$$

for $r \geq r_o$. The temperature distribution for this model is

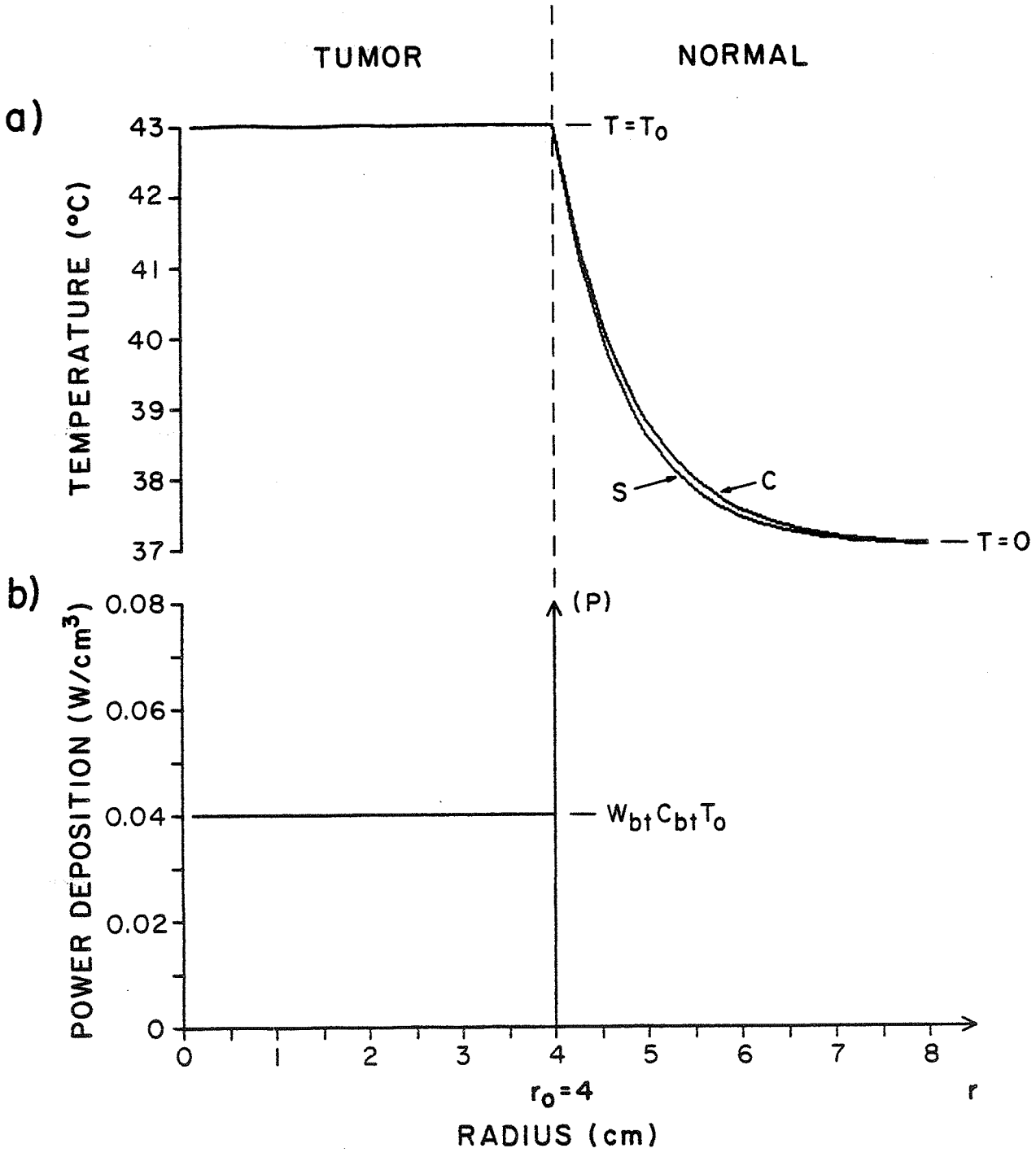

Figure 3.3. Temperature (a) and power deposition (b) distributions in the cylindrical (C) and spherical (S) tumor models. P^{ss} is given by Eq. (3.18) and Eq. (3.28) for the cylinder and sphere, respectively.

shown in Fig. 3.3(a) as a function of radial distance.

The assumption of a delta function for the power deposition at the tumor-normal tissue boundary in the radial direction is made, analogous to that assumed for the half-space tumor model. The strength of the delta function is taken as P_c^{ss}, where the subscript c indicates the cylindrical model, and is found to be the difference of the derivatives of the temperature on each side of the tumor-normal tissue boundary times the thermal conductivity:

$$P_c^{ss} = -K \left.\frac{dT(r)}{dr}\right|_{r_o^-}^{r_o^+}. \tag{3.16}$$

Evaluating the derivatives in Eq. (3.16) yields

$$P_c^{ss} = T_o \sqrt{W_{bn} C_b K_n} \; \frac{K_1(r_o \sqrt{W_{bn} C_b / K_n})}{K_0(r_o \sqrt{W_{bn} C_b / K_n})} \tag{3.17}$$

where K_0 and K_1 represent the zeroth and first order K Bessel functions, respectively. The strength of the delta function at the boundary is dependent upon r_o, the radius for the tumor. The complete power deposition pattern for the cylindrical geometry is shown in Fig. 3.3(b) as a function of radial distance.

3.2.3 Spherical Tumor Model

A more realistic analytical example is a spherical tumor surrounded by an infinitely extended region of homogeneous normal tissue. Though the normal tissue is infinite in extent, the model is applicable to most tumors because heat conduction in the normal tissue is limited to

less than several centimeters when blood perfusion is considered. Equation (3.1) may be expressed in spherical coordinates with the angular dependent terms omitted, since no angular variation in temperature is desired, to yield

$$\frac{d^2T}{dr^2} + \frac{2dT}{rdr} - \frac{W_b C_b T}{K} + \frac{Q_p^{ss}}{K} = 0. \tag{3.18}$$

For the tumor region, $r < r_o$, the temperature is fixed at T_o and the derivatives of T in this region are zero. As in the previous models, the bioheat equation in the tumor region reduces to Eq. (3.4). As noted previously, W_{bt} is not required to be constant with respect to r (in fact it can vary with angular position) for this result to hold.

In the normal region, $r > r_o$, Q_p is zero and Eq. (3.18) becomes

$$\frac{d^2T}{dr^2} + \frac{2dT}{rdr} - \frac{W_{bn} C_b T}{K_n} = 0. \tag{3.19}$$

Equation (3.19) is simplified by defining a new variable $T = S/r$ which, after substitution and simplification, yields

$$\frac{d^2S}{dr^2} - \frac{W_{bn} C_b S}{K_n} = 0. \tag{3.20}$$

The solution to Eq. (3.20) is

$$S = A\, e^{-\sqrt{W_{bn} C_b / K_n}\, r} + B\, e^{\sqrt{W_{bn} C_b / K_n}\, r} \tag{3.21}$$

which yields

$$T = \frac{A}{r}\, e^{-\sqrt{W_{bn} C_b / K_n}\, r} + \frac{B}{r}\, e^{\sqrt{W_{bn} C_b / K_n}\, r}. \tag{3.22}$$

Since T approaches zero as r approaches infinity, B = 0. Applying the boundary condition at r_o, i.e., $T = T_o$, the constant A is evaluated as

$$A = T_o r_o \, e^{\sqrt{W_{bn} C_b / K_n}\, r_o} \tag{3.23}$$

to give

$$T = \frac{T_o r_o}{r} \, e^{\sqrt{W_{bn} C_b / K_n}\, (r_o - r)} \tag{3.24}$$

for $r \geq r_o$. The complete temperature distribution is shown in Fig. 3.3(a) as a function of the radial distance r.

The power deposition required at $r = r_o$ can now be calculated from the temperature distribution, and as before it is a delta function. The strength of the delta function p_s^{ss}, where the superscript s denotes the spherical model, is found to be the product of the thermal conductivity and the difference between the derivatives of the temperature on each side of the tumor-normal tissue boundary:

$$p_s^{ss} = -K \left. \frac{dT(r)}{dr} \right|_{r_o^-}^{r_o^+}. \tag{3.25}$$

Evaluating Eq. (3.25) yields

$$p_s^{ss} = T_o \, (\sqrt{W_{bn} C_b K_n} + K_n / r_o) \tag{3.26}$$

or

$$p_s^{ss} = p_{hs}^{ss} + T_o K_n / r_o. \tag{3.27}$$

The complete power deposition pattern is shown in Fig. 3.3(b).

3.2.4 Properties of Models

The strength of the delta function at the tumor boundary is a constant for the half-space tumor model, a quotient of Bessel functions dependent upon tumor radius for the cylindrical tumor model, and a simple function of tumor radius for the spherical tumor model. The strength of the delta function is shown as a function of tumor radius in Fig. 3.4 for the three tumor models discussed. For larger tumor diameters, the strength approaches a constant value for all models, which could be used as an approximation for large tumors.

For the previous illustrations, W_b and K were chosen as constants to illustrate the analytical solution. Although these must be constant in the normal tissue, as stated previously, they need not be constant within the tumor. Studies of tumor perfusion have shown that blood flow varies from near zero in the necrotic core to elevated values in the advancing front of the tumor (Endrich et al., 1979). An example of this situation is illustrated in Fig. 3.5.

3.3 Methods

In actuality tumors are not exactly spherical and tissue parameters are not constant, so the analytical solution presented in the previous section would seldom be applicable. A three dimensional numerical solution to the problem has been developed to account for the various geometries and parameter variations encountered in a

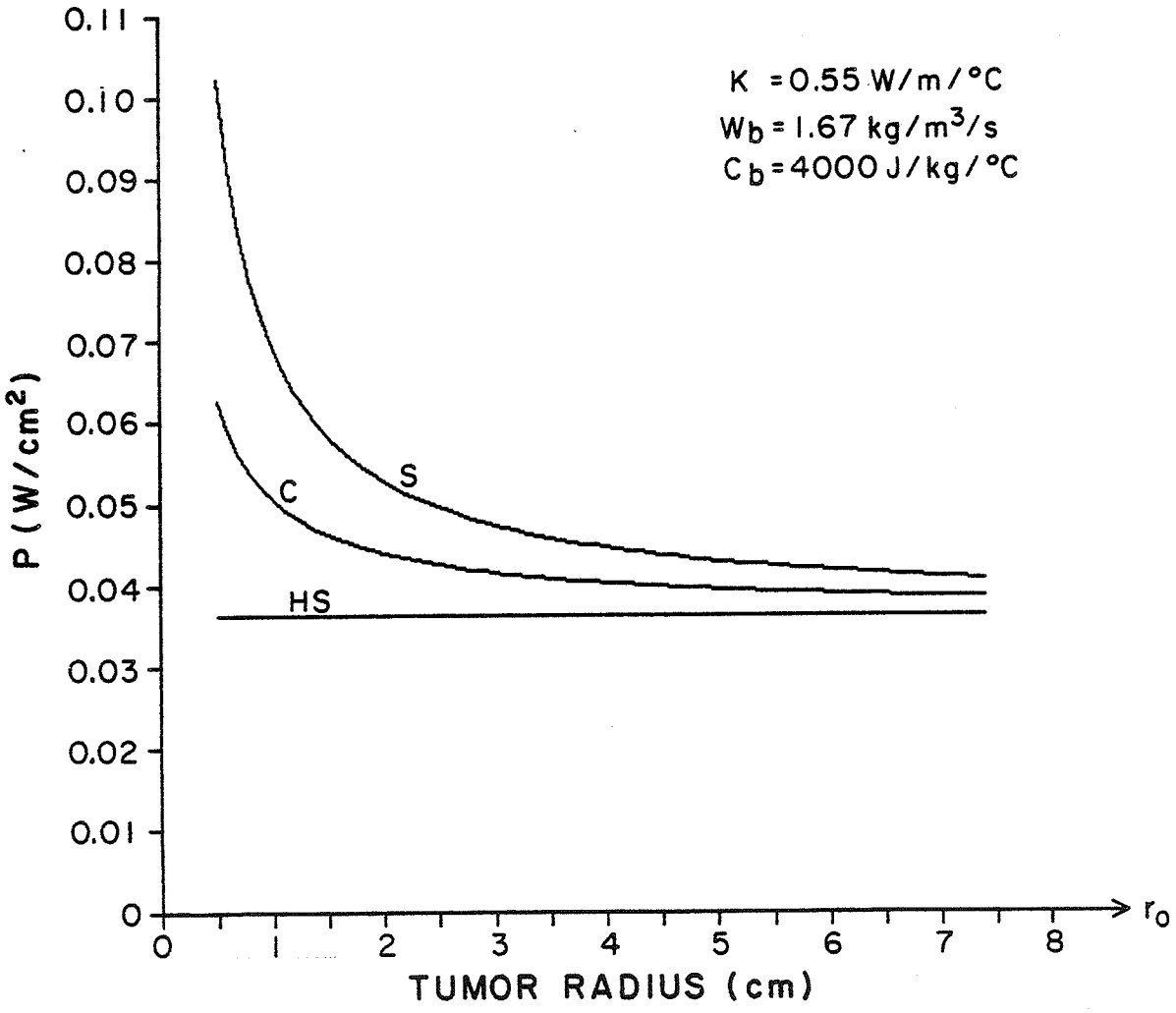

Figure 3.4. Strength of the delta function required at the tumor boundary versus tumor radius for the cylindrical (C) and spherical (S) models. The strength of the delta function required for the half-space model (HS) is included for comparison.

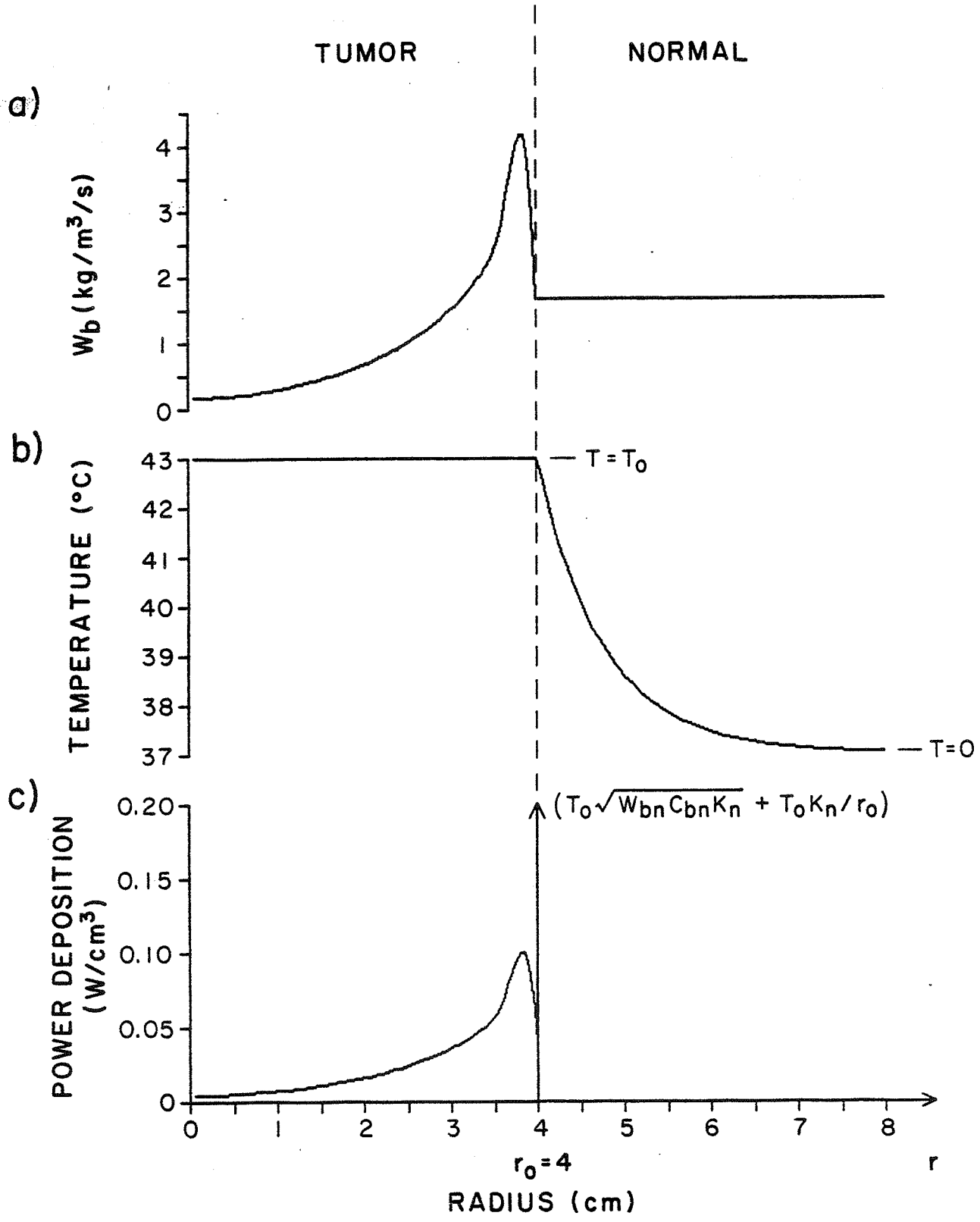

Figure 3.5. Example of variable perfusion within the tumor (a) and associated temperature (b) and power deposition (c) distributions for the spherical model.

clinical situation.

The temperature distribution required for the numerical solution was determined by first setting the temperature in the tumor region to a constant value T_o and then calculating T outside the tumor using a finite difference solution to the steady state bioheat transfer equation with $Q_p^{ss} = 0$. Such a method ensures that the bioheat transfer equation is satisfied, only positive power deposition is required, and all tumor temperatures are held at a constant value T_o. The three dimensional finite difference representation of the bioheat transfer equation used in this solution is given by

$$T_{k,m,n} = \left(K/(6K + \Delta x^2 W_b C_b) \right) \left(\frac{\Delta x^2 Q_p^{ss}}{K} + T_{k-1,m,n} + T_{k+1,m,n} + T_{k,m-1,n} + T_{k,m+1,n} + T_{k,m,n-1} + T_{k,m,n+1} \right) \quad (3.28)$$

where k, m, and n are the indices of the point at which the temperature is being calculated and Δx is the distance between sample points. The associated power deposition pattern is calculated from the temperature distribution by inverting Eq. (3.28) to yield

$$Q_p^{ss} = \frac{K}{\Delta x^2} \left(6T_{k,m,n} - T_{k-1,m,n} - T_{k+1,m,n} - T_{k,m-1,n} - T_{k,m+1,n} - T_{k,m,n-1} - T_{k,m,n+1} \right) + W_b C_b T_{k,m,n}. \quad (3.29)$$

The application of this equation to theoretical temperature distributions produces an accurate result as confirmed by comparison to the examples illustrated in the theoretical discussion (Section 3.2).

3.4 Results

The three dimensional numerical solution was applied to two tumor geometries. The first geometry considered a 4 cm cubic tumor centered at 6 cm from the skin surface. For this particular example, tumor and skin temperatures of 43 and 25°C, respectively, were chosen. Cross-sections of the complete temperature profile and associated power deposition pattern, through the center of the tumor, are shown in Fig. 3.6. The power deposition pattern exhibits the large maxima near the tumor boundary analogous to those seen in the analytic models. The constant value evident in the central region of the tumor is a result of the use of a constant value for W_{bt} in this example.

The second tumor geometry consisted of a 4 cm diameter spherical tumor located 6 cm from the body surface. Figure 3.7 shows cross-sections of the temperature profile and associated power deposition pattern through the center of the tumor. The high power deposition on the periphery of the tumor in Fig. 3.7 represents the delta function in the theoretical models, and the variation in the power deposition at the periphery is due to the imperfect repesentation of the spherical boundary in a rectangular coordinate system. This results in variations in the local curvature of the tumor boundary and the effective radius of the tumor, yielding a varying power deposition on the tumor periphery in accordance with Eq. (3.27).

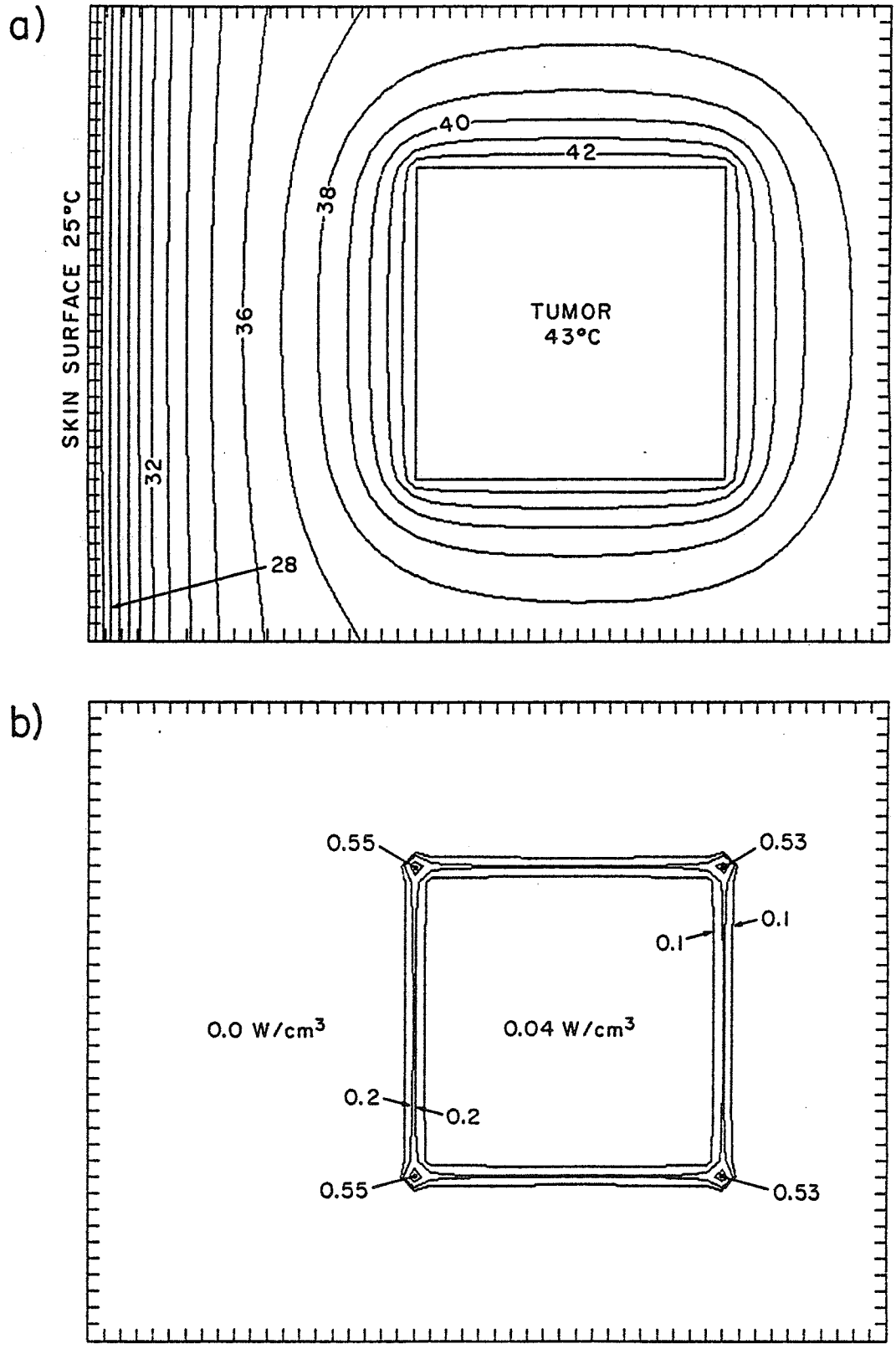

Figure 3.6. Contour plots of a cross-section of the temperature (a) and power deposition (b) distributions for a numerically calculated cubical tumor model sampled every 2 mm. Temperature contours are shown for $1^{o}C$ increments and power deposition contours are given for 0.1 W/cm^3, 0.2 W/cm^3, and 0.4 W/cm^3.

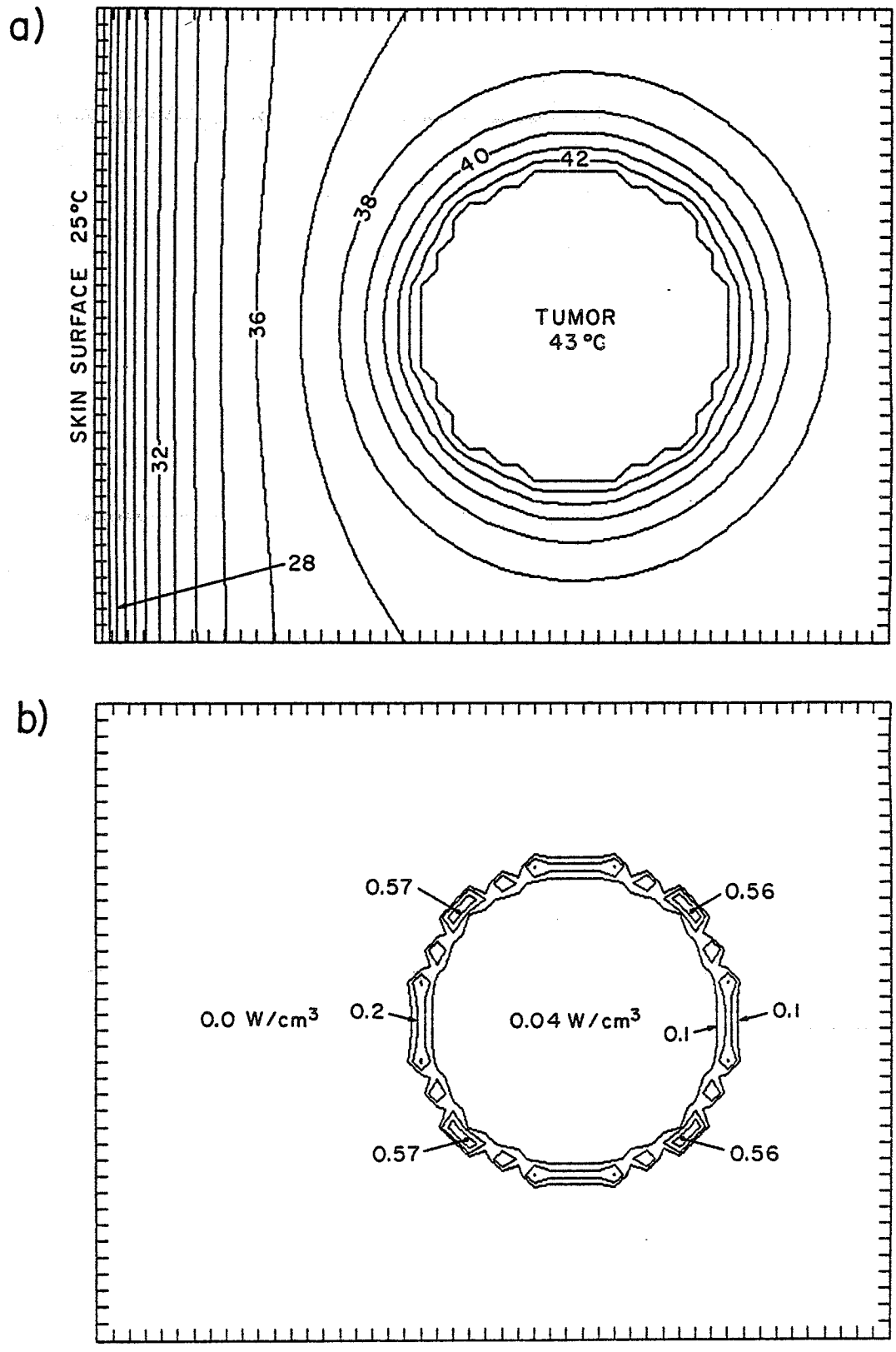

Figure 3.7. Contour plots of a cross-section of the temperature (a) and power deposition (b) distributions for a numerically calculated spherical tumor model sampled every 2 mm. Temperature contours are shown for 1°C increments and power deposition contours are given for 0.1 W/cm^3, 0.2 W/cm^3, and 0.4 W/cm^3.

3.5 Discussion

Currently, most investigators select a hyperthermia system and then select placement of sources, initial field configuration, or initial scan path based on experience and intuition. For the choice of initial field configuration and scan path, modifications are made in an iterative manner based on calculations using the bioheat transfer equation prior to treatment, or during treatment based on temperature feedback. The ultimate goal of this study is to determine an approach which will allow direct calculation of the initial treatment configuration based on the desired temperature profile, tissue thermal properties including blood perfusion, and hyperthermia system parameters such as beam size for a scanned ultrasound applicator.

As a first step towards this goal, a three dimensional numerical method for calculating the optimum power deposition pattern given the desired tumor temperature was presented in this chapter. The method can be applied to the complex tumor geometries which are encountered clinically and to tumors with nonuniform temperature dependent perfusion. The other stages of this study deal with techniques for generating the treatment configuration which will most nearly produce the desired power deposition pattern. The analysis considers the effect of such parameters as the heating of implantable sources, multiple focus systems, and the beam size and scan path. The results of these analyses are treated in Chapter 5.

CHAPTER 4

TIME DEPENDENT POWER DEPOSITION PATTERNS FOR LOCALIZED HYPERTHERMIA

4.1 Introduction

The application of the steady state bioheat transfer equation to hyperthermia has been the subject of numerous theoretical studies (Cravalho et al., 1980; Dickinson, 1984; Roemer et al., 1984; Strohbehn and Roemer, 1984). The utilization of these studies for actual tumor heating is limited to the period of time after steady state conditions have been reached and to other times when a steady state approximation is applicable. Transient bioheat analysis has typically been limited to models where the heating was constant throughout time (Van Den Berg et al., 1983) and the temperature distributions were allowed to reach steady state; no additional power deposition was provided at the onset of treatment to raise the tumor temperature to therapeutic levels.

Methods for determining power deposition patterns required to maintain a steady state uniform tumor temperature were reported in Chapter 3. In this chapter, a time dependent power deposition pattern which will raise the tumor temperature to the desired steady state level is determined using the time dependent bioheat transfer equation. This more general solution asymptotically approaches the steady state solution for large time.

4.2 Theory

For this investigation, the bioheat transfer equation is considered in its time dependent form:

$$\rho C\frac{dT}{dt} = K\nabla^2 T - W_b C_b T + Q_p. \tag{4.1}$$

As a preliminary step to an analysis using the time dependent bioheat equation, the applicability of the steady state solution was examined. This was done by applying the power deposition pattern required to maintain hyperthermic temperatures in the steady state case, as given by Eq. (3.5), and by calculating the temperature rise with time.

Examining the temperature rise at a point in the tumor core, so that the effects of the surface delta function are negligible and the gradient of the temperature can be taken as zero, Eq. (4.1) reduces to

$$\frac{dT}{dt} + \frac{W_{bt}C_b T}{\rho C} = \frac{W_{bt}C_b T_o}{\rho C}. \tag{4.2}$$

Equation (4.2) is a first order nonhomogeneous equation with solution

$$T = T_o\,(1 - e^{-W_{bt}C_b t/\rho C}) \tag{4.3}$$

and time constant $\rho C/W_{bt}C_b$. Figure 4.1 shows a plot of temperature versus time for the tumor core with typical tumor tissue parameters as given in Table 2.1. For this example, the time required for the temperature to reach

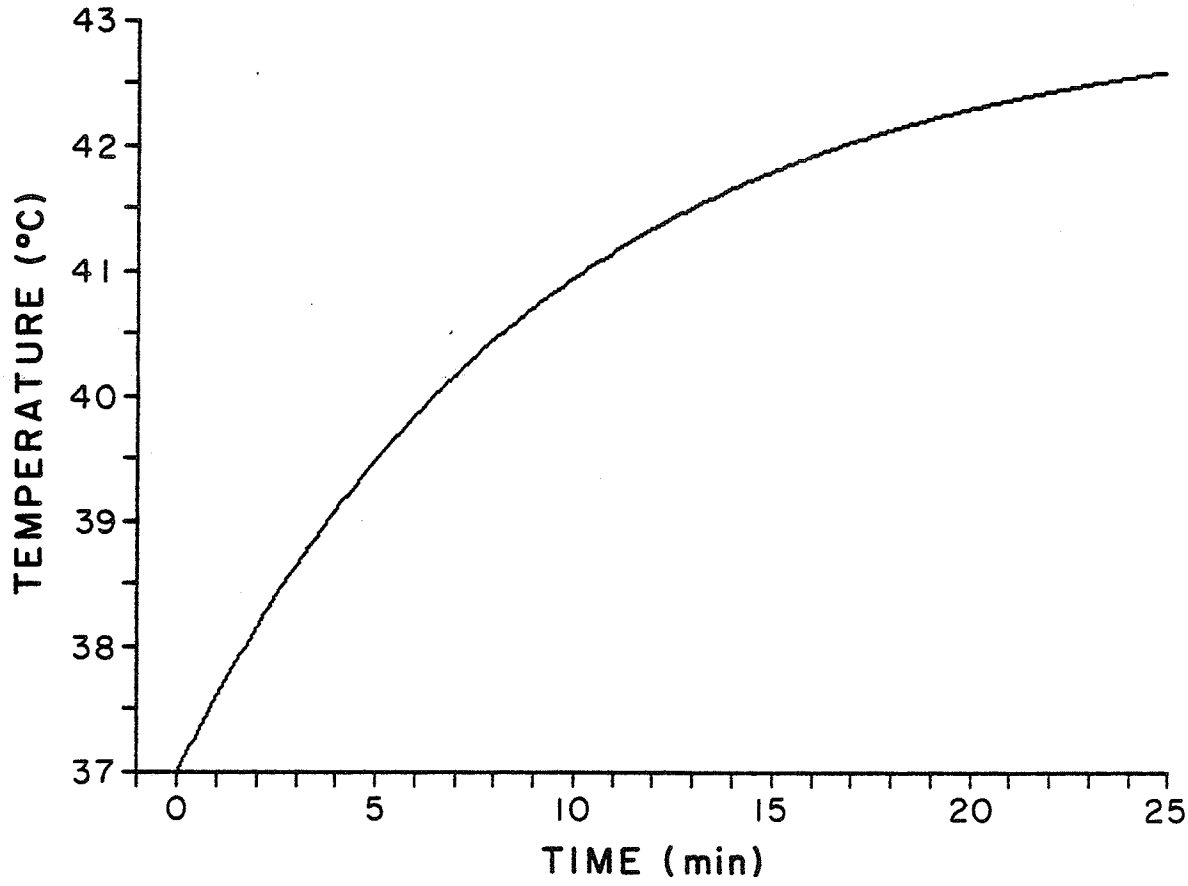

Figure 4.1. Time dependence of tumor core temperature resulting from application of steady state power deposition pattern. Heating contribution from power deposition on the tumor periphery has been neglected.

ninety percent of T_o, the steady state temperature value, is 22 minutes: a major portion of a hyperthermia session. The obvious conclusion is that the power deposition pattern required to maintain the steady state temperature is insufficient to raise the tumor temperature to the therapeutic level in a small fraction (for example 10%) of the hyperthermia session. Therefore a solution to the time dependent bioheat transfer equation must be found involving a time dependent Q_p.

The limitations on Q_p within the tumor for a transient solution are: Q_p must approach $W_{bt}C_bT_o$ (the steady state solution) for large time, Q_p is non-negative for all time, and dT/dt is limited by the power that can be supplied by a practical applicator and by the pain associated with increasing temperature too rapidly. Considering the limit on dT/dt and the simplicity which results from having a constant change of temperature with time within the tumor for the initial heating phase, a desired temperature-time relationship was chosen as shown in Fig. 4.2, with T_o and t_o as given in Table 2.1. Defining the function h(t) as

$$h(t) = \begin{cases} 0 \text{ for } t \leq 0 \\ t \text{ for } 0 \leq t \leq 1, \\ 1 \text{ for } t \geq 1 \end{cases} \tag{4.4}$$

the desired time dependent temperature can be expressed as

$$T(t) = T_o h(t/t_o). \tag{4.5}$$

The rate of temperature increase during the initial heating

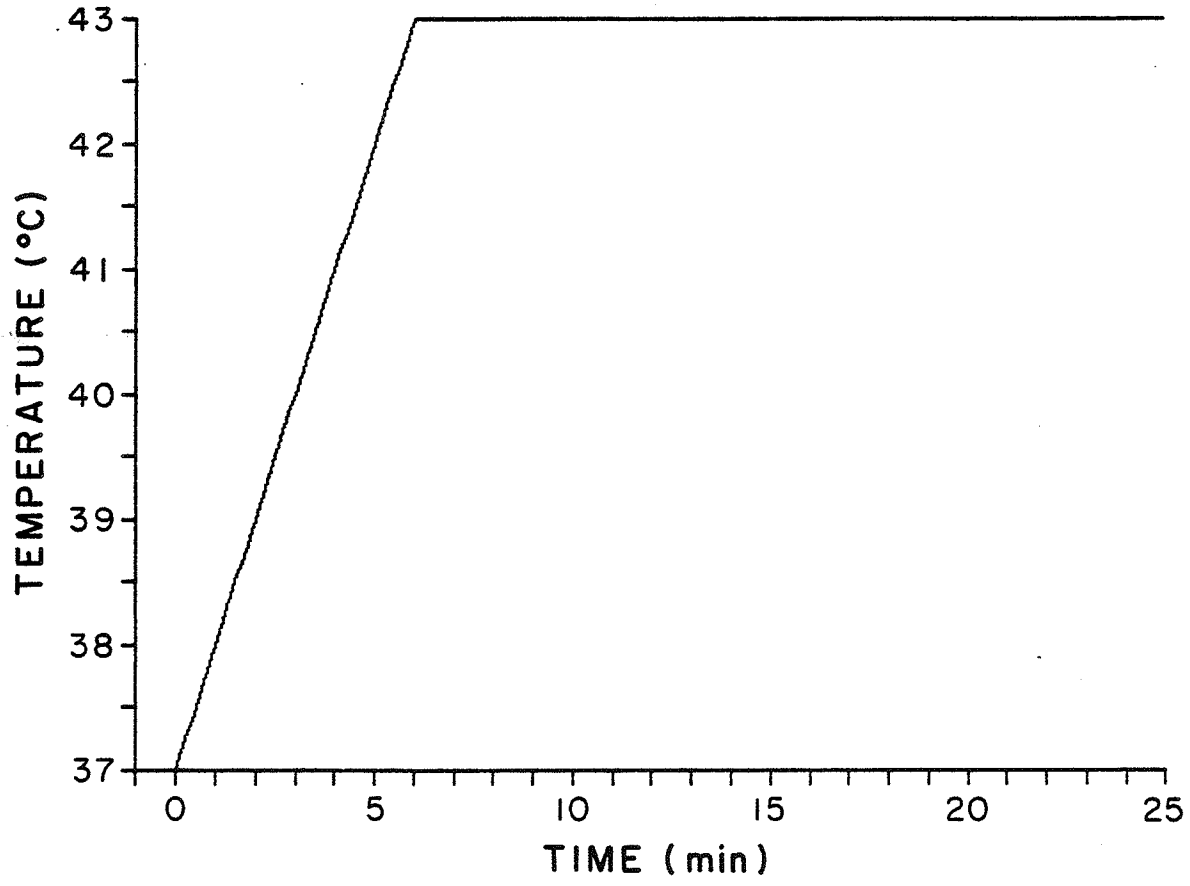

Figure 4.2. Desired tumor temperature time dependence.

phase is $R = T_o/t_o$ ($^oC/s$).

The power deposition required within the tumor to produce the desired transient temperature rise is evaluated by substituting Eq. (4.5) into the time dependent bioheat transfer equation (Eq. (4.1)). Since the tumor temperature will be raised uniformly, the Laplacian (∇^2) of the temperature is set to zero to give

$$\rho CR\,\mathrm{rect}\left(\frac{t - t_o/2}{t_o}\right) = -W_{bt}C_bT_oh(t/t_o) + Q_p^t \tag{4.6}$$

where

$$\mathrm{rect}(t) = \begin{cases} 0 \text{ for } t \leq -1/2 \\ 1 \text{ for } -1/2 \leq t \leq 1/2 \\ 0 \text{ for } t \geq 1/2 \end{cases} \tag{4.7}$$

and the superscript t indicates the time dependent solution. Solving for Q_p in Eq. (4.6) yields

$$Q_p^t = W_{bt}C_bT + \rho CR\,\mathrm{rect}\left(\frac{t - t_o/2}{t_o}\right). \tag{4.8}$$

Figure 4.3 shows Q_p^t as a function of time for the tumor parameter values given in Table 2.1 and a range of blood perfusion rates. From Eq. (4.8) it is seen that Q_p^t has two terms: the first is equivalent to the steady state solution (Eq. (3.5)) with T_o replaced by T, and the second term is equal to ρCR during the initial heating phase and zero thereafter. In this context, the significance of each term is apparent: $W_{bt}C_bT$ serves to maintain the achieved

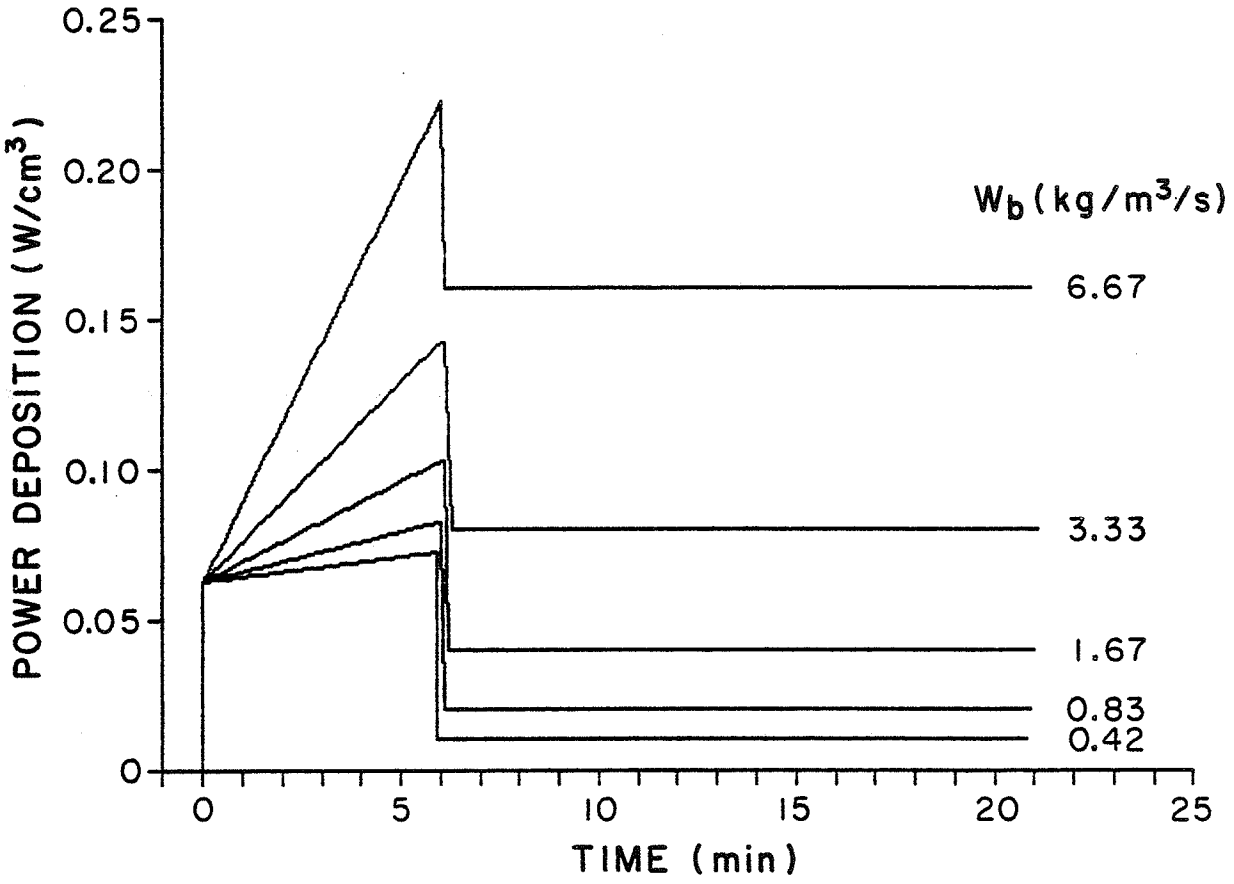

Figure 4.3. Interior power deposition Q_p time dependence for a range of blood perfusion values.

elevated temperature by compensating for heat loss due to blood perfusion, while ρCR serves to elevate the temperature at a rate of R degrees per second. The application of Eq. (4.8) is not limited to spatially invariant W_{bt}.

The time varying power deposition pattern within the tumor volume was found to be a function of tissue parameter values, but independent of tumor geometry. In contrast, the power deposition P required on the tumor boundary is a function of tumor shape. This has been determined analytically for two tumor models: an infinite half-space model and a spherical tumor model.

4.2.1 Half-Space Tumor Model

The first tumor model considered consists of two infinite half spaces: one of homogeneous normal tissue and one of tumor tissue. For such a model, the bioheat equation is a function of a single coordinate direction x, and can be simply evaluated to give Eq. (4.8) for the power deposition in the tumor region, $x < 0$. As demonstrated in Chapter 3, the strength of the power deposition delta function at the tumor boundary for a half-space model is given by

$$P_{hs} = -K \left.\frac{dT(x,t)}{dx}\right|_{x=0^-}^{0^+} . \qquad (4.9)$$

This result was derived for the steady state case, but is applicable to the time varying case as well. Thus, in order to determine P_{hs}^t, the temperature must be determined for the normal tissue region for all time so that its spatial derivative at $x = 0^+$ can be evaluated.

The temperature in the normal tissue region obeys the time dependent bioheat equation (Eq. (4.1)) with zero power deposition,

$$\rho C \frac{dT}{dt} = K_n \frac{d^2T}{dx^2} - W_{bn} C_b T, \tag{4.10}$$

subject to the boundary condition

$$T(x=0,t) = T_o h(t/t_o). \tag{4.11}$$

Assuming that T(x,t) can be expressed as a summation of separable eigenfunctions of the form v(t)u(x), and using a separation constant of $j\omega\rho C$ for Eq. (4.10) yield

$$v(t) = e^{j\omega t} \tag{4.12}$$

and

$$u(x) = e^{-(f + jg)x} \tag{4.13}$$

where

$$f + jg = \sqrt{\frac{W_{bn} C_b}{K_n} + \frac{j\omega\rho C}{K_n}}. \tag{4.14}$$

Evaluating the square root of Eq. (4.14) so that u(x) remains finite as x approaches positive infinity gives

$$f = \sqrt{\frac{W_{bn} C_b}{2K_n} \left(\sqrt{\frac{\omega^2 \rho^2 C^2}{W_{bn}^2 C_b^2} + 1} + 1 \right)} \tag{4.15a}$$

$$g = \frac{\omega}{|\omega|} \sqrt{\frac{W_{bn} C_b}{2K_n} \left(\sqrt{\frac{\omega^2 \rho^2 C^2}{W_{bn}^2 C_b^2} + 1} - 1 \right)}. \tag{4.15b}$$

The general form of the temperature can then be expressed as the integral over all eigenfunctions:

$$T(x,t) = \int_{-\infty}^{\infty} A(\omega) e^{-(f+jg)x} e^{j\omega t} \, d\omega \tag{4.16}$$

where $A(\omega)$ is a constant dependent on the boundary conditions. To determine $A(\omega)$, Eq. (4.16) is evaluated at $x = 0$ so that the boundary condition of Eq. (4.11) can be applied

$$T(x=0,t) = \frac{1}{2\pi} \int_{-\infty}^{\infty} 2\pi A(\omega) e^{j\omega t} \, d\omega . \tag{4.17}$$

Equation (4.17) is recognized as the expression of an inverse Fourier transform, so that

$$A(\omega) = \frac{1}{2\pi} F\{T(x=0,t)\} \tag{4.18}$$

where F denotes the Fourier transform. Substituting Eq. (4.11) into Eq. (4.18) yields

$$A(\omega) = \frac{1}{2\pi} F\{T_o h(t/t_o)\}, \tag{4.19}$$

or equivalently,

$$A(\omega) = \frac{1}{2\pi} F\left\{ \int_{-\infty}^{t} \frac{T_o}{t_o} \, \mathrm{rect}\left(\frac{\tau - t_o/2}{t_o} \right) d\tau \right\}. \tag{4.20}$$

The Fourier transform in Eq. (4.20) can be evaluated using transform tables (Stremler, 1977) to yield

$$A(\omega) = \frac{T_o}{j\pi\omega^2 t_o} \sin\left(\frac{\omega t_o}{2}\right) e^{-j\omega t_o/2} + \frac{T_o}{2}\,\delta(\omega). \tag{4.21}$$

Substituting this result into Eq. (4.16) and reducing yield a general expression for T in the region x > 0,

$$T(x,t) = \frac{T_o}{2} e^{-\sqrt{W_{bn}C_b/K_n}\,x} + \frac{2T_o}{\pi t_o}\int_o^\infty \frac{e^{-fx}}{\omega^2} \sin\left(\frac{\omega t_o}{2}\right) \sin\left(\omega\left(t - \frac{t_o}{2}\right) - gx\right) d\omega. \tag{4.22}$$

This integral can be computed numerically. The time dependence of the temperature distribution for a representative case is shown in Fig. 4.4.

The power deposition delta function at the tumor boundary is determined by substituting Eq. (4.22) into Eq. (4.9) and evaluating to yield

$$P_{hs}^t = \frac{T_o}{2}\sqrt{W_{bn}C_b K_n} + \frac{2K_n T_o}{\pi t_o}\int_o^\infty \frac{1}{\omega^2} \sin\left(\frac{\omega t_o}{2}\right) \left[f\sin\left(\omega\left(t - \frac{t_o}{2}\right)\right) + g\cos\left(\omega\left(t - \frac{t_o}{2}\right)\right)\right] d\omega \tag{4.23}$$

where the superscript t indicates the time dependent solution. Comparing this result with Eq. (3.10) gives

$$P_{hs}^t = P_{hs}^{ss}\left\{\frac{1}{2} + \frac{\sqrt{2}}{\pi t_o}\int_o^\infty \frac{1}{\omega^2} \sin\left(\frac{\omega t_o}{2}\right) \left[\sqrt{\sqrt{\frac{\omega^2\rho^2C^2}{W_{bn}^2C_b^2}} + 1} + 1 \sin\left(\omega\left(t - \frac{t_o}{2}\right)\right) + \sqrt{\sqrt{\frac{\omega^2\rho^2C^2}{W_{bn}^2C_b^2}} + 1} - 1 \cos\left(\omega\left(t - \frac{t_o}{2}\right)\right)\right] d\omega\right\}. \tag{4.24}$$

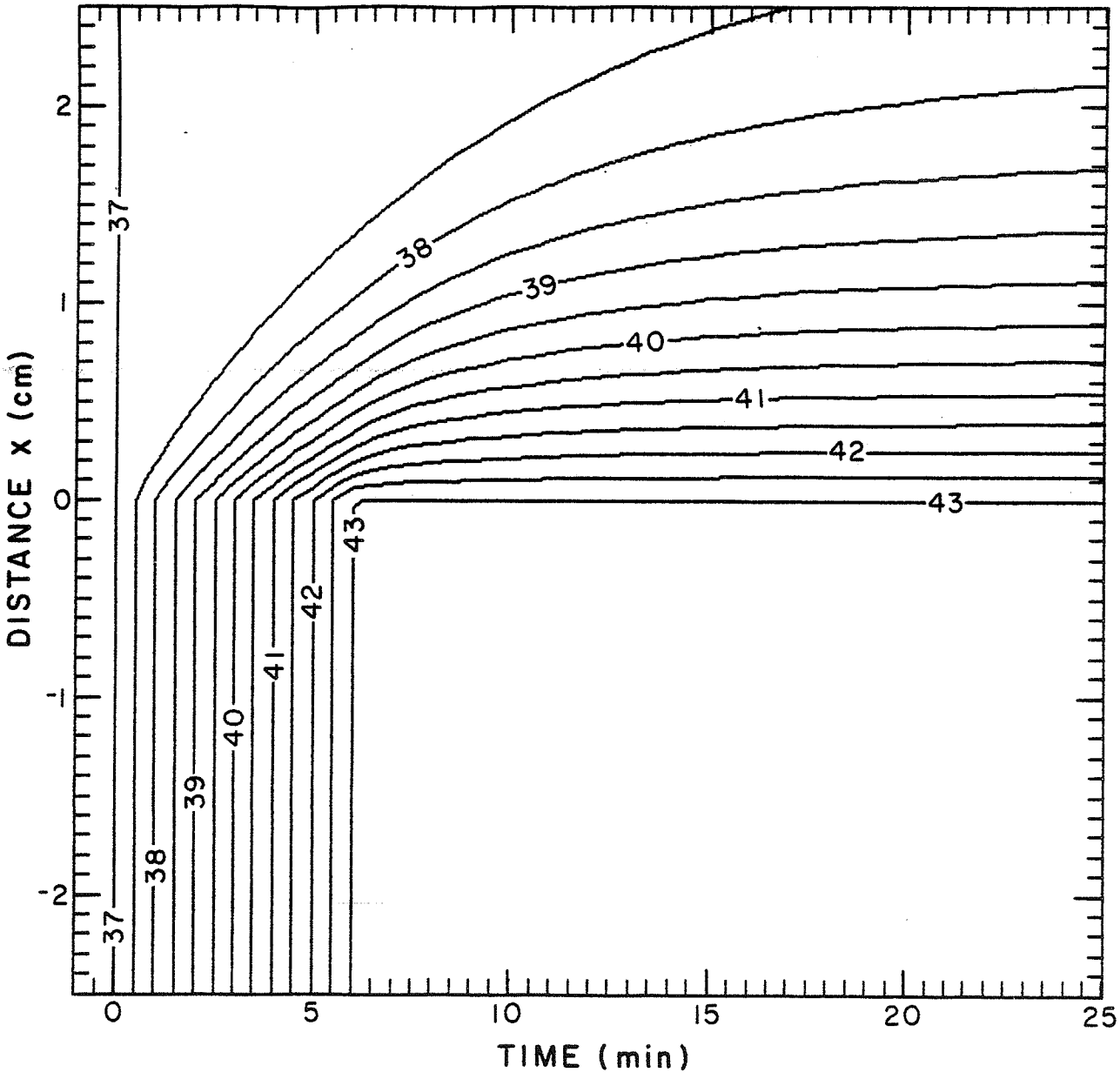

Figure 4.4. Contour plot of temperature time dependence for a cross-section of the half-space tumor model, tumor ($x < 0$) and normal tissue ($x > 0$). Temperatures are given at increments of $0.5^{o}C$.

Defining $d(t,t_o,a)$ as

$$d(t,t_o,a) = \frac{1}{2} + \frac{\sqrt{2}}{\pi t_o} \int_0^\infty \frac{1}{\omega^2} \sin\left(\frac{\omega t_o}{2}\right) \left[\sqrt{\sqrt{\omega^2 a^2 + 1} + 1} \sin\left(\omega\left(t - \frac{t_o}{2}\right)\right) + \sqrt{\sqrt{\omega^2 a^2 + 1} - 1} \cos\left(\omega\left(t - \frac{t_o}{2}\right)\right)\right] d\omega \tag{4.25}$$

yields

$$P_{hs}^t = P_{hs}^{ss}\, d(t,t_o,\rho C/W_{bn}C_b)\,. \tag{4.26}$$

The function P_{hs}^t is illustrated in Fig. 4.5 for typical tumor parameter values and various blood perfusion rates. The differences between the time dependencies of Q_p^t in the tumor interior and P_{hs}^t can be noted by a direct comparison of Figs. 4.3 and 4.5.

4.2.2 Spherical Tumor Model

The second model considered is a spherical tumor of radius r_o surrounded by an infinitely extended region of homogeneous normal tissue. Despite the infinite extent of the surrounding tissue, the spherical model is applicable to most tumors because heat conduction in the normal tissue is limited to several centimeters when blood perfusion is considered. The temperature and power deposition in the tumor region, $r < r_o$, are again given by Eq. (4.5) and Eq. (4.8), respectively. However, the power deposition delta function at the tumor boundary differs from that for

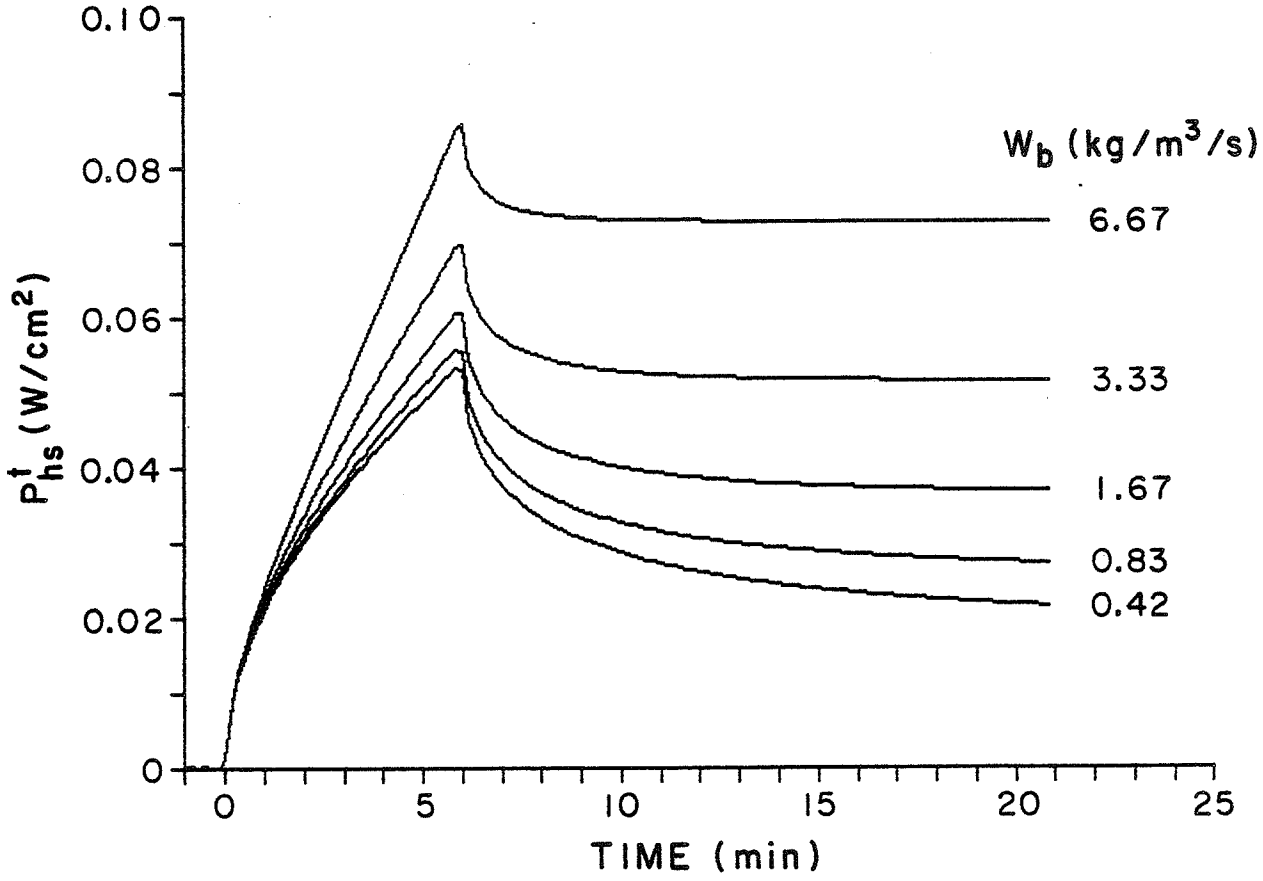

Figure 4.5. Time dependence of the strength of the delta function required at the tumor boundary for the half-space model, P^t_{hs}, for a range of blood perfusion values.

the half-space model due to the curvature of the boundary.

As before, derivation of the power deposition delta function at the tumor boundary requires determination of the temperature in the normal tissue. Outside the tumor, where $r > r_o$, there is no power deposition Q_p and Eq. (4.1) can be expressed in spherical coordinates as

$$\rho C \frac{\partial T}{\partial t} = K_n \frac{\partial^2 T}{\partial r^2} + \frac{2K_n}{r} \frac{\partial T}{\partial r} - W_{bn} C_{bn} T. \tag{4.27}$$

Again, $T(x,t)$ is assumed to be expressible as the summation of separable eigenfunctions of the form $v(t)u(r)$. Using a separation constant of $j\omega\rho C$ gives

$$v(t) = e^{j\omega t} \tag{4.28}$$

and

$$u(r) = \frac{e^{-(f + jg)r}}{r} \tag{4.29}$$

where f and g are given by Eq. (4.15). The general form of the temperature is

$$T(r,t) = \int_{-\infty}^{\infty} \frac{A(\omega)}{r} e^{(f + jg)r} e^{j\omega t} d\omega, \tag{4.30}$$

which is evaluated at $r = r_o$ for application of the boundary condition to give

$$T(r_o,t) = \frac{1}{2\pi} \int_{-\infty}^{\infty} \frac{2\pi A(\omega)}{r_o} e^{(f + jg)r_o} e^{j\omega t} d\omega. \tag{4.31}$$

Equation (4.31) has the form of an inverse Fourier transform and can be evaluated using the same method as for the half-space model to yield

$$T(r,t) = \frac{T_o r_o}{2r} e^{-\sqrt{W_{bn} C_b / K_n}(r - r_o)} + \frac{2T_o r_o}{\pi t_o r} \int_o^\infty \frac{1}{\omega^2} e^{-f(r - r_o)} \sin\left(\frac{\omega t_o}{2}\right) \sin\left(\omega\left(t - \frac{t_o}{2}\right) - g(r - r_o)\right) d\omega . \quad (4.32)$$

The time dependence of this distribution for a 2.5 cm radius tumor model is shown in Fig. 4.6. The temperature falls off over a shorter distance for the spherical model (Fig. 4.6) than for the half-space model (Fig. 4.4) because the heat is conducted outward in all three coordinate directions rather than in only one.

The strength of the delta function at the tumor periphery for the spherical model is

$$p_s^t = -K \left.\frac{dT(r,t)}{dr}\right|_{r=r_o^-}^{r_o^+} . \quad (4.33)$$

Substituting Eq. (4.32) into Eq. (4.33) and reducing yield

$$p_s^t = \frac{T_o}{2} \sqrt{W_{bn} C_b K_n} + \frac{T_o K_n}{2r_o} + \frac{2K_n T_o}{\pi t_o} \int_o^\infty \frac{1}{\omega^2} \sin\left(\frac{\omega t_o}{2}\right) \left[\left(f + \frac{1}{r_o}\right) \sin\left(\omega\left(t - \frac{t_o}{2}\right)\right) + g\cos\left(\omega\left(t - \frac{t_o}{2}\right)\right)\right] d\omega . \quad (4.34)$$

This can be further reduced and expressed in terms of previously defined functions as

$$p_s^t = p_{hs}^t + \frac{T_o K_n}{r_o} h(t/t_o) . \quad (4.35)$$

A comparison of the time dependent solution of Eq. (4.35)

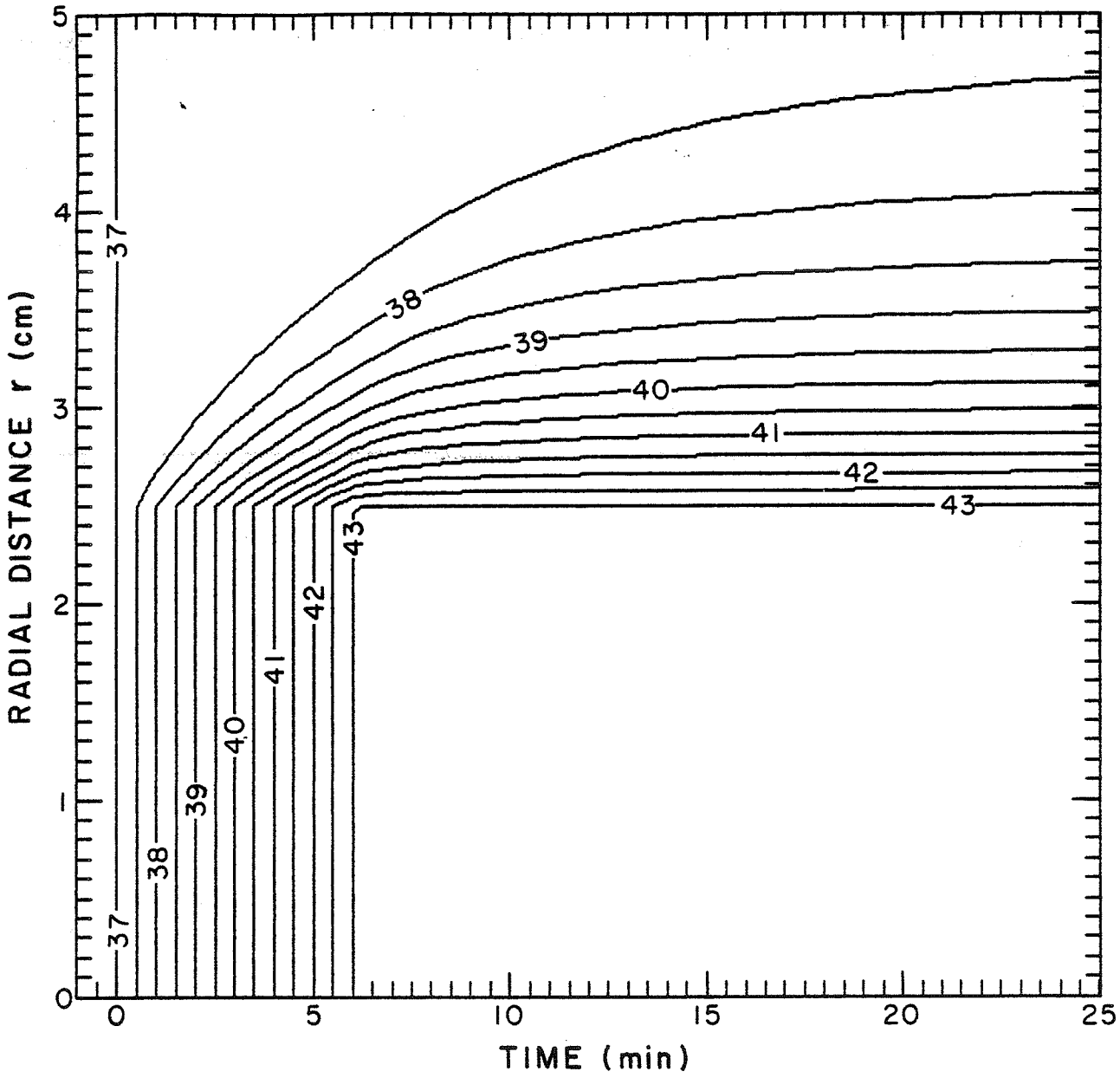

Figure 4.6. Contour plot of temperature time dependence for a cross-section of the spherical tumor model with 2.5 cm tumor radius, tumor ($r < 2.5$ cm) and normal tissue ($r > 2.5$ cm). Temperatures are given at increments of $0.5^{o}C$.

with the steady state solution of Eq. (3.27) reveals the similarities of the dependence on tumor radius of the time dependent and steady state solutions. The function P_s^t for a tumor radius of 2.5 cm is shown in Fig. 4.7 for representative tumor parameters and various blood perfusion rates. More power is required on the periphery of the spherical model (Fig. 4.7) than for the half-space model (Fig. 4.5) due to the increased heat conducted to the normal tissue.

4.2.3 Numerical Tumor Model

Applications of the preceding two models are limited to situations where normal tissue parameters are nearly constant and the normal-tumor tissue boundary geometry approaches a spherical shell or a plane. Clearly, a general numerical method, applicable to arbitrarily shaped tumors, would be desirable for clinical applications.

The steady state numerical method discussed in Chapter 3 was modified for the calculation of the time dependent solution. Since the time dependencies of the power deposition interior to the tumor and the power delta function at the tumor boundary are different, these regions are handled separately. For a tumor of arbitrary size and shape, Eq. (4.8) holds and specifies the power deposition required at each point interior to the tumor as a function of time. Equation (4.8) is valid for variable tissue parameters within the tumor as long as a uniform rate of temperature rise R is prescribed throughout the tumor. Such

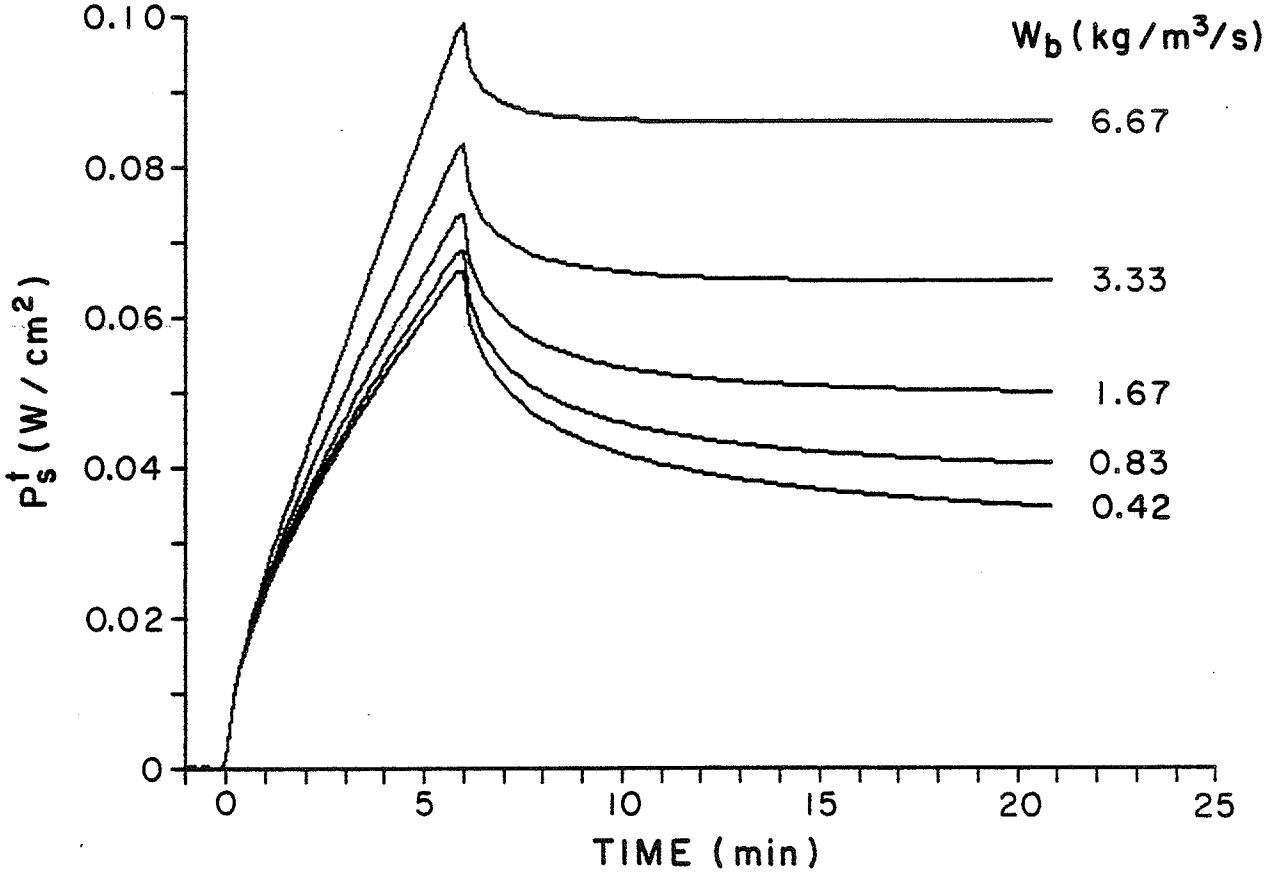

Figure 4.7. Time dependence of the strength of the delta function required at the tumor boundary for the spherical model, P_s^t, for a range of blood perfusion values. Tumor radius is 2.5 cm.

an application of Eq. (4.8) is equivalent to weighting the interior steady state solution with $h(t/t_o)$ and adding an amount ρCR throughout the tumor during the initial heating phase.

The time dependent power deposition required on the tumor boundary for an arbitrarily shaped tumor with variable tissue properties is related to the steady state numerical solution. The results represented by Eq. (4.35) can be used by defining an effective tumor radius r_{eff} as the local curvature of the tumor as represented in the numerical model. Denoting the numerical time dependent solution by P_n^t, Eq. (4.35) can be rewritten as

$$P_n^t = P_{hs}^t + \frac{T_o K_n}{r_{eff}} h(t/t_o). \tag{4.36}$$

Equation (4.36) has the same form as Eq. (4.35), so the time dependence of P_n^t is also given by Fig. 4.6 for the case of $r_{eff} = 2.5$ cm. The effective tumor radius r_{eff} is chosen at each point on the tumor boundary so that Eq. (4.36) holds. Taking the limit of Eq. (4.36) as time approaches infinity yields the steady state numerical power deposition P_n^{ss}

$$P_n^{ss} = P_{hs}^{ss} + \frac{T_o K_n}{r_{eff}}. \tag{4.37}$$

Since P_n^{ss} is known and P_{hs}^{ss} can be approximated by using the local tissue properties, the quotient $T_o K_n / r_{eff}$ can be determined. Replacing this quotient in Eq. (4.36) with its steady state equivalent and using Eq. (4.26) give

$$P_n^t = P_n^{ss}\, h(t/t_o) + P_{hs}^{ss}\, (d(t,t_o,\rho C/W_{bn}C_b) - h(t/t_o)). \quad (4.38)$$

Equation (4.38) holds for constant tissue properties outside the tumor and is used for approximating P_n^t for nearly constant tissue properties.

The time dependence of the two terms of Eq. (4.38) are shown in Fig. 4.8. The first term of Eq. (4.38) increases linearly with time until it reaches the steady state solution at time t_o where it remains throughout the duration of the treatment, while the second term increases exponentially to a limit until time t_o when it begins to decay exponentially to zero. The first term is also dependent only on the steady state numerical solution, whereas the second term is dependent on the local tissue properties in the normal tissue for evaluating P_{hs}^{ss} and $d(t,t_o,\rho C/W_{bn}C_b)$. Dependence on the effective tumor radius r_{eff} is not explicitly present, but is included in P_n^{ss}.

4.3 Results

The numerical solution discussed in the previous section was applied to a spherical tumor model in a three dimensional rectangular coordinate system. A rectangular coordinate system was used so that an arbitrary tumor geometry could be represented, and a spherical model was chosen for ease of visualization since symmetry assures that a two dimensional cross-section through the tumor center is a representative sample. A more complicated tumor geometry could have been chosen, but a complete set of cross-sections

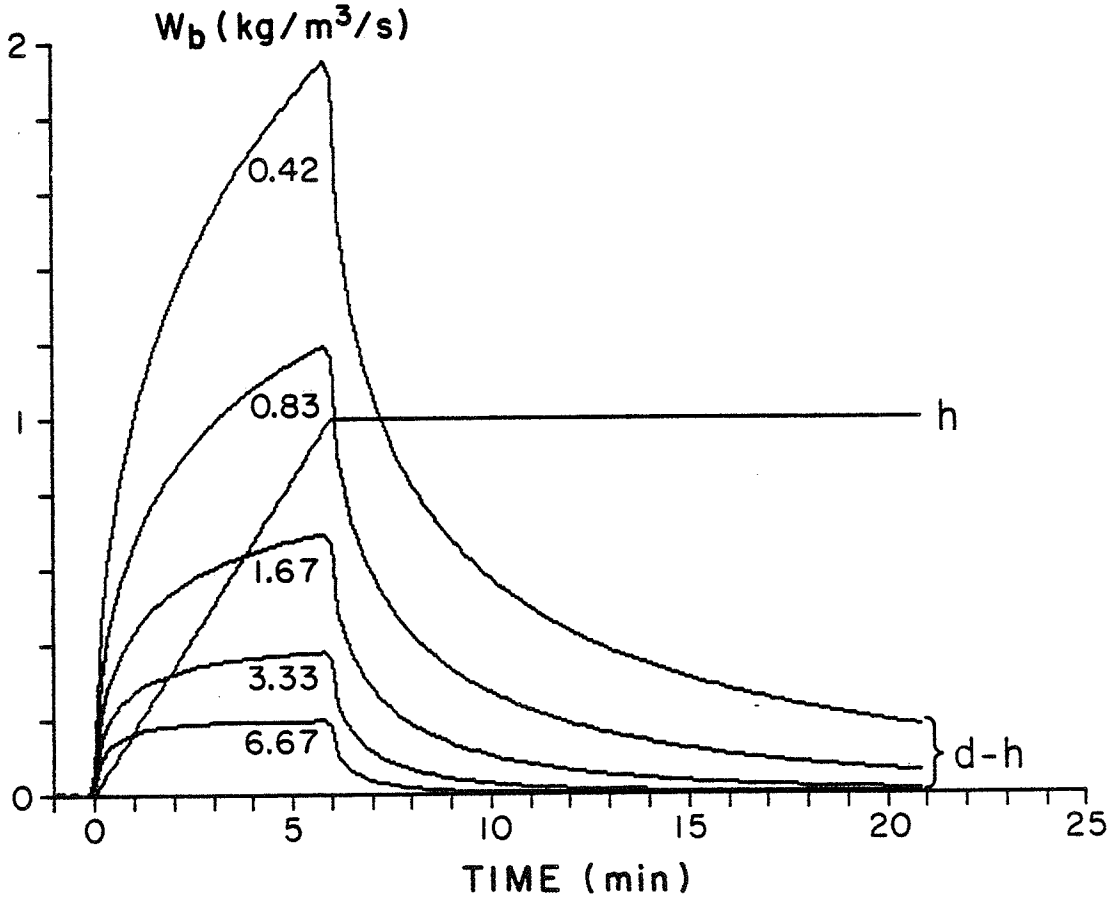

Figure 4.8. Time dependencies of the weighting functions h and d - h for P_n^{ss} and P_{hs}^{ss}, respectively, which are used for the calculation of the numerical delta function strength P_n^t. Weighting functions are shown for a range of blood perfusion values.

would have been required to characterize the power deposition pattern at a particular instant in time. Likewise, constant tissue parameters were used to simplify the illustration.

A steady state numerical solution for a 2 cm radius spherical tumor centered at a depth of 8 cm was presented in Chapter 3. A cross-section of the power deposition pattern required to maintain a constant tumor temperature for this spherical geometry is shown in Fig. 3.7 along with the resultant temperature distribution. The steady state numerical solution is used in the determination of the time dependent solution.

The power deposition from the steady state numerical solution, P_n^{ss}, and the steady state half-space solution as given by Eq. (3.10), P_{hs}^{ss}, are combined with appropriate weighting functions using Eq. (4.38) to give the time dependent power deposition at the periphery, P_n^t. When this result, P_n^t, is superimposed with the steady state result Q_p^{ss} weighted as given in Eq. (4.8), the complete numerical time dependent solution is formed. The time dependent power deposition required for the case of the spherical tumor is given in Fig. 4.9 for several representative times to illustrate the progression of heating to uniformly raise the tumor temperature to, and maintain it at, a uniform value.

4.4 Discussion

Results presented here are for the simplified case of

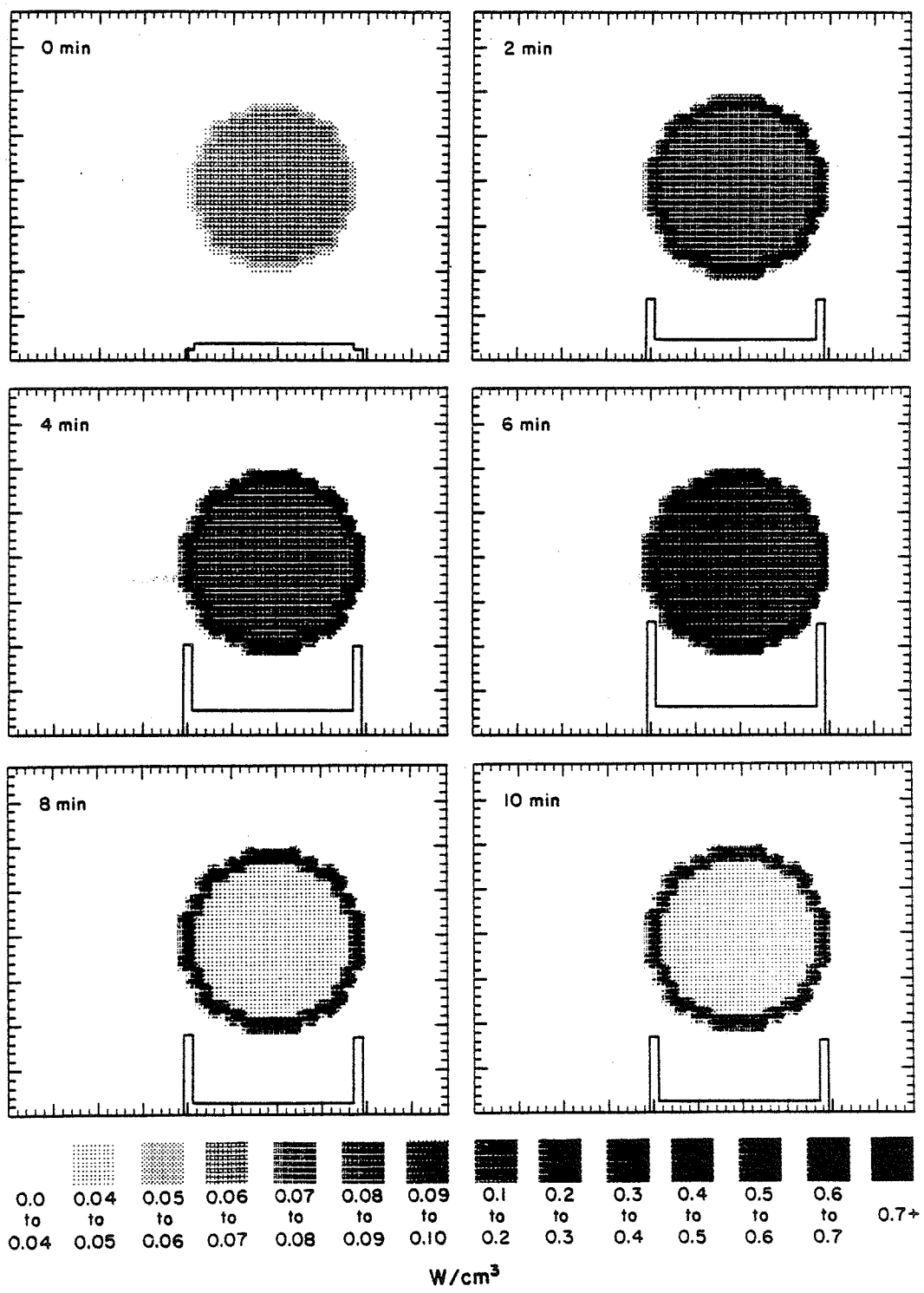

Figure 4.9. Gray scale plots of a cross-section of the power deposition for a numerically calculated spherical tumor model sampled every 2 mm with major divisions indicated every centimeter. Cross-sections are shown for times of 0, 2, 4, 6, 8, and 10 minutes. The skin surface is located at the left side of each cross-section and the tumor is centered at a depth of 8 cm. Corresponding power profiles taken through the skin surface and tumor center are presented with each cross-section.

constant, temperature independent, perfusion, an oversimplification that yields illustrative results. The numerical method can be modified to incorporate the additional complications that arise in practical applications.

The material presented in this chapter is useful for two purposes: to give an understanding of the time dependent power deposition required to achieve and maintain a uniform therapeutic temperature and to yield a numerical model that can be adapted to clinical usage. The results indicate that a more uniform power deposition pattern is desirable for raising the temperature to the therapeutic level, while reduced power deposition within the tumor relative to that at the periphery of the tumor is more suitable for maintaining the steady state. Attempting to raise the temperature by simply elevating the power levels required to maintain the steady state will cause the temperature rise within the interior region to lag behind that of the exterior regions of the tumor.

Such a detailed analysis of the power deposition patterns required to produce desired temperatures within the tumor provides the insight required to best utilize precision hyperthermia applicators. The results presented show that different power deposition patterns are necessary during the initial heating and the steady state periods of hyperthermia. Practical applications of these theoretical results have been considered and are treated in the following chapter.

CHAPTER 5

APPLICATOR CONFIGURATIONS AND SCAN PATHS FOR LOCALIZED HYPERTHERMIA

5.1 Introduction

The first microwave and ultrasound hyperthermia applicators were simple devices designed to produce collimated beams of radiated energy. Later device designs have included control of several collimated beams, focusing to allow deep heating, scanning of the focus for precision hyperthermia, and placement of multiple microwave antennas or ferromagnetic seeds within the tumor. Despite such advances in applicator design, the design criteria have remained basically the same: provide gain for deep heating and as much control over the radiated field as possible.

Control algorithms are being developed (1) to move a focus throughout a tumor following a scan path designed to produce a uniform temperature distribution, (2) to keep the temperature at a constant elevation throughout the treatment, and (3) to provide temperature information throughout the tumor based on a limited number of sample points. All of these methods have the goal of producing a uniform temperature throughout the tumor volume for the duration of the hyperthermia treatment.

In this chapter, more direct approaches towards obtaining the goal of a uniform temperature by using the results of Chapters 3 and 4 are examined. Only the steady

state solution will be considered here for illustrative purposes. The results, however, are general since the time dependent solution can be formed from the steady state results as was shown in Chapter 4.

5.2 Fourier Transform Representation

The concept behind the procedure presented in this chapter can best be illustrated by first considering the ideal case of a power deposition pattern basis function that does not change shape when its position is changed. This basis function applies to a specific hyperthermia system and would correspond to the fixed focus of a mechanically scanned ultrasonic transducer, the electronically scanned focus of an ultrasound or microwave phased array, or the heat generation pattern of an implantable ferromagnetic seed.

With a basis function that is independent of position, the power deposition pattern can be represented by the convolution of the power deposition basis function and the scan path weighted by the dwell time at each position for the case of a scanned focus. For ferromagnetic seeds, the power deposition basis function is convolved with the seed positions. However, the unknown function in either case is the scan path with dwell time weightings or the seed position, depending upon the chosen method of heating. This function will hereafter be referred to as the conforming function as it is used to conform the basis function to

produce a desired power deposition pattern. Using Q(x,y,z) to represent the power deposition for tumor heating (W/m^3), B(x,y,z) to represent the power deposition basis function (W/m^3), and C(x,y,z) to represent the conforming function, the convolution can be expressed as

$$Q(x,y,z) = C(x,y,z) * B(x,y,z). \tag{5.1}$$

Applying a Fourier transform to Eq. (5.1), the convolution becomes a multiplication in the form

$$Q(u,v,w) = C(u,v,w) \cdot B(u,v,w), \tag{5.2}$$

where u, v, and w represent spatial frequencies in the three coordinate directions. Equation (5.2) can be rearranged to solve for the conforming function

$$C(u,v,w) = Q(u,v,w) / B(u,v,w). \tag{5.3}$$

For the conforming function to be defined everywhere, a zero must be present in Q(u,v,w) at every point that a zero is present in B(u,v,w). Also, Q(x,y,z) represents the actual power deposition produced by the applicator, not $Q_p(x,y,z)$, which is the power deposition pattern required to produce a uniform temperature distribution across the tumor. Ideally, Q(x,y,z) should equal $Q_p(x,y,z)$.

A simple illustration of this approach is provided by the following one dimensional example. From the results of Chapter 3, $Q_p(x)$, the optimum Q(x), can be represented by two impulse functions of strength P and a rectangle function:

$$Q_p = P\delta(x - x_o) + P\delta(x + x_o) + W_{bt}C_bT_o\,\mathrm{rect}(x/2x_o) \qquad (5.4)$$

where the tumor is centered at $x = 0$ with width $2x_o$ and constant blood perfusion W_{bt}. The simple analytic Fourier transform of Eq. (5.4) is given by

$$Q_p(u) = 2P\cos(x_o u) + 2W_{bt}C_bT_o\sin(x_o u)/u \qquad (5.5)$$

as illustrated in Fig. 5.1(a). For the example of a focused ultrasound beam scanned parallel to the face of the focused square source (and approximately for that of a focused circular source), the focal profile is approximately

$$B(x) = (w\,\sin(2\pi x/w)/2\pi x)^2 \qquad (5.6)$$

with Fourier transform

$$B(u) = (w/2)\ \Lambda\ (wu/4\pi) \qquad (5.7)$$

where Λ represents the triangular function as shown in Fig. 5.1(b).

Division of $Q_p(u)$ by $B(u)$ would yield the ideal conforming function only if it were possible to achieve exactly $Q_p(u)$. However, it is evident that it is not possible to form the required impulse functions (producing the high frequency content in $Q_p(u)$) by using the finite width basis function $B(x)$. Also, the indiscriminate use of $Q_p(u)$ in place of $Q(u)$ yields regions of negative values in the conforming function $C(x)$, which is not possible to achieve physically. Because of these problems, $Q_p(u)$ cannot be used in place of $Q(u)$, and the lack of a straightforward

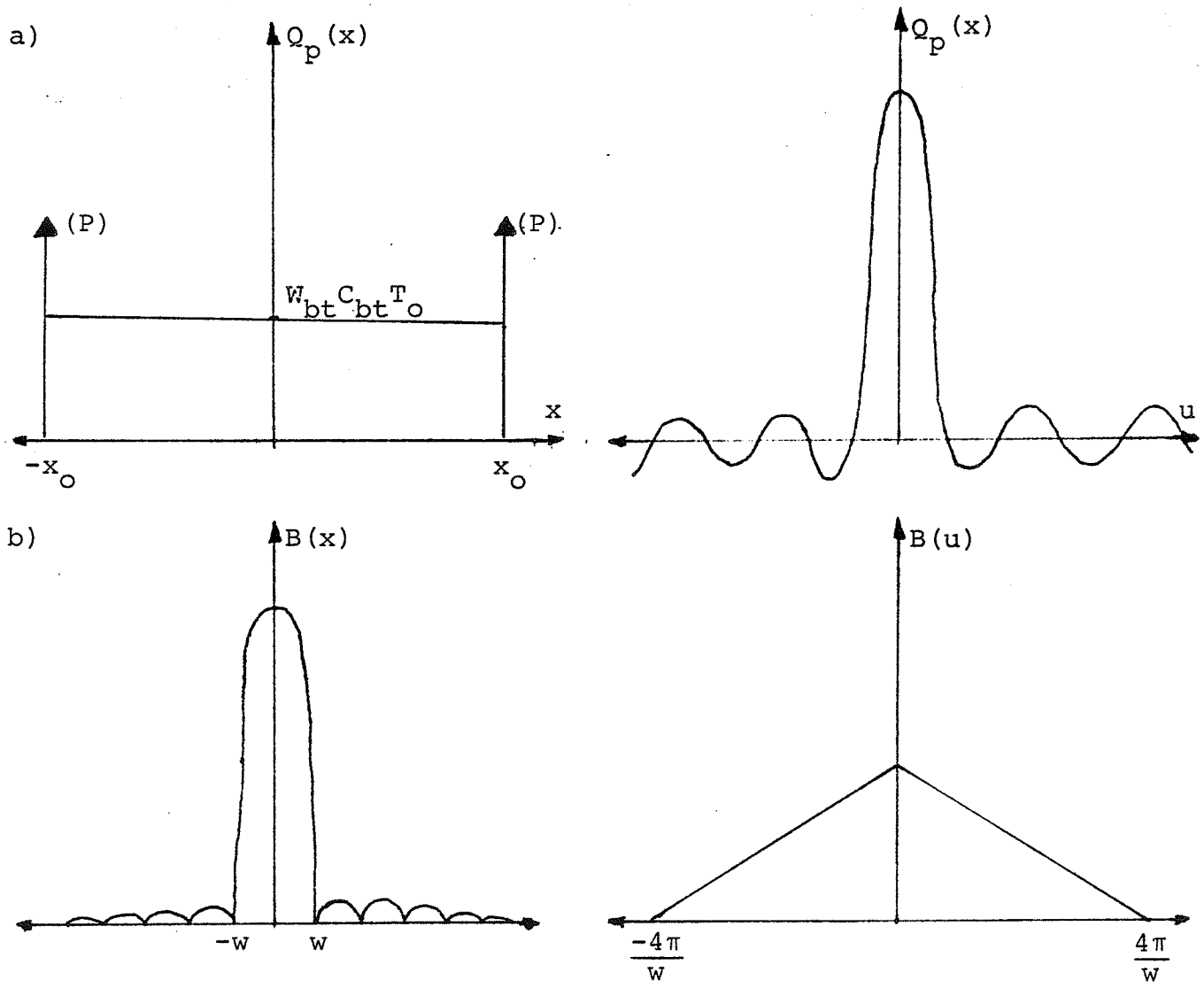

Figure 5.1. $Q_p(x)$ and $Q_p(u)$ (a), and B(x) and B(u) (b).

method to obtain Q(u) from $Q_p(u)$ limits the application of a Fourier transform approach.

However, the differences in Q(u,v,w) and $Q_p(u,v,w)$ at high spatial frequencies are not of practical importance because the temperature distribution will be smoothed by heat conduction. The allowable spatial variation can be determined by examining the effect of heat source (basis function) spacing.

5.3 Maximum Allowable Heat Source Spacing

To use the Fourier transform approach, the maximum allowable spacing between the locations of the heat sources, or scan locations, must be determined. The maximum allowable source spacing is determined by two limiting factors: the temperature reduction which occurs between the locations and the adequacy of the representation of the impulse function on the tumor periphery.

5.3.1 One Dimensional Source Spacing

The temperature drop between locations of the heat sources can be determined by applying the bioheat transfer equation. To illustrate the form of the temperature dependence between two heat source locations, a one dimensional solution will be presented. The one dimensional case represents the situation where there are two planes of applied heat and the temperature between these planes is of interest. Considering two planes of applied heat separated by a distance d, the bioheat equation has the form

$$\frac{d^2T}{dx^2} - \frac{W_{bt}C_bT}{K_n} = 0. \qquad (5.8)$$

Designating the high temperature at the planes of heating as T_h, the temperature between the two planes is given by

$$T = T_h \frac{(\sinh(\sqrt{W_{bt}C_b/K_t}\, x) + \sinh(\sqrt{W_{bt}C_b/K_t}\, (d-x)))}{\sinh(\sqrt{W_{bt}C_b/K_t}\, d)} \qquad (5.9)$$

where one plane is located at x = 0 and the other is located at x = d. Evaulating this expression at d/2 where the minimum temperature T_l occurs yields

$$T_l = T_h \operatorname{sech}(\sqrt{W_{bt}C_b/K_t}\, d/2). \qquad (5.10)$$

Equation (5.10) can be rearranged to yield an expression for the separation between the planes of heating, d, in terms of the maximum and minimum allowable tumor temperatures and the tissue parameters:

$$d = \frac{2}{\sqrt{W_{bt}C_b/K_t}} \cosh^{-1}\left(\frac{T_h}{T_l}\right). \qquad (5.11)$$

Equation (5.11) can be applied to determine appropriate scan paths for a mechanically scanned fixed focus ultrasonic applicator for specified T_h and T_l. Since the focus of such an applicator is elongated in the depth direction, scanning of the beam along two parallel paths or two concentric circles produces a close approximation to the parallel plane heat sources as illustrated here. Equation (5.11) can be used to determine an appropriate distance between adjacent scan paths for a given tumor blood perfusion and temperature tolerance, $T_h - T_l$, a relationship shown in Fig. 5.2.

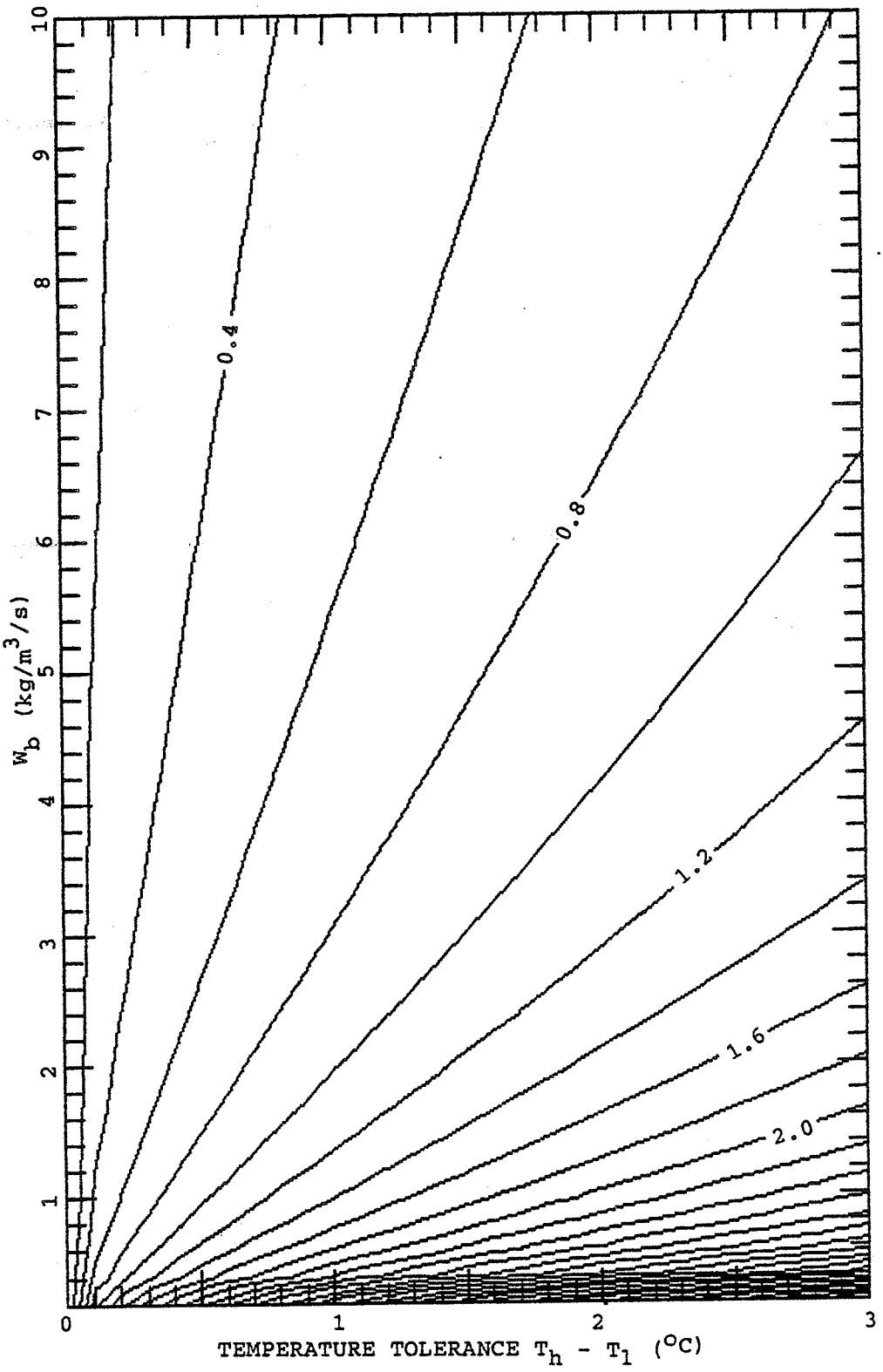

Figure 5.2. Contour plot of source spacing d in centimeters versus blood flow W_{bt} and temperature tolerance, $T_h - T_l$, for the one dimensional model. The average of T_h and T_l was fixed at 43^{o}C (with arterial temperature T_a = 37^{o}C added).

5.3.2 Two Dimensional Source Spacing

The case of line sources of heat forming the sides of a square (x = 0,d and y = 0,d) can be solved by application of Eq. (5.10) since the temperature dependence in each direction has the same form as that for the one dimensional case. The low temperature, T_l, occurs at the center of the square (x = d/2, y = d/2) and is given by

$$T_l = T_h \left(\operatorname{sech}\left(\sqrt{W_{bt}C_b/K_t}\, d/2\right)\right)^2. \tag{5.12}$$

Likewise the distance between the line sources, d, can be obtained from Eq. (5.12) as

$$d = \frac{2}{\sqrt{W_{bt}C_b/K_t}} \cosh^{-1}\left(\left(\frac{T_h}{T_l}\right)^{\frac{1}{2}}\right) \tag{5.13}$$

and is illustrated in Fig. 5.3. Equation (5.13) has application to implanted microwave antennas, which have an elongated heating pattern such that the sources are usually placed in a single plane with their major axes perpendicular to the plane. Similarly, Eq. (5.13) has applications to scanned phased array ultrasound where an elongated beam is placed at discrete locations in a cross-sectional plane of the tumor.

5.3.3 Source Spacing for Power Deposition Modulation

A possible application of the results from the two dimensional analysis is to use the spacing between focal locations produced by a scanned ultrasonic source to modulate the local intensity within the tumor. The power deposition required in the interior of the tumor to maintain

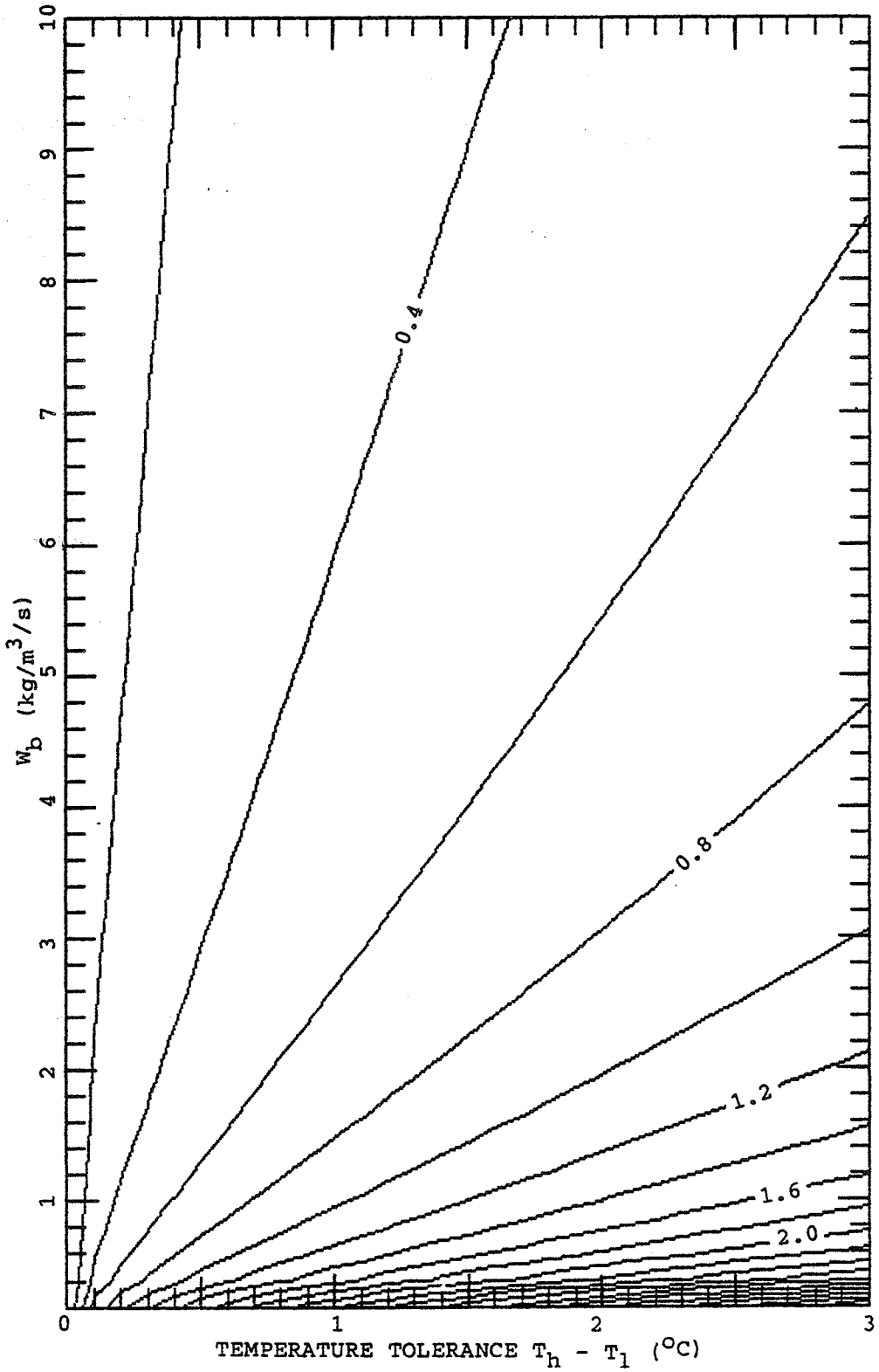

Figure 5.3. Contour plot of source spacing d in centimeters versus blood flow W_{bt} and temperature tolerance, $T_h - T_l$, for the two dimensional model. The average of T_h and T_l was fixed at 43^{o}C (with arterial temperature T_a = 37^{o}C added).

a steady temperature is given by Eq. (3.5), which when multiplied by the square of the maximum allowable distance between heat source locations gives the power required at each focal location, P_f (W/m),

$$P_f = Q_p \, d^2. \tag{5.14}$$

Substituting the result of Eq. (5.13) yields

$$P_f = 4K_t T_o (\cosh^{-1}((T_h/T_l)^{1/2})^2. \tag{5.15}$$

Using this approach, the power deposition required at each focal location is independent of tissue properties, while the focal spacing varies with blood perfusion.

5.3.4 Three Dimensional Source Spacing

The minimum spacing for a three dimensional array of heat sources with a given temperature tolerance, $T_h - T_l$, can also be calculated using the same approach:

$$d = \frac{2}{\sqrt{W_{bt} C_b / K_t}} \cosh^{-1}\left(\left(\frac{T_h}{T_l}\right)^{\frac{1}{3}}\right) . \tag{5.16}$$

The minimum spacing d is shown in Fig. 5.4 for a range of blood perfusions and temperature differences, $T_h - T_l$. The three dimensional solution has applications to the determination of acceptable spacings of ferromagnetic seeds for magnetic inductance heating. The solution also has applicability to scanned phased array ultrasonic heating where the region to be heated is shallow in depth and the length of the focus is limited in its extent.

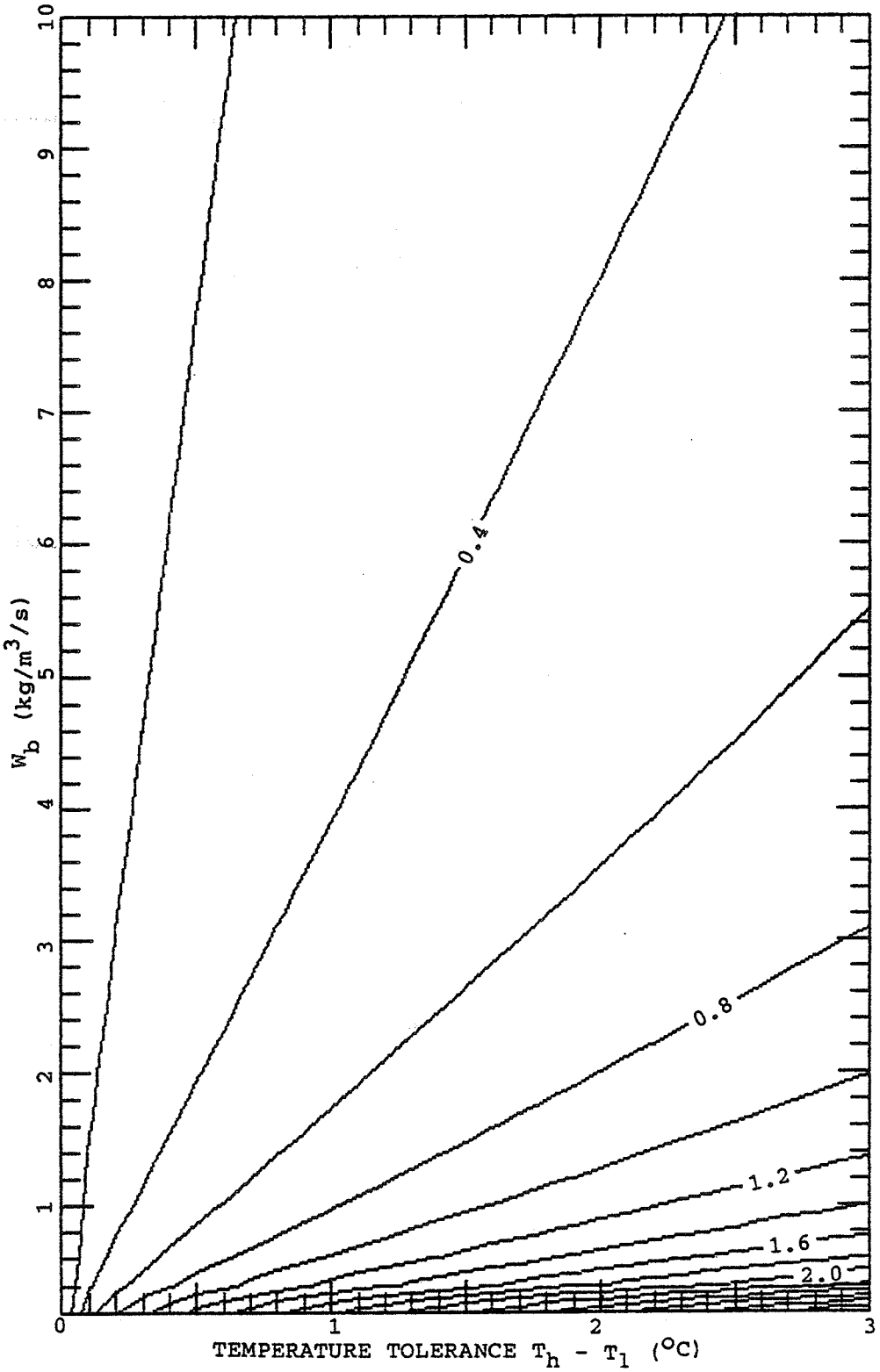

Figure 5.4. Contour plot of source spacing d in centimeters versus blood flow W_{bt} and temperature tolerance, $T_h - T_l$, for the three dimensional model. The average of T_h and T_l was fixed at 43°C (with arterial temperature T_a = 37°C added).

5.3.5 Sources of Finite Size

The results of this section can be adapted to heat deposition patterns or heat sources of finite dimensions by considering the distance d as the distance between the 3 dB levels of two adjacent sources of heat, so that the actual spacing is d plus the 3 dB heat source width. This distance correction is necessary, since when the 3 dB levels from two adjacent sources overlap, the power deposition is approximately level for the entire distance between the source centers, making the effective d equal to zero. Thus, the center of the sources can be spaced a total distance of the sum of d and the 3 dB width of the heat source.

5.4 Power Deposition Pattern Matching in One Plane with Focused Ultrasound

The formation of a good approximation to the required power deposition pattern derived in Chapters 3 and 4 can be accomplished with focused ultrasound using the results presented above. The first step in attempting to match the ideal power distribution is to calculate a suitable focal (source) spacing using the results of the previous section. The locations of the foci required to cover a cross-section parallel to the applicator face are established, making certain that the maximum focal spacing is not exceeded. An area associated with each focus, A_f, is designated. The power deposition required over each area, P_f (W/m), is then calculated by averaging the power deposition per unit volume

Q_p over A_f and multiplying by the focal area A_f:

$$P_f = \bar{Q}_p A_f, \tag{5.17}$$

equivalent to Eq. (5.14). To use this approach effectively, calibration of the applicator, i.e., knowledge of the power deposition at the desired depth (W/m) for a given input power, is required.

A one dimensional application of the bioheat equation was used to investigate the effects on this method of focal size, focal spacing, and focal placement. The linear form of the bioheat transfer equation, given in Eq. (2.17), was used. The blood perfusion, W_b, for this model was the same function of distance from the tumor boundary as shown in Fig. 3.5(a), up to 4 cm from the tumor boundary and 0.1667 $kg/m^3/s$ for greater distances. Other parameter values were as given in Table 2.1. A Gaussian was used to represent the focal shape. The modeled region extended 20 cm into the tumor region and 10 cm into the normal tissue so that boundary conditions would not affect the temperature distribution. The following figures do not show the entire modeled region, but only the region of interest.

Figures 5.5 through 5.9 show the power deposition patterns and resultant temperature distributions for focal regions of different sizes and spacings compared with the required power deposition pattern and its resultant (desired) temperature distribution, respectively. Confirmation that the desired temperature distribution can be closely matched using small (0.5 cm half power width),

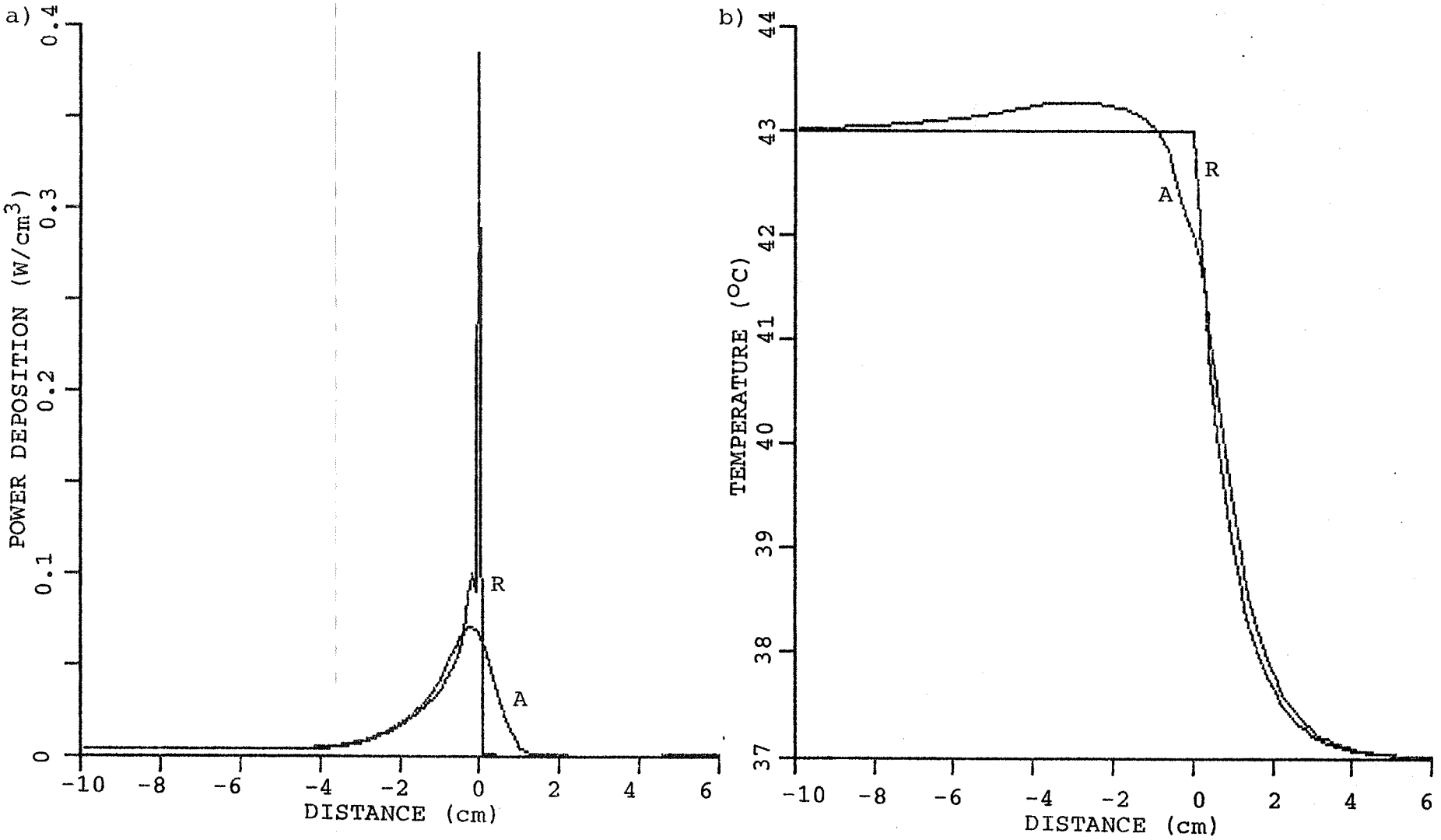

Figure 5.5. Matching of required power deposition with Gaussian function (0.5 cm half power width) spaced every 0.5 cm, starting from a focus placed directly on the tumor boundary. Required (R) and actual (A) power deposition patterns (a), and desired (R) and actual (A) temperature distributions (b) are given.

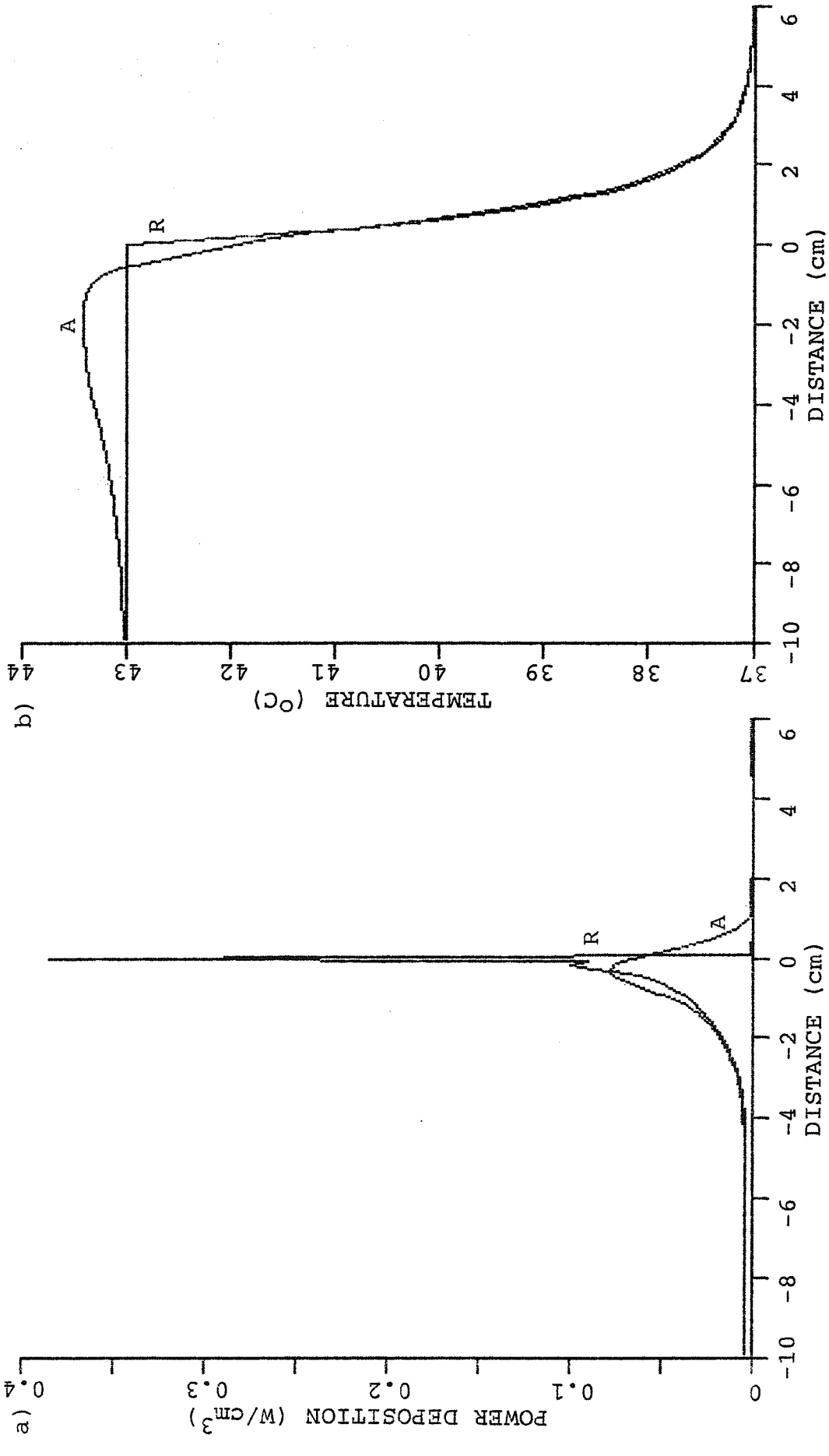

Figure 5.6. Matching of required power deposition with Gaussian function (0.5 cm half power width) spaced every 0.5 cm, starting from a focus placed 0.2 cm into the tumor from the tumor boundary. Required (R) and actual (A) power deposition patterns (a), and desired (R) and actual (A) temperature distributions (b) are given.

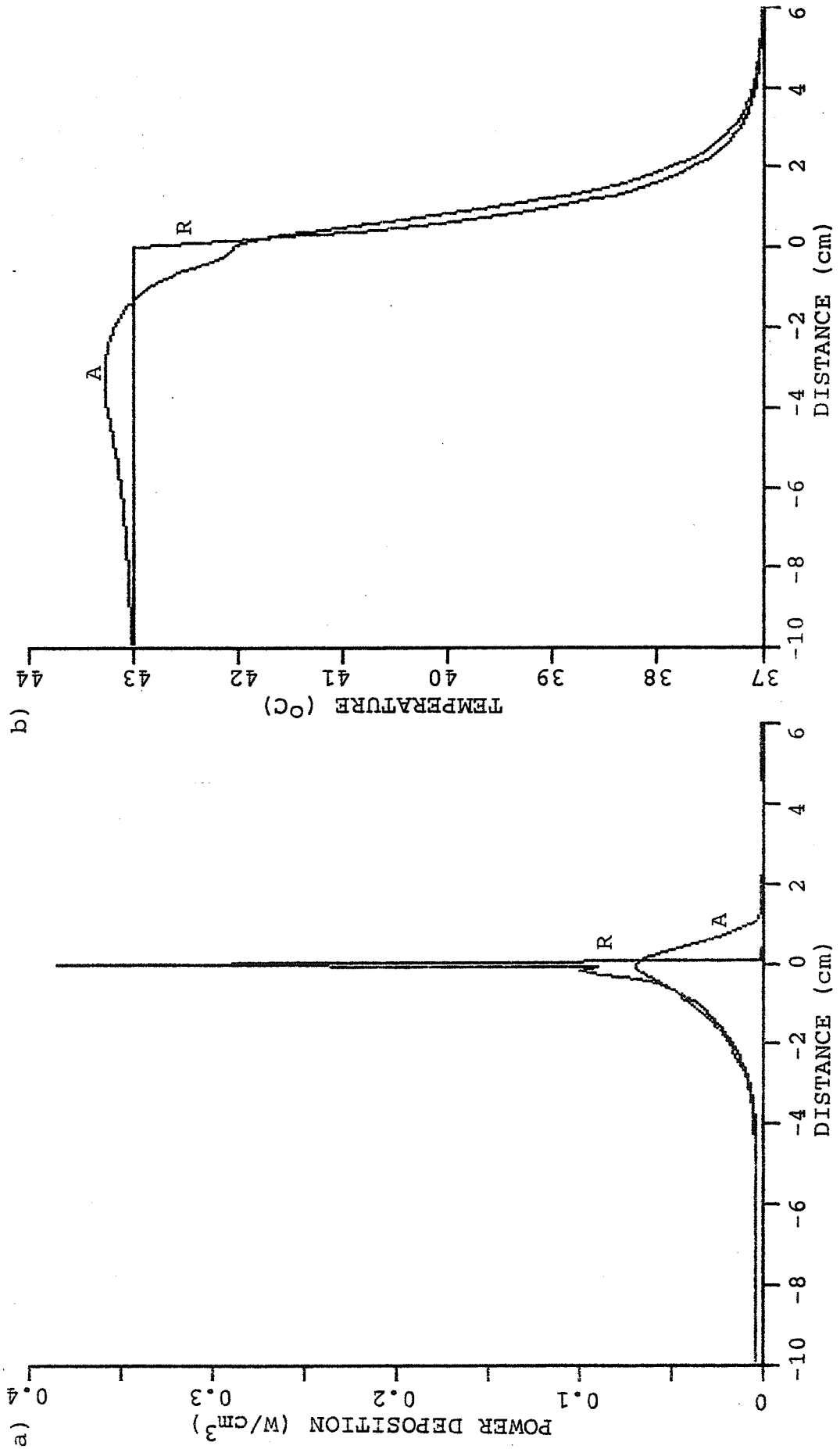

Figure 5.7. Matching of required power deposition with Gaussian function (0.5 cm half power width) spaced every 1.0 cm, starting from a focus placed directly on the tumor boundary. Required (R) and actual (A) power deposition patterns (a), and desired (R) and actual (A) temperature distributions (b) are given.

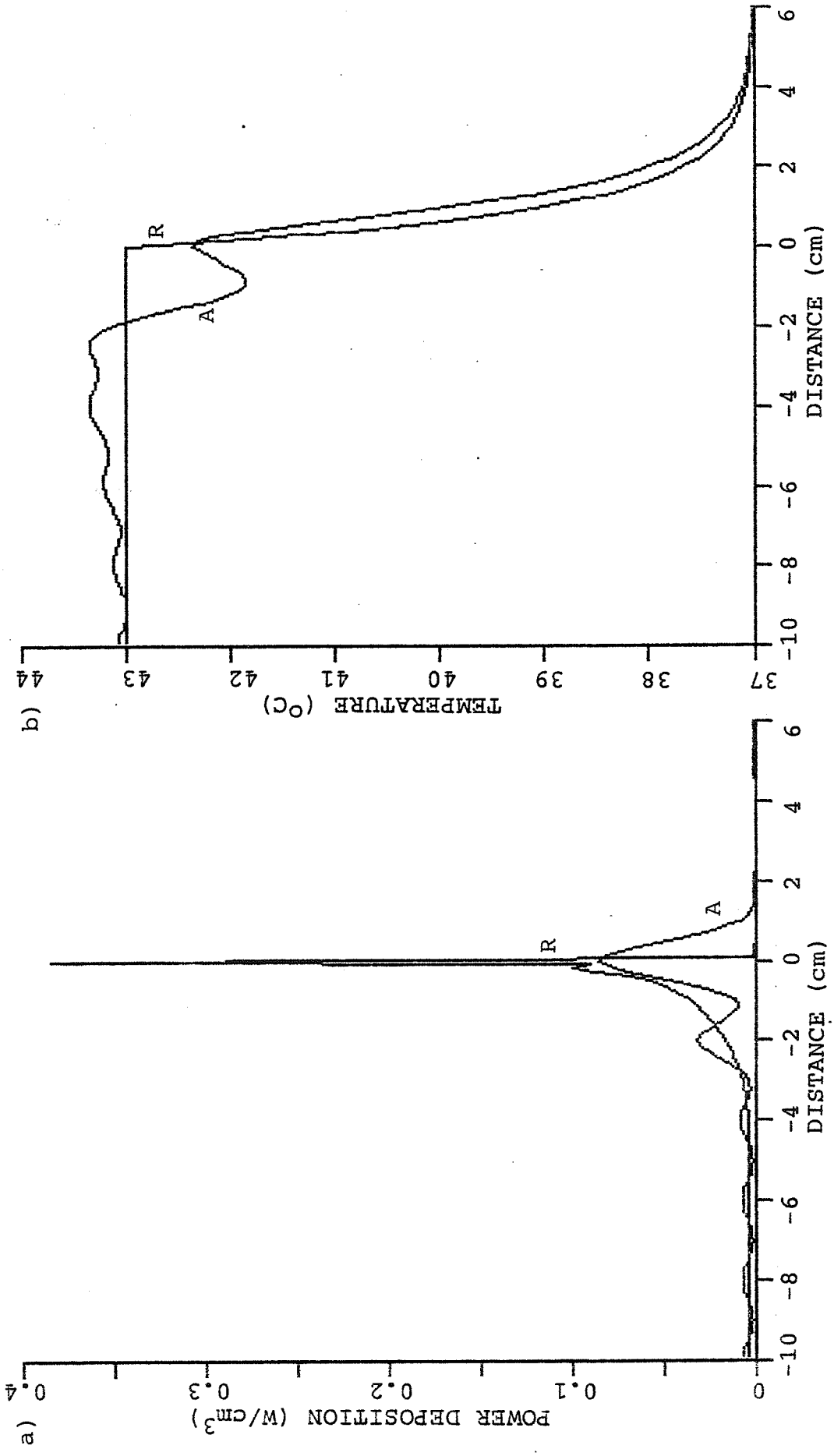

Figure 5.8. Matching of required power deposition with Gaussian function (0.5 cm half power width) spaced every 2.0 cm, starting from a focus placed directly on the tumor boundary. Required (R) and actual (A) power deposition patterns (a), and desired (R) and actual (A) temperature distributions (b) are given.

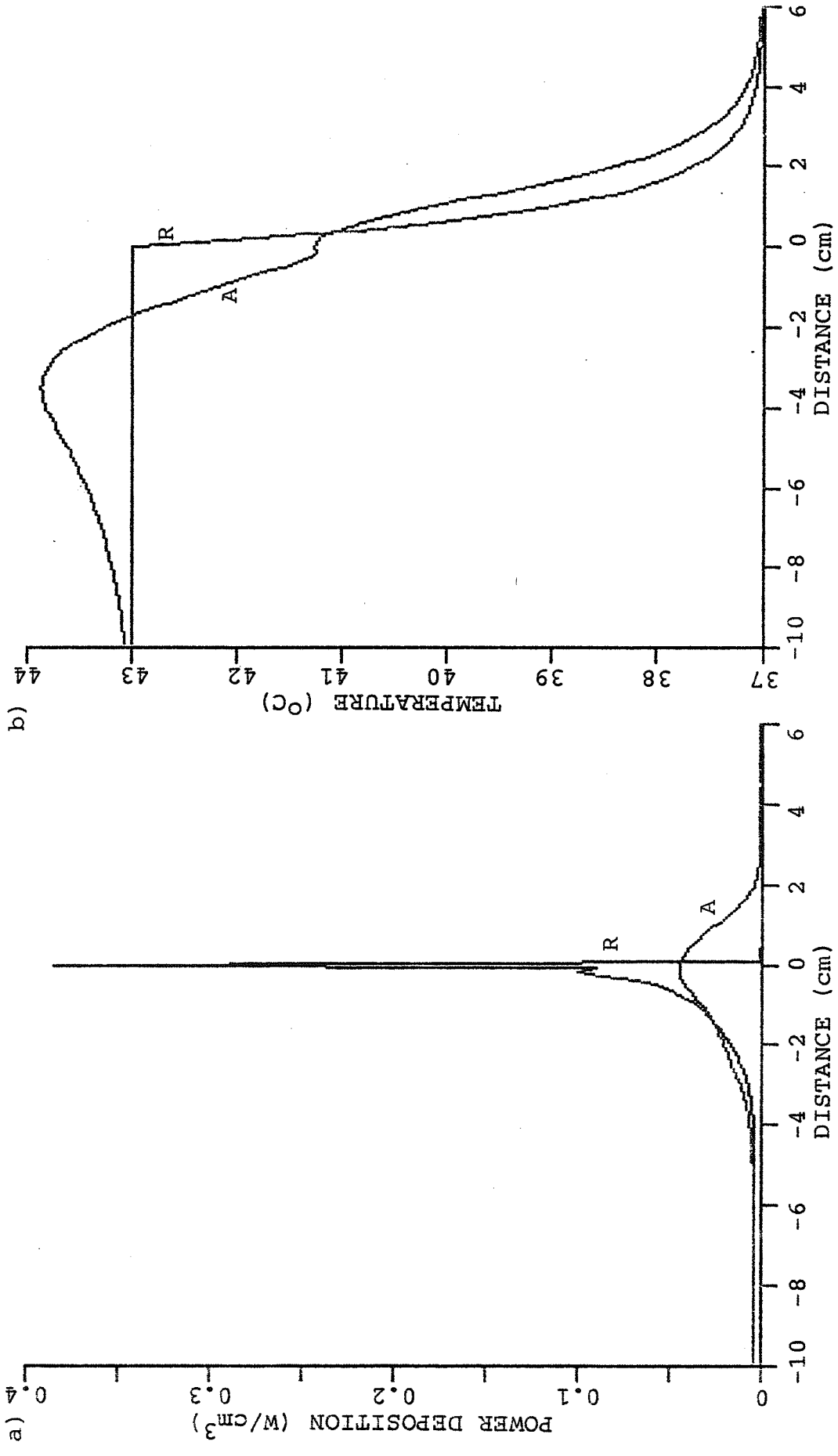

Figure 5.9. Matching of required power deposition with Gaussian function (1.0 cm half power width) spaced every 2.0 cm, starting from a focus placed directly on the tumor boundary. Required (R) and actual (A) power deposition patterns (a), and desired (R) and actual (A) temperature distributions (b) are given.

closely spaced (0.5 cm spaced) foci is shown in Fig. 5.5. Shifting this set of closely spaced foci by 0.2 cm (see Fig. 5.6) changes the resultant temperature distribution only slightly and the desired power deposition pattern is still well matched. Widening the spacing of the foci to 1.0 cm produces some degradation of the match between the desired and the realized temperature distributions, as shown in Fig. 5.7. Increasing the spacing to 2.0 cm, shown in Fig. 5.8, gives a poorer match to the required power deposition pattern and results in rippling in the temperature distribution. Increasing the size of the focus to 1.0 cm half power width, as shown in Fig. 5.9, results in significant temperature overshoot within the tumor and underheating in the highly perfused peripheral regions. These examples demonstrate the importance of precision matching of the required power deposition pattern for developing a uniform temperature distribution. Also, these figures illustrate that the focal position with respect to the tumor boundary is important along with the focal size and spacing.

5.5 Optimum Depth for One Plane of Pattern Matching with Focused Ultrasound

The method of the previous section is limited to two dimensions because, for focused ultrasound, all the energy reaching the plane where the method is being applied must pass through intervening regions of tissue. Thus, the power

deposition levels that would be determined at different depths are not independent, making a determination of three dimensional power deposition significantly more difficult. In this section the potential is investigated for setting the power deposition pattern in only one tumor cross-section, allowing the remaining volume of the tumor to be heated by the power deposited by the sound field determined for that one cross-section.

The depth at which the single power deposition cross-section should be determined is that which requires the most power from the applicator. This approach ensures that the power deposited in every cross-section of the tumor (including the power deposited in surrounding normal tissue in the cross-section) will be greater than the required power deposition for that cross-section. Using the results for the spherical tumor model of Chapter 3, the total power required in a cross section $P_{cs}(D)$ at a depth D relative to the center of the tumor of radius r_o is given by

$$P_{cs}(D) = \pi(r_o^2 - D^2)Q_p^{ss} + 2\pi r_o P_s^{ss} \qquad (5.18)$$

where $r_o > D > -r_o$. Substituting using the relations in Eq. (3.5) and Eq. (3.26) yields

$$P_{cs}(D) = T_o\pi((r_o^2-D^2)W_{bt}C_b + 2r_o\sqrt{W_{bn}C_bK_n} + 2K_n). \qquad (5.19)$$

The relative power that the applicator must deliver, $P_a(D)$, to achieve the power deposition $P_{cs}(D)$ is inversely proportional to the loss accumulated through propagation to the given depth. With an attenuation coefficient α, and

considering the loss relative to that at the tumor center, the resultant applicator power $P_a(D)$ is independent of the tumor depth and is given by

$$P_a(D) = T_o \pi e^{2\alpha D}((r_o^2-D^2)W_{bt}C_b + 2r_o\sqrt{W_{bn}C_bK_n} + 2K_n). \quad (5.20)$$

Figures 5.10 through 5.12 show the required applicator power versus distance of the plane from the center of the tumor for three tumors of different diameters and an attenuation coefficient of 0.05 nep/cm. The peak of Eq. (5.19) occurs past the center of the tumor for all sizes of tumors. This indicates that a cross-section approaching the ideal power deposition pattern should be formed past the center of the tumor for the best results using this simple approach.

The optimum depth for forming the power deposition cross-section is determined by setting the derivative of P_a equal to zero and solving for D:

$$D_{opt} = \sqrt{\frac{1}{\alpha^2 r_o^2} + 1 + \frac{2}{r_o W_{bn} C_b}\left(\sqrt{W_{bn}C_bK_n} + \frac{K_n}{r_o}\right)}. \quad (5.21)$$

The optimum depth D_{opt} is strongly dependent on both frequency and tumor radius as illustrated in Fig. 5.13. When D_{opt} is examined relative to tumor radius, r_o, as shown in Fig. 5.14, the ratio D_{opt}/r_o is found to be only weakly influenced by r_o.

The procedure of matching the required power deposition at a single plane was used with a three dimensional circularly symmetric bioheat transfer model (using Eq. 2.19)

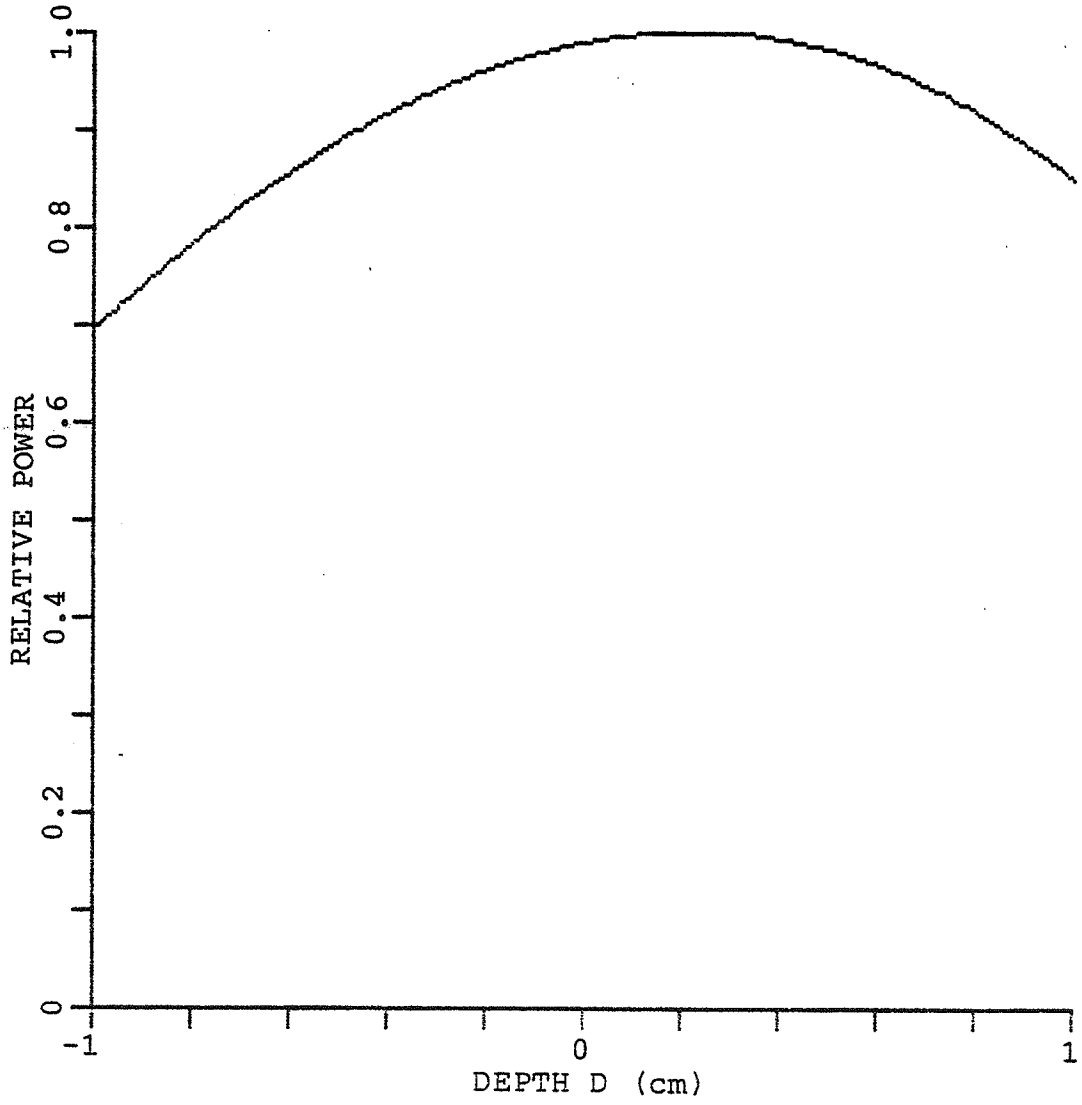

Figure 5.10. Relative applicator power required for producing ideal power deposition cross-section versus depth, shown for a 1 cm radius tumor.

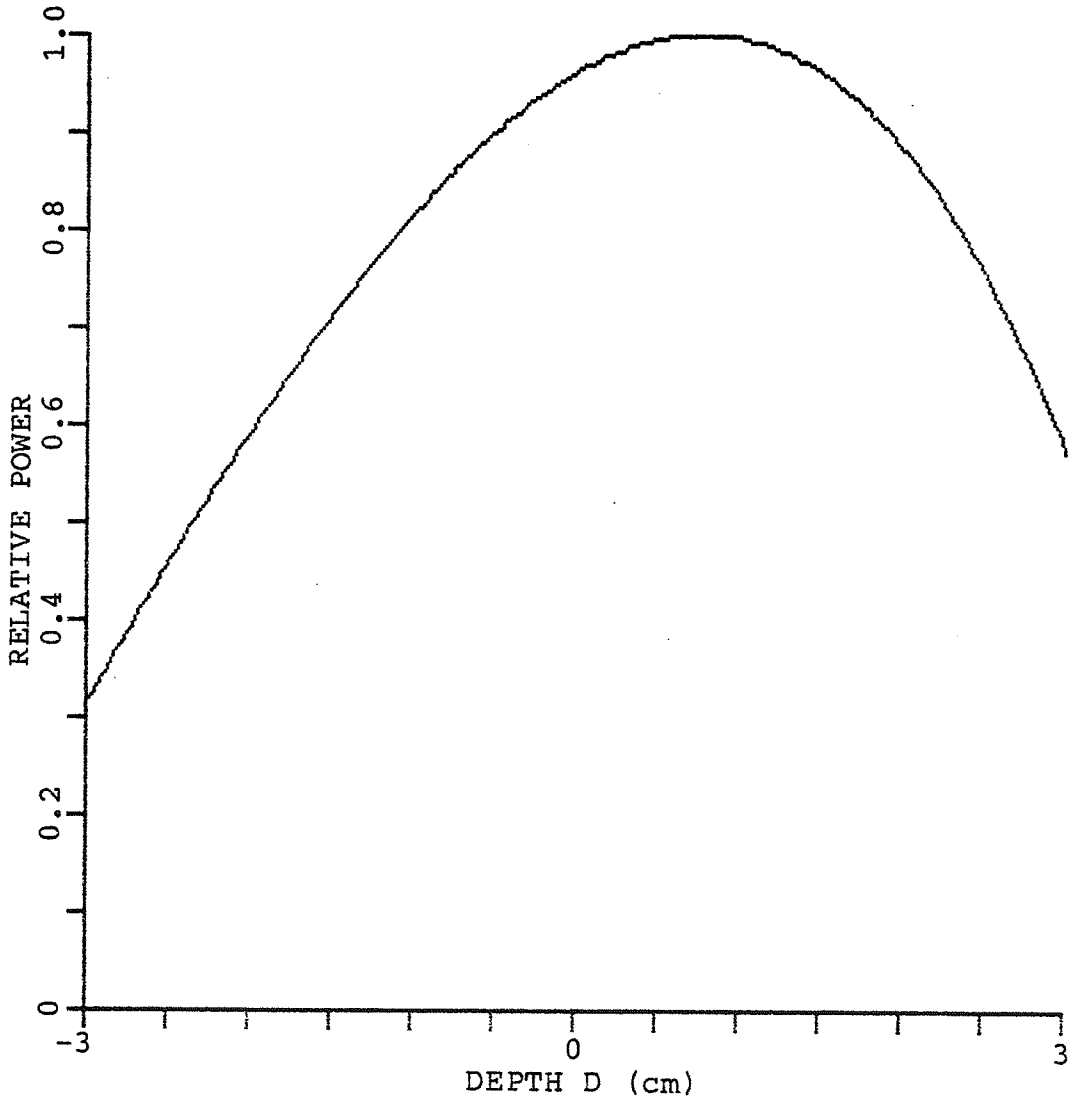

Figure 5.11. Relative applicator power required for producing ideal power deposition cross-section versus depth, shown for a 3 cm radius tumor.

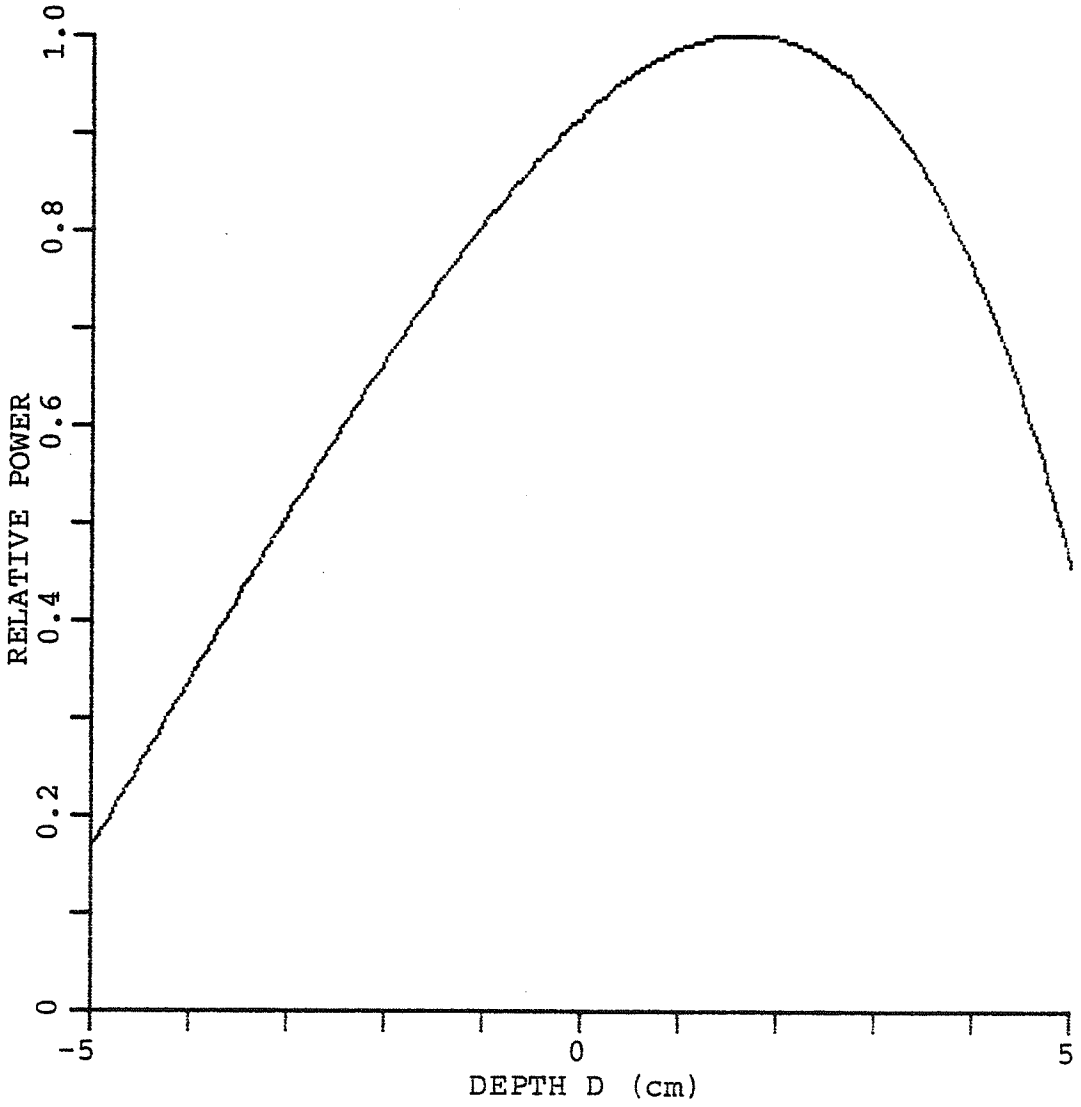

Figure 5.12. Relative applicator power required for producing ideal power deposition cross-section versus depth, shown for a 5 cm radius tumor.

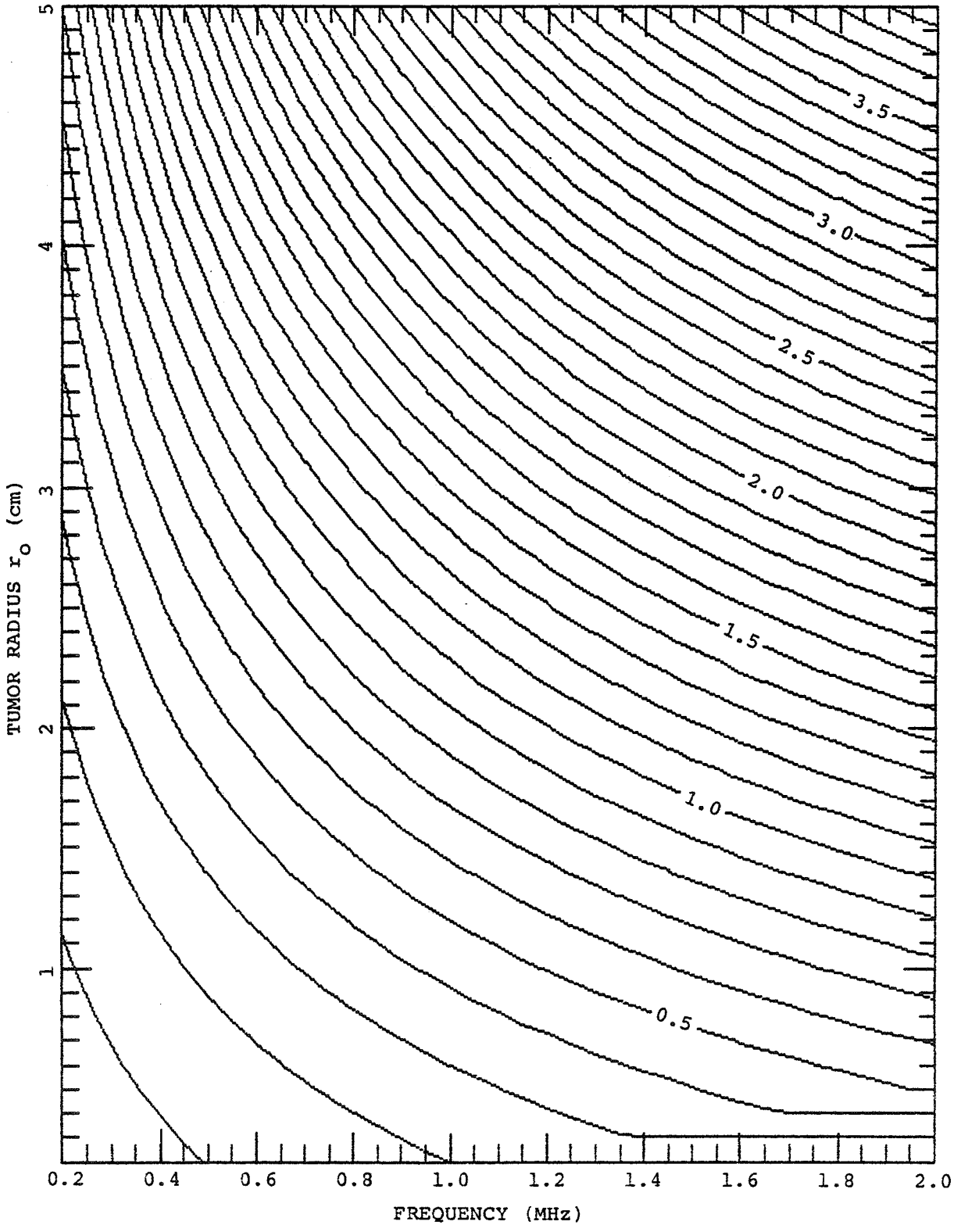

Figure 5.13. Contour plot of optimum depth in centimeters for single plane power deposition pattern matching versus frequency and tumor radius.

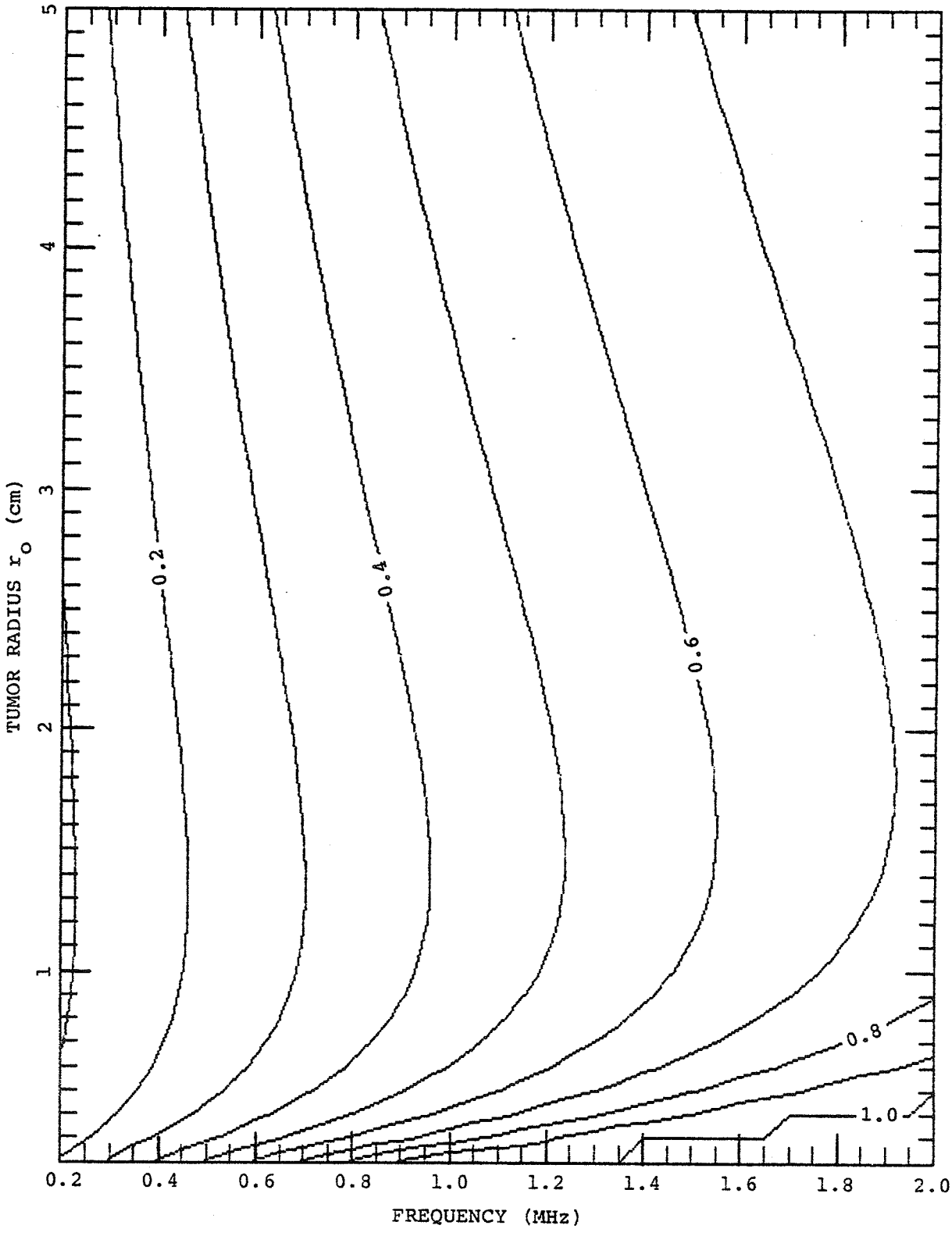

Figure 5.14. Contour plot of optimum depth relative to tumor radius for single plane power deposition pattern matching versus frequency and tumor radius.

and a focus produced by a scanned fixed focus ultrasonic applicator. The 12 cm circular applicator was focused at a depth of 12 cm and operated at 0.5 MHz, with a single focus shape as shown in Fig. 5.15. The tumor had a radius of 3 cm and was centered at a depth of 8 cm. Single plane power deposition pattern matching was applied at a depth 0.9 cm past the tumor center to yield the power deposition pattern shown in Fig. 5.16. The temperature distribution produced in a homogeneous tissue model is shown in Fig. 5.17. The even temperature distribution that results suggests that this method may be adequate for treatment planning.

5.6 Power Deposition Pattern Matching in Three Dimensions with Focused Ultrasound

The other method available for power deposition pattern matching is to match in three dimensions throughout the tumor volume. Such a method appears to be practicable only by using an iterative approach to set the scan path and power weightings.

A straightforward way to approach such a method would be to determine initially a scan path to heat the periphery, then fill in the interior region as required. The entire periphery could not be scanned directly, as there would be too much power deposition in the tumor interior when both the shallow and deep extremes of the tumor are directly heated with the required power deposition.

A more promising approach is to form the peripheral

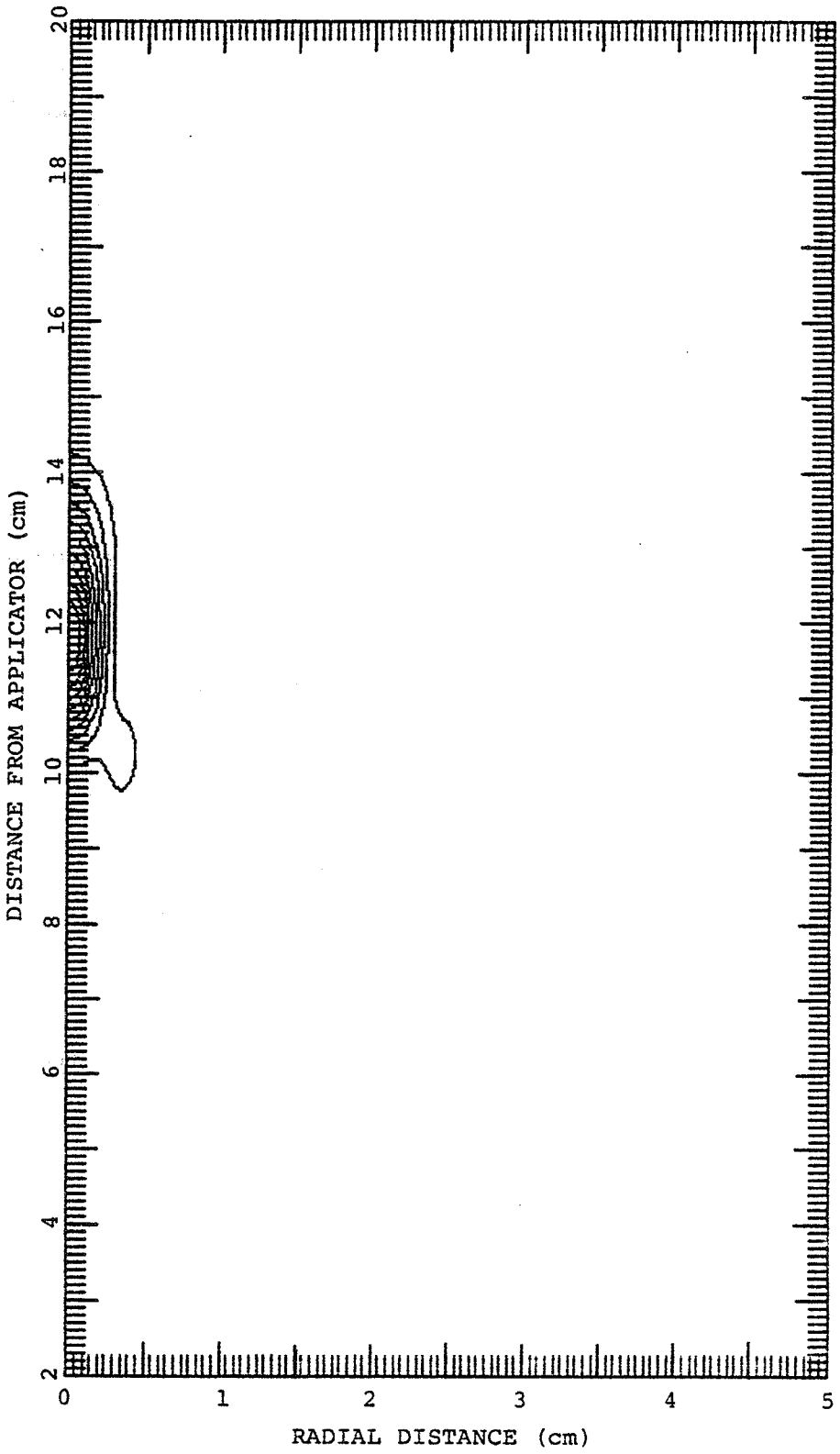

Figure 5.15. Single focus produced by 0.5 MHz 12 cm diameter ultrasound applicator focused to a depth of 12 cm. Intensity is normalized to 1 W/cm^2 and contours are given at increments of 0.1 W/cm^2.

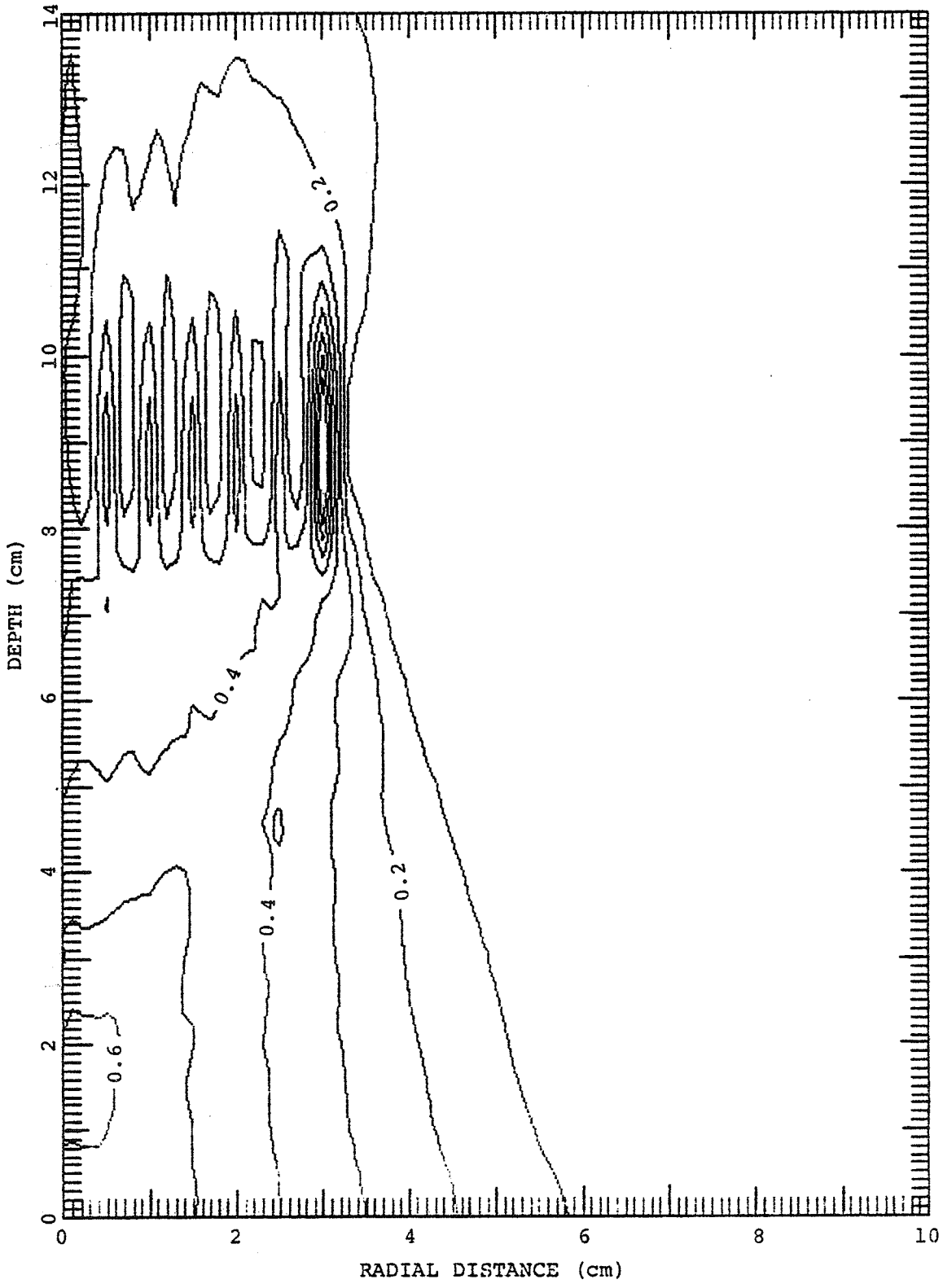

Figure 5.16. Power deposition pattern produced by single plane power deposition pattern matching using scanned fixed focused applicator. Scan paths in the tumor interior are spaced 0.5 cm. Power deposition pattern is normalized to 1 W/cm^3 and contours are given at increments of 0.05 w/cm^3. The tumor center is located at a depth of 8 cm.

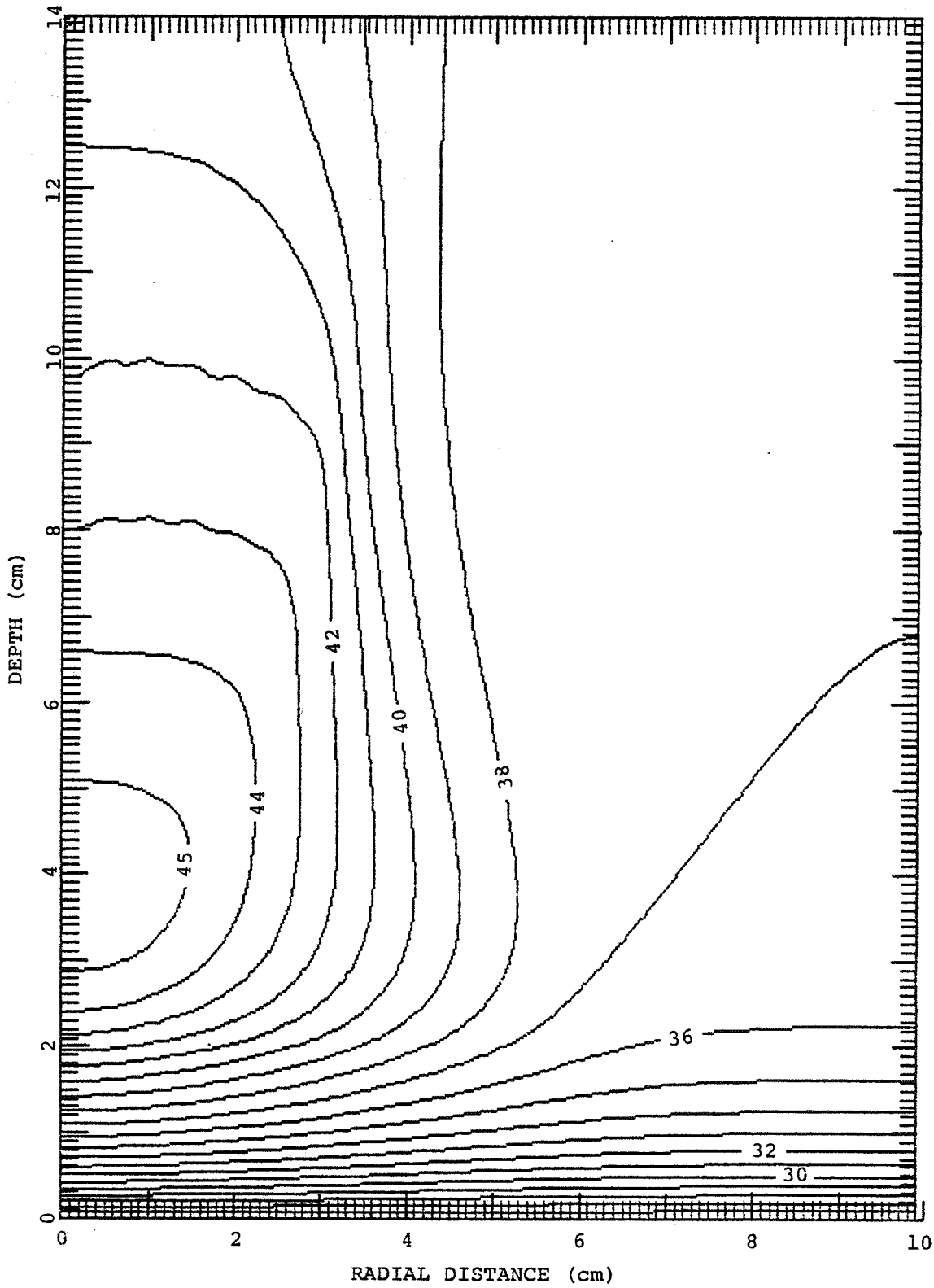

Figure 5.17. Temperature distribution produced by scanned focused applicator using the single cross-section matching method. The tumor center is located at a depth of 8 cm.

power deposition for the single plane as discussed above, add peripheral power deposition to the back of the tumor, then fill the tumor interior to the required level. The virtual independence of the power deposition on the tumor periphery at the depth of the tumor center and the interior power deposition could be used for matching in three dimensions. The three dimensional power deposition pattern matching would be very applicator specific, and is beyond the scope of this investigation.

5.7 Discussion

The eventual use of an automated method for directing hyperthermia treatments can be foreseen, with the improvement of automatic tissue classification and image production. Such an automated method is well suited for providing uniform and consistent hyperthermia treatments. Improvements to the model are still necessary to consider perfusion changes, but the model provides a starting point for directing hyperthermia treatments.

Improved hyperthermia delivery systems are necessary to provide the resolution required for matching required power deposition patterns. The design of a precision hyperthermia applicator utilizing ultrasonic phased arrays is presented in Chapter 6 with two different approaches to forming the required power deposition pattern given in Chapters 7 and 8.

CHAPTER 6

DESIGN CONSIDERATIONS FOR A HYPERTHERMIA PHASED ARRAY

6.1 Introduction

Ultrasound in the frequency range of 0.3 MHz to 3.0 MHz is considered suitable for hyperthermia applications. At the higher frequencies of this range, i.e., 2.0 to 3.0 MHz, the penetration depth is shallow and the power deposition decreases at approximately the same rate as microwave power deposition. Since the penetration depth is limited to a couple of centimeters, minimal bone heating occurs and the potential of high frequency ultrasound is similar to that of microwaves. However, with ultrasound lower frequencies can be used to give increased penetration so that deep hyperthermia is feasible.

The short wavelengths of ultrasound in this frequency range, i.e., 0.5 mm to 5.0 mm, allow for precise focusing while the longer wavelengths of microwave radiation in the appropriate frequency range for hyperthermia, i.e., 3.0 cm to 30.0 cm, provide limited focusing capability and allow much beam spreading. For microwave and ultrasound sources of the same size, the energy from the microwave source starts diverging much closer to the source because of its smaller size relative to the wavelength of the energy being radiated. Likewise, for frequencies of ultrasound and microwave radiation with similar tissue attenuation

coefficients, the depth of penetration of the ultrasound is greater due to lesser beam divergence. Thus, ultrasound allows better beam collimation and has more potential for focusing than microwaves.

Clinical testing of ultrasound hyperthermia led one group of investigators working with unfocused ultrasound transducers to conclude that the major drawback of their simple system was the lack of dynamic control of the field intensity distribution (Corry et al., 1984). They felt that the control of the intensity distribution is important because the vast majority of tumors that undergo clinical cancer treatment are irregularly shaped and involved with normal tissue, making selective hyperthermia difficult. This problem has been addressed in the design of other systems that use multielement applicators (Fessenden et al., 1984), scanned focused applicators (Dickinson, 1984), and multielement scanned focused systems. However, these increases in complexity to provide dynamic control are accompanied by complex mechanical systems and often difficulties with the patient-machine interface.

The advantages of a phased array applicator become evident when the physical limitations of mechanical scanning of a fixed focus system are considered. The mechanical equipment necessary to perform the scanning is cumbersome and must be attached directly to the scanned applicator. Often, it is contained within the water bolus above the patient. Mechanical scanning rates are also limited by the speed of the mechanical scanning apparatus while the

electronic scanning of the focus produced by a phased array is limited only by the speed of the controlling electronics and the bandwidth of the transducer.

The characteristics of a phased array applicator allow it to form a focus providing intensity gain as does a fixed focus applicator. For a two dimensional phased array with elements of size 0.7λ square or less, the directivity (peak intensity relative to total radiated power) for small steering angles is approximately equal to that of a source with a continuously varying phase, i.e., a fixed focus applicator. In addition, the focus dimensions produced by phased arrays and fixed focus sources share the same function of source size and frequency. When these properties are considered together, it is evident that a phased array with sufficiently small elements can form and scan a focus as well as a fixed beam transducer that is mechanically scanned. Thus, if a tumor geometry is present that cannot be treated with a practical phased array design, then a conventional fixed focus applicator could not be used.

An additional advantage of a phased array system is that it can easily be reconfigured to reduce hot spots. Array elements nearest to intervening bone can be shut off to reduce bone heating. The potential for manipulation of a phased array to reduce undesirable heating is not limited by physical constraints associated with the scan path as with a fixed focus applicator.

6.2 Frequency Selection

The choice of operating frequency for an ultrasonic hyperthermia system is a constrained optimization problem that yields different solutions depending upon the optimization criterion. There are considerations in the design of a phased array system for deep heating that favor the use of both lower and higher frequencies such that a compromise design must be found.

6.2.1 Efficiency Optimization

One possible optimization criterion that has been suggested previously is to maximize the heat generation at the target (tumor) depth relative to the source intensity (Christensen and Durney, 1981). For an unfocused source with intensity I_o, radiating into homogeneous muscle tissue, the intensity decays exponentially with distance as

$$I = I_o \, e^{-2 \alpha d} \tag{6.1}$$

where α is the attenuation coefficient in muscle and d is the distance into the tissue. The power deposited per unit volume is

$$Q_p = 2I \, p \alpha \tag{6.2}$$

where p is the fraction of the attenuation due to absorption, taken as 0.8 for this analysis, and $p\alpha$ represents the absorption coefficient (Nyborg, 1981). In terms of the source intensity,

$$Q_p = 2I_o\ p\ \alpha\ e^{-2\alpha d}. \qquad (6.3)$$

Since attenuation is approximately linearly related to frequency, $\alpha = \alpha_{1MHz}\ f$, where α_{1MHz} is the attenuation at 1 MHz and f is the ultrasonic frequency in MHz. Including the frequency dependence in the power deposition calculation yields

$$Q_p = 2I_o\ p\ \alpha_{1MHz}\ f\ e^{-2\alpha_{1MHz}\ f\ d}. \qquad (6.4)$$

Equation (6.4) can be solved for I_o to find the source intensity required to produce a given power deposition Q_p at the tumor depth D using unfocused ultrasound:

$$I_o = Q_p\ e^{2\alpha_{1MHz}\ f\ D}/2p\ \alpha_{1MHz}\ f\ . \qquad (6.5)$$

Figure 6.1 is a contour plot of I_o, versus tumor depth and frequency, required to produce a power deposition of 0.2 W/cm^3, a level determined to be sufficient by one group of investigators (Fessenden et al., 1985). This value is higher than the Q_p determined in Chapter 3 (0.05 W/cm^3) for the interior of a tumor, but Fessenden's result was for the treatment of small volumes, where more power deposition is required because heat conduction to normal tissue dominates. However, the particular choice of power deposition Q_p is not important because of the relative nature of this analysis. The peak of each contour in the depth direction represents the optimum frequency for that depth based on this optimization criterion. For example, the optimum operating frequency at a 10 cm depth is 0.5 MHz, based on the peak of

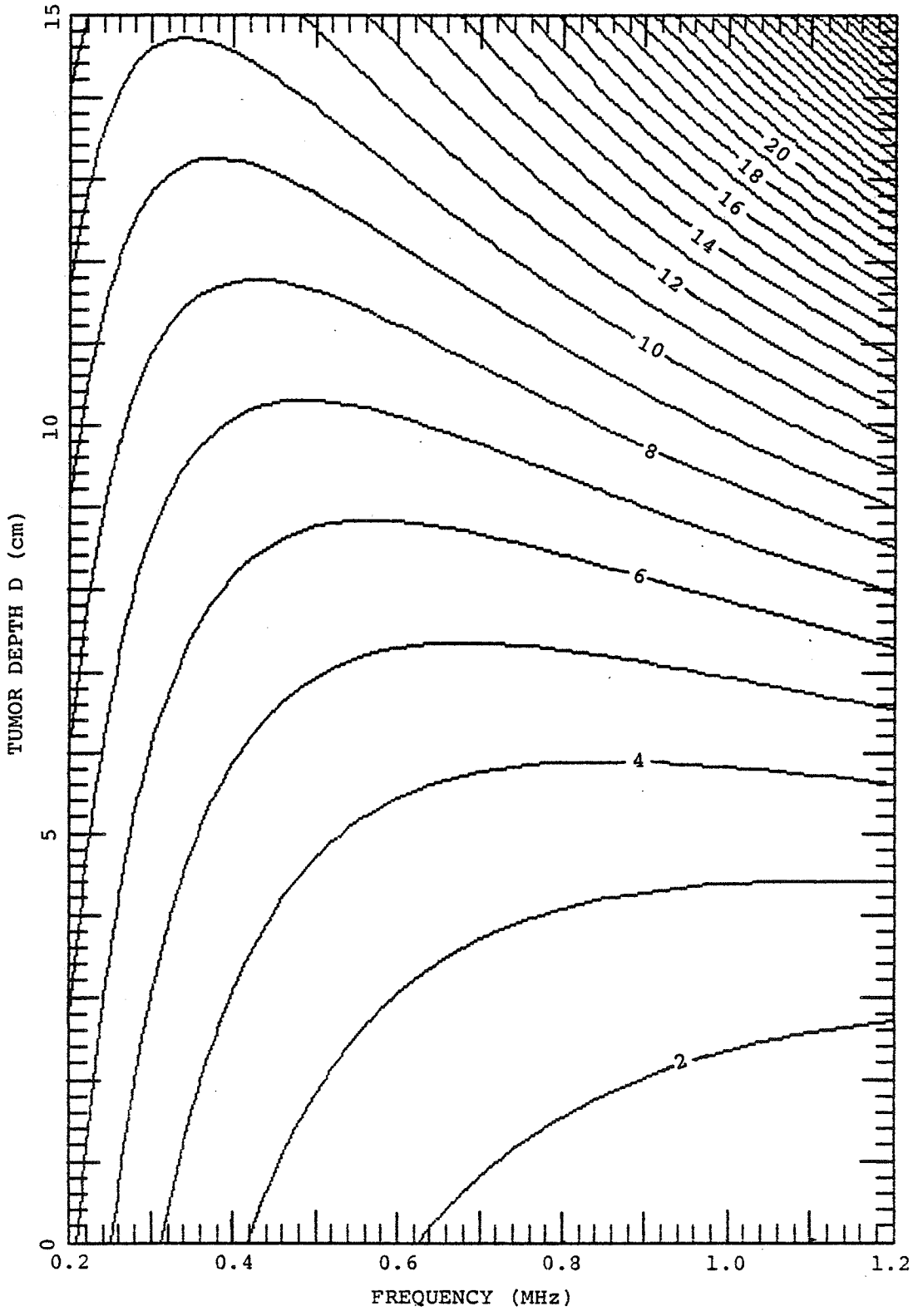

Figure 6.1. Coutour plot of required source intensity $I_o(W/cm^2)$ versus tumor depth and operating frequency for 0.2 W/cm^3 power deposition.

the 7 W/cm^2 contour. The optimum frequency can be determined for each application depth and is expressible as

$$f = 1/(2\alpha_{1MHz}\ D) \tag{6.6}$$

with the associated I_o for the same depth given by

$$I_{omin} = Q_p\ D\ e/p. \tag{6.7}$$

A graph relating optimum frequency and application depth is given in Fig. 6.2.

Such an optimization approach represents a maximization of efficiency, since it ensures that the source intensity is minimized for a desired power deposition at the tumor, which is equivalent to maximizing the power deposition for a given source intensity. One approach to the use of the efficiency criterion is to constrain the frequency choice to be within a specified tolerance of the maximum efficiency for a given depth. This approach is illustrated in Fig. 6.3, where tolerance curves have been added to the curve for the optimum choice of frequency in increments of 5 percent. Thus, for heating at a depth of 10 cm and allowing an efficiency tolerance of 10 %, frequencies in the range of 0.3 MHz to 0.76 MHz are acceptable based on the efficiency criterion. Certainly the efficiency of the system must be considered, but there are other system constraints that suggest the choice of a different frequency than would be selected based on efficiency alone.

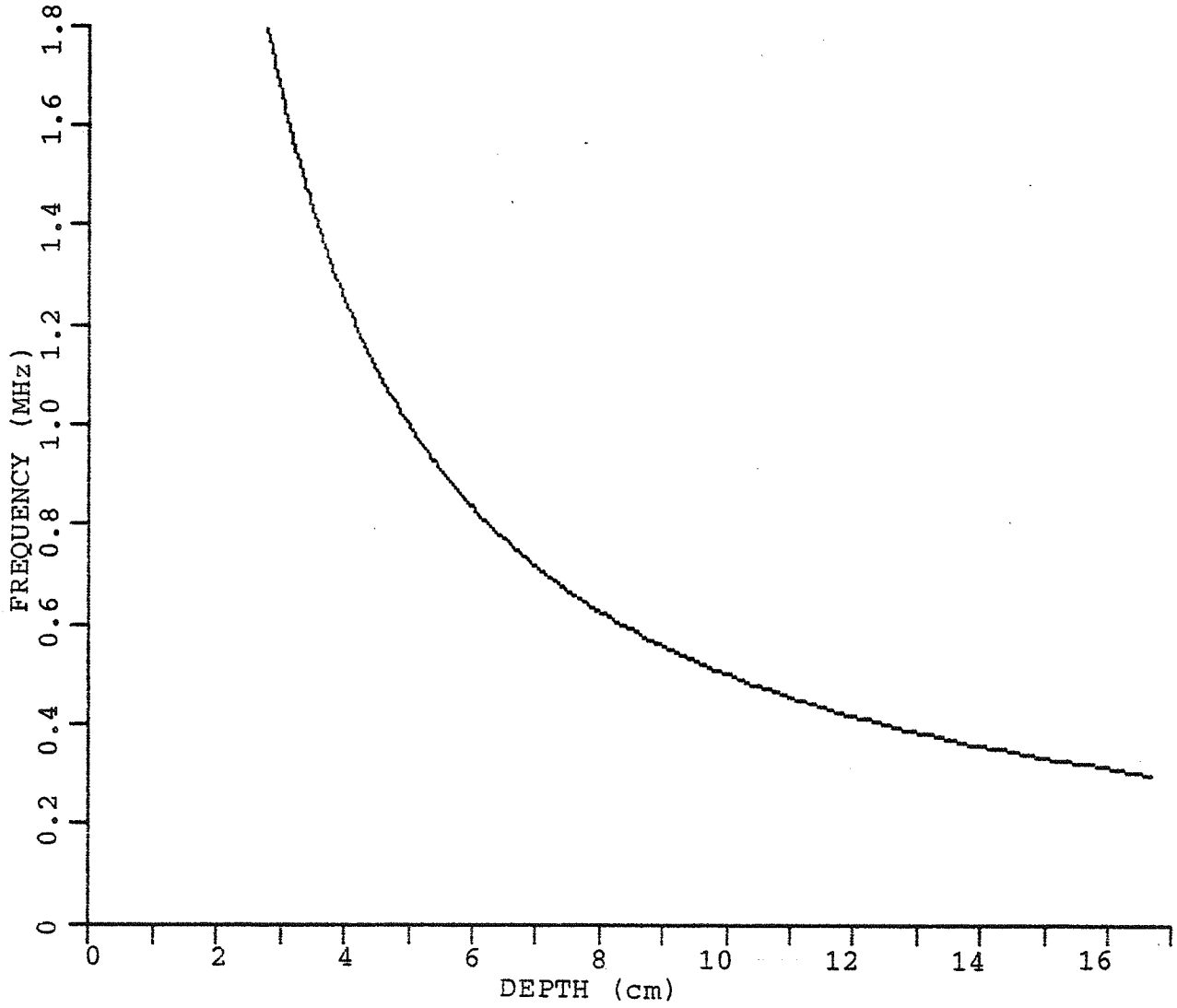

Figure 6.2. Optimum frequency versus application depth.

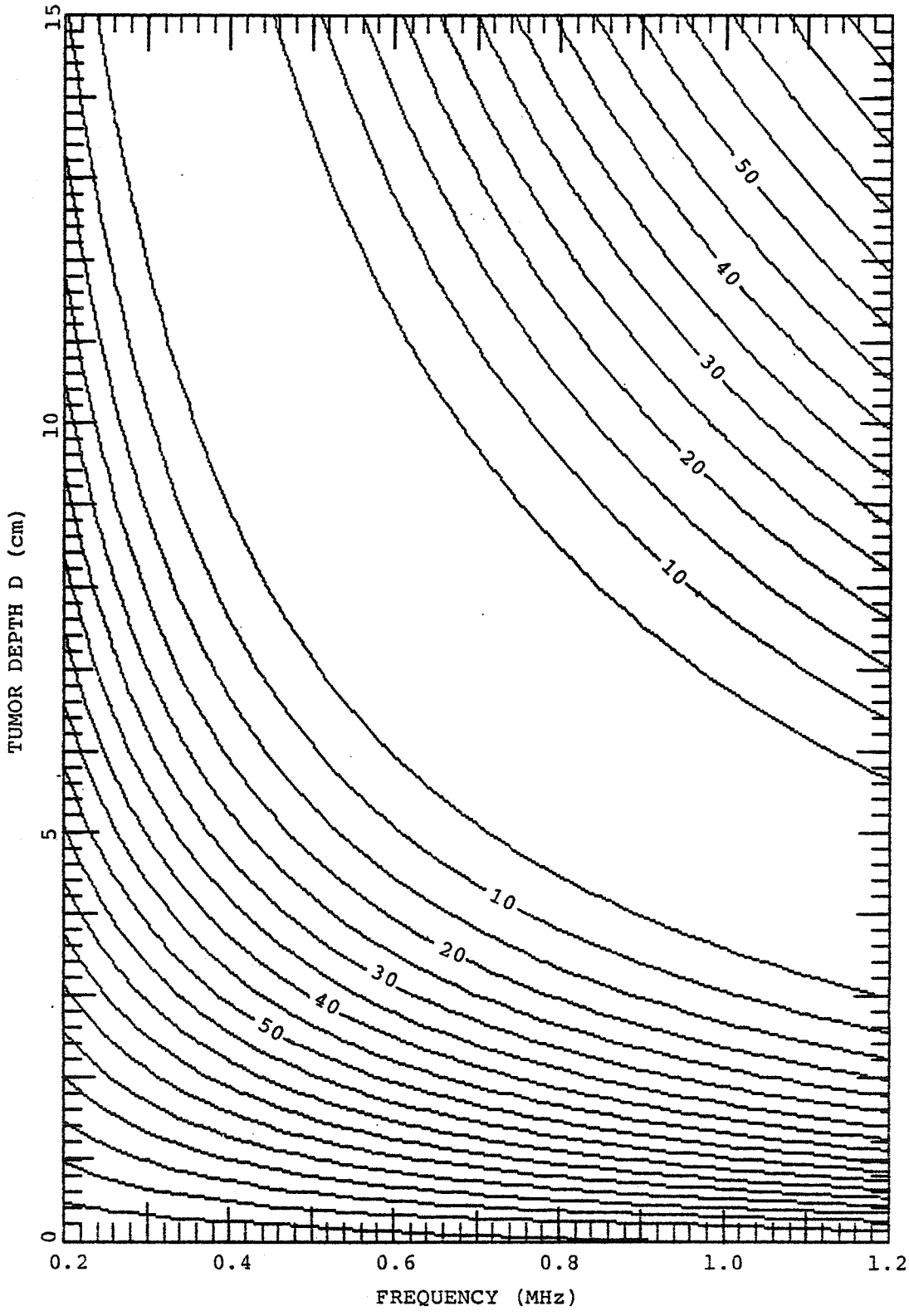

Figure 6.3. Contour plot of percent loss due to nonoptimum frequency selection versus tumor depth and frequency. Losses are relative to optimum frequency for same tumor depth.

6.2.2 Gain Optimization

Choosing a frequency based exclusively on efficiency considerations could lead to an applicator design that has little intensity gain and is incapable of heating deep tumors without overheating intervening normal tissues. Alternatively, providing sufficient gain for deep heating for a design with an efficiency based frequency choice could require an aperture impractically large for any area available on the body. Clearly, gain must also be considered in the selection of an operating frequency.

Applicator gain is considered by maximizing the intensity gain at the desired treatment depth. This approach is equivalent to minimizing the heating at the body surface as well as that of intervening tissue. Maximizing the gain is the same as choosing the maximum value of I_t/I_o, where I_t is the intensity at the tumor, for a given depth D. For an unfocused applicator, this can be represented as

$$I_t/I_o = e^{-2\alpha_{1MHz}\, f\, D}. \qquad (6.8)$$

A focused applicator uses a surface area at the source greater than the cross-sectional area of the tumor so that intensities are higher at the tumor depth, providing a gain greater than 1. For purposes of hyperthermia treatment, the gain for a focused applicator can be approximated as

$$I_t/I_o = (A_s/A_t)\, e^{-2\alpha_{1MHz}\, f\, D} \qquad (6.9)$$

where A_s is the applicator area and A_t is the tumor cross-sectional area. This definition of gain uses the

cross-sectional area of the tumor, as opposed to the area of the focal region, because the energy at the focal depth is deposited throughout the tumor cross-section. For effective deep hyperthermia, the intensity at the tumor should be higher than that at the surface. Equation (6.9) can be rearranged to solve for the ratio of applicator area to tumor cross-sectional area in terms of the intensity gain:

$$A_s/A_t = (I_t/I_o)\, e^{2\alpha_{1MHz}\, f\, D}. \qquad (6.10)$$

A contour plot of required ratios of areas (Eq. (6.10)) versus tumor depth and frequency is shown in Fig. 6.4 for $I_t/I_o = 1$, i.e., only enough gain is provided to compensate for attenuation losses. A simple comparison using Fig. 6.4 reveals that for heating at a depth of 8 cm, using 1 MHz instead of 0.5 MHz, would require an applicator of over twice the area to achieve the same intensity gain. In fact, the maximum intensity gain is always achieved by using the lowest frequency possible.

6.2.3 Bone Heating Considerations

Overheating of bone is a frequent problem with ultrasound that can lead to the termination of hyperthermia treatment before adequate temperature elevation within the tumor is achieved (Corry et al., 1984). The deeper penetration of low frequency ultrasound often leads to overheating of bone especially when unfocused sources are employed without consideration of bone location. As a result, frequencies below 0.5 MHz have been considered

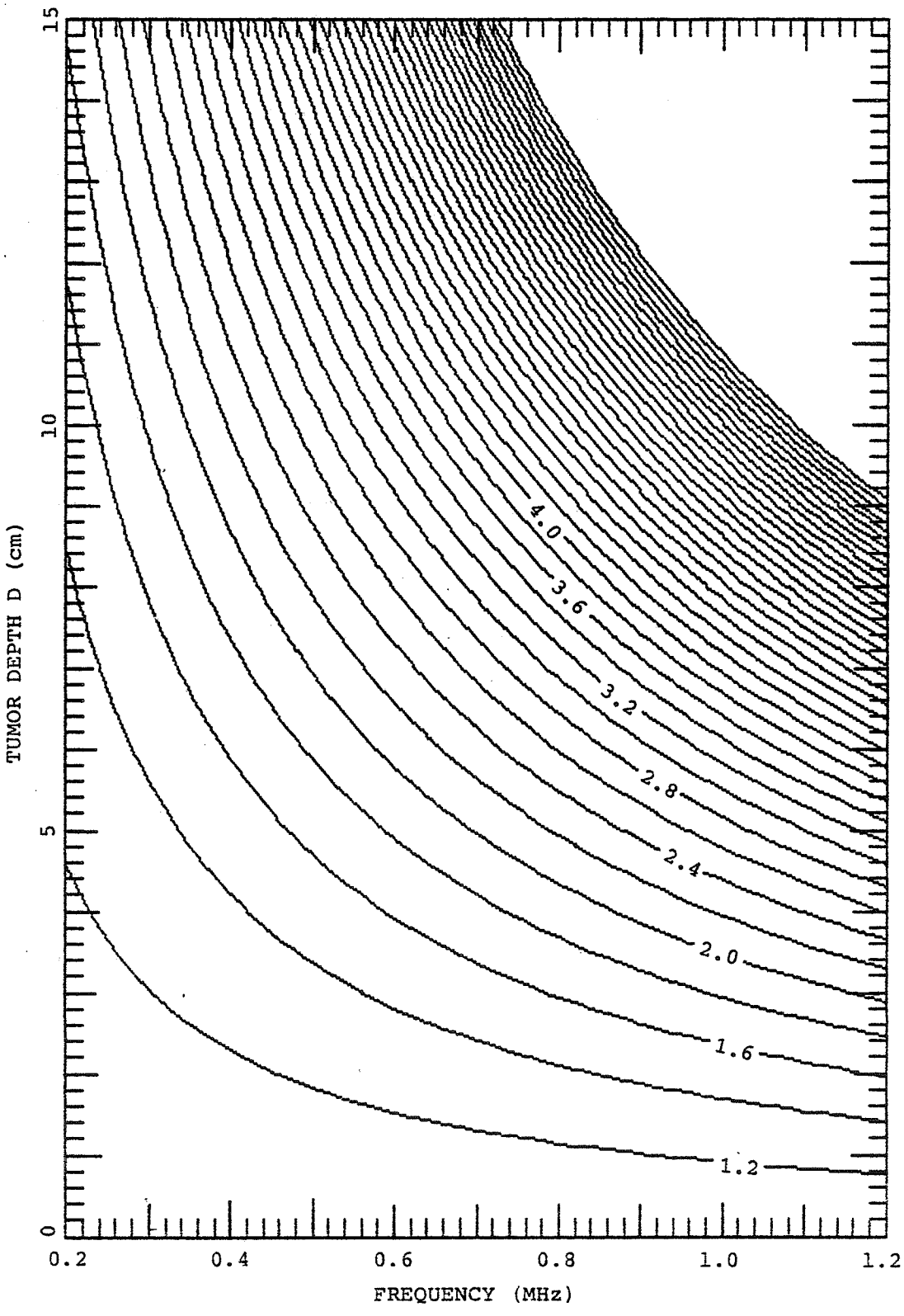

Figure 6.4. Contour plot of gain required to compensate for attenuation losses versus tumor depth and frequency.

unsuitable for hyperthermia treatment with unfocused ultrasound, which relies solely on attenuation for the reduction of intensity from the tumor region to underlying bone.

6.2.3.1 Unfocused Sources

Ultrasound from an unfocused source propagates approximately as a collimated beam, so that in a homogeneous medium the intensity decreases exponentially with distance due to attenuation. For propagation through layers of media of different properties, a simple model of human tissues, both reflection from interfaces of dissimilar tissues and the varying absorption of ultrasound for different tissues distort the simple exponential decay. Significant reflections can occur at a muscle-bone interface, with the power in the reflected wave dependent on the angle of incidence as shown in Fig. 6.5 for a frequency of 1 MHz (Chan, 1971; Chan et al., 1974; Frizzell, 1975). Also, at oblique angles of incidence some of the ultrasound energy transmitted into the bone is converted from longitudinal to shear waves which have a substantially greater absorption coefficient. The energy associated with each of these waves is shown as a function of angle of incidence in Fig. 6.5.

As the reflected power varies significantly with the angle of incidence and the typical muscle-bone interface is curved, the effect of bone cannot be modeled by a single angle of incidence. Assuming a cylindrical shape to the muscle-bone interface, as shown in Fig. 6.6, the average

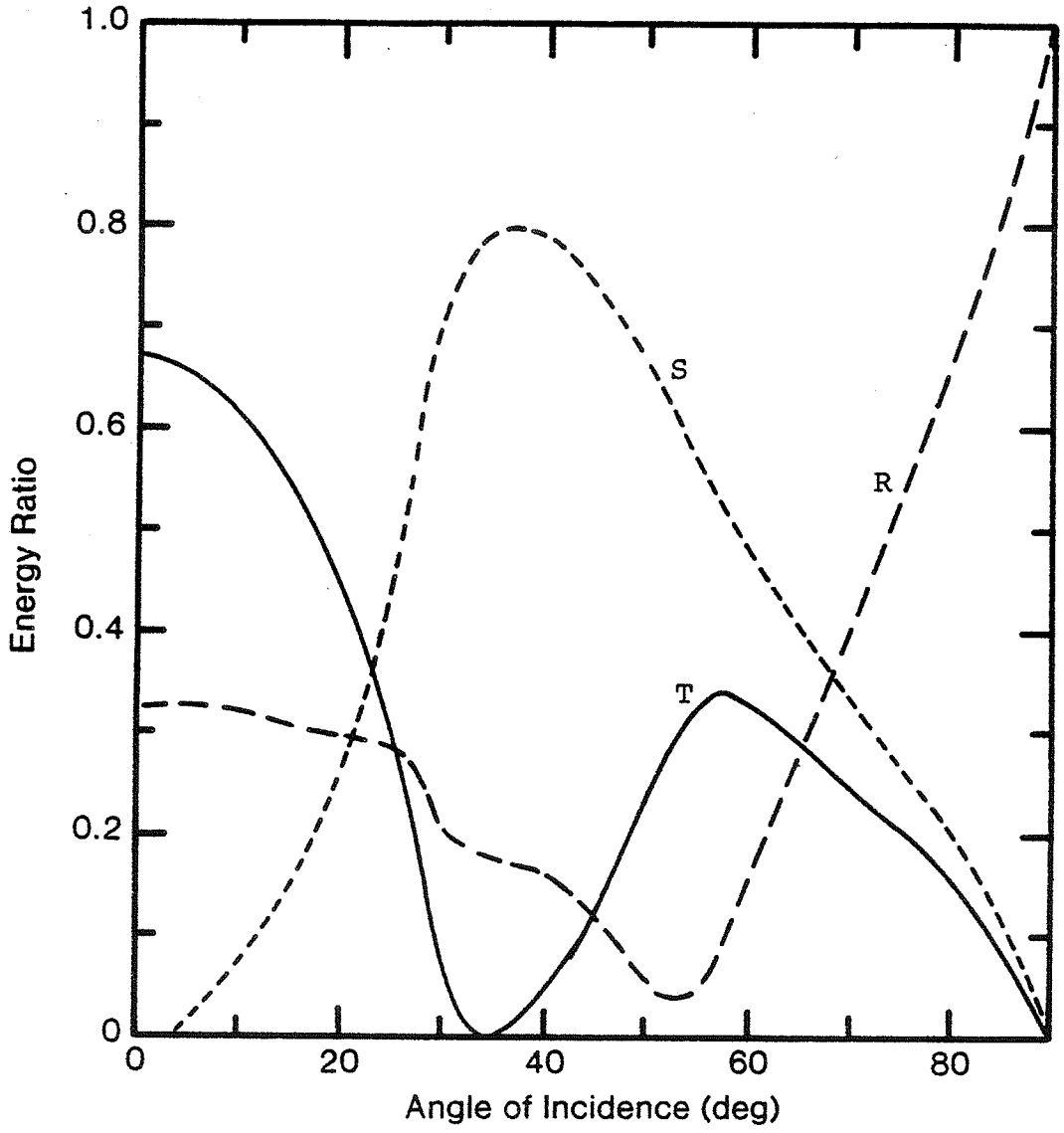

Figure 6.5. Amount of energy in reflected longitudinal wave (R), transmitted longitudinal wave (T), and transmitted shear wave (S) as a function of angle of incidence at a muscle-bone interface (from Frizzell, 1975).

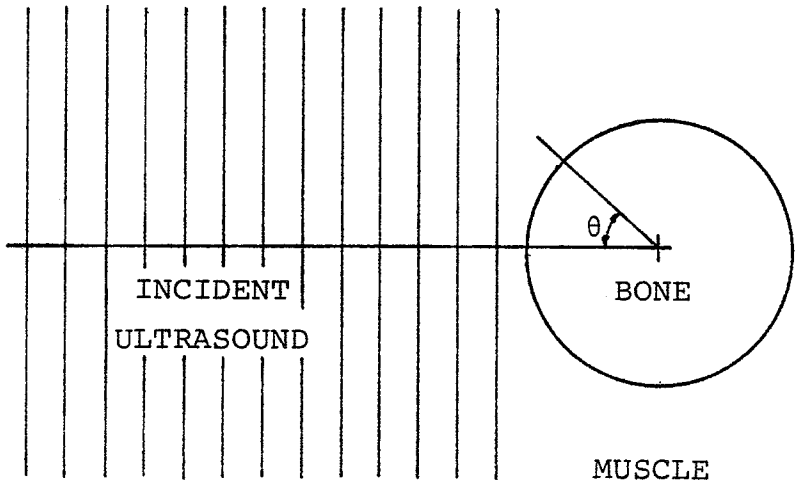

Figure 6.6. Geometry for muscle-bone interface model used for averaging transmission coefficients.

power in each of the components can be calculated by using

$$C_{avg} = \int_0^{\frac{\pi}{2}} C(\theta) \cos(\theta)\, d\theta \qquad (6.11)$$

where C represents the power, relative to the incident power, associated with a particular wave. Equation (6.11) can be used to calculate the average reflected wave power, the average transmitted longitudinal wave power, and the average transmitted shear wave power. The average power in each of these components was calculated to be 26%, 32%, and 42%, respectively.

These results along with the effect of the reflection at a fat-muscle interface were considered in a theoretical examination of ultrasonic heat generation in a fat-muscle-bone tissue model. The resultant power deposition distribution for 1 MHz is shown in Fig. 6.7 and can be compared to the results of Chan for the same frequency and various angles of incidence as shown in Fig. 6.8. The average values used in the calculation of Fig. 6.7 are approximately the same as those used by Chan for a 30 degree angle of incidence. Figure 6.9 shows the results of this model when the coefficients for 0^{o} angle of incidence are used, allowing a direct comparison with Chan's results in Fig. 6.8. The differences in these results can be attributed to small differences in the values chosen for the tissue properties (tissue properties used in this investigation are shown in Fig. 6.10).

The theoretical power deposition pattern calculated using the average transmission and reflection coefficients

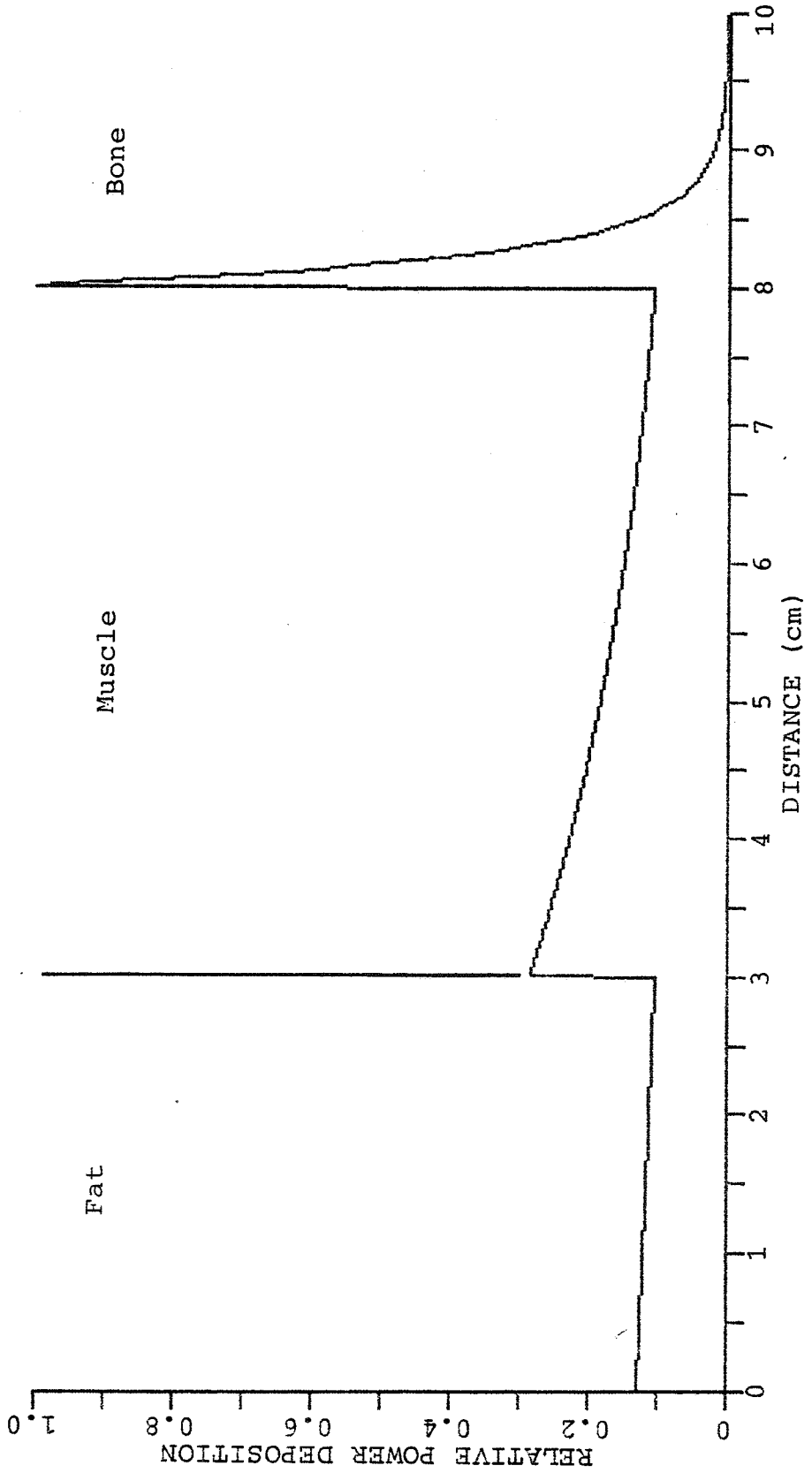

Figure 6.7. Power deposition pattern for fat-muscle-bone model subject to 1 MHz ultrasound using averaged transmission coefficients.

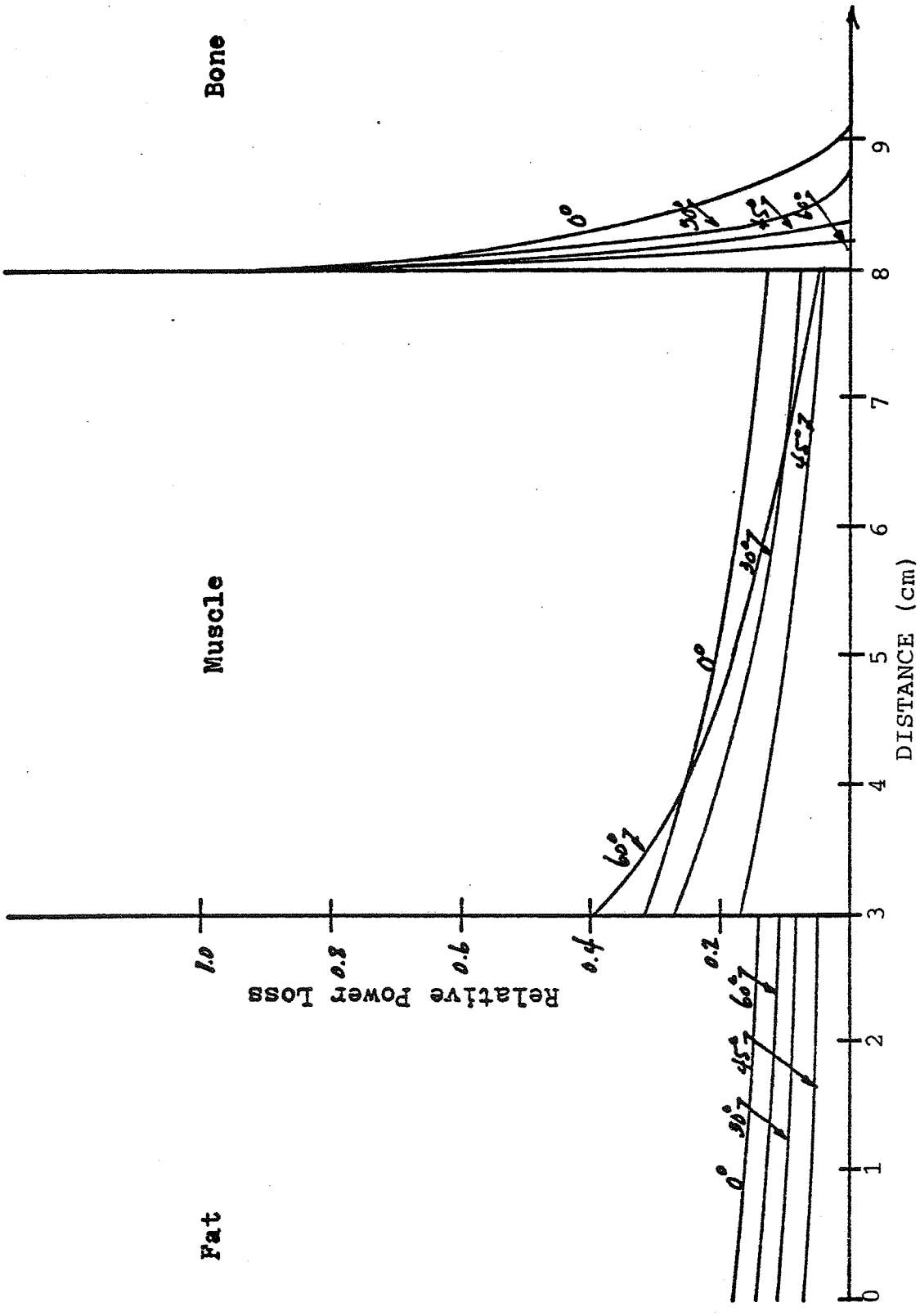

Figure 6.8. Power deposition pattern for fat-muscle-bone model subject to 1 MHz at indicated angles of incidence (from Chan, 1971).

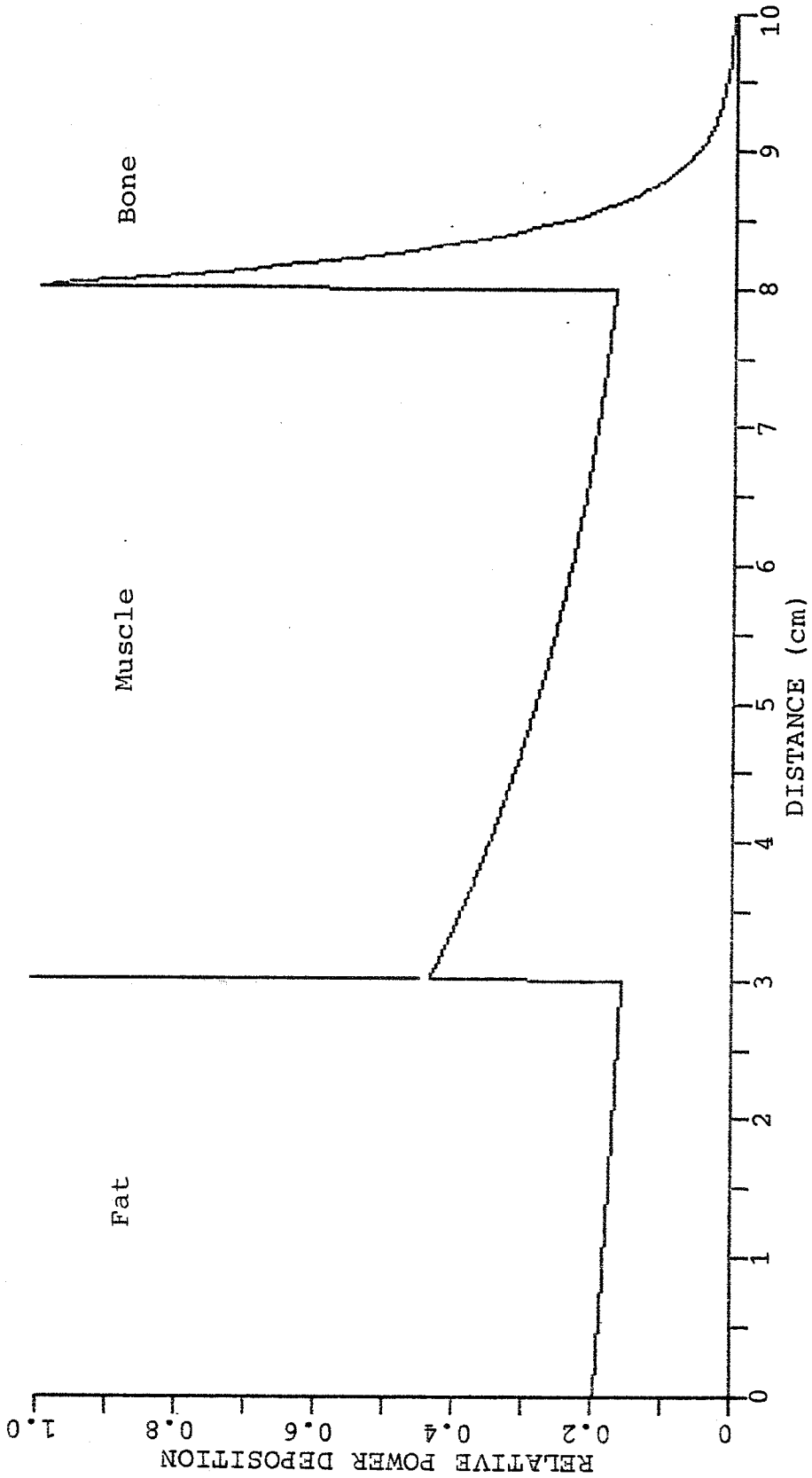

Figure 6.9. Power deposition pattern for fat-muscle-bone model subject to 1 MHz at 0^{o} incidence.

a)

PARAMETER	FAT	MUSCLE	TUMOR	MUSCLE	BONE	BONE MARROW	BONE
α (nep/cm)	0.04	0.12	0.12	0.12	1.50	1.50	1.50
K (W/m/^{o}C)	0.21	0.55	0.55	0.55	0.44	0.44	0.44

b)

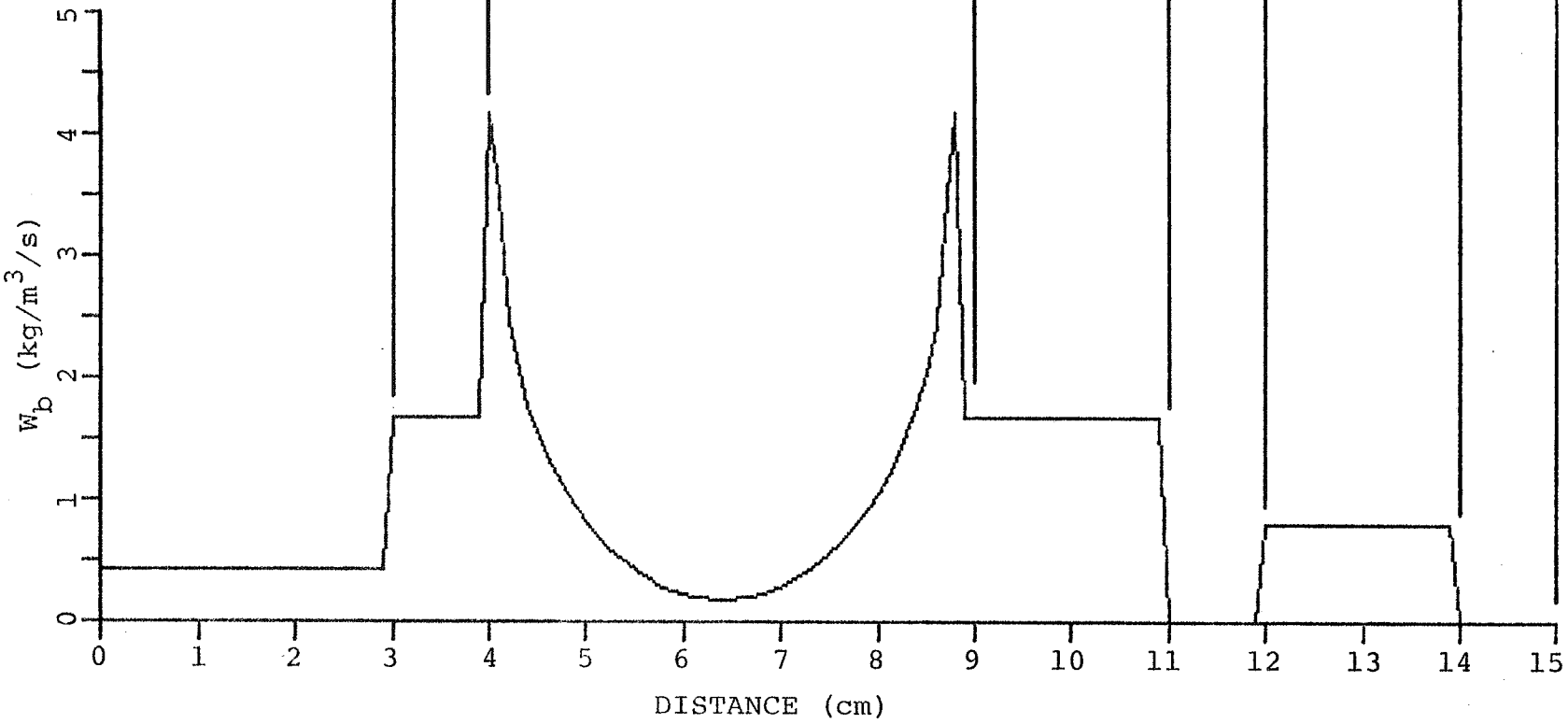

Figure 6.10. Tissue composition (a) and blood flow distribution (b) used for bone heating model.

was used to compute the temperatures. All calculations employed the finite difference solution to the bioheat transfer equation. The blood flow distribution and tissue properties for this model were as shown in Fig. 6.10, where the tumor core is taken to have a reduced blood flow associated with necrotic tissue. The skin surface was fixed at 25°C maintained by a circulating coupling fliud. Such a simple model was chosen so that results would be as general as possible and so that focusing effects could be incorporated simply into the model. The program used to make these calculations is included in Appendix F.

Temperature distributions for the range of frequencies from 0.4 MHz to 2.0 MHz were calculated using this model and are presented in Figs. 6.11 through 6.16. The temperature distributions have been normalized by adjusting the applicator power so that the temperature of the tumor center (x = 6.5 cm) is elevated to 43°C. The results demonstrate that significant bone heating occurs at lower frequencies and that significant superficial heating occurs at higher frequencies. For this particular model, temperature elevations at the bone surface exceed those at the tumor center for frequencies below 0.6 MHz. Clearly, when the increased temperature sensitivity of the bone surface is considered, the bone heating due to an unfocused, lower frequency ($f < 0.6$ MHz) applicator is unacceptable.

The use of frequencies above 1 MHz reduces bone heating, but penetration is so limited that deep hyperthermia is difficult and heating of intervening tissue

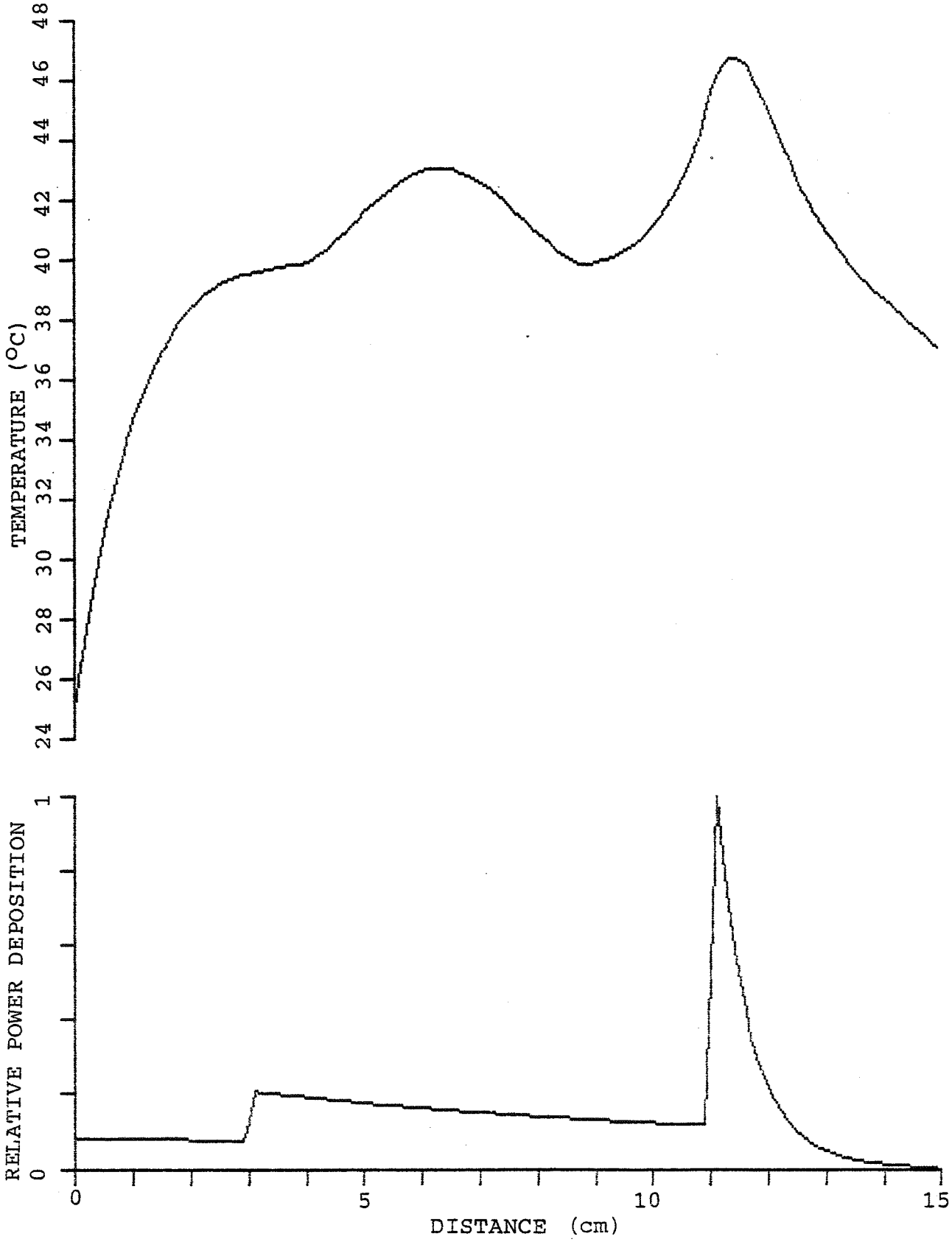

Figure 6.11. Temperature distribution produced in bone heating model with unfocused 0.4 MHz ultrasound.

Figure 6.12. Temperature distribution produced in bone heating model with unfocused 0.6 MHz ultrasound.

Figure 6.13. Temperature distribution produced in bone heating model with unfocused 0.8 MHz ultrasound.

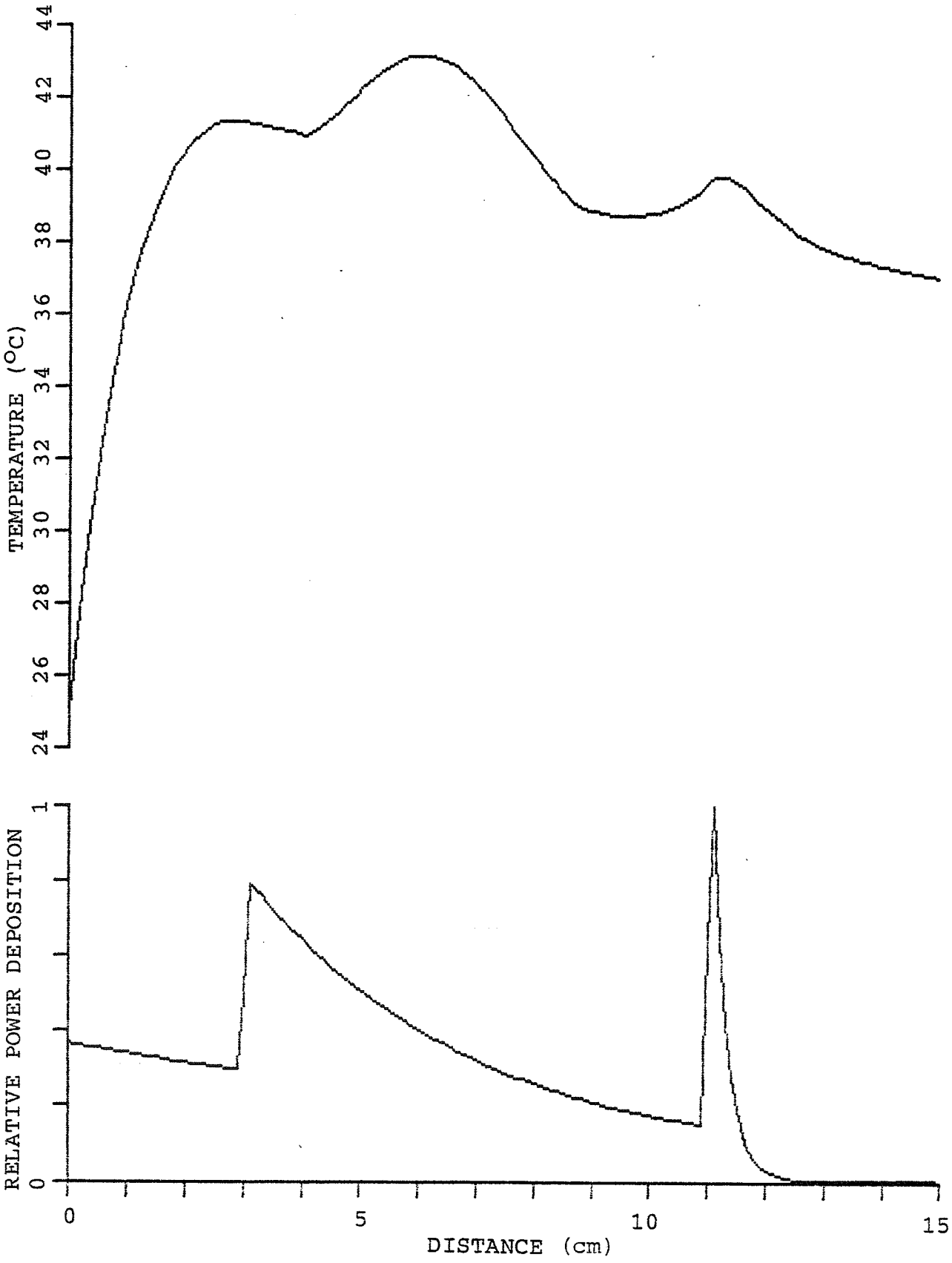

Figure 6.14. Temperature distribution produced in bone heating model with unfocused 1.0 MHz ultrasound.

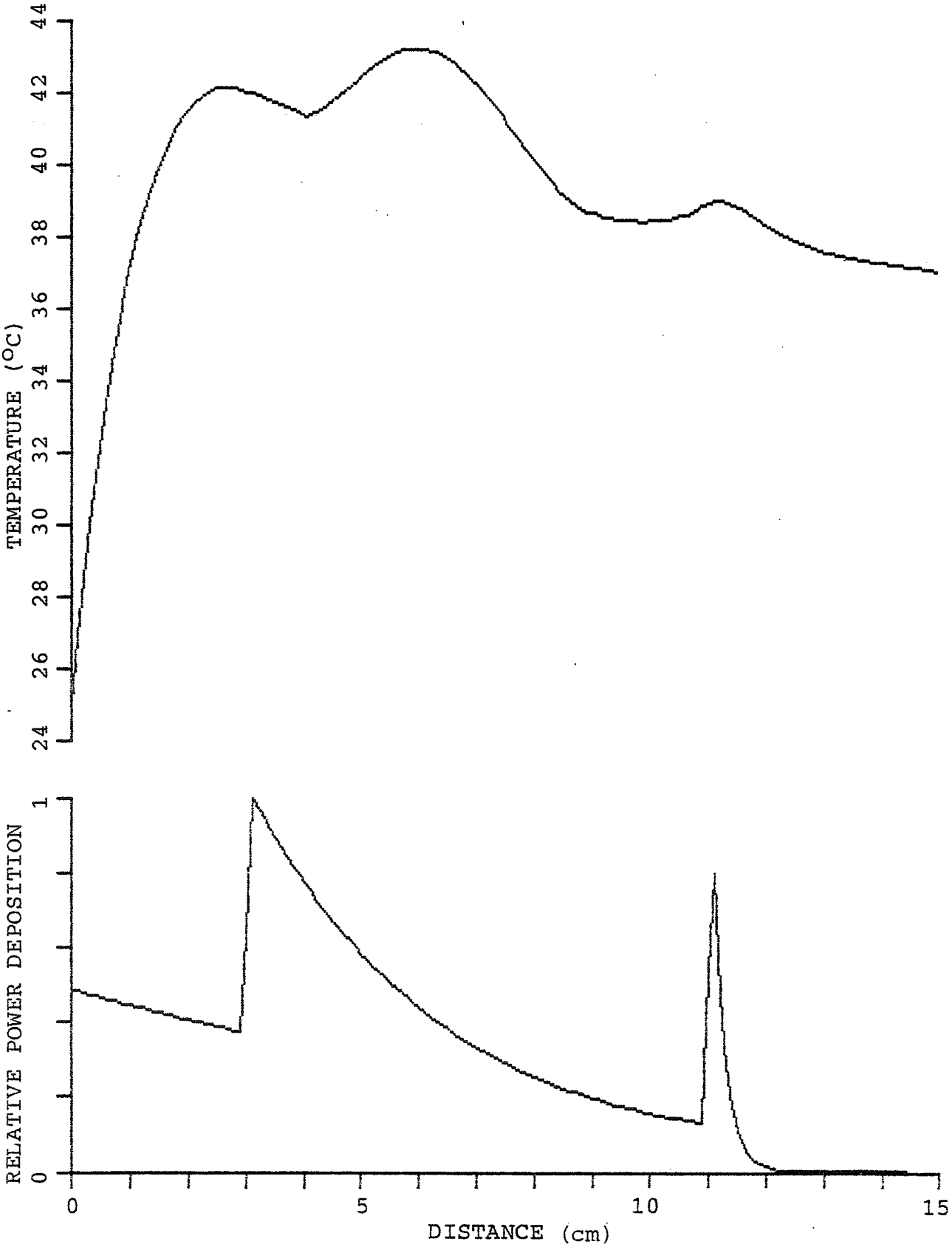

Figure 6.15. Temperature distribution produced in bone heating model with unfocused 1.2 MHz ultrasound.

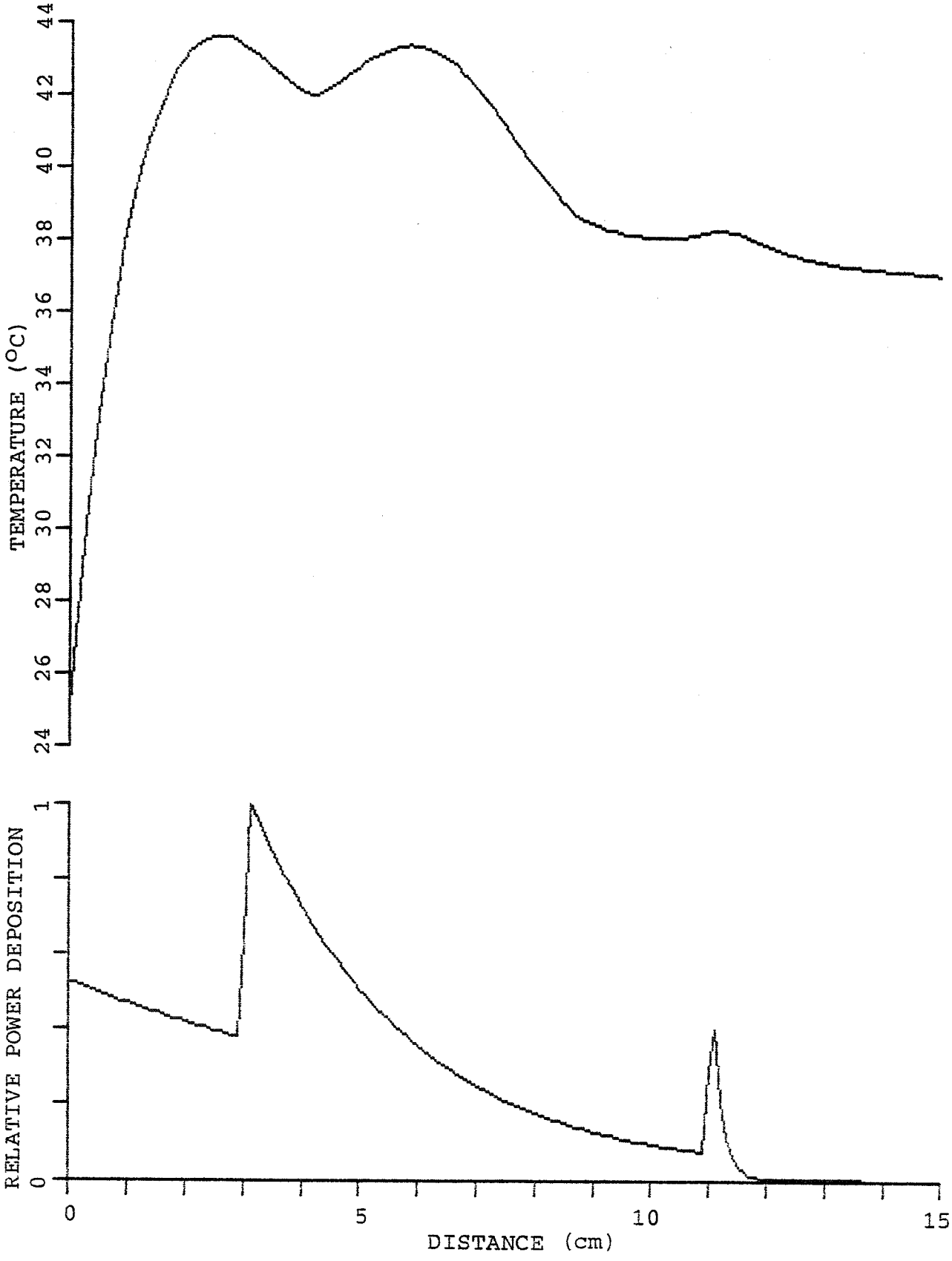

Figure 6.16. Temperature distribution produced in bone heating model with unfocused 1.5 MHz ultrasound.

becomes a problem. Even with the surface cooling, excessive temperature elevations are observed in the fat layer for frequencies greater than 1 MHz. The higher temperatures within the fat layer occur due to the low blood perfusion and thermal conductivity of fat. The tradeoff between penetration and bone heating in the choice of frequency is evident for unfocused ultrasound.

These results show good agreement with the experimental measurements of scanned focused bone heating made by Hynynen (Hynynen, 1986b). The measurements used a focused source, but are applicable to the unfocused case because of the gain reduction due to scanning. With 1 MHz scanned sonication, Hynynen found that the temperature elevation at the bone surface was several fold higher than at the focal region in the muscle in front of the bone. Even using four focused beams overlapped at the focus depth, the maximum temperature elevation occurred at the bone surface for focus-bone surface separation distances of less than 4 cm. Application of 3.58 MHz ultrasound removed the selective bone heating, and the maximum temperature elevation moved to the skin surface. These results are in qualitative agreement with those of this study. Better agreement with these experimental results could be obtained by modelling the actual geometry and the effects of focusing.

6.2.3.2 Focused Sources

Selective heating of the tumor tissue can be enhanced by using focused ultrasound sources which increase heat

generation at the tumor relative to the surrounding normal tissue and the body surface. Simple models of the intensity gain for one dimensional and two dimensional phased array focusing have been used to examine the lessening of bone heating when focused systems are employed.

6.2.3.2.1 Linear Array Focusing

Linear array focusing has been proposed as a means of configuring phased arrays for hyperthermia treatment (Ocheltree et al., 1984; Frizzell et al., 1985). The intensity gain can be modeled by considering the applicator area A_s, the tumor cross-sectional area A_t, and an intermediate beam cross-sectional area A(d) at a depth d as illustrated in Fig. 6.17. The intermediate cross-sectional area can be modeled as a linear interpolation between the applicator area and the tumor cross-sectional area

$$A(d) = A_t + |1 - d/D|(A_s - A_t) \qquad (6.12)$$

where D is the depth of the center of the tumor from the skin surface. The absolute value of 1 - d/D is employed in Eq. (6.12) to extend the applicability of the result to depths greater than D by representing the divergence of the heating pattern past the tumor as well as the convergence before the tumor. From this relation, the average power deposition Q_{1D} at a depth d for one dimensional focusing can be expressed as

$$Q_{1D} = Q(d)A_t / A(d) \qquad (6.13)$$

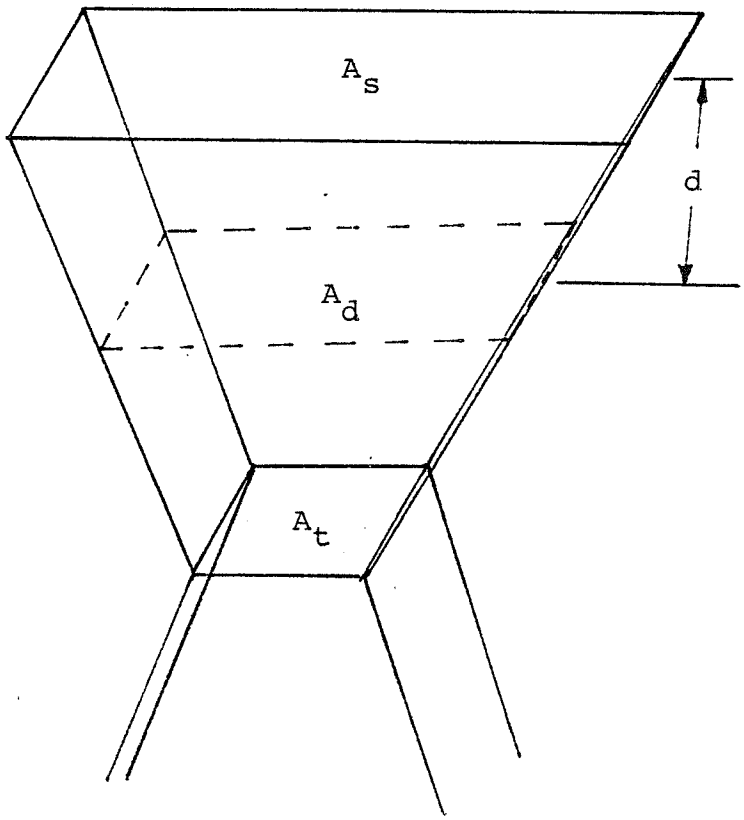

Figure 6.17. Geometry used for linear array focusing model.

where Q(d) is the power deposited at a depth d as calculated previously for an unfocused source.

This power deposition for one dimensional focusing was computed and used with the bioheat equation model described in Section 6.2.3.1 to calculate the temperature distributions resulting from treatment with a range of frequencies, with a value of $A_s/A_t = 4$, as shown in Figs. 6.18 through 6.21. Comparison of these results with the corresponding unfocused results reveals significantly less bone heating for the focused applicators.

Examining the elevation of the bone surface temperature relative to the tumor center temperature (fixed at 43°C), an equivalence is noted between a 1 MHz unfocused source (Fig. 6.14) and a 0.6 MHz focused source (Fig. 6.19) with $A_s/A_t = 4$. Both applicators heat the bone to approximately 40°C. This comparison indicates that increasing the gain, i.e., increasing A_s/A_t, has the same beneficial effect on bone heating as increasing the frequency. The effects of frequency and gain can be investigated using the simplified model of bone heating that follows.

A simplified comparison of the effects of increasing frequency and increasing gain can be made by assuming that all the power transmitted into the bone is absorbed within a short distance from the bone surface. Thus, the heat generation in the bone relative to the heat generation in the tumor can be expressed as the ratio of the intensity transmitted into the bone divided by the power deposition at the tumor center:

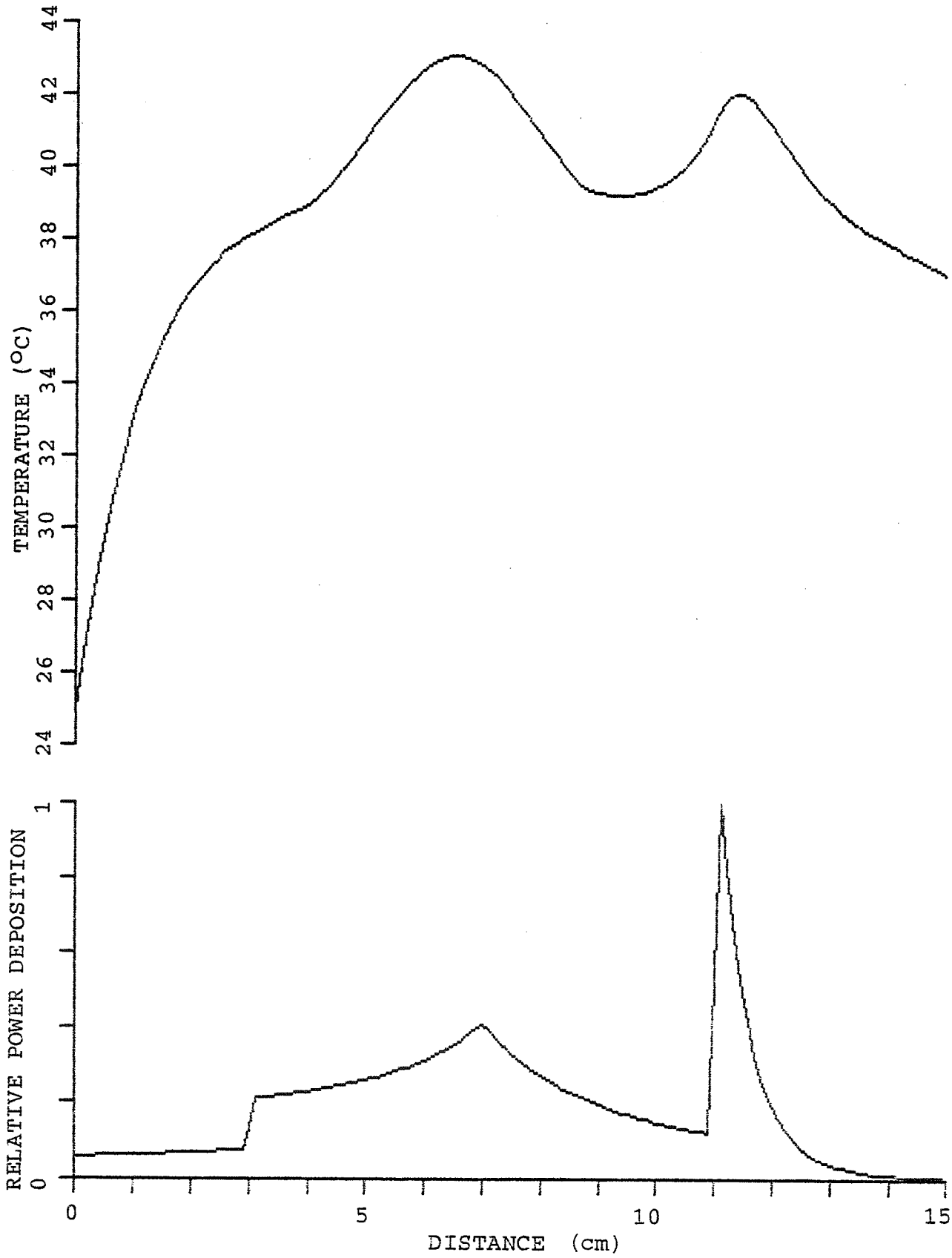

Figure 6.18. Temperature distribution produced in bone heating model with focused 0.4 MHz ultrasound. Linear gain of 4.

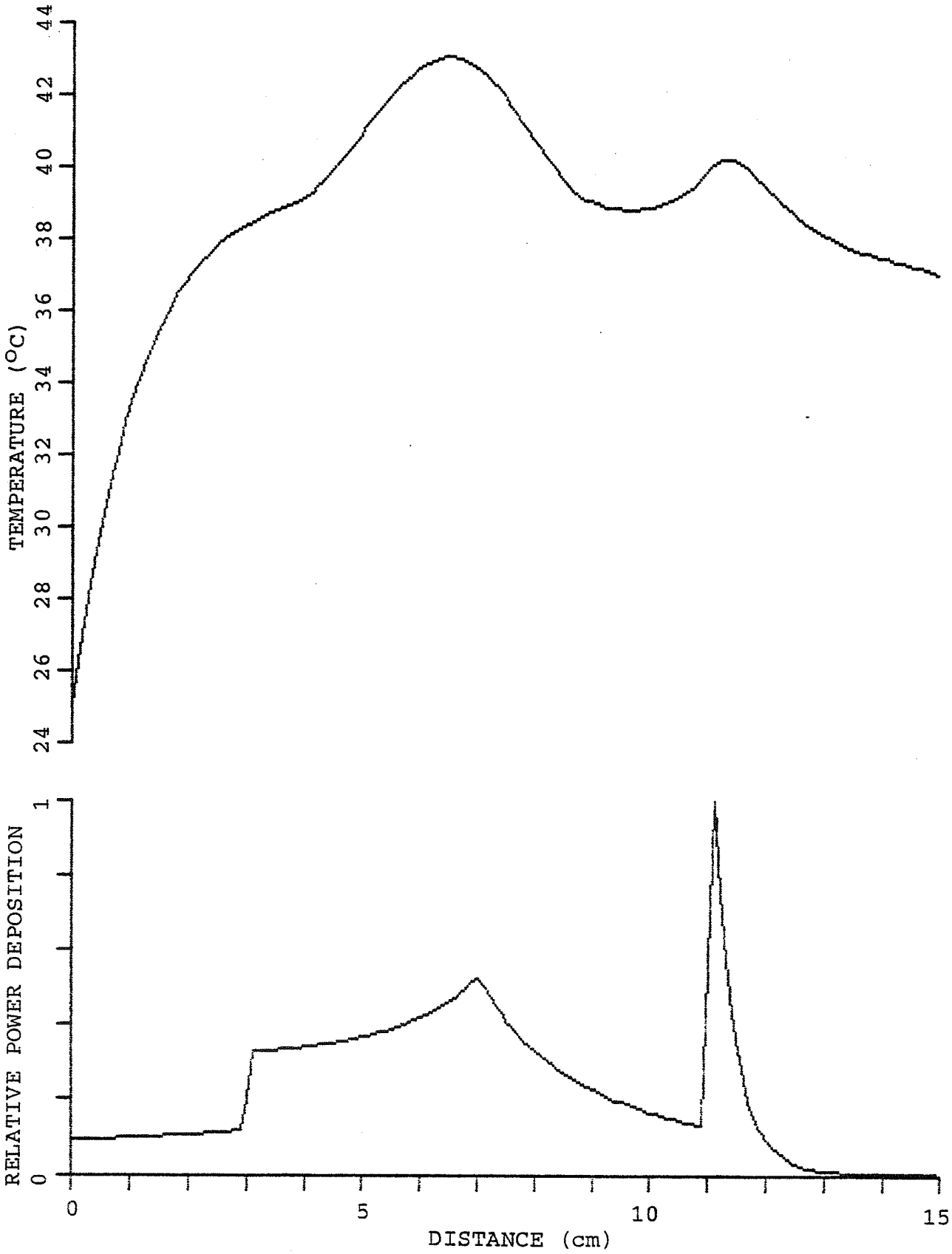

Figure 6.19. Temperature distribution produced in bone heating model with focused 0.6 MHz ultrasound. Linear gain of 4.

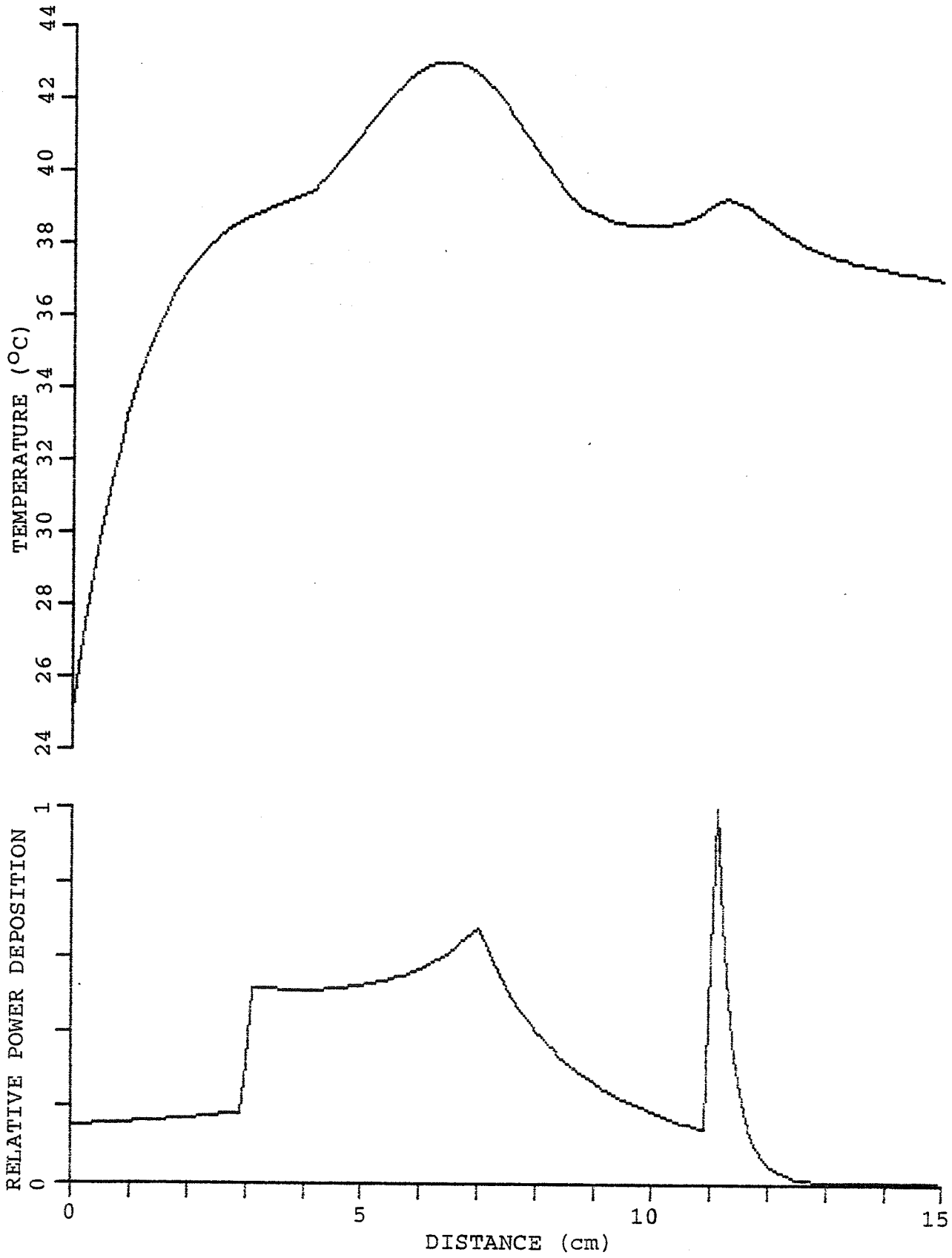

Figure 6.20. Temperature distribution produced in bone heating model with focused 0.8 MHz ultrasound. Linear gain of 4.

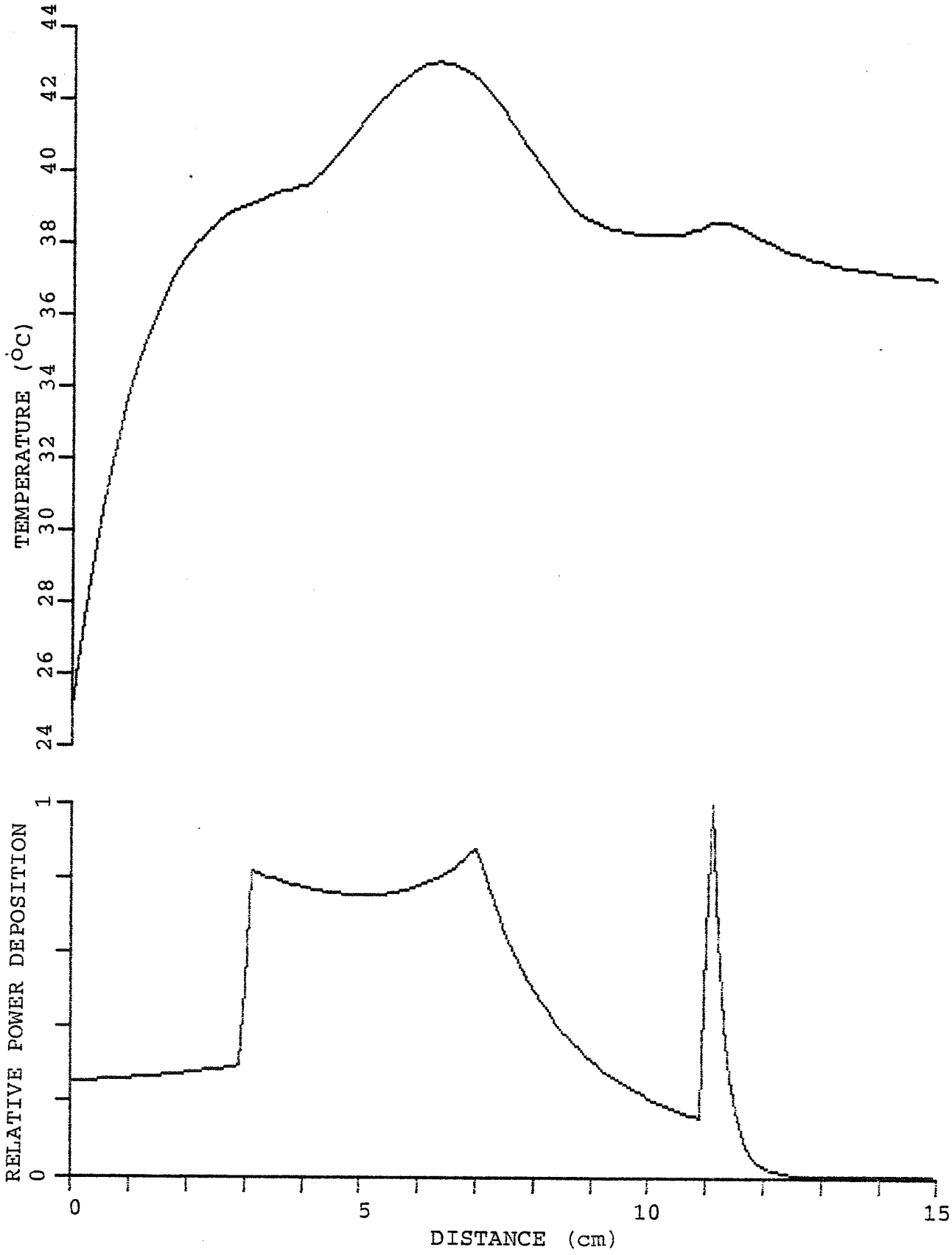

Figure 6.21. Temperature distribution produced in bone heating model with focused 1.0 MHz ultrasound. Linear gain of 4.

$$H_B = \frac{T_B \, e^{2\alpha_{1MHz} f(D - B)}}{2\alpha_{1MHz} pf[1 + |1 - B/D|(A_s/A_t - 1)]} \qquad (6.14)$$

where T_B is the fraction of energy transmitted into the bone and B is the depth of the bone.

A contour plot of H_B versus the ratio A_s/A_t and frequency is shown in Fig. 6.22. Lines of constant H_B in Fig. 6.22 indicate designs having approximately the same severity of bone heating. The similar reduction in bone heating that occurs with increases in frequency and gain are evident, and the greater proportional change with increases in frequency should be noted. From Fig. 6.22, a 1 MHz unfocused ($A_s/A_t = 1$) source has bone heating equivalent to that of a 0.6 MHz focused source with $A_s/A_t = 3$ due to the simplifications used in this model. This result is slightly different from the result obtained using the temperature distributions, where the equivalence occurred with a 0.6 MHz focused source with $A_s/A_t = 4$. However, this model does present a general relation for considering the relative effects of frequency and gain on bone heating, which is also approximately correct quantitatively.

6.2.3.2.2 Two Dimensional Array Focusing

Hyperthermia applicators that have been proposed that provide gain in two dimensions include circularly scanned fixed focus transducers (Lele, 1980), fixed annular focusing transducers (Beard et al., 1982), and annular and sector vortex phased arrays (Cain et al., 1986). A two dimensional phased array can also be used to provide gain in two

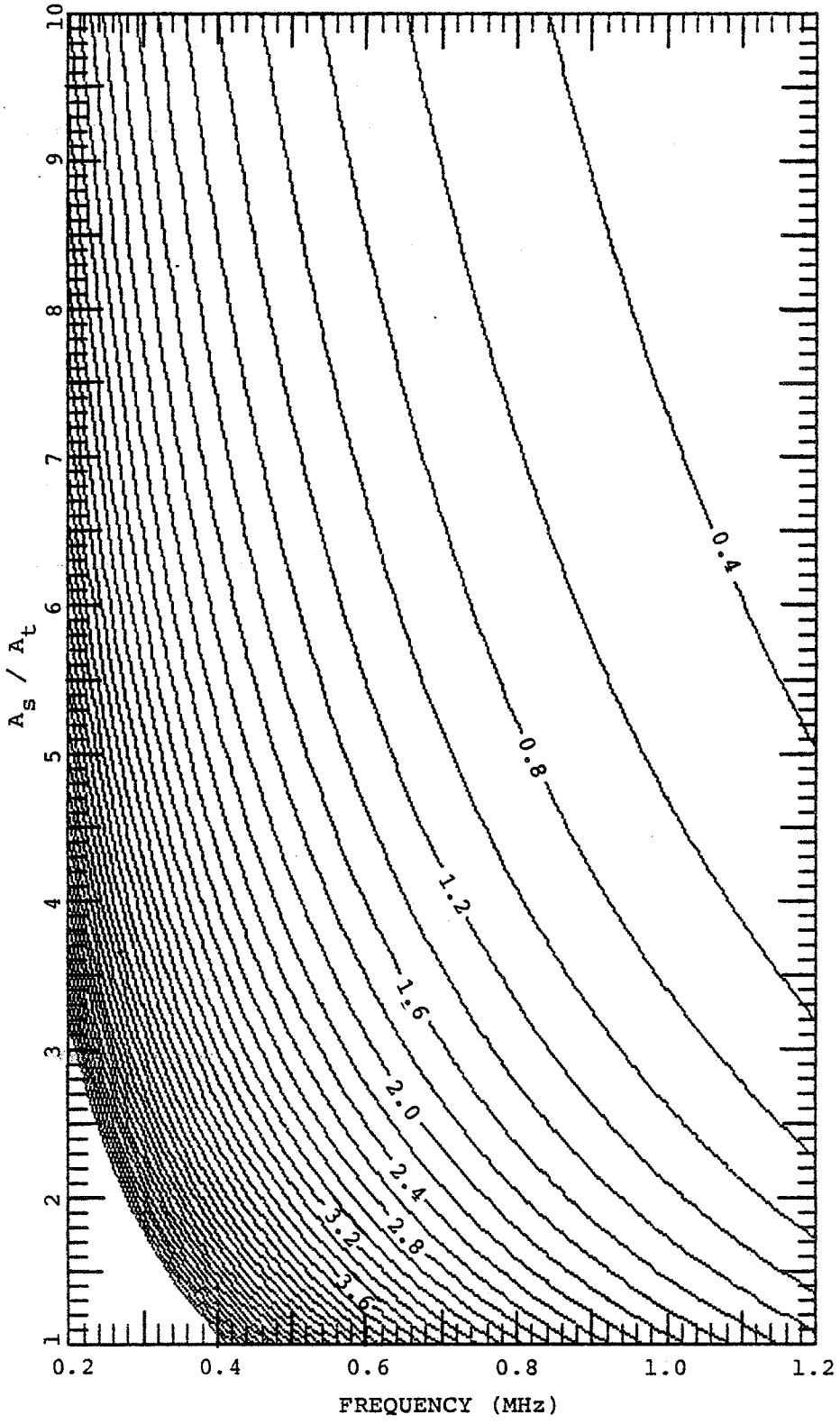

Figure 6.22. Contour plot of relative bone heating H_B versus frequency and gain for linear focusing model.

dimensions as illustrated in Fig. 6.23. As for a one dimensional focused system, a simple approximation to the beam cross-sectional area is made by interpolating between the applicator area and the tumor cross-sectional area to give

$$A(d) = A_t(1 + |1 - d/D|(\sqrt{A_s/A_t} - 1))^2 \qquad (6.15)$$

where the absolute value sign has been used to extend this model past the tumor region. The average power deposition Q_{2D} for two dimensional focusing can then be expressed as

$$Q_{2D} = Q(d)A_t / A(d). \qquad (6.16)$$

As with one dimensional focusing, power deposition patterns, for a range of frequencies and gains, were used in the calculation of temperature distributions. Results are shown in Figs. 6.24 through 6.27, and as expected, are very similar to the one dimensional focusing for the same gain. However, for this simple model, the power deposition in the intervening tissue is lower for the one dimensional model when cases with equal gain are compared. This would not be expected to occur in actual practice, as the longer paths to the tumor from each end of a one dimensional gain applicator would result in greater losses, reducing the overall gain.

A simplified model was also considered for the case of two dimensional focusing. The relative bone heating was expressed as

$$H_B = \frac{T_B\, e^{2\alpha_{1MHz} f(D - B)}}{2\alpha_{1MHz} pf[1 + |1 - B/D|(\sqrt{A_s/A_t} - 1)]^2}. \qquad (6.17)$$

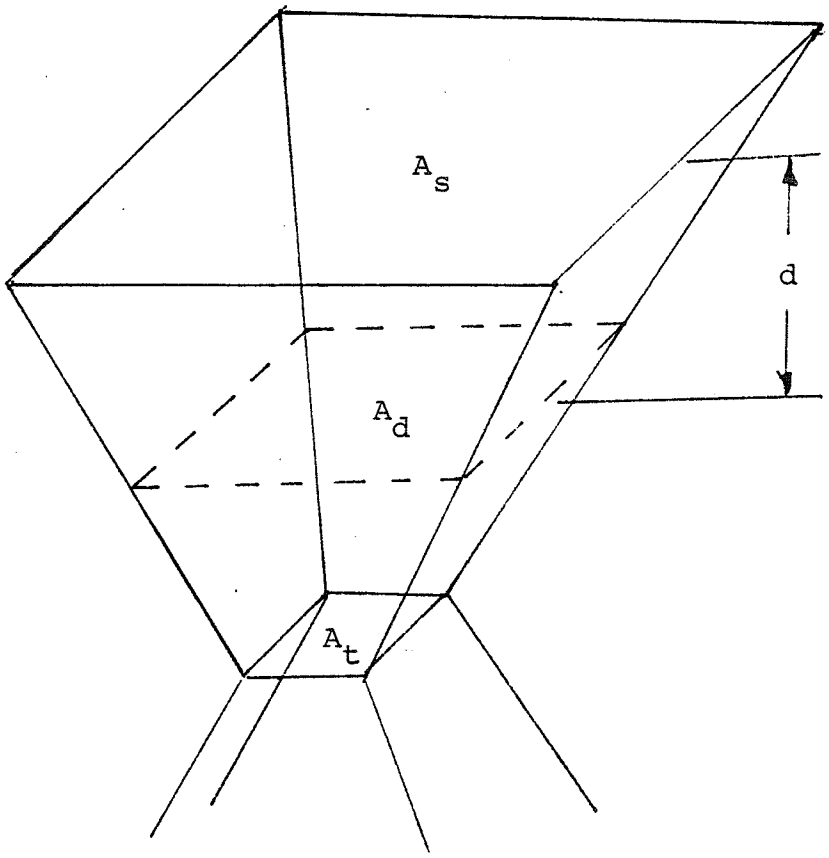

Figure 6.23. Geometry used for two dimensional array focusing model.

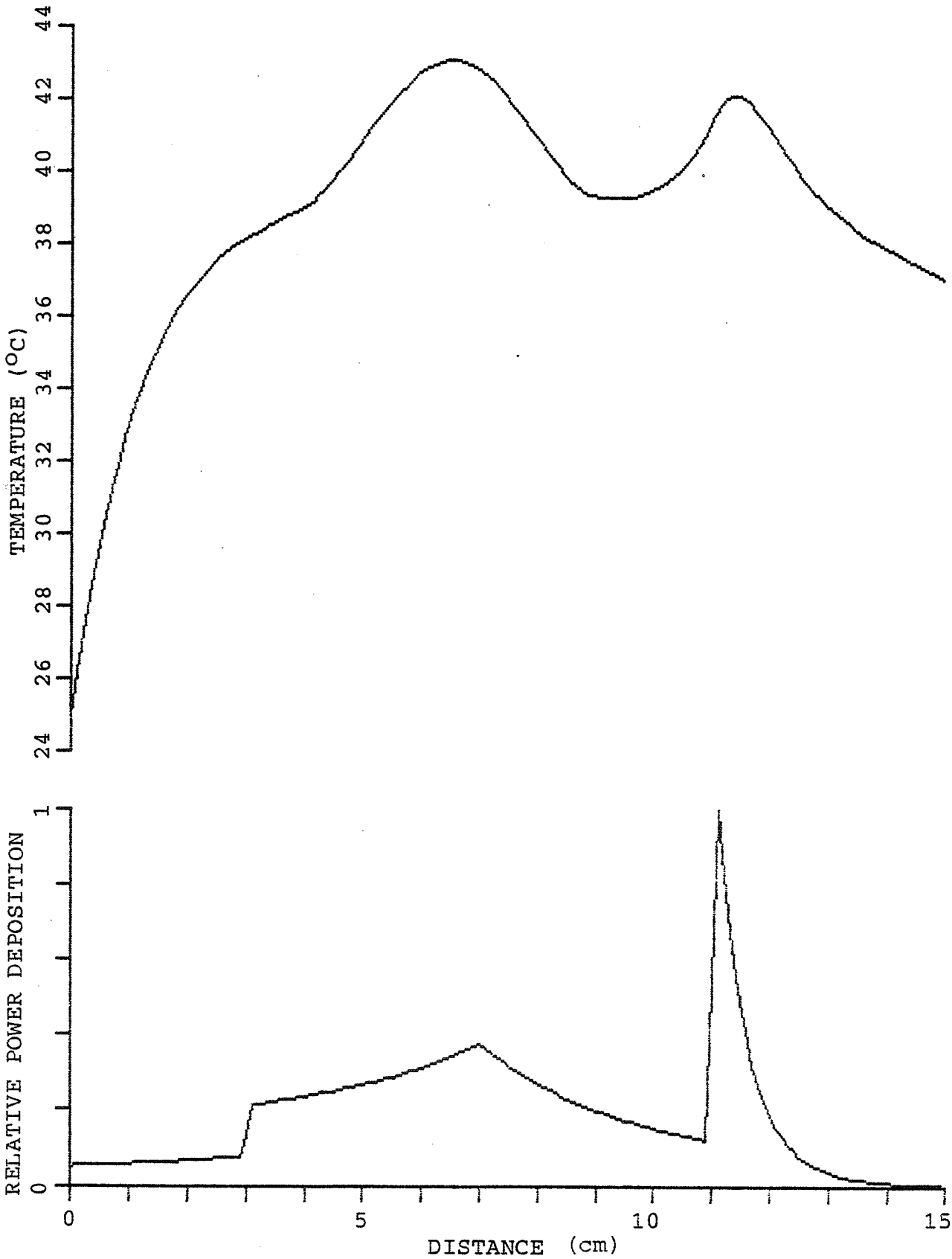

Figure 6.24. Temperature distribution produced in bone heating model with focused 0.4 MHz ultrasound. Two dimensional gain of 4.

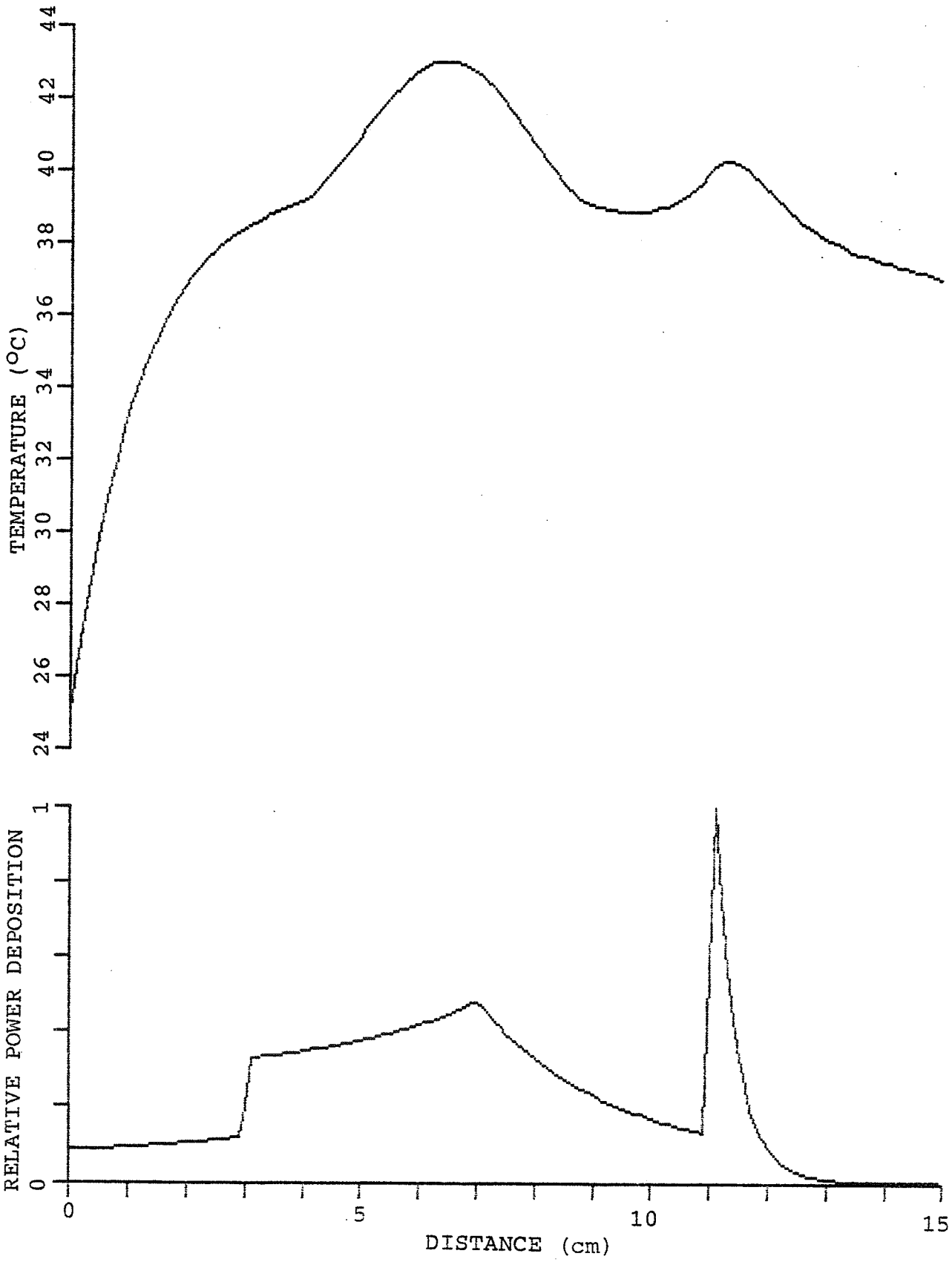

Figure 6.25. Temperature distribution produced in bone heating model with focused 0.6 MHz ultrasound. Two dimensional gain of 4.

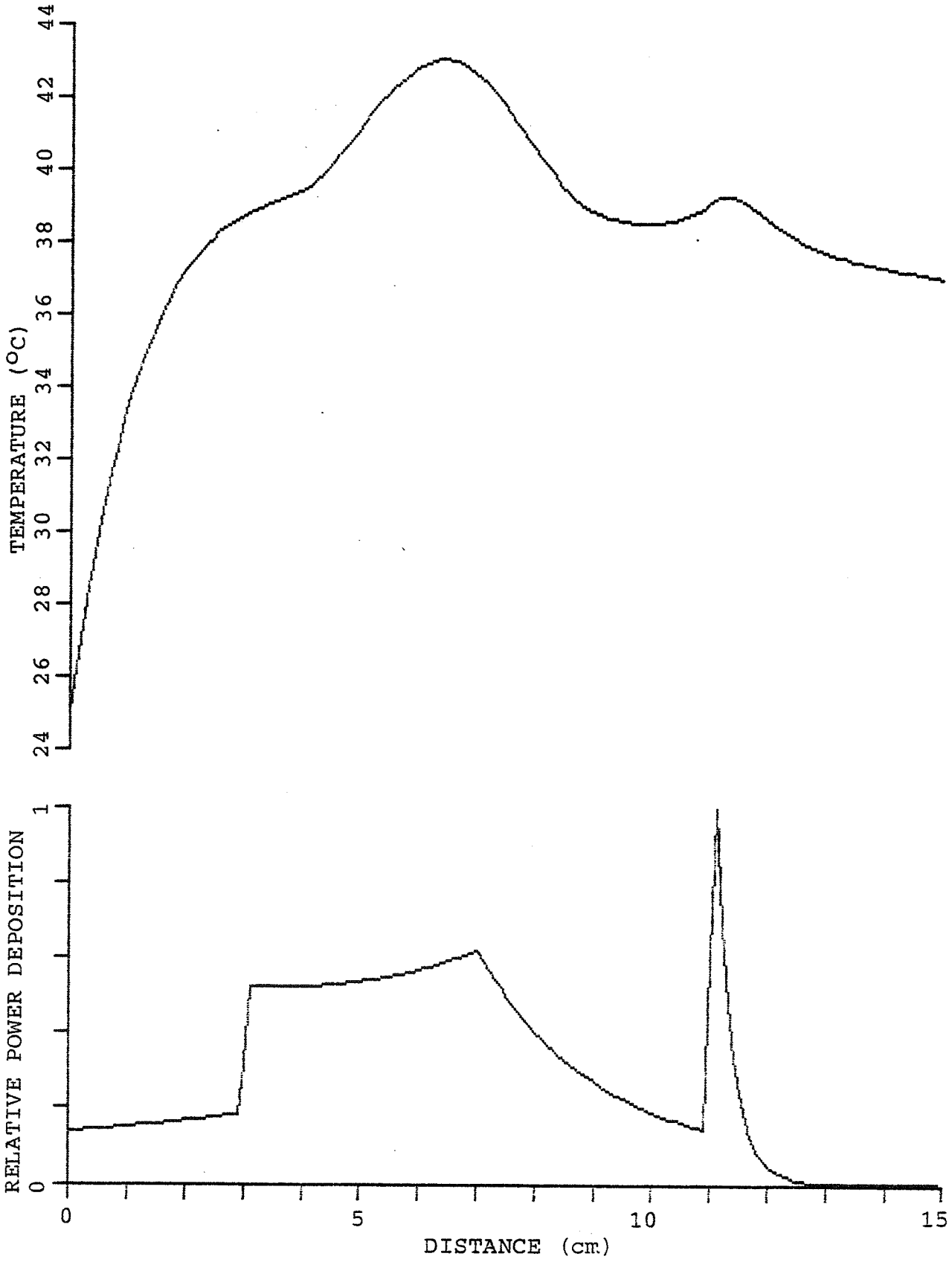

Figure 6.26. Temperature distribution produced in bone heating model with focused 0.8 MHz ultrasound. Two dimensional gain of 4.

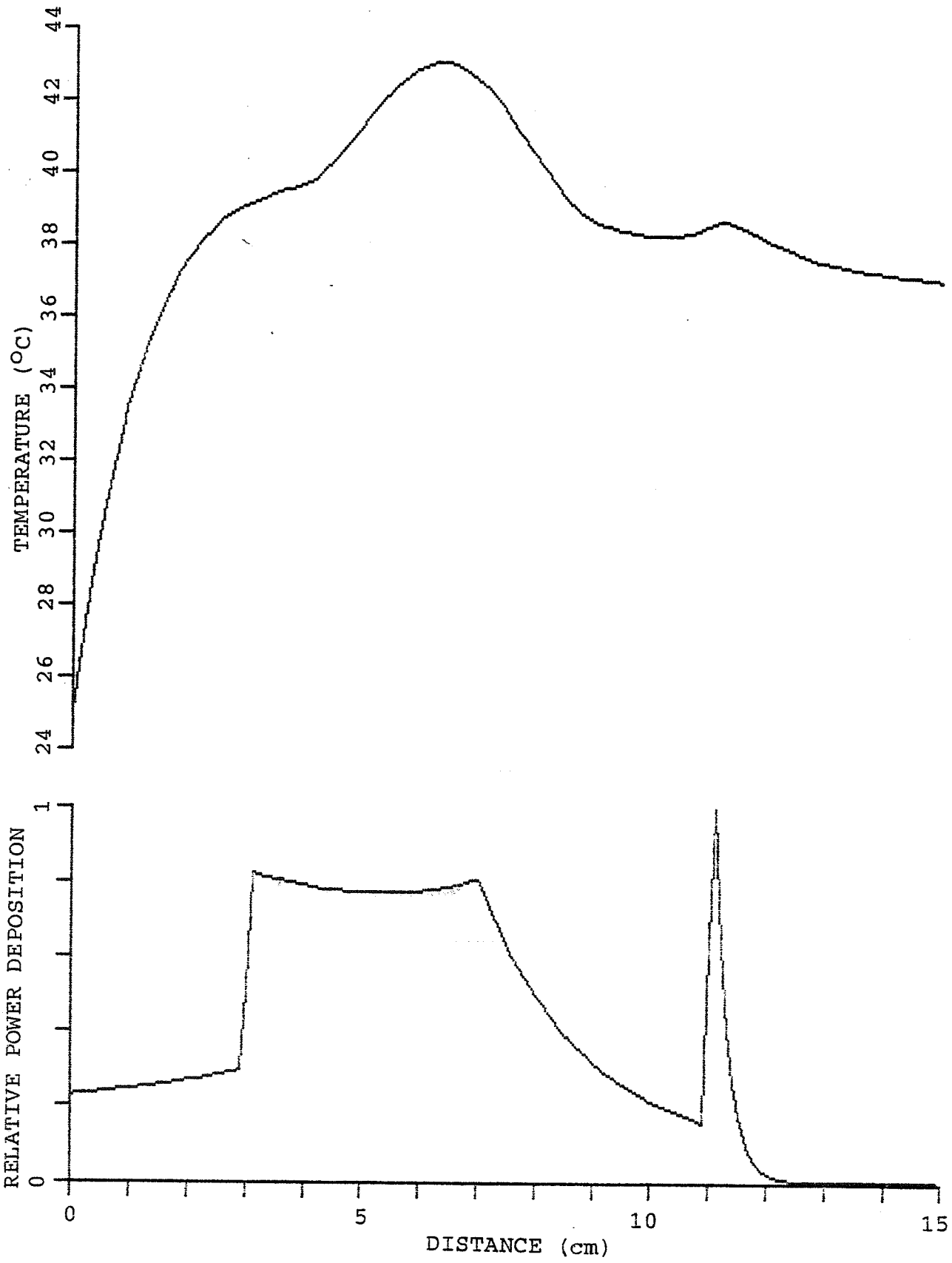

Figure 6.27. Temperature distribution produced in bone heating model with focused 1.0 MHz ultrasound. Two dimensional gain of 4.

The frequency and gain dependencies of this function are shown in Fig. 6.28. This is approximately the same result as for one dimensional focusing, except that the two configurations are not equivalent, in that a high gain is much easier to achieve using two dimensional focusing.

6.2.4 Tissue Inhomogeneity Considerations

An additional advantage of the use of lower frequencies for deep ultrasound hyperthermia becomes apparent when phase error due to variation of the velocity of propagation in different tissues is considered. Consider that two different paths of propagation from the applicator to the focus have a constant time delay difference as a result of differences in velocities along the propagation path. The phase error associated with the fixed time delay will be proportional to frequency. Consequently, the degradation of the focus due to propagation velocity differences will be more severe with higher frequency.

The magnitude of the problem of tissue inhomogeneities can be illustrated by considering a simple case. Assume that to reach the focus, the sound travels through 6 cm of tissue where the velocity of propagation varies linearly from an average of 1490 m/s at one end of the array to 1510 m/s at the other array end. If the phases applied to the array elements are computed assuming a constant propagation velocity, the ultrasound signals from the ends of the array will arrive at the focus with a time difference of 0.533 μs. Assuming that the signals arriving from different elements

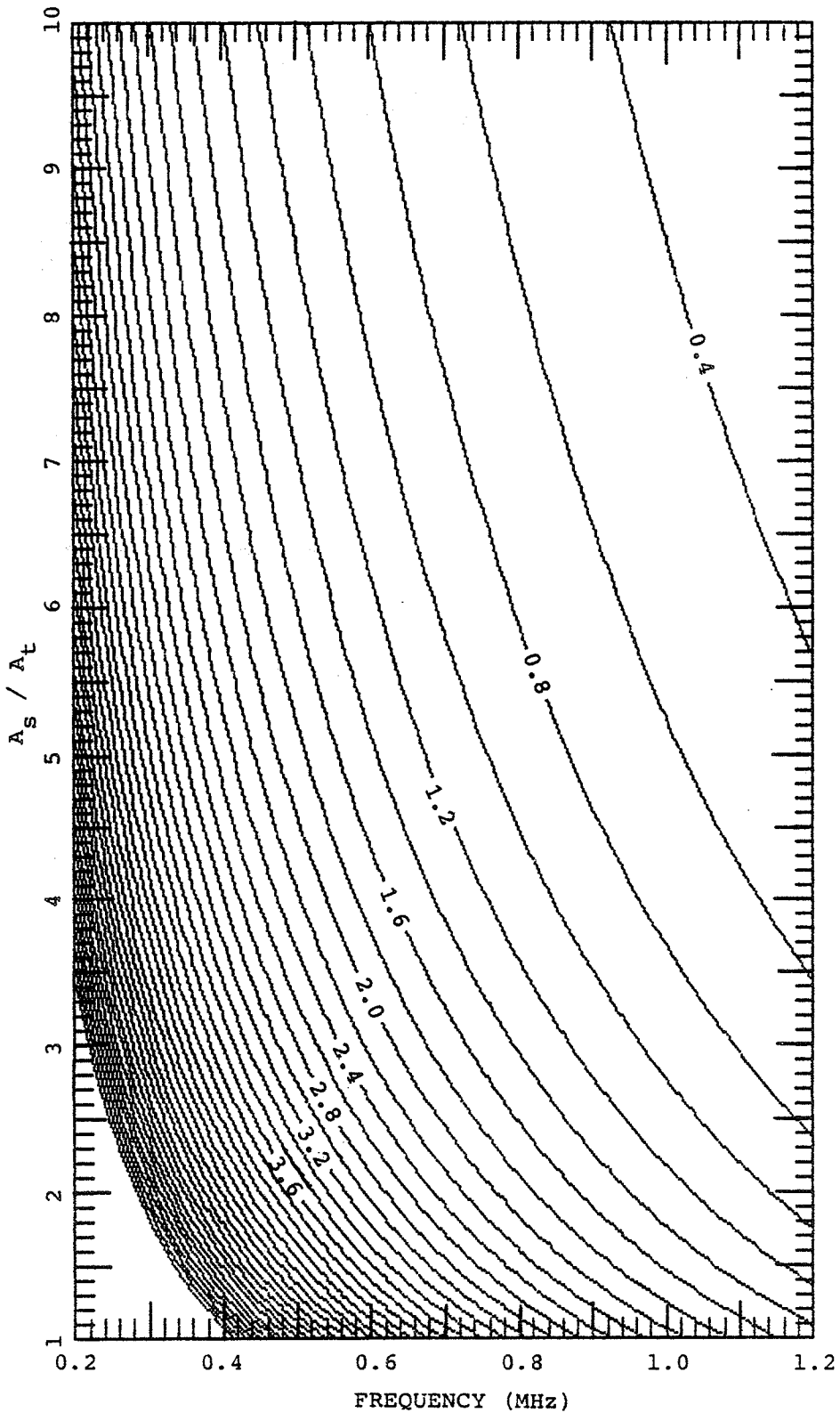

Figure 6.28. Contour plot of relative bone heating H_B versus frequency and gain for two dimensional focusing model.

of the array are uniformly distributed over this time interval, the degradation of the focus can be calculated for different frequencies. Using T to represent the period, i.e., T = 1/f, the intensity at the focus relative to the no loss situation can be formulated as

$$I_{rel} = \left(\frac{T}{2\pi(0.533)} \int_{\frac{-\pi(0.533)}{T}}^{\frac{\pi(0.533)}{T}} e^{j\phi} \, d\phi \right)^2 \qquad (6.18)$$

which reduces to

$$I_{rel} = \left(\frac{T}{\pi(0.533)} \sin\left[\frac{\pi(0.533)}{T} \right] \right)^2 . \qquad (6.19)$$

Evaluating this result for the cases of 0.5 MHz and 1.0 MHz yields relative intensities of 0.787 and 0.352, respectively. The focal intensity at 1 MHz is lessened to a much greater degree than that at 0.5 MHz. Although focus spreading would accompany this reduction so that the energy deposited in the tumor would not be lessened to this large an extent, tissue inhomogeneity considerations favor the use of lower frequencies.

6.2.5 Element Size Considerations

The size of the elements for a hyperthermia phased array is limited by directivity considerations. For an array with elements larger than one wavelength across, grating lobes appear in the field reducing the directivity of the array. The reduced directivity of the array means that not as much power is delivered to the tumor region and that the gain of the array is reduced. The power within the grating lobes also provides undesired heating outside the

tumor.

The most significant design criterion affecting element size selection is the size of the element in wavelengths. Consequently, to design a linear array at 1 MHz with similar grating lobe rejection properties and the same total area as one operating at 0.5 MHz, twice as many array elements would be required. Likewise, a two dimensional array with twice the frequency would require four times as many array elements. Also, at the higher frequency more gain would be required to compensate for attenuation losses, so that a 1 MHz array would require a larger area and significantly more elements.

6.2.6 Focus Size Considerations

When simple phasing is used with a phased array to produce a focus at a single point, the focus size is very strongly related to the frequency. The focus size determines the resolution of the system and the number of scan locations and maximum intensity if scanning is used. Alternatively, a focus can be formed in the shape of the tumor by using a more complex phasing scheme, as will be demonstrated in Chapter 8. The choice of the size of the focus generally involves a tradeoff between the precision available at higher frequencies and the lower peak intensities at lower frequencies.

6.2.7 Cavitation and Nonlinear Considerations

Both cavitation and nonlinear sound propagation occur for high intensities of ultrasound. The maximum intensity

usable for ultrasound hyperthermia is limited by the occurrence of cavitation, while nonlinear effects provide beneficial additional power deposition at the focus.

Cavitation should be avoided in hyperthermia because it produces uncontrollable tissue damage. Generally, cavitation is prevented by using higher frequencies, since to produce a given power deposition Q_p a lower local intensity is required:

$$I_t = Q_p/(2p\ \alpha_{1MHz}\ f). \tag{6.20}$$

For unfocused and unscanned systems, this simple relationship governs the design.

6.2.7.1 Frequency Dependence of Maximum Intensity

Scanned focused systems where peak intensities are inversely related to the focal cross-sectional area exhibit a more complex relation. The width of a focus, w_f, is inversely proportional to the width of the source, L, and inversely proportional to the frequency:

$$w_f = c_1/(f \cdot L) \tag{6.21}$$

where c_1 is a constant. The cross-sectional area of the focus can then be expressed as:

$$A_f = (c_1/(f \cdot L))^2. \tag{6.22}$$

For a small focal area, a higher peak intensity will be required at the focus to produce the same average intensity achieved using a larger focus. The maximum intensity I_{max}

is simply the required average intensity I_t multiplied by the ratio of the tumor cross-sectional area A_t to the focus cross-sectional area:

$$I_{max} = I_t(A_t/A_f) . \quad (6.23)$$

Substituting Eq. (6.20) and Eq. (6.22) yields

$$I_{max} = Q_p A_t L^2 f/(2\ p\ \alpha_{1MHz} c_1^2) . \quad (6.24)$$

The significance of this relation lies in the frequency dependence: using a higher frequency requires a higher maximum intensity to produce the same average power deposition. This result implies that for a cavitation limit independent of frequency (below 2.0 MHz), scanned focused ultrasound favors the use of low frequencies while unfocused ultrasound favors higher frequencies. Thus, the approach of using higher frequencies to avoid cavitation as with unfocused ultrasound does not apply to scanned focused ultrasound.

6.2.7.2 Magnitude of Maximum Intensity

The large aperture necessary to provide sufficient intensity gain for deep hyperthermia causes a phased array to produce a very small focal region of approximately a wavelength across and several wavelengths in depth. Since the focal size produced by such an array is typically 2 to 6 mm across and 5 to 30 mm in length, and the target volume is typically much larger, the required scan path consists of a large number of focal locations. For a large number of

focal locations, the dwell time at each point is small and very high focal intensities are required to produce a time averaged intensity suitable for hyperthermia. The use of very high focal intensities, i.e., intensities greater than 100 W/cm^2, brings in additional complications of nonlinear sound propagation and cavitation.

The order of magnitude of the focal intensity for scanned ultrasound hyperthermia in typical applications can be easily calculated. For an array operating at a frequency of 0.5 MHz, a frequency suitable for deep hyperthermia, the focal size is dependent on the size of the array and the tissue properties and would be approximately 0.4 cm by 0.4 cm for a two dimensional phased array, yielding a focal cross-sectional area of 0.16 cm^2. To heat a tumor with a 6 cm diameter cross-section and an extent in depth of one focal length, division of the tumor cross-sectional area by the focal cross-sectional area provides the number of scan positions: 176. Assuming a required power deposition of 0.2 W/cm^3 as used previously and using Eq. (6.20), the average intensity I_{avg} can be calculated. Using $\alpha = 0.04$ nep/cm and $p = 0.8$, typical values for muscle tissue at 0.5 MHz, the average intensity is calculated as 2.5 W/cm^2. From this, the maximum intensity is simply the average intensity divided by the number of focal locations necessary to cover the tumor, yielding a maximum intensity of 442 W/cm^2. This intensity is well within the region where cavitation (Frizzell, 1983) and nonlinear sound propagation have been observed (Swindell, 1985), but far less than the levels

required to produce cavitation in brain and liver with focused ultrasound.

Nonlinear sound propagation is advantageous because the nonlinear effects cause an enhancement of heating at the focus due to production of higher harmonics which have a larger absorption coefficient than the fundamental. Because of this phenomenon, additional gain is present, enhancing tumor heating by up to a factor of two. The minor disadvantage of nonlinear sound propagation is that computer modeling of the sound field is much more difficult since a single frequency field can no longer be assumed and fields for a range of frequencies must be calculated or simplifying approximations made (Swindell, 1985). Also, for intensities where nonlinear propagation is significant, the cavitation threshold is approached.

Cavitation causes nonthermal tissue damage when high intensities are present, and consequently the focal intensity level must be limited to avoid cavitation. Several studies have investigated the cavitation threshold frequency dependence in tissue for the diagnostic frequency range, 1 to 25 MHz, while the hyperthermia frequency range, 0.3 to 2.0 MHz, has remained largely unexplored.

The tradeoffs between cavitation and nonlinear propagation need to be studied to determine if the gains from nonlinear propagation are more significant than the occurrence of cavitation within the tumor. Both cavitation and nonlinear sound propagation can be avoided by the formation of multiple foci. This is done by forming foci at

several locations simultaneously rather than scanning a single focus through each of the separate focal locations and is discussed in Chapter 8. This enlarged focus can either be made sufficiently large to cover the entire tumor, or it can be scanned over the tumor volume.

6.3 Design Results

Clearly, there is not a single frequency that is suitable for all applications. Since gain, tissue inhomogeneity, and element size consideration favor the use of low frequency, the lowest frequency acceptable for the depth and chosen efficiency tolerance (see Fig. 6.3) should be used. When the potential for bone heating is present, frequencies extending to the maximum allowable under the efficiency constraint can be used, depending on the proximity of the bone to the tumor.

For deep heating in the range of 5 to 15 cm, a selection of phased array applicators with frequencies ranging from 0.3 MHz to 1 MHz should be available. If only a single applicator were available, the most useful frequency range appears to be from 0.4 to 0.6 MHz. The availability of multiple frequency phased array applicators is not unreasonable; the same applicator controller can be used for multiple applicators.

Sufficient applicator gain to compensate for attenuation losses is recommended, providing additional benefits with respect to overheating of bone. More gain is

recommended and certainly desirable, although the gain available may be dictated by a practical limit on the number of elements.

In the following two chapters, a phased array design is presented that uses linear arrays to reduce the number of elements required. The reduction in the required number of elements is accompanied by a reduction in the potential for achieving high gains. Using a linear array system does provide considerable reduction in system complexity; other simplifications of two dimensional array systems have been considered and are presented in Chapter 9.

CHAPTER 7

SCANNING OF PHASED ARRAY FOCUS TO UNIFORMLY HEAT A TUMOR

7.1 Introduction

A two dimensional phased array allows focal placement in three dimensions and produces intensity gain in two dimensions, but is too complex and costly since each element of the array requires its own phasing circuitry and amplifier. An alternative approach is to use a series of separate linear arrays stacked in the y-direction, as shown in Fig. 7.1, and to change the excitation from one group of arrays to another to provide scanning in the y-direction (Ocheltree et al., 1984). The desired scanning in the y-direction can be achieved by exciting the linear arrays in groups of three adjacent arrays and switching among various groups of three arrays. This provides the required beam width in the y-direction, since at the nearfield-farfield transition, the distance for operation of the array, the one half power beam width is approximately one third the y-dimension of the source (See Figs. 2.4 through 2.8 for a confirmation of this property.).

In this chapter, a stacked linear phased array applicator design is presented. Theoretical comparisons are made between power deposition patterns resulting from electronic scanning of the phased array and mechanical scanning of a fixed focus transducer.

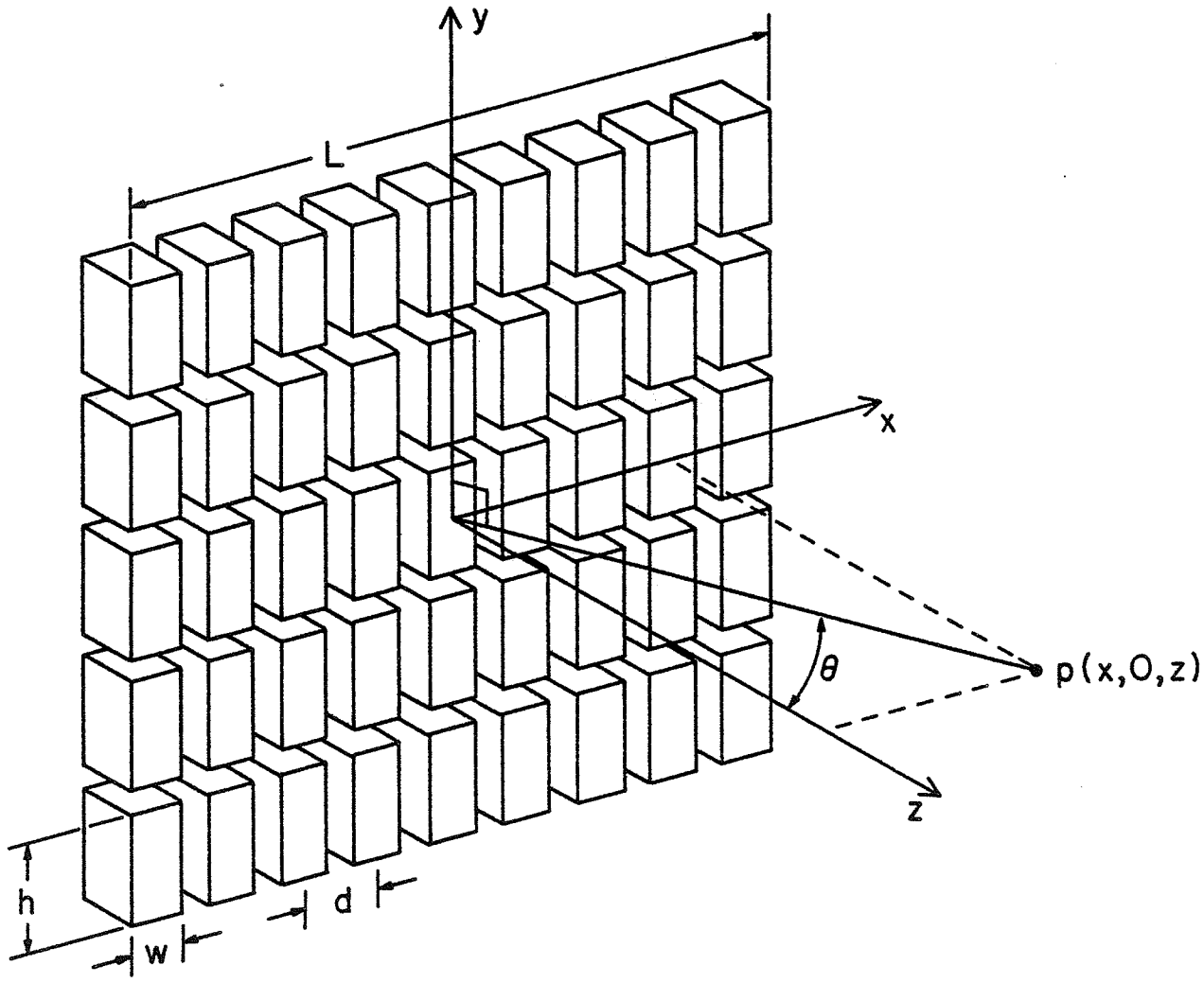

Figure 7.1. Stack of five linear phased arrays.

7.2 Array Design

Heating of a deep seated tumor by a surface applicator requires that sufficient intensity gain be present so that the loss of intensity due to attenuation is more than compensated such that the resultant intensity at the tumor is greater than that at the surface (see Section 6.2.2 and Fig. 6.4). The array gain for the stacked phased array applicator considered in this study was maximized by choosing as large an array length as currently practical, L = 20 cm, and the minimal frequency within a 20% efficiency tolerance, f = 0.25 MHz. This frequency choice is too low to be practical for any heating adjacent to bone, but is adequate for a comparison with a fixed focus applicator of the same frequency.

The other design parameters of a stacked linear phased array are dictated by the choice of operating frequency, array length, and treatment depth. The element spacing, d (see Fig. 7.1), is selected to be between 0.5λ and 1.0λ to avoid grating lobes. The element width, w, is simply the element spacing minus the minimum gap between elements (0.125 mm for this study). The array height, h, is chosen so that the nearfield-farfield transition region for the height of three arrays occurs at the desired operating depth D:

$$h = \sqrt{4\lambda D/9} \ . \qquad (7.1)$$

For an operating depth D = 8 cm, an array height h = 1.5 cm is required. A sufficient number of arrays in the stack is required to span the tumor cross-section. Phase quantization to 4 bits, giving resolution to 22.5 degrees, provides negligible losses due to quantization errors (see Ocheltree, 1984). Table 7.1 lists the array parameters as determined here.

Table 7.1. Parameters of stacked array.

Array length	L	20 cm
Number of elements		64
Element width	w	3.0 mm
Element spacing	d	3.125 mm
Array height	h	1.5 cm
Number of stacks		8
Total array height		12 cm
Phase quantization		4 bits

7.3 Comparison of Stacked Linear Phased Array and Fixed Focus Transducer

The performance of a stacked linear phased array applicator can be evaluated by comparing it to an equivalent

fixed focus applicator. The applicators are compared by calculating, using the field calculation routine described in Chapter 2, the power deposition patterns with and without scanning.

The tumor for this study was an 8 cm diameter sphere centered at a depth of 6 cm. For this comparison, the scan path was chosen as circular, around the periphery of the tumor at a depth of 6 cm. Such a scan path has been shown to produce a uniform therapeutic temperature throughout the tumor volume for a poorly perfused tumor (Cravalho et al., 1980). A value of 0.7 dB/MHz/cm was chosen for the attenuation of normal and tumor tissues. A 2 cm water path was selected for both applicators to allow for the coupling medium, which might also provide surface cooling, and for clearance for the mechanically scanned fixed focus applicator. Based on the design parameters for the array presented in the previous section, an operating frequency of 0.25 MHz was used for each applicator.

The surface area of the stacked linear phased array applicator was 240 cm^2. Consequently, a 10 cm diameter was chosen for the fixed focus applicator to provide a comparable surface area in the plane of the source (254 cm^2) for the particular scan path used in this comparison. Though the two applicators have markedly different shapes and sizes, as shown in Fig. 7.2, their scanned surface areas are approximately equivalent. A summary of the two applicators is given in Table 7.2.

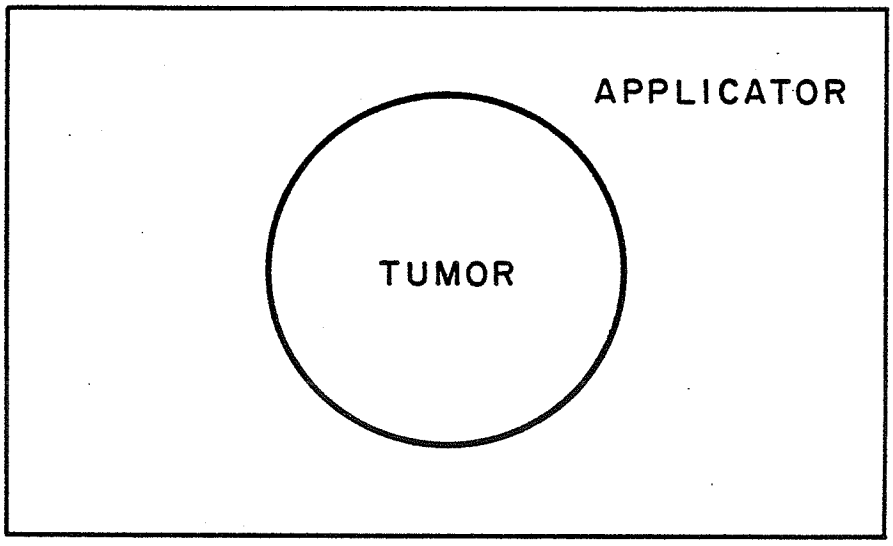

APPLICATOR AREA - 240 cm^2

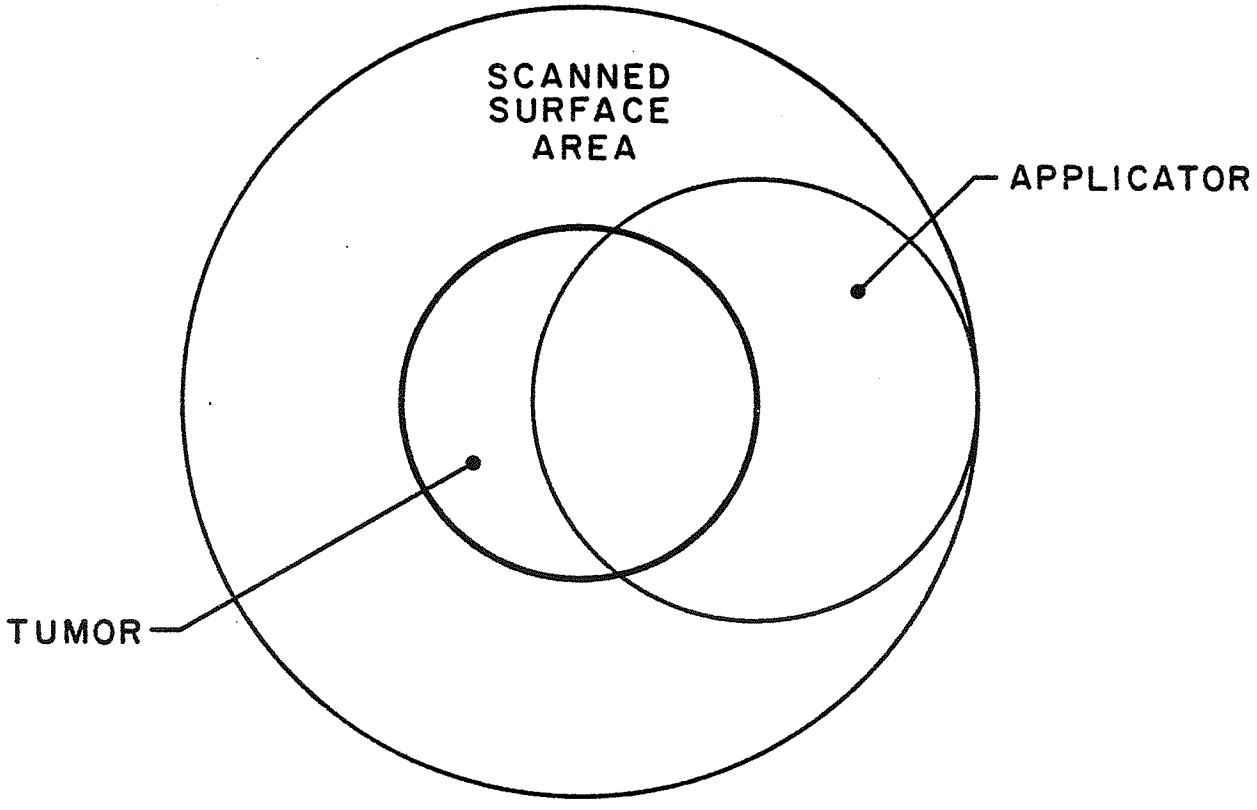

SCANNED SURFACE AREA - 254 cm^2

Figure 7.2. Comparison of stacked linear phased array applicator surface area (top) and scanned surface area of fixed focus applicator (bottom).

Table 7.2. Parameters for applicators used in this comparison.

	Phased Array Applicator	Fixed Focus Applicator
Frequency	0.25 MHz	0.25 MHz
Applicator Area	240 cm^2	78.5 cm^2
Scanned Surface	240 cm^2	254 cm^2
Focusing Depth	8 cm	8 cm

The power deposition pattern without scanning is provided for each applicator in Figs. 7.3 and 7.4. The pattern produced by the phased array, Fig. 7.4a, represents a slice through the focus in the x-z plane. The extent of the focus in the y-direction at the 3 dB level is approximately the height of one array, 1.5 cm (see Fig. 7.4b). The size of the focus produced by the phased array is smaller in the x-z plane than that produced by the fixed focus applicator because of the larger aperture of the phased array in the x direction.

The scan for the fixed focus applicator is continuous whereas the focal region for the phased array must be scanned by moving it among discrete positions. These positions must be determined from consideration of the scan path and the focal characteristics of the applicator, so that a nearly uniform power deposition is produced over the tumor periphery. This requires that the distance between phased array scan locations be approximately the same as the

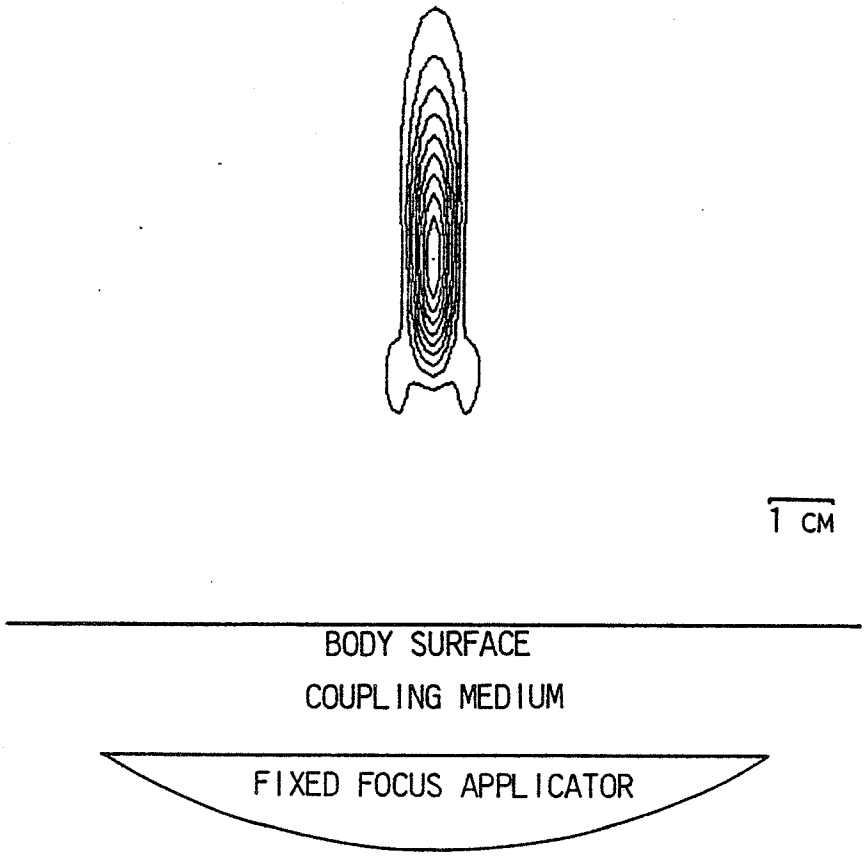

Figure 7.3. Power deposition patterns for single focus locations produced by fixed focus applicator. The pattern is normalized to 1 W/cm^3 and contours are given in increments of 0.1 W/cm^3.

a)

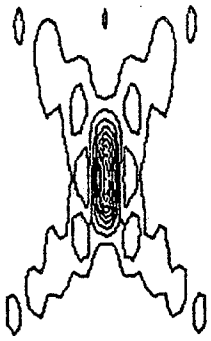

1 CM

BODY SURFACE

COUPLING MEDIUM

STACKED ARRAY APPLICATOR

b)

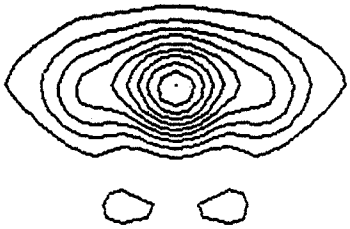

1 CM

BODY SURFACE

COUPLING MEDIUM

THREE EXCITED ARRAYS

STACKED ARRAY APPLICATOR

Figure 7.4. Power deposition patterns for single focus locations produced by the stacked array applicator. The patterns are normalized to 1 W/cm^3 and contours are given in increments of 0.1 W/cm^3. The patterns for the stacked array applicator are made phased (with 4 bit quantization) to produce a focus at x=0 cm (See Fig. 7.1 for coordinates). Figure 7.4a is the pattern in the x-z plane and Fig. 7.4b is the pattern in y-z plane.

3 dB dimension of the focus in each direction. An additional complexity of the phased array focusing is that when the focus is off axis, the elliptical shape of the focus is rotated, as illustrated in Fig. 7.5. However, the rotation of the focus is not significant enough to severely affect the scanned power deposition pattern of the phased array applicator.

The scanned power deposition pattern of the fixed focus applicator is easily calculated from its unscanned power deposition pattern since the shape of the focus is the same for all scan positions. The focus sweeps out a circle with its 3 dB power levels as shown in Fig. 7.6a. The power deposition pattern in the x-z plane cross section, displayed in Fig. 7.7, shows that there are no high intensity regions away from the desired path. This single cross section of the scanned power deposition pattern defines the field for any point since circular symmetry exists.

The phased array applicator was scanned in a circular path by placing the focus at the specific locations illustrated in Fig. 7.6b. The focal locations are chosen so that the number of focal positions in each 45 degrees of arc is a constant. For actual implementation of phased array scanning, a larger number of focal locations might be chosen for a more continuous distribution, and the time spent at each location would be adjusted to provide the desired power deposition pattern. as discussed in Chapter 5. The approach used in this study was chosen for its computational efficiency. Since each focal location has its own

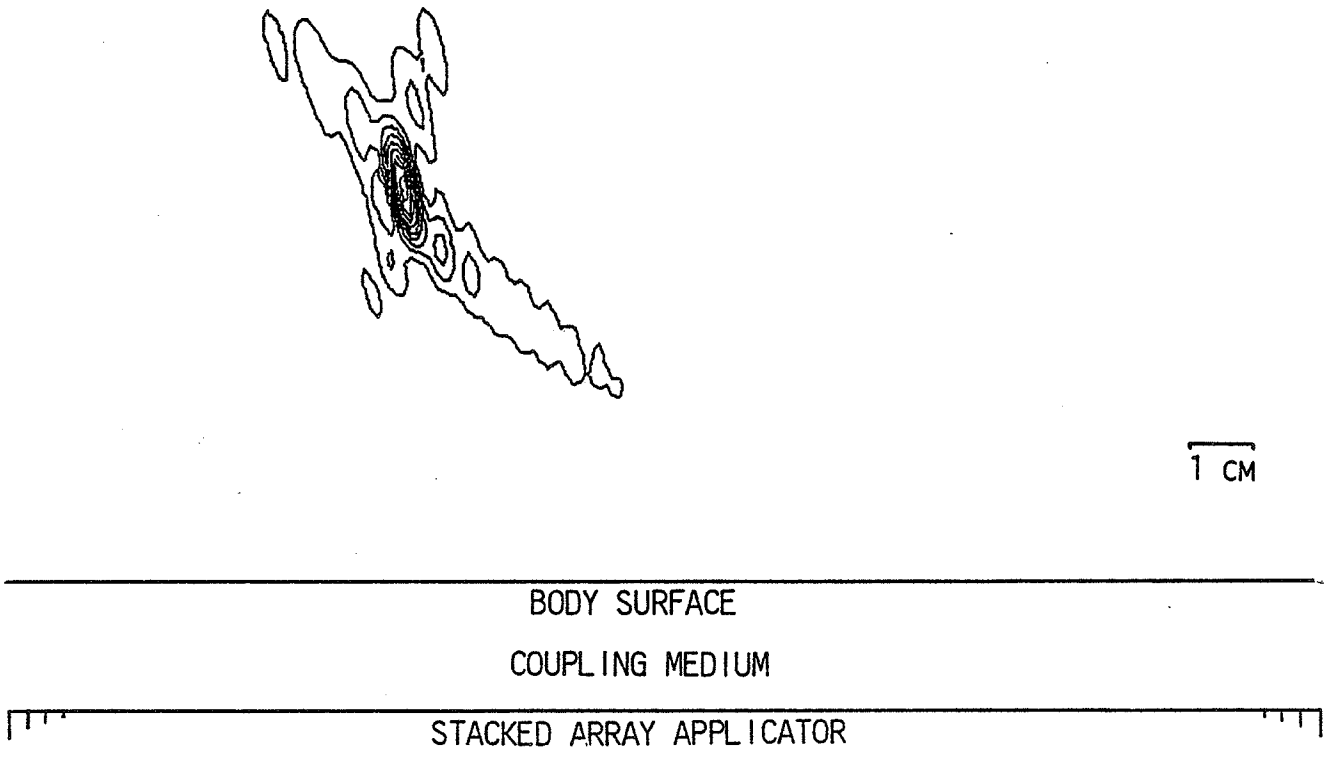

Figure 7.5. Power deposition pattern in the x-z plane for a single focus location produced by the stacked array applicator at x=40 cm. All other parameters are the same as in Fig. 7.3.

a)

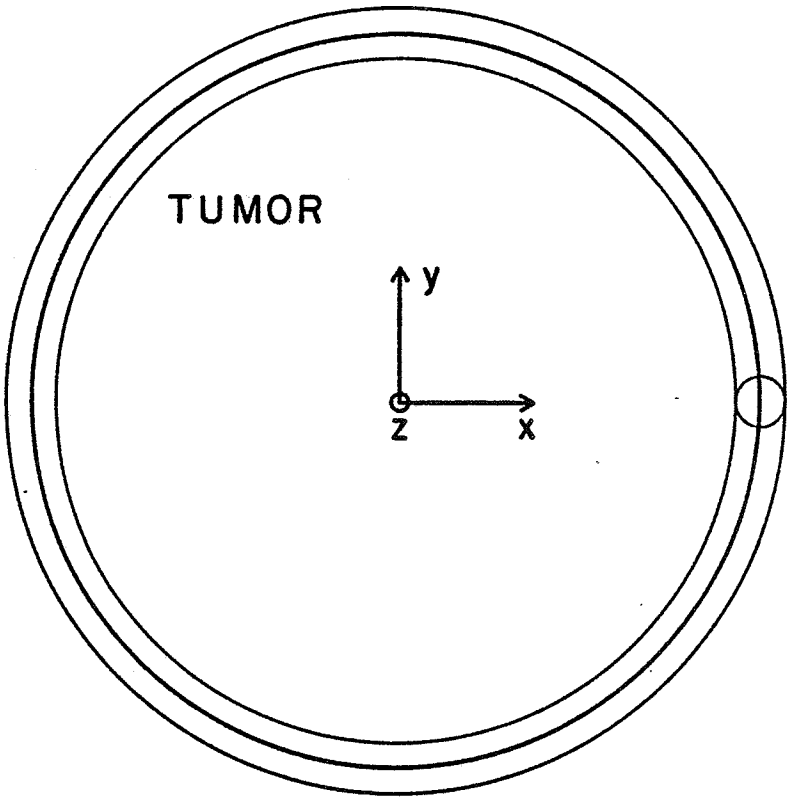

b)

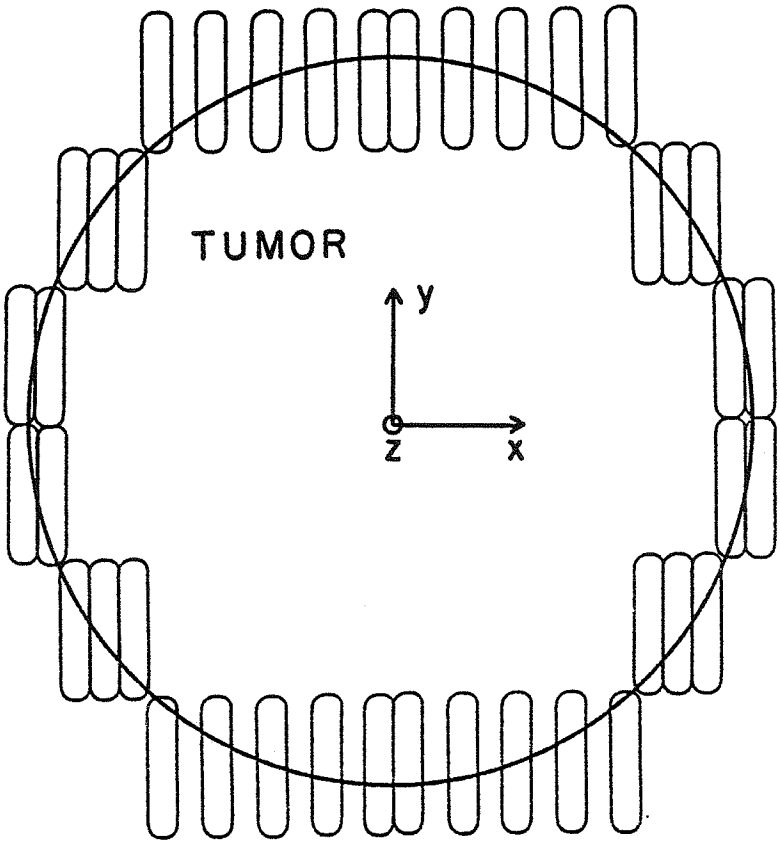

Figure 7.6. Scan paths for circular scanning of the fixed focus (Fig. 7.6a) and stacked array (Fig. 7.6b) applicators. The 3 dB limits of each scan are indicated.

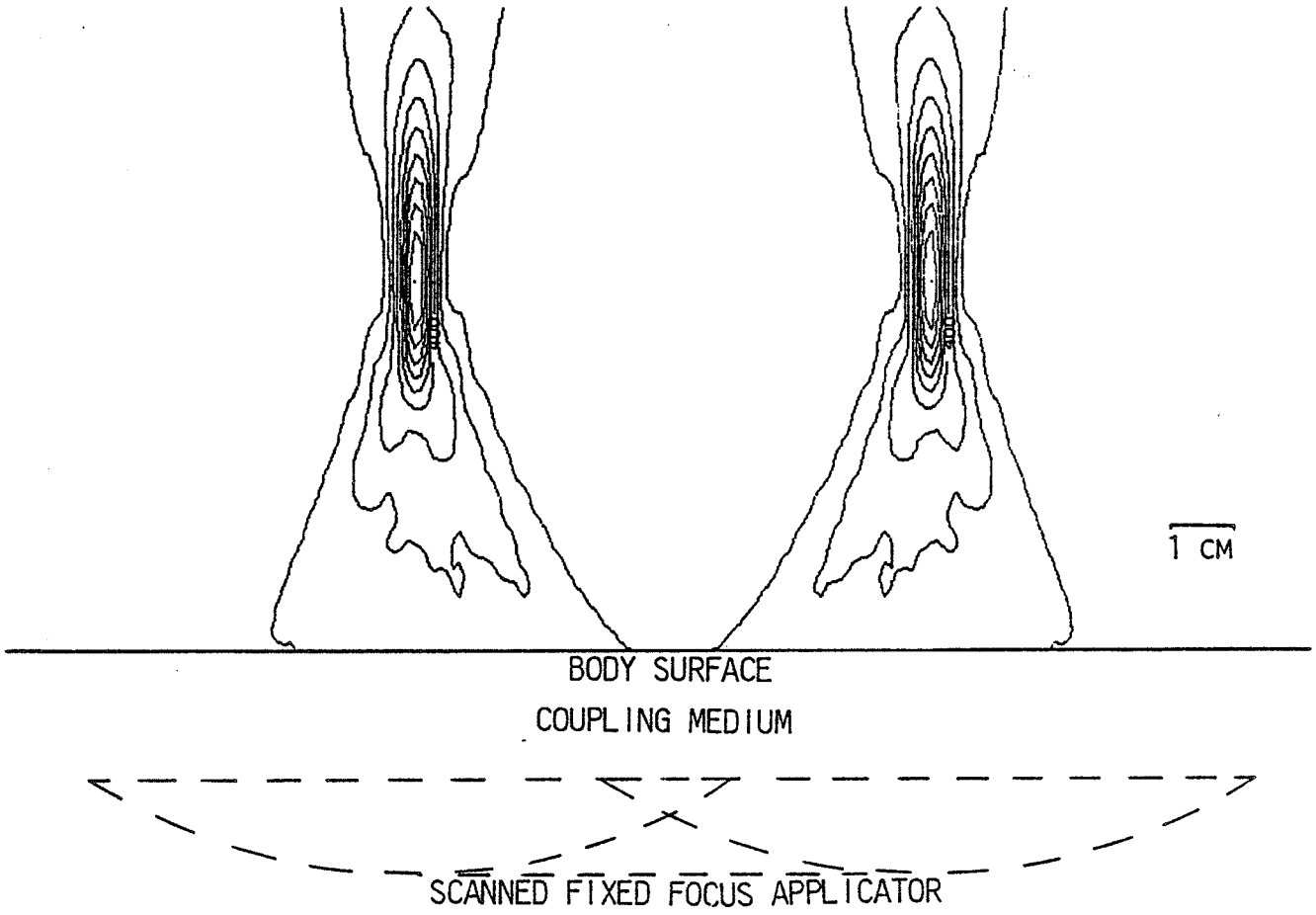

Figure 7.7. Power deposition patterns for a circular scan path produced by the fixed focus applicator. The pattern is displayed using the same parameters as Fig. 7.3.

charateristic shape and the field contribution from each must be calculated separately, it is preferable to use a smaller number of locations for simulation purposes.

The power deposition pattern in an x-z cross section is shown in Fig. 7.8. It should be noted that an area of high power deposition, greater than 40% of the peak, appears at the center of the field toward the surface of the applicator and has the potential for causing undesired heating of intervening tissue. However, for this particular tumor size and depth, the 0.4 contour area lies at the front surface of the spherical tumor and would serve to provide additional heating to the tumor. The source of this high power deposition area is evident when the skewed focal region of Fig. 7.5 is examined. The single power deposition section shown in Fig. 7.8 characterizes only one cross section of the field volume since there is no circular symmetry for the power deposition pattern of the scanned phased array applicator.

7.4 Discussion

A stacked linear phased array applicator can be designed to provide the required intensity gain for heating deep seated tumors. However, initial comparisons suggest that the array may be more likely than a fixed focus applicator to produce hot spots in intervening tissue when each applicator is scanned.

The production of hot spots in intervening tissue can

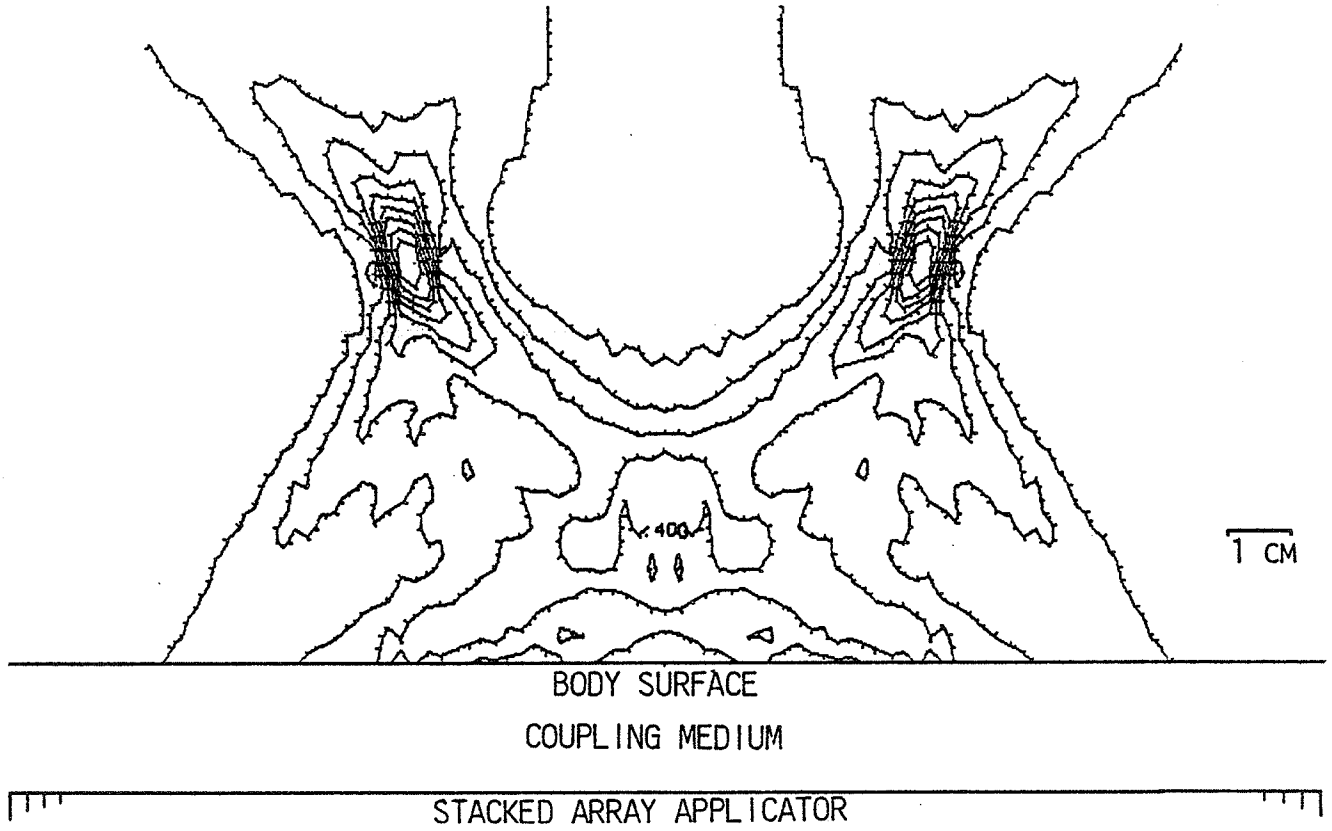

Figure 7.8. Power deposition patterns for a circular scan path stacked array array in a x-z plane section. The pattern is displayed using the same parameters as Fig. 7.3. Figure 7.8 is produced by phasing (with 4 bit quantization) the array to sequentially scan the focus positions shown in Fig. 7.6b.

be decreased by exciting only the portions of the array closest to the focal location. Thus, the excitation of the array could be shifted in both the x and y directions to follow the focal position, in much the same way as the fixed focus transducer is moved along its scan path. The same overall gain would be provided, because the entire applicator surface area is still being used for heating. Another alternative to phased array scanning is the formation of an enlarged focus, as described in Chapter 8.

CHAPTER 8
SHAPING OF PHASED ARRAY FOCUS TO UNIFORMLY HEAT A TUMOR

8.1 Introduction

The dynamic focusing capability of an ultrasonic phased array can be used in diagnosis to produce a high resolution image. However, when a phased array is made of sufficient size to provide the intensity gain necessary for deep hyperthermia, the resulting focus is too small to heat a tumor volume without some manipulation of the focus. The focusing characteristics of an ultrasonic phased array can be altered to heat a larger volume by two different methods: electronic scanning of the small focus or the formation of an enlarged focus or specially designed field shape. A combination of these two methods could also be used.

Electronic scanning of the focus is performed by changing the driving phases to each array element so that the focus is moved throughout the desired volume along a defined path. For a typical hyperthermia application the path would follow the periphery of the tumor, so that heat conduction and blood flow would transmit heat to the tumor interior and a uniform temperature distribution would result (Lele, 1980). Consequently, control over the energy deposition pattern is much more important than producing a uniform energy deposition pattern. Control of the power deposition pattern was the objective in the analysis that follows.

8.2 Theory

Both cavitation and nonlinear sound propagation effects can be avoided by the formation of multiple foci. By forming foci at several locations simultaneously rather than scanning a single focus to each of the separate focal locations, the dwell time is increased and the intensity is decreased. This enlarged focus can be made sufficiently large to cover the entire tumor, or it can be scanned over the tumor volume along a path which includes fewer sites.

The formation of a single focus is straightforward, as all the elements of the array are phased so that the sound from each source arrives with the same phase at the focus. For forming multiple foci, the ideal phasing of each array element is not so obvious, since every element cannot be phased so that all signals arriving at every focus is in phase. A method for determining an optimum set of phases for multiple focus generation follows.

The simplified problem of M omnidirectional sources used for producing N foci in a lossless medium, as shown in Fig. 8.1, will be examined. The result, however, can be applied to the situation of directional sources in attenuating media, as occurs with a hyperthermia phased array. The solution can be obtained by considering the optimum phase θ_{opt} for a single source S_m. The phase on source S_m that would add constructively, i.e., completely in phase, to form the n^{th} focus F_n is designated by θ_n. Thus, if the source is excited with a signal of phase θ, the

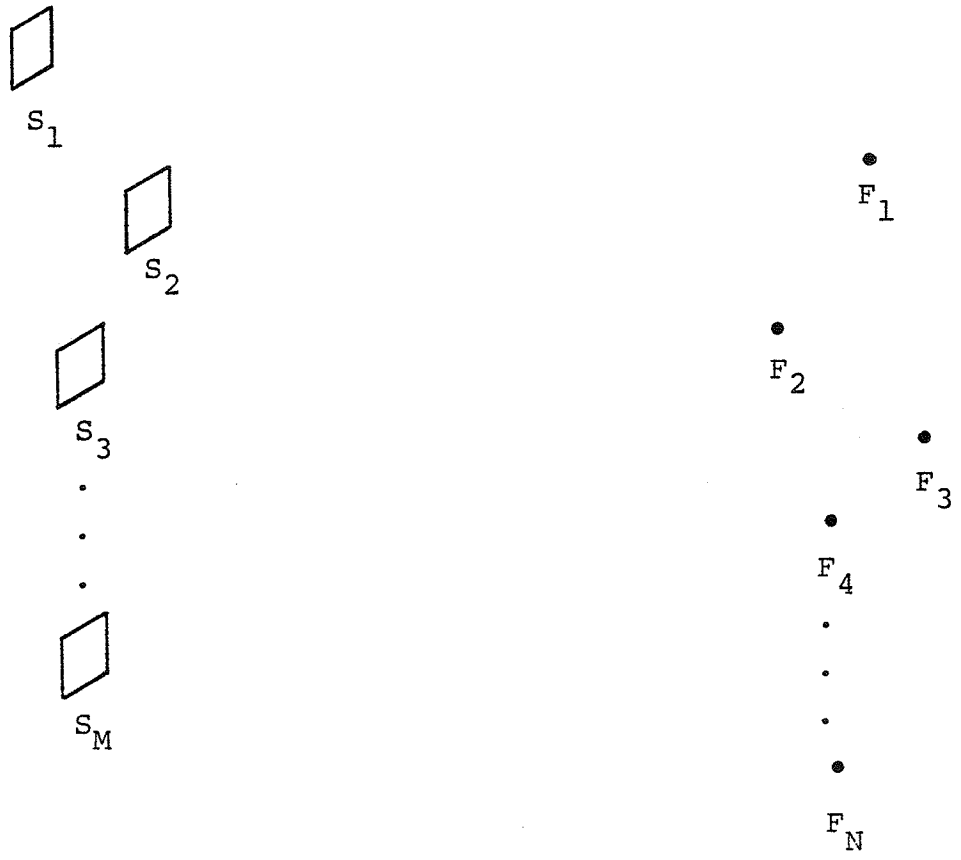

Figure 8.1. Geometry for forming N foci using M sources.

component of the signal that adds constructively at the focus F_n is given by $\cos(\theta - \theta_n)$. Since the objective is to maximize the contribution to all N focal locations, θ_{opt} is the phase that maximizes the sum

$$\sum_{n=1}^{N} A_n \cos(\theta - \theta_n) \tag{8.1}$$

where A_n is the magnitude of the desired relative amplitude at the n^{th} focus. Since the maximum of this function occurs where the derivative is zero, the optimum phase is the solution to the equation

$$0 = \sum_{n=1}^{N} A_n \sin(\theta_{opt} - \theta_n) \tag{8.2}$$

subject to the constraint that the second derivative is less than zero giving the additional condition

$$0 < \sum_{n=1}^{N} A_n \cos(\theta_{opt} - \theta_n). \tag{8.3}$$

Designating the positive real sum of Eq. (8.3) by R and adding to Eq. (8.2) multiplied by j yield

$$\sum_{n=1}^{N} A_n \Big(\cos(\theta_{opt} - \theta_n) + j\sin(\theta_{opt} - \theta_n) \Big) = R. \tag{8.4}$$

This may be rewritten as

$$\sum_{n=1}^{N} A_n e^{j(\theta_{opt} - \theta_n)} = R \tag{8.5}$$

and rearranged to yield

$$\sum_{n=1}^{N} A_n e^{-j\theta_n} = Re^{-j\theta_{opt}}. \tag{8.6}$$

Equating real and imaginary components of Eq. (8.6) yields

$$\sum_{n=1}^{N} A_n \cos\theta_n = R\cos\theta_{opt} \tag{8.7}$$

$$\sum_{n=1}^{N} A_n \sin\theta_n = R\sin\theta_{opt} . \tag{8.8}$$

Dividing Eq. (8.8) by Eq. (8.7) yields

$$\tan\theta_{opt} = \sum_{n=1}^{N} \sin\theta_n / \sum_{n=1}^{N} \cos\theta_n . \tag{8.9}$$

This is exactly the same phase that is obtained by a simple summing of the complex signals required for each focus, $e^{j\theta}n$, weighted by the desired relative amplitude A_n.

An enlarged focus is produced by producing multiple adjacent foci as described above (Tucker, 1956). The complex driving signal S_m for the m^{th} element to produce N foci is

$$S_m = s_{m,1} + s_{m,2} + s_{m,3} + \ldots + s_{m,N} \tag{8.10}$$

where $s_{m,n}$ is the signal that is required on the m^{th} element to produce a focus at the n^{th} focal position. A higher amplitude can be produced at a given focal position by increasing the magnitude of the $s_{m,n}$ term in the summations. To produce a similar heating pattern using the scanned approach, the driving signal for the n^{th} array element would be cycled through the set of signals $(s_{m,1}, s_{m,2}, s_{m,3}, \ldots, s_{m,N})$. The multiple foci can be chosen to conform the power deposition pattern to the shape of the tumor, hereafter referred to as conformal focusing.

One disadvantage of conformal focusing is that while it produces the desired intensities at the specified focal locations, higher intensities can be produced at other locations due to the formation of an interference pattern. Practically, intensities can be set in only one surface equidistant from the applicator and the quality of the conformed focus severely degrades as the number of focal locations in the pattern approaches the number of array elements. The conformal approach also requires driving amplitude control, an additional complication, although conformal focusing can be used with fixed driving amplitude with some degradation of the focus.

8.3 Methods

Conformal focusing has been investigated for use with a stacked linear phased array applicator design, as previously described by the author in Chapter 3 and would be applicable to a tapered linear phased array applicator (Benkeser, 1985). This approach is evaluated by examining a simple linear phased array. A frequency of 0.4 MHz was chosen to allow for sufficient penetration for deep hyperthermia. An array length of 20 cm was chosen as representative of the aperture required to provide sufficient gain for deep hyperthermia. The array was divided into 64 elements of 3 mm width and 45 mm height, and an attenuation coefficient of 0.08 nepers/cm/MHz was used for all tissues.

8.4 Results

A cross section of the energy deposition pattern of a single focus produced by this array was computed and is shown in Fig. 8.2, normalized to the maximum intensity and with contours at 0.1 interval. Scanning of this focus through x = (-2.4, 0.0, 2.4) mm at z = 100 mm to produce a pattern three focal widths wide is shown in Fig. 8.3. Conformal focusing at x = (-2.4, 0.0, 2.4) mm and z = 100 mm produced the focus of Fig. 8.4, where maxima greater than the focal intensity occur along the center axis. This effect is not as evident when the conformal focusing produces widely spaced foci as shown in Fig. 8.5.

8.5 Discussion

A suitable combination of scanning and conformal focusing could serve to suppress the disadvantages of each approach. Conformal focusing could be used to increase the size of the focus used for scanning so that the intensity could be reduced to lessen the chance of occurrence of cavitation. Alternatively, scanning of a conformal focus resembling a comb could be used to cover a large volume while supressing the interference effects arising when the multiple foci are closely spaced. More investigation of focusing alternatives is required to determine the optimum combination of these approaches.

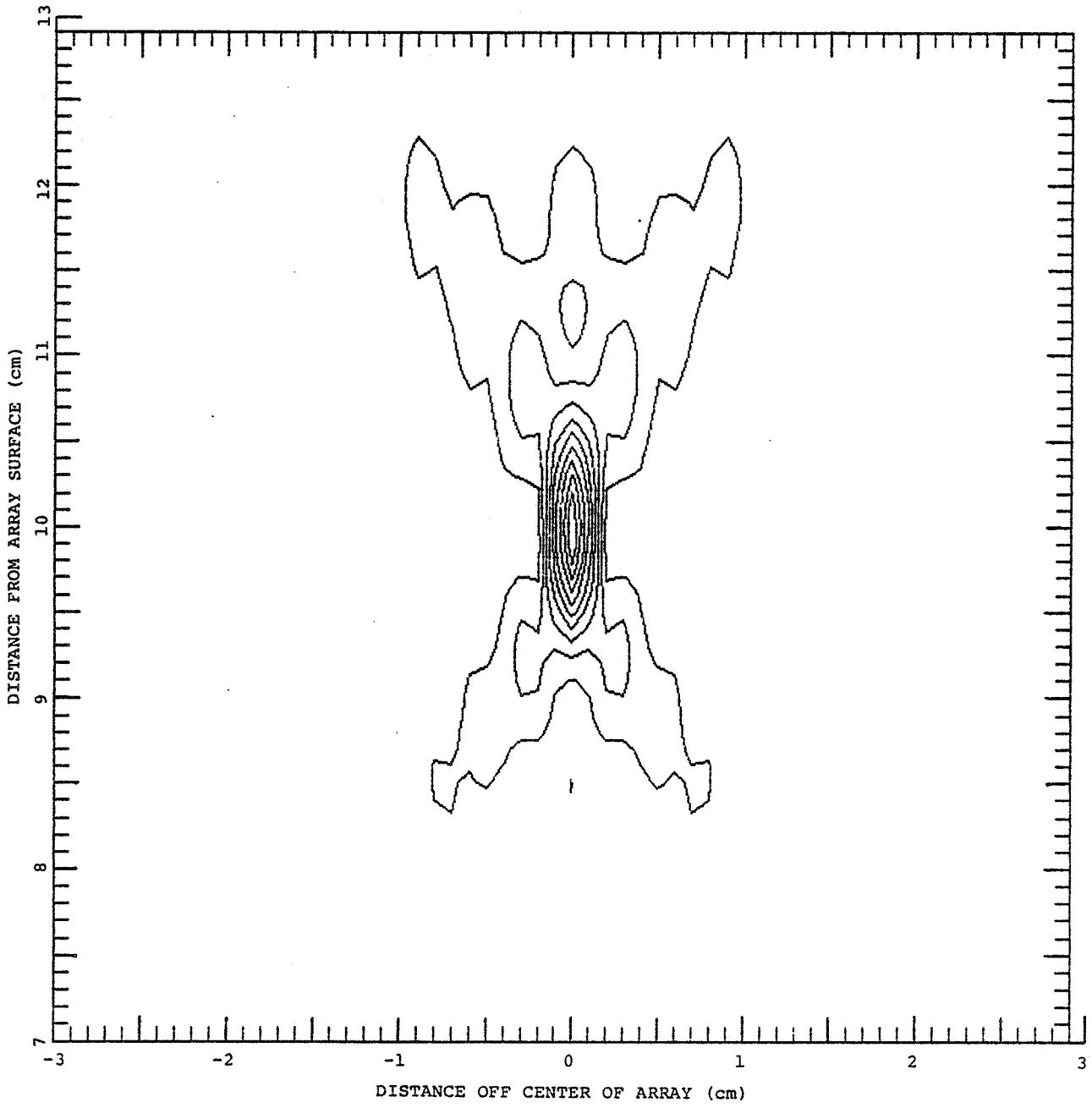

Figure 8.2. Single focus produced by phased array. The intensity is normalized to 1 W/cm^2 and contours are given at levels of 0.1 W/cm^2.

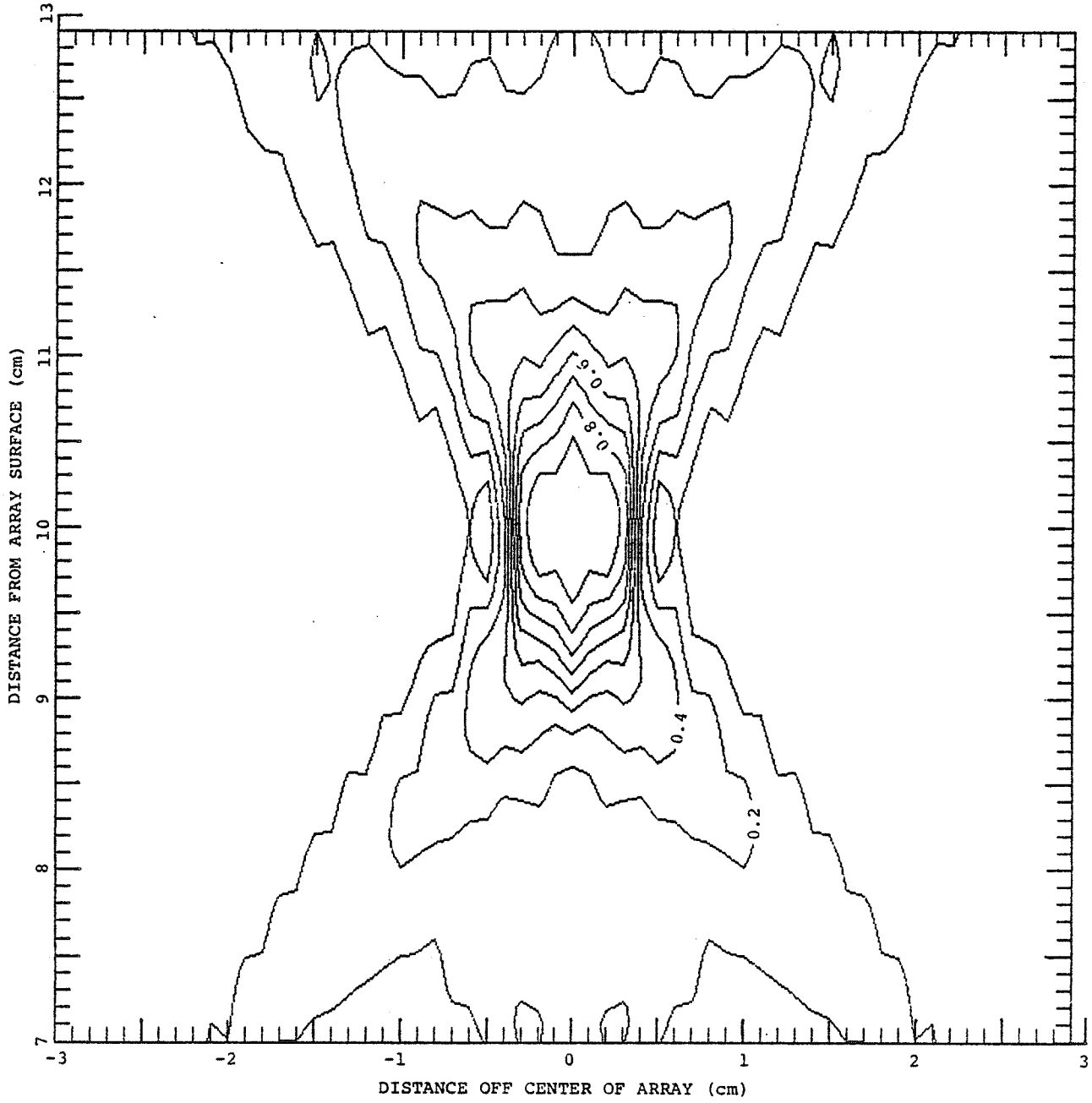

Figure 8.3. Scanning of focus through x = (-2.4, 0.0, 2.4) to produce a broadened focus. The intensity is normalized to 1 W/cm^2 and contours are given at levels of 0.1 W/cm^2.

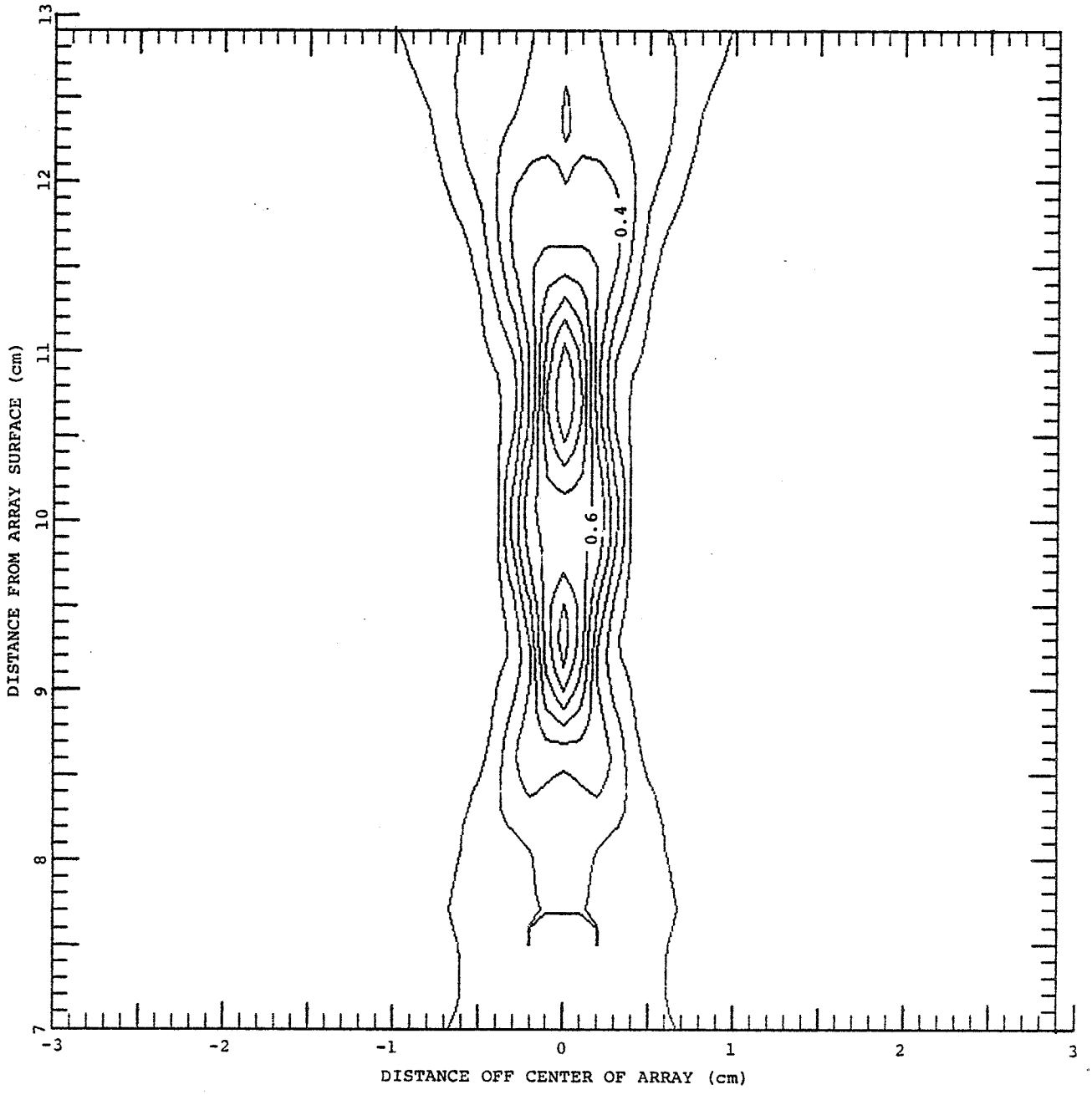

Figure 8.4. Broadened focus produced by focusing at three locations simultaneously (x = (-2.4, 0.0, 2.4) mm). The intensity is normalized to 1 W/cm^2 and contours are given at levels of 0.1 W/cm^2.

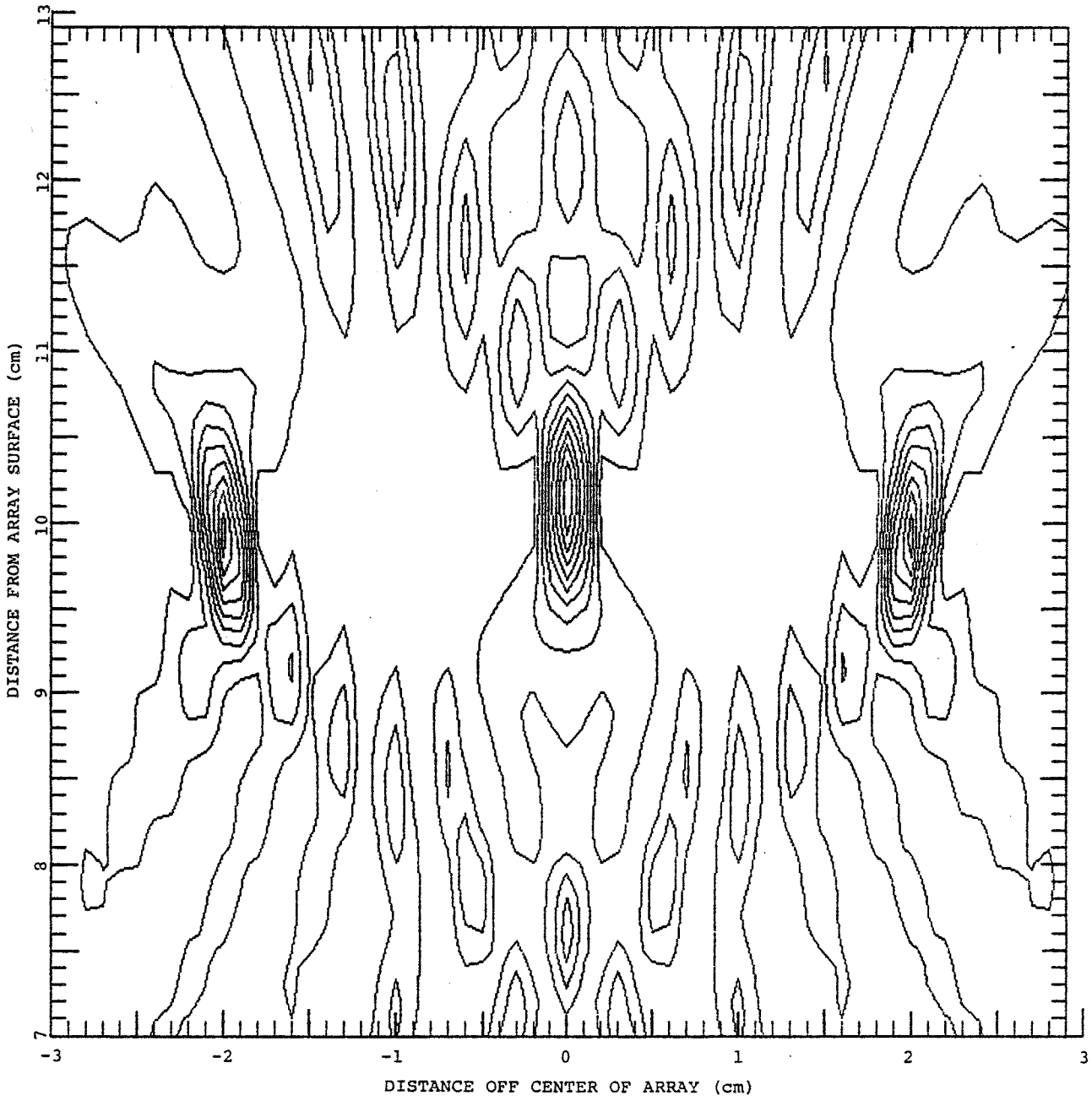

Figure 8.5. Simultaneous production of three foci with phased array at x = (-20.0, 0.0, 20.0). The intensity is normalized to 1 W/cm^2 and contours are given at levels of 0.1 W/cm^2.

CHAPTER 9

RECOMMENDATIONS FOR FUTURE STUDY

9.1 Alternative Configurations for Surface Applicators

The variations in the nearfield of circular applicators cause hot spots which lead to patient discomfort when treating surface tumors. The nearfield variations can be reduced by using applicators consisting of multiple square sources as indicated in Chapter 2 (Benkeser, 1985; Underwood, 1987). This nearfield smoothing can be explained by qualitatively considering the effect of the square corners added to the overall response of a circular source. The corner regions can be considered as providing shading, i.e., a tapering of excitation versus radial distance from the applicator center, making the excitation closer to a Gaussian distribution, which produces a smooth nearfield region.

The uniformity in the nearfield of a square source suggests that more uniform nearfields could be produced by designing applicators with multiple Gaussian weighted sources, which would be difficult to construct, or applicators composed of triangular sources. A triangular source would be expected to have a more uniform nearfield than a square source since its effective radial weighting is even closer to that of a Gaussian. These alternative multielement applicator configurations for treating source tumors should be investigated further.

9.2 Required Power Deposition Pattern Determination

The numerical model presented in Chapters 3 and 4 for calculating required power deposition patterns should be further developed for clinical applications. The time and temperature dependences of blood perfusion should be incorporated to make the model more realistic. The incorporation of temperature dependence of blood perfusion in the steady state model is straightforward. However, including the effects of time and temperature dependence of the blood perfusion in the time dependent model would involve evaluating the function $d(t,t_o,\rho C/W_{bn}C_b)$ for a variable W_{bn} to determine the required peripherial power deposition. For both models, changes in the blood perfusion in the tumor interior require a proportionate change in the power deposition in accordance with Eq. (4.13).

Automatic tissue classification and assignment of blood perfusion rates could be used for defining the tumor geometry and parameters. Such a system, as currently used by Roemer at the University of Arizona, would use information from CAT (computer aided tomography) scans and diagnostic ultrasound to determine tissue types and geometries. Noninvasive means of blood perfusion and temperature measurement would also aid in the clinical usage of this model.

9.3 Required Power Deposition Pattern Formation

An efficient method for closely approximating the

required power deposition pattern by using a scanned phased array system needs to be determined. It is expected that an iterative approach is necessary, although a more direct approach, such as using a Fourier transform, would be preferred. Difficulties with an iterative approach would include selecting an appropriate measure of the matching of the required power deposition pattern and determining when a satifactory solution has been obtained. Alternative schemes for phasing the elements of the array, such as partial excitation of the array or enlarged focus formation, need to be considered further.

9.4 Construction and Testing of Practical Linear Phased Array Applicator

A prototype linear phased array applicator needs to be built to test the theoretically derived design constraints. Deviations in the focal pattern from the theoretical results need to be considered when determining a suitable scan path or focus formation to approximate the required power deposition pattern discussed in Chapters 3 and 4. Nonlinear effects need to be measured and compared with theory (Goss and Fry, 1981).

9.5 A Two Dimensional Array Design

Two dimensional phased array designs should be investigated further. One approach to simplifying the construction of a two dimensional array is to use a small

number of amplifiers to produce the desired frequency with all possible required phases. The actual phases required on each element can be quantized to the nearest 45 degrees without significant degradation of the focus (Ocheltree, 1984), so that only eight amplifiers would be required. The phase for each element would then be selected from the eight available phase shifted signals.

The selection of the phase for each element requires three bits. These three bits could be determined by filling an array of shift registers with the appropriate phasing information. To move the focus laterally the width of one element, the phase information would be shifted in the registers in the same direction. Scanning using such a method would be done sequentially in planes parallel to the face of the applicator. To scan in a plane at a different depth from the applicator surface, new phase information would be shifted in from the edge of the array of registers to provide focusing at the new depth.

The hardware requirements for this design of a two dimensional phased array controlling system are extensive, but not impractical. A 32 by 32 element array with 3 bits of phase information would require 8 amplifers, 1024 analog multiplexers, and 384 shift registers. In addition, enough memory would be required to store the phasing information for a single focus at each desired scan depth. The system would be complicated, but the benefits of electronic focusing and scanning and the high gain possible from a two dimensional array make the system worthy of consideration.

APPENDIX A

RECTANGULAR SOURCE FIELD PROGRAM

```
C  PROGRAM TO CALCULATE FIELD FOR RECTANGULAR SOURCE.
C  DIMENSIONS ARE IN WAVELENGTHS.
C  WRITTEN 6/24/84 BY K. B. OCHELTREE.
C  MODIFIED 11/20/86 BY K. B. OCHELTREE.
C
C  DIMENSIONS ARE AC(NX,NZ),Z(NX,NZ).
      COMPLEX AC(41,80),WT,EXPARG,TEMP
      DIMENSION Z(41,80)
      DATA PI/3.1415926536/
C
C  SI1 IS LENGTH OF SIDE IN X DIRECTION.
C  SI2 IS LENGTH OF SIDE IN Y DIRECTION.
C  XS IS X STARTING LOCATION.
C  ZS IS Z STARTING LOCATION.
C  NX IS NUMBER OF X FIELD POINTS.
C  NZ IS NUMBER OF Z FIELD POINTS.
C  XST,ZST ARE THE STEP SIZES BETWEEN POINTS.
      DATA NX,NZ/41,80/
C
      WRITE(6,100)
 100  FORMAT(' ENTER SIDE LENGTHS:'$)
      READ(5,*)SI1
      READ(5,*)SI2
      XS=-0.5*SI1
      XST=SI1/FLOAT(NX-1)
      ZST=SI1**2/FLOAT(NZ)
      ZS=ZST
      FAR=10.
      CAK=2.*PI
      DO 200 J=1,NZ
      DO 200 I=1,NX
 200  AC(I,J)=CMPLX(0..0.)
C
C  CALCULATE FIELD.
      XD=SI1/2.+XS
      YD=0.
      ZD=ZS
      NHD2L=1000
      SNW=XD
      DO 960 IZ=1,NZ
        NH=2+INT(SI2/SQRT(ZD/FAR))
        NHD2=NH/2
        IF(NHD2.GT.100)NHD2=100
        IF(NHD2 .EQ. NHD2L)GO TO 840
        YINC=SI2/FLOAT(NHD2*2)
        CNSTY=PI*YINC
 840    YD=YD+YINC/2.
        NW=1+INT(SI1/SQRT(ZD/FAR))
        IF(NW.GT.200)NW=200
        XINC=SI1/FLOAT(NW)
```

```
          CNSTX=PI*XINC
             XD=XD-XINC/2.
             WT=CMPLX(XINC*YINC,0.)
             SNH=YD
             DO 920 L=1,NW
                SNX=XD
                DO 900 M=1,NHD2
                   DO 880 IX=1,NX
                      ARG=SQRT(XD**2+YD**2+ZD**2)
                      XARG=CNSTX*XD/ARG
                      SINCX=1.
                      IF(ABS(XARG) .GT. .0001)SINCX=SIN(XARG)/XARG
                      YARG=CNSTY*YD/ARG
                      SINCY=1.
                      IF(ABS(YARG) .GT. .0001)SINCY=SIN(YARG)/YARG
                      EXPARG=CEXP(CMPLX(0.,-ARG*CAK))
                      TEMP=EXPARG*WT*CMPLX(SINCX*SINCY/ARG,0.)
                      AC(IX,IZ)=AC(IX,IZ)+TEMP
                      XD=XD+XST
  880              CONTINUE
                   XD=SNX
                   YD=YD+YINC
  900           CONTINUE
                YD=SNH
                XD=XD-XINC
  920        CONTINUE
             XD=SNW
             YD=0.
             ZD=ZD+ZST
             NHD2L=NHD2
  960   CONTINUE
C
C  FIND MAXIMUM AND NORMALIZE.
             DO 20 IZ=1,NZ
             ZMAX=0.0
             DO 10 IX=1,NX
             Z(IX,IZ)=CABS(AC(IX,IZ))
             ZMAX=AMAX1(Z(IX,IZ),ZMAX)
    10       CONTINUE
             DO 20 IX=1,NX
             Z(IX,IZ)=20.*ALOG10(Z(IX,IZ)/ZMAX)
    20       CONTINUE
C
C  CONTOUR PLOT OF FIELD.
          CALL CONREC(Z,NX,NX,NZ,-6.,-3.,3..0,-1,0)
          CALL FLUSH
          STOP
          END
```

APPENDIX B

PHASED ARRAY FIELD PROGRAM

```
C   PROGRAM TO CALCULATE ARRAY OF POINTS FOR MAKING A CONTOUR PLOT.
C   THIS HANDLES MULTIPLE FOCAL LOCATIONS PRODUCED BY LINEAR
C   PHASED ARRAY.
C   WRITTEN 5/16/85 BY KEN OCHELTREE.
C
C   DIMENSIONS ARE Z(NX,NZ),AC(NX,NZ),XF(NF),YF(NF),ZF(NF).
       DIMENSION XF(20),YF(20),ZF(20),Z(60,60)
       COMPLEX AC(60,60)
C
C   SET ARRAY PARAMETERS.
C   FR IS FREQUENCY IN KHZ.
C   AT IS ATTENUATION AT 1 MHZ IN NEPERS/CM.
C   NE IS NUMBER OF ELEMENTS IN ARRAY.
C   HT IS HEIGHT OF ARRAY ELEMENTS IN MM.
C   WI IS WIDTH OF ARRAY ELEMENTS IN MM.
C   SP IS CENTER TO CENTER SPACING OF ELEMENTS IN MM.
C   IQ IS NUMBER OF BITS QUANTIZATION (IQ=0 MEANS NO QUANTIZATION).
       DATA FR,AT,NE,HT,WI,SP,IQ/400.,.08,64,45.,3.,3.125,0/
C
C   SET FOCUS LOCATION PARAMETERS.
C   NF IS NUMBER OF POINTS IN SCAN PATH.
C   TI IS ARRAY OF TIMES AT EACH SCAN POINT.
C   XF IS VECTOR OF X FOCUS LOCATIONS.
C   YF IS VECTOR OF Y FOCUS LOCATIONS.
C   ZF IS VECTOR OF Z FOCUS LOCATIONS.
       DATA NF,XF(1),YF(1),ZF(1)/7,0.,0..100./
       DATA XF(2),YF(2),ZF(2)/2.4,0.,100./
       DATA XF(3),YF(3),ZF(3)/-2.4,0.,100./
       DATA XF(4),YF(4),ZF(4)/4.8,0.,100./
       DATA XF(5),YF(5),ZF(5)/-4.8,0.,100./
       DATA XF(6),YF(6),ZF(6)/7.2,0.,100./
       DATA XF(7),YF(7),ZF(7)/-7.2,0.,100./
C
C   SET FIELD POINT LOCATION PARAMETERS.
C   XS IS X STARTING LOCATION.
C   YS IS Y STARTING LOCATION.
C   ZS IS Z STARTING LOCATION.
C   NX IS NUMBER OF X FIELD POINTS.
C   NZ IS NUMBER OF Z FIELD POINTS.
C   ST IS THE STEP SIZE BETWEEN POINTS.
       DATA XS,YS,ZS,NX,NZ,ST/-30.,0.,70.,60,60,1./
C
C   LOOP ON NUMBER OF FOCUS LOCATIONS.
       ZMAX=0.0
       DO 5 IZ=1,NZ
       DO 5 IX=1,NX
       Z(IX,IZ)=0.0
  5    CONTINUE
       DO 20 I=1,NF
       CALL FXZ(FR,AT,NE,HT,WI,SP,IQ,XF(I),YF(I),ZF(I),
```

```
     1XS,YS,ZS,NX,NZ,ST,AC)
          DO 15 IX=1,NX
          DO 10 IZ=1,NZ
          Z(IX,IZ)=Z(IX,IZ)+CABS(AC(IX,IZ))**2
          ZMAX=AMAX1(ZMAX,Z(IX,IZ))
 10       CONTINUE
 15       CONTINUE
  20   CONTINUE
       DO 60 I=1,NX
       DO 60 J=1,NZ
       Z(I,J)=Z(I,J)/ZMAX
 60    CONTINUE
C
C  CONTOUR PLOT.
       CALL CONREC(Z,NX,NX,NZ,0.,1.,.1,0,-1,-682)
       CALL FLUSH
       STOP
       END
C
C  SUBROUTINE TO CALCULATE FIELD PRODUCED BY ONE FOCAL POINT.
       SUBROUTINE FXZ(FR,AT,NE,HT,WI,SP,IQ,XF,YF,ZF,XS,YS,ZS,
      &NX,NZ,ST,PC)
       COMPLEX RAI(128),PC(NX,NZ),WT,EXPARG,TEMP
       DATA PI/3.1415926536/
       FAR=5.
       WAVE=1500./FR
       PIDW=PI/WAVE
       CAK=2.*PIDW
       SPACT=FLOAT(NE-1)*SP
       ATT=AT*(FR/1000.)**1.1
C  CONVERT ATTEN TO NP/MM.
       ATT=ATT/10.
       IQQ=2**IQ
C  CALCULATE PHASES FOR ELEMENTS TO ACHIEVE A FOCUS.
       XVAL=-SPACT/2.
       DO 680 I=1,NE
          RDIST=SQRT((XF-XVAL)**2+ZF**2)
          CAR=CAK*RDIST
          XVAL=XVAL+SP
          IF(IQQ .EQ. 1)GO TO 660
          CAR=2.*PI*AINT(.5+FLOAT(IQQ)*CAR/(2.*PI))/FLOAT(IQQ)
 660      CONTINUE
          RAI(I)=CMPLX(COS(CAR),SIN(CAR))
 680   CONTINUE
C
C INITIALIZE ARRAY.
       DO 760 J=1,NZ
       DO 760 I=1,NX
 760   PC(I,J)=CMPLX(0..0.)
C
C  CALCULATE FIELD.
       XA=-SPACT/2.
       ZD=ZS
       DO 1000 IZ=1,NZ
         NH=1+INT(HT/SQRT(WAVE*ZD/FAR))
```

```
      YINC=HT/FLOAT(NH)
      CNSTY=PIDW*YINC
      NW=1+INT(WI/SQRT(WAVE*ZD/FAR))
      XINC=WI/FLOAT(NW)
      CNSTX=PIDW*XINC
      AREA=XINC*YINC
      XP=XS
      DO 980 IX=1,NX
          XNE=XA
          DO 940 IE=1,NE
            WT=RAI(IE)*AREA
            XE=(XINC-WI)/2.
            DO 920 IW=1,NW
              YE=(YINC-HT)/2.
              XD=XP-(XNE+XE)
              DO 900 IH=1,NH
                YD=YS-YE
                ARG=SQRT(XD**2+YD**2+ZD**2)
                XARG=CNSTX*XD/ARG
                SINCX=1.
                IF(ABS(XARG) .GT. .0001)SINCX=SIN(XARG)/XARG
                YARG=CNSTY*YD/ARG
                SINCY=1.
                IF(ABS(YARG) .GT. .0001)SINCY=SIN(YARG)/YARG
                EXPARG=CEXP(CMPLX(-ARG*ATT,-ARG*CAK))
                TEMP=EXPARG*WT*CMPLX(SINCX*SINCY/ARG,0.)
                PC(IX,IZ)=PC(IX,IZ)+TEMP
                YE=YE+YINC
900           CONTINUE
              XE=XE+XINC
920         CONTINUE
            XNE=XNE+SP
940       CONTINUE
        XP=XP+ST
980   CONTINUE
      ZD=ZD+ST
1000  CONTINUE
      RETURN
      END
```

APPENDIX C

THREE DIMENSIONAL BIOHEAT TRANSFER PROGRAM

```
C  PROGRAM TO CALCULATE THE NECESSARY HEATING FOR A UNIFORM
C  TUMOR TEMP OF 43 DEGREES.
C  THIS PROGRAM IS FOR A SPHERICAL TUMOR.
C  BASED ON PROGRAM BY CHARLES CAIN.
C  ENTERED 11/1/84 BY KEN OCHELTREE.
      PARAMETER (IM=60,JM=60,KM=60,IMM1=59,JMM1=59,KMM1=59)
      PARAMETER (DT=.0001,G=1.86,G1=-.86)
      DIMENSION T(IM,JM,KM),WQ(IM,JM,KM)
      DIMENSION X(JM),Y(JM)
C
C  SET CONSTANTS.
C
C  SET STEP SIZE.
      DX=0.002
C  SET TUMOR SIZE.
      TRAD=10.
      R2=TRAD**2
      XCEN=FLOAT(IM+1)/2.
      YCEN=FLOAT(JM+1)/2.
      ZCEN=FLOAT(KM+1)/2.
C  SET THERMAL CONDUCTIVITY PARAMETERS (W/DEG/M).
      CK=0.55
C  SET BLOOD FLOW PARAMETERS (KG/M**3/SEC).
      WB=1.67
C  SET TEMPERATURE AT BOUNDARY.
      TB=37.
      TS=25.
      TSB=TS-TB
C  SET BLOOD SPECIFIC HEAT (W/DEG/KG).
      CB=4000.
C  SET OVER-RELAXATION GAIN (1<G<2).
C     G=1.86
C     G1=1.-G
C  SET CONVERGENCE CRITERIA.
C     DT=0.01
C
C  CALCULATE FLOATING POINT CONSTANTS.
C
      DX2=DX*DX
      A=DX2/CK
      WCA=WB*CB*A
      CS=G/(6.+WCA)
C
C  ZERO POWER DISTRIBUTION MATRIX.
      DO 160 K=1,KM
      DO 160 J=1,JM
      DO 160 I=1,IM
 160  WQ(I,J,K)=0.
C
C  SET INITIAL VALUE FOR TEMPERATURE AT NODES.
```

```
      DO 100 J=1,JM
      DO 100 K=1,KM
 100  T(1,J,K)=TSB
      DO 101 K=1,KM
      ZR=FLOAT(K)-ZCEN
      DO 101 J=1,JM
      YR=FLOAT(J)-YCEN
      DO 101 I=2,IM
      XR=FLOAT(I)-XCEN
      T(I,J,K)=0.
      IF(XR**2+YR**2+ZR**2.LE.R2)T(I,J,K)=6.0
 101  CONTINUE
C
C  ITERATION LOOP.
      LOOP=0
 199  NN=0
C  CALCULATE NORMAL TISSUE TEMPERATURE AND TUMOR TEMPERATURE.
      DO 220 K=1,KM
      KM1=K-1
      KP1=K+1
      IF(KM1.EQ.0)KM1=2
      IF(K.EQ.KM)KP1=KMM1
      DO 215 J=1,JM
      JM1=J-1
      JP1=J+1
      IF(JM1.EQ.0)JM1=2
      IF(J.EQ.JM)JP1=JMM1
      DO 210 I=2,IMM1
      IF(T(I,J,K).EQ.6.0)GOTO 210
      TOLD=T(I,J,K)
      T(I,J,K)=CS*(T(I,J,KP1)+T(I,J,KM1)+T(I,JP1,K)+T(I,JM1,K)
     1+T(I+1,J,K)+T(I-1,J,K)+WQ(I,J,K))+G1*TOLD
      IF(ABS(T(I,J,K)-TOLD).GT.DT)NN=NN+1
 210  CONTINUE
      TOLD=T(IM,J,K)
      T(IM,J,K)=CS*(T(IM,J,KP1)+T(IM,J,KM1)+T(IM,JP1,K)
     1+T(IM,JM1,K)+T(IMM1,J,K)+T(IMM1,J,K)+WQ(IM,J,K))+G1*TOLD
      IF(ABS(T(IM,J,K)-TOLD).GT.DT)NN=NN+1
 215  CONTINUE
 220  CONTINUE
      LOOP=LOOP+1
      WRITE(6,*)LOOP,NN
      IF(NN.GT.0)GO TO 199
      DO 300 K=1,KM
      DO 300 J=1,JM
      DO 300 I=1,IM
      T(I,J,K)=T(I,J,K)+TB
 300  CONTINUE
C
C  CONTOUR PLOT DATA.
C
      CALL CONREC(T(1,10,KM/2),IM,50,41,25.1,100.1,0.5,0,0,0)
      CALL FRAME
C  INVERT TEMP TO FIND POWER.
      DO 320 K=1,KM
```

```
      DO 320 J=1,JM
      DO 320 I=1,IM
320   T(I,J,K)=T(I,J,K)-TB
      DO 700 K=2,KMM1
      DO 700 J=2,JMM1
      DO 700 I=2,IMM1
      WQ(I,J,K)=((6.+WCA)*T(I,J,K)-T(I-1,J,K)-T(I+1,J,K)-
     1T(I,J-1,K)-T(I,J+1,K)-T(I,J,K-1)-T(I,J,K+1))/A
      IF(WQ(I,J,K).LT.0.)WQ(I,J,K)=0.
700   CONTINUE
      WRITE(1)((WQ(I,J,KM/2),I=1,IM),J=1,JM)
      CALL EZCNTR(WQ(1,1,KM/2),IM,JM)
      CALL FLUSH
      STOP
      END
```

APPENDIX D

LINEAR BIOHEAT TRANSFER PROGRAM

```
C   PROGRAM TO CALCULATE TEMPS IN HALF-SPACE MODEL.
C   BASED ON PROGRAM BY CHARLES CAIN.
C   ENTERED 1/23/84 BY KEN OCHELTREE.
      DIMENSION X(602),T(301),TT(301),WQ(301),WQT(301),C(301)
      DIMENSION BAS(302),FN(3),WB(301)
      DIMENSION TEMP(322)
      FN(1)=160.
      FN(2)=160.
      FN(3)=2.
      JMAX=301
      JST=201
      JT=200
C   SET THERMAL CONDUCTIVITY PARAMETERS (W/DEG/M).
      CKM=0.55
C   SET BLOOD FLOW PARAMETERS (KG/M**3/SEC).
      WBM=1.67
      TB=37.
C   SET BLOOD SPECIFIC HEAT (W/DEG/KG).
      CB=4000.
C   SET STEP SIZE.
      DX=0.001
C   SET OVER-RELAMATION GAIN (1<G<2).
      G=1.86
      G1=G-1.
C   SET CONVERGENCE CRITERIA.
      DT=0.001
C   SET PARAMETER FOR STOPPING ITERATION.
      NSTOP=0
C   ZERO POWER DISTRIBUTION.
      DO 150 J=1,JMAX
 150  WQ(J)=0.
C
C   CALCULATE FLOATING POINT CONSTANTS.
      DX2=DX*DX
      AM=DX2/CKM
C
C   MAKE MULTIPLIER MATRIX.
      DO 164 J=1,160
      X(J)=FLOAT(J-100)*DX*100.
 164  X(J+160)=X(J)
      DO 165 J=1,JMAX
      WB(J)=WBM
      IF(J.GT.JT)GOTO 165
      XX=9.4*100*DX*FLOAT(J-200)/4.0
      WB(J)=.1666667
      IF(XX.LE.-9.4)GOTO 165
      WB(J)=4.16666-15.625*(XX+.4)**2
      IF(XX.LT.-.4)WB(J)=2.916666-1.25*COSD(180.*(XX-.6))
      IF(XX.LE.-.9)WB(J)=3.187924068E0-3.021257402E0*SQRT(1-
     1(XX+9.4)**2/72.83713857E0)
```

```
 165  C(J)=G*1./(2.+CB*AM*WB(J))
C
C  MODIFY POWER DISTRIBUTION MATRIX.
 175  CONTINUE
      DO 180 J=1,JMAX
 180  WQ(J)=WQ(J)*AM
C
C  SET INITIAL VALUE FOR TEMPERATURE AT NODES.
C
      DO 101 J=1,JMAX
      T(J)=0.
      IF(J.LE.200)T(J)=6.
 101  CONTINUE
C
C  ITERATION LOOP.
      LOOP=0
 199  NN=0
C  CALCULATE NORMAL TISSUE TEMPERATURE AND TUMOR TEMPERATURE.
      DO 220 J=JST,JMAX-1
      XIJ=C(J)*(T(J+1)+T(J-1)+WQ(J))-G1*T(J)
      IF(ABS(XIJ-T(J)).GT.DT)NN=NN+1
 220  T(J)=XIJ
      LOOP=LOOP+1
      WRITE(6,666)LOOP,NN
 666  FORMAT(' ',2I5)
      IF(NN.GT.NSTOP)GO TO 199
C
C  INVERT TEMPERATURE DISTRIBUTION TO FIND POWER.
      DO 760 J=2,JMAX-1
      WQT(J)=G*T(J)/C(J)-T(J+1)-T(J-1)
 760  CONTINUE
      WQT(1)=G*T(1)/C(1)-2.*T(2)
      WQT(301)=WQT(300)
      DO 780 J=1,JMAX
 780  WQT(J)=WQT(J)/AM
      DO 750 J=1,JMAX
      T(J)=T(J)+TB
 750  CONTINUE
      IF(JST.EQ.2)GOTO 222
      DO 770 J=1,160
      TT(J)=T(J+100)
 770  CONTINUE
C
C  CODE FOR BASIS FUNCTION WEIGHTING
C
      JST=2
      WRITE(6,500)
 500  FORMAT(' ENTER 3DB WIDTH OF BASIS FUNCTION IN MM:'$)
      READ(5,*)X3DB
      CONST=1.3011224*X3DB
      WRITE(6,501)
 501  FORMAT(' ENTER SPACING OF BASIS FUNCTION IN MM:'$)
      READ(5,*)SPACE
      WRITE(6,502)
 502  FORMAT(' ENTER SHIFT FOR CENTER OF BASIS IN MM:'$)
```

```
      READ(5,*)SHIFT
      BAS(1)=1.
      POW=BAS(1)
      DO 151 I=1,301
      BAS(I+1)=EXP(-1.*(FLOAT(I)/CONST)**2)
      POW=POW+2.*BAS(I+1)
  151 CONTINUE
      DO 152 I=1,302
  152 BAS(I)=BAS(I)/POW
      IFIN=INT(SPACE/2.)
      DO 300 I=200+SHIFT,1,-SPACE
      WT=WQT(I)
      IF(IFIN.EQ.0)GOTO 153
      DO 153 K=1,IFIN
      WEV=1.0
      IF(SPACE/FLOAT(IFIN).EQ.2..AND.K.EQ.IFIN)WEV=0.5
      IF(I-K.LE.0)GOTO 153
      WT=WT+WEV*(WQT(I-K)+WQT(I+K))
  153 CONTINUE
      DO 300 J=1,301
      IARG=1+IABS(I-J)
      WQ(J)=WQ(J)+WT*BAS(IARG)
  300 CONTINUE
      DO 302 J=1,160
      IF(WQ(J+100).LT.0.0)WQ(J+100)=0.
      IF(WQT(J+100).LT.0.0)WQT(J+100)=0.
      TEMP(J)=.000001*WQ(J+100)
  302 TEMP(J+160)=.000001*WQT(J+100)
      CALL DIFYPLT(X,TEMP,-2,FN,' ','DISTANCE (cm)',
     1'POWER DEPOSITION (W/cm**3)',1.,2.5,4.2,4.8)
      GOTO 175
  222 CONTINUE
      DO 303 J=1,160
      TEMP(J)=T(J+100)
  303 TEMP(J+160)=TT(J)
      TEMP(321)=37.
      TEMP(322)=44.
      X(321)=-10.
      X(322)=-10.
      CALL DIFYPLT(X,TEMP,3,FN,' ','DISTANCE (cm)',
     1'TEMPERATURE (oC)',4.7,0.,4.2,4.8)
      CLOSE(98,DISP='PRINT/DELETE')
      STOP
      END
```

APPENDIX E

CYLINDRICAL BIOHEAT TRANSFER PROGRAM

```
C   PROGRAM FROM CHARLES CAIN TO CALCULATE STEADY STATE
C   TEMPERATURE DISTRIBUTIONS IN A TWO-DIMENSIONAL
C   MULTI-LAYERED CYLINDRICAL MODEL.
C   ENTERED 1/23/84 BY KEN OCHELTREE.
      DIMENSION SCAN(101,141),T(141,101),WQ(141,101),C(141,101)
      DIMENSION TEMP(101,141)
C
C   SET CONSTANTS.
C
C   SET GEOMETRICAL PARAMETERS OF CYLINDRICAL MODEL (M).
      RMAX=0.099
      ZMAX=0.140
      RTUM=0.03
      ZTUM=0.06
      ZCEN=0.08
      ZR1=0.003
      ZR2=0.003
      ZS=0.000
      ZF=0.020
      ZM=0.030
C   SET THERMAL CONDUCTIVITY PARAMETERS (W/DEG/M).
      CKS=0.55
      CKF=0.55
      CKM=0.55
      CKV=0.55
      CK1=0.55
      CK2=0.55
      CK3=0.55
C   SET BLOOD FLOW PARAMETERS (KG/M**3/SEC).
      WBS=1.667
      WBF=1.667
      WBM=1.667
      WBV=1.667
      WB1=1.667
      WB2=1.667
      WB3=1.667
C   SET TEMPERATURE AT BOUNDARY.
      TB=37.
      TS=25.
      TSB=TS-TB
C   SET BLOOD SPECIFIC HEAT (W/DEG/KG).
      CB=4000.
C   SET STEP SIZE.
      D=0.001
C   SET OVER-RELAXATION GAIN (1<G<2).
      G=1.86
      G1=G-1.
C   SET CONVERGENCE CRITERIA.
      CC=0.001
C   SET BLOOD SPECIFIC HEAT (W/DEG/KG).
```

```
      CB=4000.
C   SET PARAMETER FOR STOPPING ITERATION.
      NSTOP=2
C
C   CALCULATE INTEGER GEOMETRICAL LIMIT CONSTANTS.
C
      IMAX=ZMAX/D+1.5
      JMAX=RMAX/D+1.5
      IS=ZS/D+1.
      IF=ZF/D+.5+IS
      IM=ZM/D+.5+IF
      IZ=ZCEN/D+1.5
      IZZ=ZTUM/D/2.+.5
      IZR1=ZR1/D+.5
      IZR2=ZR2/D+.5
      I1=IZ-IZZ
      I2=I1+IZR1
      I3=I2+IZR2
      I6=IZ+IZZ
      I5=I6-IZR1
      I4=I5-IZR2
      J3=RTUM/D+1.5
      J2=J3-IZR1
      J1=J2-IZR2
C
C   READ IN POWER DISTRIBUTION.
C
      READ(1)SCAN
      CALL CONREC(SCAN,101,101,141,0.1,0.9,0.1,0,-1,0)
      CALL FRAME
      DO 150 J=1,101
      DO 150 I=1,141
      WQ(I,J)=100000.*SCAN(J,I)
 150  IF(I.LT.IF)WQ(I,J)=WQ(I,J)/3.
C
C   CALCULATE FLOATING POINT CONSTANTS.
C
      DD=D*D
      AS=DD/CKS
      AF=DD/CKF
      AM=DD/CKM
      AV=DD/CKV
      A1=DD/CK1
      A2=DD/CK2
      A3=DD/CK3
C
      WCAS=WBS*CB*AS
      WCAF=WBF*CB*AF
      WCAM=WBM*CB*AM
      WCAV=WBV*CB*AV
      WCA1=WB1*CB*A1
      WCA2=WB2*CB*A2
      WCA3=WB3*CB*A3
C
      CS=1./(4.+WCAS)
```

```
      CF=1./(4.+WCAF)
      CM=1./(4.+WCAM)
      CV=1./(4.+WCAV)
      C1=1./(4.+WCA1)
      C2=1./(4.+WCA2)
      C3=1./(4.+WCA3)
C
      CS0=1./(6.+WCAS)
      CF0=1./(6.+WCAF)
      CM0=1./(6.+WCAM)
      CV0=1./(6.+WCAV)
      C10=1./(6.+WCA1)
      C20=1./(6.+WCA2)
      C30=1./(6.+WCA3)
C
C  MAKE MULTIPLIER MATRIX.
C
      DO 160 I=1,IMAX
      CX=CV0
      IF(I.LE.IM)CX=CM0
      IF(I.LE.IF)CX=CF0
      IF(I.LE.IS)CX=CS0
      IF(I.GE.I1.AND.I.LE.I6)CX=C10
      IF(I.GE.I2.AND.I.LE.I5)CX=C20
      IF(I.GE.I3.AND.I.LE.I4)CX=C30
 160  C(I,1)=CX*G
      DO 165 J=2,JMAX
      DO 165 I=1,IMAX
      CX=CV
      IF(I.LE.IM)CX=CM
      IF(I.LE.IF)CX=CF
      IF(I.LE.IS)CX=CS
      IF(I.GE.I1.AND.I.LE.I6.AND.J.LE.J3)CX=C1
      IF(I.GE.I2.AND.I.LE.I5.AND.J.LE.J2)CX=C2
      IF(I.GE.I3.AND.I.LE.I4.AND.J.LE.J1)CX=C3
 165  C(I,J)=CX*G
C
C  MODIFY POWER DISTRIBUTION MATRIX.
C
      DO 180 J=1,JMAX
      DO 180 I=1,IMAX
      AX=AV
      IF(I.LE.IM)AX=AM
      IF(I.LE.IF)AX=AF
      IF(I.LE.IS)AX=AS
      IF(I.GE.I1.AND.I.LE.I6.AND.J.LE.J3)AX=A1
      IF(I.GE.I2.AND.I.LE.I5.AND.J.LE.J2)AX=A2
      IF(I.GE.I3.AND.I.LE.I4.AND.J.LE.J1)AX=A3
 180  WQ(I,J)=WQ(I,J)*AX
C
C  SET INITIAL VALUE FOR TEMPERATURE AT NODES.
C
      DO 100 J=1,JMAX
 100  T(1,J)=TSB
      DO 101 J=1,JMAX
```

```
      DO 101 I=2,IMAX
 101  T(I,J)=0.
C
C  ITERATION LOOP.
C
 198  LOOP=0
C CALCULATE TEMPERATURE ON CENTER AXIS.
 199  NN=0
      DO 200 I=2,IMAX-1
      TIJ=T(I,1)
      XIJ=C(I,1)*(4.*T(I,2)+T(I-1,1)+T(I+1,1)+WQ(I,1))-G1*TIJ
      IF(ABS(XIJ-TIJ).GT.CC)NN=NN+1
 200  T(I,1)=XIJ
C  CALCULATE NORMAL TISSUE TEMPERATURE AND TUMOR TEMPERATURE.
      DO 225 J=2,JMAX-1
      DR=1./((J-1)*2)
      DR0=1.-DR
      DR1=1.+DR
      DO 220 I=2,IMAX-1
      TIJ=T(I,J)
      XIJ=C(I,J)*(T(I,J+1)*DR1+T(I,J-1)*DR0+T(I+1,J)+T(I-1,J)
     1+WQ(I,J))-G1*TIJ
      IF(ABS(XIJ-TIJ).GT.CC)NN=NN+1
 220  T(I,J)=XIJ
      TIJ=T(IMAX,J)
      XIJ=C(IMAX,J)*(T(IMAX,J+1)*DR1+T(IMAX,J-1)*DR0+2.*
     1T(IMAX-1,J)+WQ(IMAX,J))-G1*TIJ
      IF(ABS(XIJ-TIJ).GT.CC)NN=NN+1
      T(IMAX,J)=XIJ
 225  CONTINUE
      DO 230 I=2,IMAX-1
      TIJ=T(I,JMAX)
      XIJ=C(I,JMAX)*(T(I,JMAX-1)*2.+T(I+1,JMAX)+T(I-1,JMAX)
     1+WQ(I,JMAX))-G1*TIJ
      IF(ABS(XIJ-TIJ).GT.CC)NN=NN+1
      T(I,JMAX)=XIJ
 230  CONTINUE
      LOOP=LOOP+1
      WRITE(6,666)LOOP,NN
 666  FORMAT(' ',2I5)
      IF(NN.GT.NSTOP)GO TO 199
      WRITE(6,*)T(IZ,1),NN
C
C  CHECK TEMPERATURE AT CENTER.
C  IF NOT 6 C, ADJUST POWER.
      IF(ABS(T(IZ,1)-6.).LT..1)GOTO 197
      FAC=6./T(IZ,1)
      DO 196 I=1,IMAX
      DO 196 J=1,JMAX
 196  WQ(I,J)=FAC*WQ(I,J)
      GOTO 198
 197  CONTINUE
C
C  CONTOUR PLOT DATA.
      DO 456 I=1,IMAX
```

```
      DO 456 J=1,JMAX
      TEMP(J,I)=T(I,J)+TB
456   CONTINUE
      CALL CONREC(TEMP,101,JMAX,IMAX,25.,65.,1.,0,-1,0)
      CALL FLUSH
      STOP
      END
```

APPENDIX F

BONE HEATING MODELING PROGRAM

```
C  PROGRAM TO CALCULATE TEMPS FOR FAT/MUSCLE/BONE MODEL.
C  ENTERED 11/14/86 BY KEN OCHELTREE.
      DIMENSION X(402),T(201),TT(201),Q(201),WQ(201),C(201)
      DIMENSION FN(2),WB(201)
      DIMENSION TEMP(322)
      FN(1)=150.0
      JF=30
      JM1=40
      JT=90
      JM2=110
      JB=120
      JBM=140
      JMAX=150
      TFAT=.03
      TMUS=.08
C
C  SET CONSTANTS.
C
C  SET THERMAL CONDUCTIVITY PARAMETERS (W/DEG/M).
      CKF=0.21
      CKM=0.55
      CKB=.44
      CKBM=.44
C  SET BLOOD FLOW PARAMETERS (KG/M**3/SEC).
      WBF=0.41667
      WBM=1.667
      WBB=0.
      WBBM=.8
      TB=37.
C  SET BLOOD SPECIFIC HEAT (W/DEG/KG).
      CB=4000.
C  SET STEP SIZE.
      D=0.001
C  SET OVER-RELAXATION GAIN (1<G<2).
      G=1.86
      G1=G-1.
C  SET CONVERGENCE CRITERIA.
      DT=0.001
C  SET PARAMETER FOR STOPPING ITERATION.
      NSTOP=0
C
C  CALCULATE FLOATING POINT CONSTANTS.
      DX2=D*D
      AF=DX2/CKF
      AM=DX2/CKM
      AB=DX2/CKB
      ABM=DX2/CKBM
C
C  SET POWER DISTRIBUTION.
 777  CALL LAYERS(TFAT,TMUS,Q)
```

```
      DO 150 J=1,JMAX
 150  WQ(J)=100000.*Q(J)
C
C  MODIFY POWER DISTRIBUTION MATRIX.
 175  CONTINUE
      DO 180 J=1,JMAX
      AX=AB
      IF(J.LE.JM2)AX=AM
      IF(J.LE.JF)AX=AF
 180  WQ(J)=WQ(J)*AX
C
C  MAKE MULTIPLIER MATRIX.
      DO 165 J=1,JMAX
      X(J)=.1*FLOAT(J-1)
      AX=ABM
      WB(J)=WBBM
      IF(J.GT.JB.AND.J.LE.JBM)GOTO 165
      AX=AB
      WB(J)=WBB
      IF(J.GT.JM2)GOTO 165
      AX=AF
      WB(J)=WBF
      IF(J.LE.JF)GOTO 165
      AX=AM
      WB(J)=WBM
      IF(J.LE.JM1.OR.J.GT.JT)GOTO 165
      XX=9.4*(ABS(FLOAT(J-(JT+JM1)/2)*2./FLOAT(JM1-JT))-1.)
      WB(J)=4.16666-15.625*(XX+.4)**2
      IF(XX.LT.-.4)WB(J)=2.916666-1.25*COSD(180.*(XX-.6))
      IF(XX.LE.-.9)WB(J)=3.187924068E0-3.021257402E0*SQRT(1-
     1(XX+9.4)**2/72.83713857E0)
 165  C(J)=G*1./(2.+CB*AX*WB(J))
C
C  SET INITIAL VALUE FOR TEMPERATURE AT NODES.
C
      DO 101 J=1,JMAX
      T(J)=0.
 101  CONTINUE
      T(1)=-12.
C
C  ITERATION LOOP.
C
 198  LOOP=0
 199  NN=0
C  CALCULATE NORMAL TISSUE TEMPERATURE AND TUMOR TEMPERATURE.
      DO 220 J=2,JMAX-1
      XIJ=C(J)*(T(J+1)+T(J-1)+WQ(J))-G1*T(J)
      IF(ABS(XIJ-T(J)).GT.DT)NN=NN+1
 220  T(J)=XIJ
      LOOP=LOOP+1
      IF(NN.GT.NSTOP)GO TO 199
      JMID=(JM1+JT)/2
      WRITE(6,*)LOOP,NN,T(JMID)
      IF(ABS(T(JMID)-6.).LT.0.01)GOTO 197
      FAC=6./T(JMID)
```

```
      DO 196 J=1,JMAX
 196  WQ(J)=WQ(J)*FAC
      GOTO 198
C
 197  DO 750 J=1,JMAX
      T(J)=T(J)+TB
 750  CONTINUE
      CALL DIFYPLT(X,T,1,FN,' ',' ','TEMPERATURE (oC)',0.,
     13.,-6.0,5.)
      CLOSE(98,DISP='PRINT/DELETE')
      GOTO 777
      END
C  DISTANCES ARE IN CM IN THIS SUBROUTINE. INPUT IS IN M.
C AVERAGED OVER ALL ANGLES.
      SUBROUTINE LAYERS(TFAT,TMUS,Q)
      DIMENSION A(1005),D(1005),Q(201),QTEMP(201),X(201)
      WRITE(6,90)
  90  FORMAT(' ENTER: F(MHZ), # GAIN DIM, APP/TUM, HEAT DPTH:')
      READ(5,*)FR,ID,RA,DEP
      IF(FR.EQ.0.)STOP
      TF=TFAT*100.
      TM=TMUS*100.
      AF=.04*FR
      AFE=-.08*FR
      AM=.12*FR
      AME=-.24*FR
      AB=1.5*FR
      ABE=-3.*FR
      ASB=2.6*FR
      ASBE=-5.2*FR
      AMX=0.
      DO 100 I=1,1005
      D(I)=.02*FLOAT(I-1)
      IF(D(I).GT.TF+TM)GOTO 40
      IF(D(I).GT.TF)GOTO 20
C CALCULATE POWER DEPOSITION IN FAT.
      A(I)=AF*EXP(AFE*D(I))
     1+.04*AF*EXP(TF*AFE+AFE*(TF-D(I)))
     2+.26*.96*AF*EXP(TF*AFE+2.*TM*AME+AFE*(TF-D(I)))
      GOTO 60
C CALCULATE POWER DEPOSITION IN MUSCLE.
  20  A(I)=.96*AM*EXP(TF*AFE+AME*(D(I)-TF))
     1+.26*.96*AM*EXP(TF*AFE+TM*AME+AME*(TF+TM-D(I)))
      GOTO 60
C CALCULATE POWER DEPOSITION IN BONE.
  40  A(I)=.32*.96*AB*EXP(TF*AFE+TM*AME+ABE*(D(I)-TF-TM))
     1+.42*.96*ASB*EXP(TF*AFE+TM*AME+ASBE*(D(I)-TF-TM))
  60  AMX=AMAX1(AMX,A(I))
 100  CONTINUE
      DO 14 I=1,1005
  14  A(I)=A(I)/(1.+ABS(1.-D(I)/DEP)*(RA**(1./FLOAT(ID))-1.))**ID
      X(1)=0.
      Q(1)=(5./3.)*(A(1)+A(2)+A(3))
      QMAX=Q(1)
      DO 201 I=2,201
```

```
      X(I)=.1*FLOAT(I-1)
      N=5*(I-1)+1
      Q(I)=A(N-2)+A(N-1)+A(N)+A(N+1)+A(N+2)
201   QMAX=AMAX1(QMAX,Q(I))
      DO 202 I=1,201
202   QTEMP(I)=Q(I)/QMAX
      CALL DIFYPLT(X,QTEMP,-1,150.,' ','DISTANCE (cm)',
     1'RELATIVE POWER DEPOSITION',1.,2.5,6.0,2.6)
      RETURN
      END
```

APPENDIX G

FIXED FOCUS FIELD PROGRAM

```
C  PROGRAM TO CALCULATE THE PRESSURE FIELD PRODUCED BY A CIRCULAR
C  FOCUSED TRANSDUCER IN AN ATTENUATING MEDIUM.
C  WRITTEN 10/18/84 BY KENNETH OCHELTREE.
C  PROGRAM USES NCAR CONTOUR PLOTTING.
C  RESULTS ARE USED TO RUN CIRCSCAN.
C
      COMPLEX PC(101,181),EXC
      DIMENSION PM2(101,181)
C  DATA NECESSARY FOR RUNNING THIS PROGRAM IS
C  DIA       DIAMETER OF FOCUSED TRANSDUCER IN MM.
C  FR        FREQUENCY OF TRANSDUCER IN KHZ.
C  FOC       FOCAL DISTANCE OF TRANSDUCER IN MM.
C  NXP       NUMBER OF FIELD POINTS CALCULATED IN X DIRECTION.
C  XSP       INCREMENT BETWEEN ADJACENT X POINTS IN MM.
C  NZP       NUMBER OF FIELD POINTS CALCULATED IN Z DIRECTION.
C  ZST       MINIMUM Z FOR CALCULATED FIELD POINTS IN MM.
C  ZSP       INCREMENT BETWEEN ADJACENT Z POINTS IN MM.
C  ATT       ATTENUATION AT 1MHZ FOR MEDIUM IN NEPERS/CM.
      DATA  DIA,   FR,   FOC,   NXP,   XSP,    NZP,   ZST,   ZSP,   ATT/
     1    120.,  500.,120.,   101,    0.5,   181,   20.,    1.0,   .1/
      DATA PI/3.1405926536/
C
C  A SLICE THROUGH CENTER IS ENOUGH TO CHARACTERIZE ENTIRE FIELD.
      ATT=.1*ATT*(FR/1000.)**1.1
      PIDW=PI*FR/1500.
      CAK=2.*PIDW
C  CALCULATE SIZE OF INCREMENTAL AREAS.
      DELTA=SQRT(ZST*600./FR)
      DELTA=2.5
      DELX=DELTA
      IF(DIA/DELTA .LT. 20.) DELX=.05*DIA
C  CALCULATE NUMBER OF VERTICAL STRIPS TO USE.
      NW=INT(.9999+DIA/DELX)
      XINC=DIA/FLOAT(NW)
      CNSTX=PIDW*XINC
      WRITE(6,50)NW,XINC
   50 FORMAT(' THERE ARE',I3,' STRIPS OF WIDTH',F5.2)
C  DIVIDE EACH STRIP INTO SECTIONS.
      RAD=DIA/2.
      RAD2=RAD**2
C  CALCULATE FIELD.
      DO 80 IX=1,NXP
      DO 80 IZ=1,NZP
   80 PC(IX,IZ)=(0.,0.)
      XE=-RAD+XINC/2.
      DO 160 IW=1,NW
         YHT=SQRT(RAD2-XE**2)
         NH=INT(.9999+YHT/DELTA)
         YINC=YHT/FLOAT(NH)
         WRITE(6,60)NH,YINC
```

```
 60      FORMAT(' THERE ARE',I3,' VERTICAL DIVISIONS OF HT',F5.2)
         CNSTY=PIDW*YINC
         YE=YINC/2.
         DO 141 IH=1,NH
            R01=SQRT(XE**2+YE**2+FOC**2)
            ZD=ZST
            DO 120 IZ=1,NZP
               XD=XE
               DO 100 IX=1,NXP
                  R21=SQRT(XD**2+YE**2+ZD**2)
                  ARG=R01-R21
                  XARG=CNSTX*XD/R21
                  SNCX=1.
                  IF(ABS(XARG) .GT. .0001)SNCX=SIN(XARG)/XARG
                  YARG=CNSTY*YE/R21
                  SNCY=1.
                  IF(ABS(YARG) .GT. .0001)SNCY=SIN(YARG)/YARG
                  EXC=CEXP(CMPLX(-R21*ATT,-ARG*CAK))
                  C21=ZD/R21
         PC(IX,IZ)=PC(IX,IZ)+EXC*CMPLX(C21*SNCX*SNCY/R21/R01,0.)
                  XD=XD+XSP
 100           CONTINUE
               ZD=ZD+ZSP
 120        CONTINUE
            YE=YE+YINC
 141     CONTINUE
         XE=XE+XINC
 160  CONTINUE
      PMAX=0.0
      DO 200 IX=1,NXP
         DO 180 IZ=1,NZP
            PM2(IX,IZ)=(CABS(PC(IX,IZ)))**2
            PMAX=AMAX1(PMAX,PM2(IX,IZ))
 180     CONTINUE
 200  CONTINUE
      DO 300 IX=1,NXP
      DO 300 IZ=1,NZP
 300  PM2(IX,IZ)=PM2(IX,IZ)/PMAX
      WRITE(1)PM2
      CALL CONREC(PM2,NXP,NXP,NZP,0.1,1.,0.1,0,0,-682)
      CALL FLUSH
      STOP
      END
```

REFERENCES

Beard, R. E., R. L. Magin, L. A. Frizzell, and C. A. Cain, "An annular focus ultrasonic lens for local hyperthermia treatment of small tumors," Ultrasound in Med. and Biol. , vol. 8, No. 2, pp. 177-184, 1982.

Benkeser, P. J., "Unfocused multielement and tapered phased array ultrasound transducers for hyperthermia," Ph.D. Thesis, Dept. Electrical Engr., Univ. of Illinois, Urbana, Illinois, 1985.

Bowman, H. F., "Heat transfer and thermal dosimetry," J. Microwave Power, vol. 16, pp. 121-133, 1981.

Cain, C. A., personal communication, 1985.

Cain, C. A. and S.-I. Umemura, "Concentric-ring and sector-vortex phased-array applicators for ultrasound hyperthermia," IEEE Trans. Microwave Theory Tech., vol. MTT-34, pp. 542-551, 1986.

Cavicchi, T. J., and W. D. O'Brein, Jr., "Heat generated by ultrasound in an absorbing medium," J. Acoust. Soc. Am., vol. 76, pp. 1244-1245, 1984.

Chan, A. K., "Thermal effects due to the propagation of acoustic waves in biological tissues," Ph.D. Thesis, Dept. Electrical Engr., Univ. of Washington, Seattle, Washington, 1971.

Chan, A. K., R. A. Sigelmann, and A. W. Guy, "Calculation of therapeutic heat generated by ultrasound in fat-muscle-bone layers," Trans. on Biomed. Eng., vol. BME-21, pp. 280-284, 1974.

Chen, M. M., and K. R. Holmes, "Microvascular contributions in tissue heat transfer," Ann. N Y Acad. Sci., vol. 335, pp. 137-150, 1980.

Christensen, D. A., and C. H. Durney, "Hyperthermia production for cancer therapy: a review of fundamentals and methods," J. Microwave Power, vol. 16, pp. 89-105, 1981.

Corry, P. M., K. Jabboury, E. P. Armour, and J. S. Kong, "Human cancer treatment with ultrasound," IEEE Trans. Sonics and Ultrason., vol. SU-31, pp. 444-456, 1984.

Cravalho, E. G., L. R. Fox, and J. C. Kan, "The application of the bioheat equation to the design of thermal protocols for local hyperthermia," Ann. N Y Acad. Sci., vol. 335, pp. 86-97, 1980.

Dickinson, R. J., "An ultrasonic system for local hyperthermia using scanned focused transducers," IEEE Trans. on Biomed. Eng., vol. BME-31, pp. 120-125, 1984.

Endrich, B., H. S. Reinhold, J. F. Gross, and M. Intaglietta, "Tissue perfusion inhomogeneity during early tumor growth in rats," J. Nat. Cancer Inst., vol. 62, pp. 387-393, 1979.

Fessenden, P., E. R. Lee, T. L. Anderson, J. W. Strohbehn, J. L. Meyer, T. V. Samulski, and J. B. Marmor, "Experience with a multitransducer ultrasound system for localized hyperthermia of deep tissues," IEEE Trans. on Biomed. Eng., vol. BME-31, pp. 126-135, 1984.

Florrisson, C., "Ultraschalltechnik; ein Bericht uber das Erreichte," Kongressbericht der Erlanger Ultraschall-Tagung, S. Hirzel, Zurich, p. 19, 1949.

Freedman, A., "Sound field of a rectangular piston," J. Acoust. Soc. Am., vol. 32, pp. 197-209, 1960.

Frizzell, L. A., "Ultrasonic heating of tissues," Ph.D. Thesis, Dept. Electrical Engr., Univ. of Rochester, Rochester, New York, 1975.

Frizzell, L. A., C. S. Lee, P. D. Aschenbach, M. J. Borrelli, R. S. Morimoto, and F. Dunn, "Involvement of ultrasonically induced cavitation in the production of hind limb paralysis of the mouse neonate," J. Acoust. Soc. Am., vol. 74, pp. 1062-1065, 1983.

Frizzell, L. A., P. J. Benkeser, K. B. Ocheltree, and C. A. Cain, "Ultrasound phased arrays for hyperthermia treatment," Proc. of IEEE 1985 Ultrason. Symp., pp. 930-935, 1985.

Goss, S. A., and F. J. Fry, "Nonlinear acoustic behavior in focused ultrasonic fields: observations of intensity dependent absorption in biological tissue," IEEE Trans. Sonics and Ultrason., vol. SU-28, pp. 21-25, 1981.

Hahn, G. M., "Hyperthermia for the engineer: a short biological primer," IEEE Trans. on Biomed. Eng., vol. BME-31, pp. 3-8, 1984.

Halac, S., R. B. Roemer, J. R. Oleson, and T. C. Cetas, "Magnetic induction heating of tissue: Numerical evaluation of tumor temperature distributions," Int. J. of Radiat. Oncol. Biol. Phys., vol. 9, pp. 881-891, 1983.

Horvath, J., "Ultraschallwirkung beim menschlichen Sarkom," Strahlentherapie vol. 75, p. 119, 1944.

Hynynen, K., "Generation of ultrasonic fields and the acoustic properties of tissues," Chapter 4 in Hyperthermia, D. J. Watmough and W. M. Ross, Ed., Blackie & Son Limited, Glasgow, pp. 76-98, 1986a.

Hynynen, K., "The effect of nonlinear propagation and tissue interfaces on the temperature distribution during scanned, focussed ultrasound hyperthermia," Proc. of IEEE 1986 Ultrason. Symp., In press, 1986b.

Jain, R. K., "Bioheat transfer: mathematical models of thermal systems," Chapter 2 in Hyperthermia in Cancer Therapy, F. K. Storm, Ed., G. K. Hall Medical Publishers, Boston, pp. 9-46, 1983.

Kantor, G., "Evaluation and survey of microwave and radiofrequency applicators," J. Microwave Power, vol. 16, pp. 135-150, 1981.

Kremkau, F. W., "Cancer therapy with ultrasound: a historical review," J. Clinical Ultrasound, vol. 7, pp. 287-300, 1979.

Lele, P. P., "Induction of deep, local hyperthermia by ultrasound and electromagnetic fields," Radiat. Environ. Biophys., vol. 17, pp.205-217, 1980.

Lele, P. P., and K. J. Parker, "Temperature distributions in tissues during local hyperthermia by stationary or steered beams of unfocused or focused ultrasound," Brit. J. Cancer, vol. 45, Suppl. V, pp. 108-121, 1982.

Lyons, B. E., R. H. Britt, and J. W. Strohbehn, "Localized hyperthermia in the treatment of malignant brain tumors using an interstitial microwave antenna array," IEEE Trans. on Biomed. Eng., vol. BME-31, pp. 53-62, 1984.

Marmor, J. B., D. Pounds, and G. M. Hahn, "Clinical studies with ultrasound-induced hyperthermia," Nat. Cancer Inst. Monogram, vol. 61, pp. 333-337, 1980.

Myers, G. E., Analytical Methods in Conduction Heat Transfer, McGraw-Hill, Inc., New York, pp. 233-319, 1971.

Nussbaum, G. H., E. J. Seppi, E. G. Shapiro, and B. Emami, "Shaping of lateral heating fields with 'Helios:' a flexible multibeam ultrasound device for deep-tumor hyperthermia," Radiat. Res., 34th proc., p. 30, 1986.

Nyborg, W. L., "Heat generation by ultrasound in a relaxing medium," J. Acoust. Soc. Am., vol. 70, pp. 310-312, 1981.

Ocheltree, K. B., "Theoretical analysis of ultrasonic linear

phased arrays for hyperthermic treatment," M.S. Thesis, Dept. Electrical Engr., Univ. of Illinois, Urbana, Illinois, 1984.

Ocheltree, K. B., P. J. Benkeser, L. A. Frizzell, and C. A. Cain, An ultrasonic phased array applicator for hyperthermia, IEEE Trans. Sonics and Ultrason., vol. SU-31, pp. 526-531, 1984.

Ocheltree, K. B., and L. A. Frizzell, "Determination of power deposition patterns for localized hyperthermia: a transient analysis," Submitted to Int. J. of Hyperthermia, 1987.

Oleson, J. R., "A review of magnetic induction methods for hyperthermia treatment of cancer," IEEE Trans. on Biomed. Eng., vol. BME-31, pp. 91-97, 1984.

Roemer, R. B., W. Swindell, S. T. Clegg, and R. ,L. Kress, "Simulation of focused, scanned ultrasonic heating of deep-seated tumors: the effect of blood perfusion," IEEE Trans. on Sonics and Ultrason., vol. SU-31, pp. 457-466, 1984.

Short, J. G., and P. F. Turner, "Physical hyperthermia and cancer therapy," Proc. of IEEE, vol. 68, pp. 133-141, 1980.

Stauffer, P. R., T. C. Cetas, A. M. Fletcher, D. W. DeYoung, M. W. Dewhirst, J. R. Oleson, and R. B. Roemer, "Observations on the use of ferromagnetic implants for inducing hyperthermia," IEEE Trans. on Biomed. Eng., vol. BME-31, pp. 76-90, 1984.

Stauffer, P. R., T. C. Cetas, and R. C. Jones, "A system for producing localized hyperthermia in tumors through magnetic induction of ferromagnetic implants," Nat. Cancer Inst. Monogram, vol. 61, pp. 483-487, 1980.

Storm, F. K., D. L. Morton, L. R. Kaiser, W. H. Harrison, R. S. Elliott, T. H. Weisenburger, R. G. Parker, and Haskell, "Clinical radiofrequency hyperthermia: a review," Nat. Cancer Inst. Monogram, vol. 61, pp. 343-350, 1980.

Stremler, F. G., Introduction to Communication Systems, (Reading, Mass.: Addison-Wesley), pp. 75-100, 1977.

Strohbehn, J. W., and R. B. Roemer, "A survey of computer simulations of hyperthermia treatments," IEEE Trans. on Biomed. Eng., vol. BME-31 pp. 136-149, 1984.

Strohbehn, J. W., B. S. Trembly, E. B. Douple, and D. C. de Sieyes, "Evaluation of an invasive microwave system for heating deep-seated tumors," Nat. Cancer Inst.

Monogram, vol. 61, pp. 489-491, 1980.

Swindell, W., "A theoretical study of nonlinear effects with focused ultrasound in tissues: an acoustic brag peak," Ultrasound in Med. and Biol., vol. 11, No. 1, pp. 121-130, 1985.

Taylor, L. S., "Implantable radiators for cancer therapy by microwave hyperthermia," Proc. of IEEE, vol. 68, pp. 142-149, 1980.

Tucker, D. G., "Some aspects of the design of strip arrays," Acustica, vol. 6, pp. 403-411, 1956.

Underwood, H. R., E. C. Burdette, K. B. Ocheltree, and R. L. Magin, "A multielement ultrasonic hyperthermia applicator with independent element control," To appear in Int. J. Hyperthermia, 1987.

Van Den Berg, P. M., A. T. De Hoop, A. Segal, and N. Praagman, "A computational model of the electromagnetic heating of biological tissue with application to hyperthermic cancer therapy," IEEE Trans. on Biomed. Eng., vol. BME-30, pp. 797-805, 1983.

Zemanek, J., "Beam behavior within the nearfield of a vibrating piston," J. Acoust. Soc. Am., vol. 49, pp. 181-191, 1971.

VITA

Kenneth B. Ocheltree was born on June 8, 1960 in Norfolk, VA. He graduated from Lake Taylor High School, Norfolk, VA, in 1978.

In 1978, he began studies at Virginia Polytechnic Institute and State University in Blacksburg, VA. He graduated in 1982 summa cum laude in the Honors Program with a B.S. degree in Electrical Engineering.

Mr. Ocheltree began graduate studies at the University of Illinois in 1982. After a semester as a teaching assistant, he started working for Professor Leon A. Frizzell as a research assistant. He completed the work for an M.S. in Electrical Engineering in 1984.

Mr. Ocheltree has continued working with Professor Frizzell for his Ph.D. research. Papers published as a result of this work include "An ultrasonic phased array applicator for hyperthermia," by K. B. Ocheltree, P. J. Benkeser, L. A. Frizzell, and C. A. Cain in IEEE Transactions on Sonics and Ultrasonics, vol. SU-31, pp. 526-531, 1984; and "Determination of power deposition patterns for localized hyperthermia: a steady state analysis," by K. B. Ocheltree and L. A. Frizzell to appear in International Journal of Hyperthermia. While at the University of Illinois, appointments have included a Radiation Oncology Traineeship from the National Institutes of Health and a Caterpillar Fellowship.